Thermal power plant steel creep deformation measurement using digital image correlation

by
Melody van Rooyen

Dissertation presented for the degree of Doctor of Philosophy in the Faculty of Engineering at Stellenbosch University

The financial assistance of the National Research Foundation (NRF) in part towards this research is hereby acknowledged. Opinions expressed and conclusions arrived at, are those of the author and are not necessarily to be attributed to the NRF

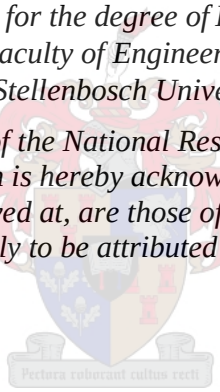

Supervisor: Prof Thorsten Hermann Becker

December 2020

Declaration

By submitting this dissertation electronically, I declare that the entirety of the work contained therein is my own, original work, that I am the sole author thereof (save to the extent explicitly otherwise stated), that reproduction and publication thereof by Stellenbosch University will not infringe any third party rights and that I have not previously in its entirety or in part submitted it for obtaining any qualification.

This dissertation includes three original papers published in peer-reviewed journals or books and one unpublished publication. The development and writing of the papers (published and unpublished) were the principal responsibility of myself and, for each of the cases where this is not the case, a declaration is included in the dissertation indicating the nature and extent of the contributions of co-authors.

Date: December 2020

Abstract

Following the rapid expansion of populations and industries with a concomitant rise in the demand for electricity in South Africa, increased focus has been directed to the structural health monitoring of critical components of aging thermal power plants. Long-term operation at high temperatures and loads encountered by plant components results in the degradation of material properties through creep exposure. Assessing creep damage using conventional creep testing poses several challenges in terms of large sampled material requirements for manufacturing standard specimen geometries. This is often not possible for service-retrieved material due to the limited availability for destructive sample removal. This dissertation documents a novel experimental technique that employs digital image correlation (DIC) to characterise the creep damage of service-exposed power plant steel through creep deformation measurement across nonuniform temperature and stress fields. Through the full-field property of DIC, multiple properties are measured from single specimens of X20CrMoV12-1 (X20) piping steel supplied by Eskom in virgin and various stages of service exposure.

Initial development of the technique involves a stereo-DIC setup adapted for high temperature deformation measurement. A temperature profile ranging from 550 – 600 °C is applied using resistive heating from a Gleeble thermomechanical simulator and measured using infrared imaging. Near-uniform stress profiles result from appropriate specimen geometry and region of interest selection. Several temperature-dependent elastic moduli and Poisson's ratios are measured from single specimens of virgin X20. Creating an extension to accelerated creep tests (shorter-term tests conducted at higher stresses and temperatures than encountered in service) used on virgin and various ex-service X20 states is explored. Creep curves at several temperatures are successfully realised from single specimens and are useful for identifying differences in creep resistance between ex-service levels in line with traditional damage classification through surface cavity density replication. Microstructural quantification using electron microscopy shows subgrain and $M_{23}C_6$ precipitate growth as well as Laves phase precipitation in higher damage states of X20. For middle damage classes, it is highlighted that several complementary damage assessment methods are necessary to identify differences in material deterioration. Zener-Hollomon parameters calculated from DIC-measured strains over the temperature profiles serve as suitable damage indicators.

Single camera DIC measurement of creep curves across spatially varying stress profiles is achieved with a waisted specimen design in a traditional creep testing setup for medium-term tests. Virgin X20 creep curves at 140 – 150 MPa are used to calibrate baseline parameters for a continuum damage mechanics model. Subsequently, the model is optimised for subgrain and precipitate parameters using the corresponding ex-service X20 creep responses. These microstructural-based parameters serve as comparative damage sensors that agree with traditional cavity and hardness-based methods.

This dissertation reveals that a wealth of creep data can be extracted from fewer X20 specimens, which is highly beneficial in characterising material integrity in a supplementary manner to existing methods. Expansion to small samples through small punch creep testing is also initiated. Although beyond the scope of this work, future aspirations are that these approaches will be integrated into life management philosophies to better guide inspection and maintenance strategies.

Opsomming

Die vinnige uitbreiding van bevolkings en industrieë en ‘n gepaardgaande toename in die vraag na elektrisiteit in Suid-Afrika veroorsaak dat toenemende fokus gerig word op die strukturele integriteit monitering van kritiese komponente in verouderende termiese kragstasies. Langtermyn bedryf teen hoë temperature en ladings wat komponente in aanlegte ondervind, lei tot die agteruitgang van materiaaleienskappe as gevolg van blootstelling aan kruip. Om kruipskade te assesseer deur konvensionele metodes bring verskeie uitdagings mee in terme van die hoeveelheid van materiaal monsters wat benodig word vir vervaardiging van standaard geometrieë. Dikwels is dit onmoontlik om groot monsters materiaal te versamel, as gevolg van die beperkte beskikbaarheid van materiaal vir destruktiewe toetse. Hierdie proefskrif dokumenteer ‘n oorspronklike eksperimentele tegniek wat digitale beeld korrelasie (DBK) gebruik om die kruipskade van kragstasie staal te karrakteriseer deur kruipdeformasie meting oor nie-uniforme temperatuur- en spanningsvelde. Verskeie eienskappe van enkele monsters X20CrMoV12-1 (X20) pypstaal, voorsien deur Eskom, word gemeet deur die volle-veld eienskap van DBK. Die monsters sluit nuwe staal sowel as beskadigde staal in.

Die oorspronklike ontwikkelde tegniek maak gebruik van ‘n stereo-DBK-opstelling aangepas vir hoë temperatuur deformasie metings. ‘n Temperatuur profiel wisselend van 550 – 600 °C word aangewend deur van weerstandsverhitting van ‘n Gleeble termomeganiese nabootser gebruik te maak en word gemeet met ‘n infrarooi kamera. Amper-uniforme spanningsprofiele kan verkry word deur gepaste monster geometrieë en areas van belangstelling te kies. Verskeie temperatuur-afhanklike modulusse van elastisiteit en Poisson-verhoudings word gemeet van enkele monsters van nuwe X20 staal. Aanpassing van die tegniek by versnelde kruiptoetse (korttermyn toetse wat uitgevoer word by hoër spannings en temperature as wat komponente indiens ervaar) op nuwe en verskeie dienslewes van X20 staal is ondersoek. Kruipkurwes by verskillende temperature word suksesvol gemeet van enkele monsters en is nuttig om verskille in kruipweerstandigheid te identifiseer tussen eks-indiens vlakke in lyn met tradisionele skade klassifikasie deur oppervlak mikroholte digtheid replikasie. Mikrostruktuur kwantifisering deur gebruik van elektron mikroskope wys subkorrel en $M_{23}C_6$ presipitaat-groei, sowel as Laves fase presipitering in hoër skadevlakke van X20 staal. Dit word beklemtoon dat vir gematigde skadevlakke verskeie komplimenterende metodes nodig is om die skade te assesseer om verskille in agteruitgang in die materiaal te identifiseer. Zener-Hollomon parameters wat vanuit vervormings oor die temperatuur profiele bereken word, dien as gepaste skade aanwysers.

Enkel-kamera DBK meting van kruipkurwes regoor ruimtelik-varieërende spanningsprofiele word behaal deur ‘n uurglas monster ontwerp in ‘n tradisionele kruiptoets-opstelling vir middelmatige termyn toetse. Kruipkurwes van nuwe X20 staal by 140 – 150 MPa word gebruik om basislyn parameters te kalibreer vir ‘n kontinue skade meganika model. Gevolglik word die model vir subkorrel en presipitaat parameters geöptimeer van die bypassende eks-indiens X20 staal kruipmetings. Hierdie mikrostruktuurgebasseerde parameters dien as vergelykende skade sensors wat ooreenstem met die tradisionele mikroholte- en hardheidsgebaseerde metodes.

Hierdie proefskrif onthul dat ‘n magdom kruipdata uit ‘n kleiner hoeveelheid X20 staal monsters onttrek kan word, wat voordelig is in die karakterisering van materiaal integriteit in ‘n aanvullende wyse tot bestaande metodes. Uitbreiding tot klein monsters deur klein-pons kruiptoetsing word ook in werking gestel. Alhoewel dit buite die bestek van hierdie werk strek, sluit toekomstige doelwitte in dat hierdie benaderings geïntegreer word in leeftyd bestuursfilosofieë om inspeksie- en instandhoudingstrategieë te verbeter.

Acknowledgements

I would like to extend my gratefulness to all those who assisted in the completion of this document. Firstly, I would like to express my gratitude to my supervisor, Prof Thorsten Becker, for his unfaltering support, inspiring advice and motivation during the course of my studies. As an academic mentor, the research gained great depth by following his expertise. As a life coach, Thorsten enhanced my perseverance, emotional well-being as well as my time management techniques. My sincere thanks also go to Dr Mahmoud Mostafavi for sharing his expertise regarding creep modelling and for inspiring the initial research concept for damage characterisation and future work for small punch creep testing.

Besides my supervisor, I would also like to acknowledge the staff of the Centre for Materials Engineering at the University of Cape Town for their willingness to assist in aspects of my experimentation. I am particularly grateful to Prof Rob Knutsen, Dr Sarah George and Mrs Penny Louw who granted me access to the Centre's laboratories. Special thanks is offered to Dr Johan Westraadt and Dr Genevéve Marx at the Centre for HRTEM (High Resolution Transmission Electron Microscopy) at Nelson Mandela University who assisted extensively with the microscopy in this work. Furthermore, gratitude is extended to the Eskom Power Plant Engineering Institute (EPPEI) Material Science Specialisation staff and students for supplying piping material and for providing enlightening feedback on the research results. This research would not have realised without the funding provided by the EPPEI program, the Technology and Human Resources for Industry Programme of the National Research Foundation as well as the Thuthuka Funding [grant number TTK13070320379]. My personal bursars, the Frank Wilhelm Scholarship, have also been extremely helpful and generous with their support. These initiatives provided a stable platform for my skill development and postgraduate education that would otherwise not have been possible.

My appreciation is also shown for the substantial support provided by my fellow students Mr Gerrit ter Haar, Dr Matthew Molteno and Mr Nur Dhansay in the Materials Engineering Research Group at the University of Stellenbosch. Within the same group, I thank Prof Deborah Blaine for her willingness to grant me access to her laboratories. The perseverance shown by the Mechanical Engineering Workshop staff and Mr Cobus Zietsman during the machining of my specimens is also highly valued. I am further appreciative of the assistance provided by members of the Solid Mechanics Research Group of the University of Bristol, in particular Prof Peter Flewitt, Prof David Knowles, Mr Satyajit Dey, Mr Steve Harding, Ms. Erin Holland and Dr Xander Warren. My thankfulness is also attributed to Dr Danielle Becker for her time spent on proofreading this dissertation.

Finally, I am grateful to my family, especially my loving mother Christina Johanna (née Westermann) and late father Frederick Petro van Rooyen, for their words of encouragement and inspiration during the entirety of my studies. Thanks is also owed to my sisters and brother for their positive and motivational tactics. Last but not the least, I would like to extend my sincere thankfulness to my fiancé Kevin Neaves for all his valued contributions, encouragement and his continuous motivation during my studies.

Dedication

For my dear father Frederick Petro van Rooyen, who guided and cheered every small step forward I took until his passing. We will meet again by the Big Tree in the Tsitsikamma, my Dad.

Table of contents

List of figures

Page

List of tables

Page

List of abbreviations

2D	Two-dimensional
3D	Three-dimensional
ADF	Annular Dark Field
ASTM	American Society for Testing and Materials
BMD	Bird-Mukherjee-Dorn
BS(E)	Backscatter Electron
CBS	Concentric Backscatter
CCD	Charge-Coupled Device
CDM	Continuum Damage Mechanics
CEN	European Committee for Standardisation
DIC	Digital Image Correlation
DVC	Digital Volume Correlation
EBSD	Electron Backscatter Diffraction
ECD	Equivalent Circle Diameter
EDM	Electrical Discharge Machining
EDS	Energy Dispersive X-Ray Spectrometry
EFTEM	Energy-Filtered Transmission Electron Microscopy
EPPEI	Eskom Power Plant Engineering Institute
EPRI	Electric Power Research Institute
ESKOM	Electricity Supply Commission
EXH	High damage X20 steel
EXL	Low damage X20 steel
EXM	Medium damage X20 steel
FEG	Field Emission Gun
FE(M)	Finite Element (Methods/Model)
FIB	Focused Ion Beam
FL	Focal Length
FOV	Field of View
GOS	Grain Orientation Spread
HAZ	Heat-Affected Zone
HT	High-Temperature
iDICs	International Digital Image Correlation Society
IPF	Inverse Pole Figure
KAM	Kernel Average Misorientation
KS	Kurjumov-Sachs
LED	Light-Emitting Diode
LMP	Larson-Miller Parameter
LT	Low-Temperature
LVDT	Linear Variable Differential Transducer
NETD	Noise-Equivalent Temperature Difference
NDE	Nondestructive Evaluation
NMU	Nelson Mandela University

OU	Open University
P91	X10CrMoVNb9-1 steel
PAG(B)	Prior Austenite Grain (Boundary)
PMMA	Poly(methyl methacrylate)
RMSE	Root Mean Square Error
RO	Ramberg-Osgood
ROI	Region of Interest
SA	South Africa(n)
SEM	Scanning Electron Microscope/Microscopy
SP(C)T	Small Punch (Creep) Test
STEM	Scanning Transmission Electron Microscope/Microscopy
SU	University of Stellenbosch
TEM	Transmission Electron Microscope/Microscopy
TMF(S)	Tempered Martensitic-Ferritic (Steel)
TKD	Transmission Kikuchi Diffraction
UCT	University of Cape Town
UK	United Kingdom
UoB	University of Bristol
VFM	Virtual Fields Method
WD	Working Distance
X20	X20CrMoV12-1 steel
(ZN)CC	Zero-Normalised Cross-Correlation
(ZN)SSD	Zero-Normalised Sum of Squared Differences

List of symbols

A	Zener-Hollomon pre-exponent
A_c	Average cavity area
A_M	Bird-Mukherjee-Dorn pre-exponent
a_i	Lighting scale coefficient
$a_0 \dots a_{11}$	Coefficients of pointwise horizontal displacement polynomial
B	Dislocation mobility
B_i	Initial high-angle block width
b	Magnitude of Burgers vector
b_i	Lighting offset constant
$b_0 \dots b_{11}$	Coefficients of pointwise vertical displacement polynomial
C	Power law coefficient
C_{LMP}	Larson-Miller constant
C_{ZNSSD}	Correlation coefficient calculated using ZNSSD
c	Speed of light
$D_{C,P,S,x}$	Cavity, precipitate, subgrain and arbitrary damage parameter, respectively
$\dot{D}_{C,P,S,x}$	Cavity, precipitate, subgrain and arbitrary damage parameter rate, respectively
D_o	Diffusivity frequency
d_c	Cavity diameter
E, E_{RT}	Elastic modulus at temperature and room temperature, respectively
ECD	Equivalent circle diameter of cavity
F	Force
FT	Colour filter transmission
F_i	Reference subset grey intensity value
F_{lens}	LED lens correction factor
$F_{min,nor}$	Minimisation and normalised minimisation objective function, respectively
$\bar{F}, \bar{G}$	Average reference and deformed subset grey intensity value, respectively
$\bar{F}_i$, $\bar{G}_i$	Difference between reference and deformed intensities at point i and subset average reference and deformed intensities, respectively
f	Precipitate volume fraction
G	Shear modulus
G_i	Deformed subset grey intensity value
h	Planck's constant
$h_{e,o}$	Ex-service and virgin X20 Vickers hardness, respectively
H, H^*	Normalised kinematic backstress and maximum normalised kinematic backstress, respectively
I	Blackbody radiation
I_{noise}	Surface radiation noise
I_{REL}	Relative radiant LED power
I_{signal}	LED lighting signal intensity
K''	High-angle block contribution to kinematic backstress

K_P	Precipitate coarsening pre-exponent
$K_{S1,S2}$	Strain activated and thermally activated subgrain coarsening parameters, respectively
$K_{1,2}$	Rate of reference stress evolution and steady-state value of reference stress, respectively
k	Boltzmann constant
k_A	Detachment factor constant
k_N	Cavitation constant
k_P	Precipitate Ostwald ripening rate constant
k_S	Subgrain growth coefficient (exponential law)
L_e	LED irradiance
LMP	Larson-Miller parameter
M	Half subset size
M_T	Taylor factor
$N_{c,r}$	Surface area cavity density and surface cavity density at rupture, respectively
N_V	Number volume density of precipitates
n	Stress exponent
$n_{c,p}$	Number of curves and points, respectively
np	Ostwald ripening exponent
P, P_i	Precipitate diameter and initial precipitate diameter, respectively
P_{LED}	LED radiometric power
P_Z	Zener pinning pressure
$Q, Q_{P,S}$	Creep, precipitate and subgrain growth activation energy, respectively
QE	Quantum efficiency
q^i	Creep stage-dependent exponent
R	Universal gas constant
R_c	Hourglass curvature radius
R_e	Reflectance
r_i	Initial LED spot radius
$S, S_{i,\infty}$	Subgrain short width, initial and steady-state subgrain short width, respectively
T, T_m	Temperature and melting temperature
t, t_r	Time and time to rupture, respectively
t_z	Specimen thickness
$u_{x,y}$	In-plane *x* and *y*-directional displacements
w_i	Minimum hourglass specimen width
x_i, x_i'	Horizontal pixel position in reference and deformed subset, respectively
x_o, x_o'	Horizontal central pixel position in reference and deformed subset, respectively
y_j, y_j'	Vertical pixel position in reference and deformed subset, respectively
y_o, y_o'	Vertical central pixel position in reference and deformed subset, respectively
Z	Zener-Hollomon parameter
Z_o	Distance from object to camera pinhole aperture

z_{WD}	Working distance
α	Hyperbolic sine law material constant
α_i	Creep stage-dependent constant
α_{LED}	LED lens angle
γ	Boundary surface energy per area
ΔZ	Deviation of planarity of object in 2D DIC
$\varepsilon^{Exp}, \varepsilon^{Pred}$	Experimental and CDM model predictions, respectively
$\varepsilon, \varepsilon_{c,i,r}$	Uniaxial, creep, instantaneous and rupture strain, respectively
$\dot{\varepsilon}, \dot{\varepsilon}_{m,ss}$	Creep, minimum creep and steady-state creep rate, respectively
$\varepsilon_{RR,\theta\theta}$	Meridional and circumferential small punch strains, respectively
$\varepsilon_{x,y,xy}$	In-plane uniaxial strain in *x* and *y*-direction and shear strain respectively
ε_z	Out-of-plane strain
ε_0'	Characteristic creep pre-exponent
θ	Average subgrain misorientation
λ	Wavelength
$\lambda_{M23C6,P}$	$M_{23}C_6$ and general interparticle spacing, respectively
λ_D	Damage tolerance/creep ductility factor
ν	Poisson's ratio
ρ_m	Mobile dislocation density
$\sigma, \sigma_{t,x,y}$	Uniaxial, true, x-direction and y-direction stresses, respectively
σ_e	Effective stress
σ_o	Threshold stress
σ_{or}	Orowan stress due to precipitate strengthening
σ_{ro}	CDM reference stress
σ_{ss}	Backstress due to solid solution strengthening
$\sigma_{ya,yt}$	Analytical and true stress in y-direction of hourglass specimens, respectively
σ_ρ	Backstress due to dislocation hardening
$\dot{\sigma}_{ro}$	Reference stress evolution in CDM model
$\dot{\sigma}_{yt}$	True stress rate in y-direction of hourglass specimens
τ	Shear stress
ϕ	Photometric transformation function

1 Introduction

Since 2008, South African (SA) communities and industries have faced a series of power outages as part of a load shedding schedule to prevent overloading of the national grid (Black Thursday, 2014). The resulting suspense of industrial, commercial, mining, agricultural and residential operations during power interruptions stifles economic growth. During the rotational load shedding in 2015, the retail industry alone, for instance, encountered a loss of approximately R 14 billion in revenue whilst spending R 700 million on alternative power sources (Goldberg, 2015). This has garnered increased attention to methods of sustaining reliable plant operation beyond the design lifetimes of the current fleet of thermal power stations operated by SA's local electricity utility, the Electricity Supply Commission (Eskom).

Plant reliability is largely tied to the material integrity and life management of the critical components that comprise the station systems and structures. One of the most prevalent damage mechanisms that limit the material life of components exposed to high temperatures over long time periods (> 20 years) is known as creep. Creep has long been the subject of focus of many materials-and plant maintenance-related journals and refers to the time-dependent deformation that is driven by applied stress and temperature. Remnant life estimation of creep-exposed materials, such as the X20CrMoV12-1 (X20) steel used for the main steam pipework in Eskom's current fleet, depends on an informed assessment of the in-service material state as strength is lost due to microstructural creep damage processes during exposure.

In the past decade, image correlation has evolved as a numerical tool for measuring full-field (over the entire surface measured) surface deformations through registration of differences in digital images taken of a loaded surface (Schreier, Orteu & Sutton, 2009:1). The versatility in experimental mechanics of image-based deformation measurement has been demonstrated in the extraction of various material properties for a range of materials (Orteu, 2009). One of the pertinent advantages of the full-field and non-invasive characteristics of image correlation is the ability to extract multiple deformation-based material properties at high temperatures from a single specimen. This has given impetus to the use of such techniques to characterise the properties of long-term, service-aged power plant steels that are often extracted in small amounts during infrequent planned shutdowns (Morris *et al.*, 2007). This work aims to draw on this ability for the development of a material-efficient damage characterisation framework.

This dissertation concerns the development of techniques based on image correlation capable of capturing tensile and creep-related deformation of X20 steel at various service exposures that can be used to identify the current material damage state. This doctoral project is an expansion of earlier MEng work by the author that focused on a stereo (two-camera) imaging technique for the extraction of thermomechanical and accelerated creep parameters of X20 steel at high temperatures. Following the MEng project, doctoral work commenced in 2016 at the University of Stellenbosch (SU). For the first two years, the original technique was refined through additional Gleeble thermomechanical testing at the Centre of Materials Engineering at the University of Cape Town (UCT). After this, advanced microstructural characterisation (based on the work of Marx (2019)) was performed on tested specimens in collaboration with the Centre for High Resolution Transmission Microscopy at the Nelson Mandela University (NMU). Electron microscopy facilities available at the Central Analytical Facilities in SU were also employed to this end. The application of a single-camera DIC technique to a waisted specimen geometry design for creep deformation measurements (pioneered by Muyupa *et al.* (2017)) occurred from 2017 – 2019 at the Open University (OU) in the United Kingdom (UK)

under the auspices of Dr. Alex Forsey. Parallel to this, a specialised small punch rig and stereo-microscope image correlation technique for small disc analysis was developed for a preliminary study at the Mechanical Engineering Department of the University of Bristol (UoB) in the UK under the guidance of Dr. Mahmoud Mostafavi (Vijayanand *et al.*, 2020).

The current work therefore expands on the parent project to include the comparative assessment of damage based on creep deformation of various service-aged X20 thermal plant piping steel whilst preserving material economy. The aim of the dissertation is to present a framework for creep deformation measurement for assessing creep damage using image correlation whilst exploring the underlying microstructural manifestations of creep degradation.

1.1 Project background

The lifeblood of a thriving economy is a stable supply of electricity that can trace the demand of expanding communities and industries. As the reserve margin between the supply and demand of electricity narrows, Eskom has been pressured to extend the operating lives of is fleet of coal-fired thermal power plants which supply over three-quarters of the country's energy needs (Jestin *et al.*, 2014). This is evident from Figure 1.1[1] which reveals that in 2016, over 85 % of the coal-fuelled stations were in operation beyond their original design life.

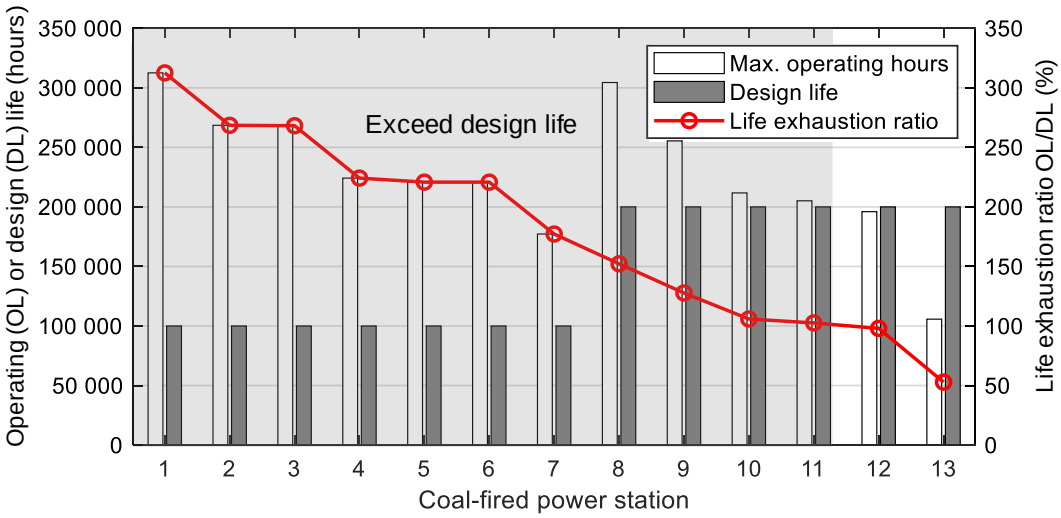

Figure 1.1: Life exhaustion of existing coal-fuelled Eskom plants at the end of 2016. Updated from Molokwane (2013)

Life extension should be achieved without a sacrifice in plant reliability which is heavily dependent on the proper functioning of critical plant components that are often subjected to aggressive environments, high temperatures and high loads (Wedderburn *et al.* 2012). In combination with prolonged operation beyond the designed life expectancy, these conditions have a detrimental effect on the material condition of aging systems. Maximising plant reliability therefore requires the monitoring of the integrity and residual life of the wide variety of materials that constitute the critical systems of power stations. The information obtained from life and condition monitoring of power plant materials not only guides inspection,

[1] Power station names have been omitted due to a confidentiality agreement with Eskom. Two new, incomplete coal-fired power station builds have been excluded from the illustration.

replacement and maintenance strategies, but also prevents the economic loss associated with catastrophic failure and subsequent power outages (Douglas, 1996; Paterson & Wilson, 2002).

The importance for material integrity assessment within the power generation industry was demonstrated in 2008 (and later between 2015 and 2019), when SA experienced nationwide power outages. Subsequent investigations revealed that leaks from boiler tubing accounted for a loss of over 20 % of the power-producing capability of these stations, resulting in forced outages (NERSA, 2008:24). Boiler tubes are categorised as high temperature and pressure (HTP) components as they are often subjected to temperatures as high as 600 °C with internal pressures exceeding 25 MPa, depending on the class of thermal power station (Shibli, 2011:273-274). The material damage levels of HTP components is one of the key limiting factors to the extension of the service life of power utilities beyond their original projected design life (Douglas, 1996; Dobrzański *et al.*, 2011).

Unwanted deformation and defect formation associated with creep damage mechanisms are one of the principle life-limiters of HTP components (such as steam pipework, headers as well as superheater and reheater tubing within boilers) during service (EPRI, 2007:8-7). A typical example of creep failure of power plant piping, ranging from initial crack development to final rupture, is shown in Figure 1.2 (Ali, 2014:10).

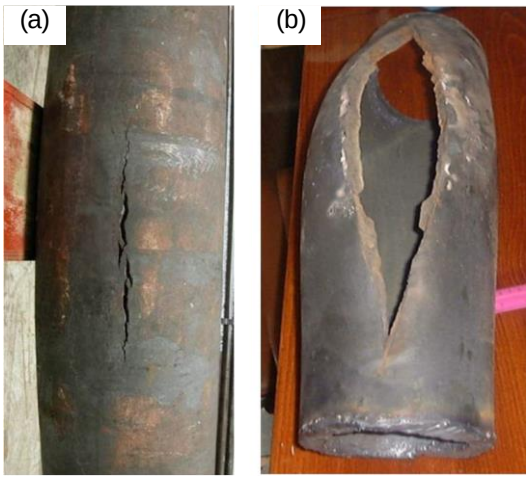

Figure 1.2: Example of creep-related piping failure including (a) initial crack formation and (b) final rupture (Ali, 2014: 10)

In response to the pressures of component life extension through material integrity assessment, Eskom launched the Eskom Power Plant Engineering Institute (EPPEI) Materials Science Specialisation Centre in 2012. This area of specialisation was established in partnership with UCT and SU and directs focus towards condition and life monitoring of power engineering steels. Several Master's and doctoral projects have been completed within this division at SU, including measurement of fracture properties using volume image correlation (Molteno, 2017), modelling ductile fracture through peridynamic theory and surface image correlation (Conradie, 2015), application of surface image correlation to small samples (Huchzermeyer, 2017) as well as several creep-related projects in progress at UCT (Jestin *et al.*, 2014).

This work feeds into the EPPEI initiative through the creep damage characterisation of the X20 grade steel which forms the bulk of the material typically employed in boiler tubing, turbines

and main steam pipework in Eskom's current fossil fuel power stations. Due to its long operating history, power stations are comprised of X20 material with a spectrum of damage levels for a range of operating hours, often categorised as low, medium to high damage based on conventional nondestructive evaluation (NDE) methods, such as cavity replication (Molokwane, 2013:67). Several limitations in these damage assessment techniques have been identified (Sposito *et al.*, 2010; Parker & Siefert, 2018), requiring improvement in the field of material condition monitoring of in-service components for effective plant maintenance.

1.2 Condition monitoring in thermal power plants

There are economic benefits associated with condition monitoring of HTP components given that the resulting annual plant maintenance accounts for less than 1 % of the cost of total reconstruction (van Zyl *et al.*, 2005). Eskom currently employs progressive inspection policies that involve a three-level phased approach to the condition monitoring of plant materials (EPRI, 2007). On the most basic level, the plant history of operating conditions is used to initially screen high-risk components and obtain an initial remnant life estimate (based on creep rupture analysis for piping, for instance). Should the remaining life fall short of design requirements, the next level is implemented in which NDE is performed to assess the extent of defect formation. Confirmation of damage triggers the final level that requires sampling of material for more in-depth integrity studies which ultimately ascertain whether maintenance scheduling, repair or replacement is required for continued safe operation (Scheepers *et al.*, 2010). This work is primarily concerned with this final level of condition assessment.

Following years of experience in the maintenance of power generation units, plant operators have several assessment techniques at their disposal (Bolton *et al.*, 1980; Bhadeshia *et al.*, 1998; Sposito *et al.*, 2010). Broadly, plant health indicators include: observations of microstructural degradation (growth in second-phase particles, grains, etc.); manifestations of damage (cavities and voids formed during service) and a reduction in mechanical strength (based on hardness, tensile, creep tests, etc.). In the context of this work, damage is used as a collective term that includes all aspects of the aforementioned material degradation due to creep[2].

At Eskom, the NDE technique of metallographic replication to study cavity formation is extensively employed for field evaluation of component health due to its relative simplicity and ease of preparation (Parker & Siefert, 2018). There have been situations, however, where such techniques were unable to provide a safety margin for maintenance measures for X20 components due to the propensity of this material to delay damage indicators to high life fractions (Trück *et al.*, 1991). Despite this, replica evaluation is still a useful tool for baseline assessments given the wealth of condition evaluation experience that is annually collected from over 60 000 replica at Eskom, contributing to a database of over one million entries (van Zyl *et al.*, 2005). Microstructural parameters can also be studied using replica with minimal material extraction, providing indications of damage. However, this task is complicated by the large amount of heterogeneity present in X20 microstructure coupled with the requirement of high resolution microscopy to observe fine features typical of particle-strengthened steels (Gupta *et al.*, 2015).

[2] Historically, creep damage refers to the intergranular decohesion that results in the formation of microscale cavities that eventually coalesce to form macroscale cracks (Lemaitre, 1996: 5). The adoption of damage as an umbrella term for all forms of material degradation in this work is inspired by continuum damage mechanics formulations where damage parameters are assigned to capture the evolution of both microstructural and cavity evolution (Semba *et al.*, 2008). This is directly investigated in Chapter 7.

Besides replication, the mechanical creep testing of extracted sample material provides the most conclusive creep data (Maharaj *et al.* 2009). Standard uniaxial creep tests can, for instance, provide the creep strain and strain rate of a material, which are common properties employed in component life prediction through constitutive (Hosseini *et al.*, 2012) and damage models (Dyson & Leckie, 1988).

Despite being a well-established technique for creep property measurement, creep tests have several limitations. The time-dependent nature of creep in plant materials makes the extraction of properties from laboratory experiments costly and time-consuming. In order to match the long service times of power plant steels, creep tests exceeding 200 000 h (approximately 23 years) have been performed on pre-service material (Kovpak, 1998). Within the context of life management, such tests are impractical as the time available for HTP life management has been greatly limited due to power demands, requiring techno-economic decisions to be made in an accelerated yet informed manner. Furthermore, practical difficulties during experimentation as well as variation in steel composition and heat treatment often result in creep rates with excessive scatter and no bearing on the actual material properties (Roy *et al.*, 2013).

Post-exposure creep testing (performed on sampled service-exposed material), on the other hand, has long been a preferred method for condition monitoring as the starting microstructure is more representative of in-service conditions (Bolton *et al.*, 1980; Regis & D'Angelo, 1989). However, these tests are specimen-intensive in order to obtain a sense of repeatability through a scatter band of the resulting data. Each stress-temperature testing condition requires an individual specimen, necessitating the removal of large spool sections which is often not feasible due to material limitations or constraints on repair times. Moreover, the spatial resolutions of traditional strain measurements made within these tests are unable to capture highly localised strain fields typically encountered across microstructurally complex regions, such as welds (Maharaj *et al.*, 2009).

As a workaround, plant engineers often employ small-sample techniques, such as small punch creep testing (SPCT)[3], that require scooping or core drilling of a small amount of material to manufacture discs in the order of 8 mm diameter by 0.5 mm thickness (EPRI, 2007:11.4). Site-specific material extraction is possible for measuring aged weld creep behaviour using SPCT and in most cases the sampled component is still operable (Hurst & Matocha, 2015). However, there is evidence to suggest that sample excavation sites act as stress-raisers during service that severely limit the component life and require remediation (Rouse *et al.*, 2013). The standard output data of such tests are load-displacement curves which require a thorough correlative study with uniaxial testing to obtain the equivalent steady stress-strain counterpart (Gupta *et al.*, 2015). This requirement precludes the economy of material and effort originally sought from small-scale accelerated testing.

1.3 The role of digital image correlation in creep deformation measurement

A candidate technology for maximised property extraction from a single specimen is a class of full-field measurement techniques based on photomechanical image processing, known as digital image correlation (DIC). The basic operating principle of DIC involves locating correspondences between a reference digital image and subsequent images acquired from a

[3] The application of SPCT to measuring the embrittlement of ex-service, low-alloy steam turbine rotor steel from an Eskom power plant is demonstrated in an EPPEI-based Master's thesis by Tshamano (2017) at UCT.

material surface during loading (Pan, 2011). Surface deformations are then obtained by discretising the area of interest into smaller regions (termed subsets) and tracking their positions relative to the undeformed image based on the matching of grey level intensities. The tracking algorithm depends on a suitable random variation in contrast provided by a speckle pattern on the observed material surface (Sutton *et al.*, 2000).

Input images employed by DIC can be sourced from any imaging device, ranging from commercial cameras and light microscopes to scanning electron microscopes. This flexibility makes DIC length-scale-independent and is thus applicable to measurements made across nano- to macroscale areas (Ren *et al.*, 2015). With careful control of speckle pattern quality, displacement measurement accuracies of up to 0.01 pixels are possible (Reu, 2012). Extensions to multiple camera systems in stereo-DIC have allowed measurements on curved surfaces and when out-of-plane motion of the test piece is unavoidable (Jones & Iadicola, 2018). For these reasons, DIC has seen growing popularity for the measurement of elastic material properties (at small strains), fracture and fatigue behaviour for a range of materials including aluminium alloys, refractory ceramics, nuclear grade graphite and composites (Orteu *et al.*, 2007; Fazzini *et al.*, 2011; Becker *et al.*, 2012; Busca *et al.*, 2014). The adoption of DIC in industrial applications has also encouraged ongoing efforts to standardise its use (Jones & Iadicola, 2018).

Arguably, the greatest strength of DIC lies in the ability to provide spatially resolved material properties when the measured displacement and strain fields are combined with other spatially varying experimental parameters such as stress, temperature or material character[4]. Coupled with the inherent noncontact nature of imaging methods, the potential therefore exists for DIC to overcome the temperature limits and sizable footprints of conventional strain gauges and extensometers during high-temperature creep testing (Gales *et al.*, 2012). In this manner, an increased density of creep deformation data can be obtained from a single specimen (typically 1 000 to 10 000 measurement points) whilst experimentation time and material use is reduced in comparison to standard methods (Avril *et al.*, 2008).

Based on the presented argument, it is no surprise that DIC has taken up a role as a condition-monitoring technique in thermal power plants. Online creep strain monitoring together with defect detection of parent and weld sections of pressurised piping has been investigated, with particular focus oriented towards improving speckle pattern durability between maintenance intervals within the harsh operating conditions of power stations (Morris *et al.*, 2007; Maharaj *et al.*, 2009). There have been few attempts, however, to fully exploit the rich density of creep deformation measurements that can be made using DIC across spatially distributed stress or temperature fields. To add to this, there has also been no attempt to interface DIC with post-service creep testing. Consequently, the recourse to full-field approaches is necessary from the perspective of the economy of the sampling volume of limited ex-service X20[5]. Such an approach has the potential, alongside other assessment techniques, to guide informed decisions regarding component repair and replacement and improve plant survivability.

1.4 Summary of project aims

The core purpose of the project is the development of a set of techniques that employ DIC to measure deformation across spatially varying temperature or stress fields applied to single specimens of X20 power plant steel. The aim is to utilise the developed techniques for high-

[4] Such as the gradient of microstructures across different areas of the heat-affected zones encountered in welds.
[5] Ex-service X20 supplied by Eskom often have operating times ranging from 100 000 to 200 000 h (11 to 23 years).

temperature measurement of temperature-dependent tensile properties as well as temperature- and stress-dependent creep parameters.

In the context of preserving thermal power plant structural integrity, the overarching intent is the use of the developed techniques as creep damage assessment aids to complement existing condition-monitoring tools. As a result, exploration into the feasibility of using the developed techniques to assess creep damage of X20 at various levels of service exposure lies at the core of this work. Such efforts are closely paired with the observation of microstructural manifestations of damage using advanced electron microscopy techniques. Although beyond the scope of the current study, the work potentially serves as a useful contribution to the incorporation of DIC into plant integrity management through the guidance of effective maintenance strategies. Further details regarding the project objectives and scope are covered in Chapter 3.

1.5 Dissertation outline

For readers who wish to direct their focus to specific chapters instead of a front-to-back approach, the following section summarises the philosophy surrounding the document structure. The chapters presented below, aside from Chapters 2, 3 and 8, follow the development of DIC-based techniques for different purposes in a consecutive fashion and are presented in the form of predominantly self-contained journal articles that have either been submitted or have been accepted. Each of these chapters contain a preamble specifying the contributions offered by co-authors. Post-submission summaries discussing the insight gained following the article submission conclude the chapters of accepted journal articles. On account of this format, no standalone literature study has been performed. Instead, a general overview of key concepts is provided in a background study in Chapter 2 and a revision of relevant literature is provided in the introductory subsections of each chapter formatted as a paper. As each chapter is meant to be a standalone element, some repetition will exist with respect to the continuity of the dissertation as a whole.

Chapter 2 provides relevant background information including concepts of creep deformation, cavitation and microstructural manifestations of creep damage, especially regarding X20 steels employed in the thermal power industry. An overview of the working principles of DIC with respect to processing parameters as well as the associated resolution and uncertainty inherent to this technology is also briefly provided.

The core hypothesis of this work is developed in Chapter 3 with particular focus placed on the list of research aims and objectives that are ordered to reflect the development of the techniques from Chapters 4 to 7. This chapter also outlines the scope and motivations for choices of materials, equipment and experimental methods.

Chapter 4 introduces a technique for extracting multiple temperature-dependent tensile properties from single specimens of virgin X20 using the freedom of spatial measurement offered by DIC. The challenges of high noise-to-signal ratios associated with measuring small (tensile) strains at high temperatures using DIC is introduced and mitigated in Section 4.3, setting a foundation for subsequent chapters that involve high-temperature strain measurement.

This technique is extended to accelerated creep testing using variable temperature profiles in Chapter 5 where comparisons in DIC-measured creep curves are made between various ex-service states of X20. The effect of nonuniform thermal profiles on the resulting stress

distribution within specimens is also investigated. Results are compared with conventional testing and the impact of such accelerated creep testing on the microstructure is also detailed through advanced microscopy and statistical methods of comparison.

Chapter 6 compares several damage assessment techniques based on mechanical and microstructural observations of the relative deterioration of ex-service X20. Quantitative analysis is performed on the DIC-based results of Chapter 5 by using constitutive creep models that are then linked to quantitative microstructural observations of pre-tested ex-service X20.

The observations of Chapters 5 and 6 are used to establish the damage indicators of interest to ex-service X20 in Chapter 7. This chapter adapts an existing continuum damage mechanics creep model for damage parameter extraction using DIC over spatially varying stress fields. Microstructural foundations of these parameters are also explored and compared between material states.

Finally, Chapter 8 entails discussions that critically assess the merits and downfalls of the various proposed techniques and how these methods contribute to the overarching goal of material-efficient damage characterisation of service-retrieved materials. The foundations of future work involving *ex situ* SPCT strain measurements using DIC is introduced in this chapter, creating links to the recommendations of complementary structural integrity techniques to existing procedures currently adopted by Eskom. This dissertation concludes with Chapter 9 which provides a succinct summary of valuable contributions made by this work in line with the research objectives highlighted in Chapters 1 and 3.

2 Background reading

The following chapter introduces creep behaviour of fossil energy power plant steels, specifically X20 steel, as well as conventional and unconventional testing methods. Due to the extensive use of the DIC technique in this work, an overview of the working principles is also provided.

2.1 Creep deformation and damage behaviour of power engineering alloys

Following the concern of the impact of power plants on climate change and fossil fuel consumption, efforts have been focussed throughout history on raising the thermodynamic efficiencies of steam cycles. This is mainly achieved by raising the steam temperatures and selecting high temperature-resistant steel alloys for steam piping and other critical components (Viswanathan *et al.* 2006). The extreme temperature and pressure conditions over an extended service life introduce the damage mechanisms of creep. Broadly, creep is defined as the time-dependent deformation that occurs when a mechanically stressed material is subjected to temperatures in excess of 40 % of its absolute melting temperature (Hertzberg *et al.*, 2012:190). Various mechanisms are responsible for the evolution of creep in a material which are, in turn, a function of time, temperature, stress and the evolution of underlying microstructural elements.

2.1.1 Creep curves and mathematical modelling

The classical representation of metallic creep behaviour is a three-stage creep curve, as shown in Figure 2.1a and b, which traces the creep strain ε_c and rate over time t, respectively. Firstly, when the load is applied, there is an instantaneous elastic (or plastic) strain response ε_i. During primary creep, the creep rate $\dot{\varepsilon}_c$ is initially accelerated but decreases towards a steady rate $\dot{\varepsilon}_{ss}$ in the secondary stage. The decreasing creep rate is attributed to a strain hardening effect that results from the reduction in dislocation mobility. This effect is balanced with thermal recovery during the secondary stage, where dislocations gain the ability to climb obstacles and annihilate through diffusional processes. The steady-state creep regime usually occupies the longest duration of the creep test. The final stage is known as the tertiary stage and involves acceleration in creep rate until final rupture of the specimen at time t_r and rupture strain of ε_r (Abe, Kern & Viswanathan, 2008:5). In this stage, a number of microstructurally related damage mechanisms occur, including grain growth, changes in second-phase morphology and the formation of creep voids, cavities and cracks (Aghajani, 2009).

Most heat-resistant steels employed in engineering applications, however, display creep curves that differ from the classical shape. Ongoing evolution of the microstructure of these alloys occurs during creep, resulting in the lack of a steady-state stage (Aghajani *et al.*, 2009). Instead an inflection point follows the primary creep stage, resulting in a minimum creep rate $\dot{\varepsilon}_m$ before creep rates accelerate into the tertiary stage as shown in Figure 2.1b. The curve shape is also influenced by the test stress σ and temperature T, with higher stresses and temperatures resulting in higher creep rates and shorter rupture times (Callister, 2007:240).

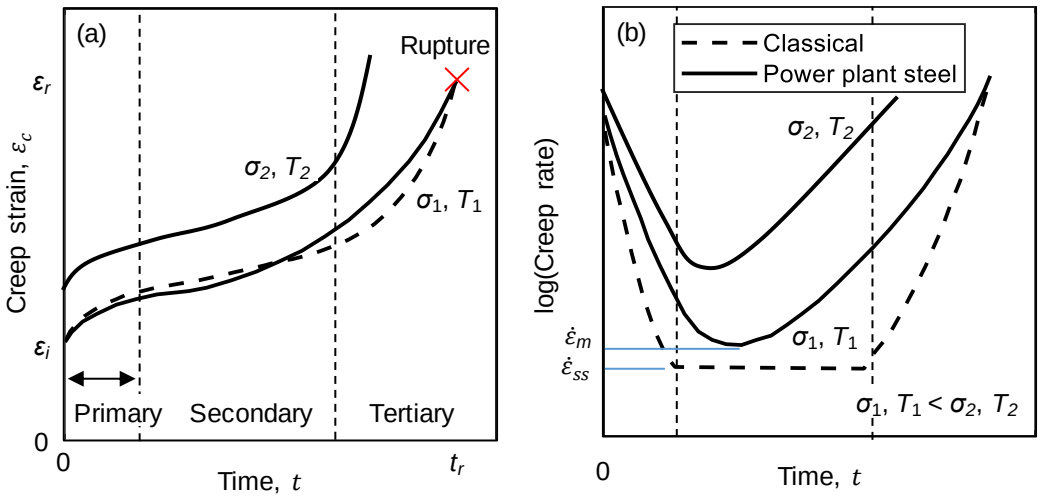

Figure 2.1: Shapes of (a) creep strain-time and (b) rate-time curves that result from uniaxial constant-load creep tests. The effect of increasing stress σ and temperature T is also indicated

Power plant component life estimation relies heavily on the sensible characterisation of the material creep behaviour which involves accurate representation of creep curves. To this end, a wealth of phenomelogical constitutive equations have been proposed, an overview of which can be found in Penny & Marriott (1995). On the most basic level, creep curve modelling consists of strain-time analytical forms such as $\varepsilon_c = \sum_{i=1}^{3} \alpha_i t^{q_i}$ time exponent q_i is 1/3 for the primary stage (i = 1), 1 for the secondary stage (i = 2) and 3 for the tertiary stage (i = 3) and α_i is the associated constant (Benham, Crawford & Amstrong, 1996:575). As indicated in Figure 2.1, however, these constants were unable to capture the stress dependence of creep rates leading to descriptions of the secondary creep rate $\dot{\varepsilon}_m$ by the Norton relation modified with an Arrhenius rate equation (Gupta *et al.*, 2015):

$$\dot{\varepsilon}_m = C \exp\left(-\frac{Q}{RT}\right)\sigma^n \qquad (2.1)$$

where C is a temperature-dependent constant, Q is the activation energy, R is the universal gas constant and n is the stress exponent.

The ability of Equation (2.1) to capture the rate-controlling mechanism responsible for creep through calculation of n and Q has long been the impetus to its extensive application in power plant steel creep analysis (Shrestha *et al.*, 2012). Across large stress ranges, however, the operating creep deformation mechanism changes resulting in a change in the stress dependency of the strain rate. These limitations were later resolved using the hyperbolic sine power law $(\sinh(\alpha\sigma))^n$ (where α is a material constant) in lieu of the power law in Equation (2.1) (Hertzberg *et al.*, 2012:169). Finally, full descriptions of creep curves have been achieved by incorporating the hyperbolic sine law into a continuum damage mechanics (CDM) framework (McLean & Dyson, 2002). CDM formulations (Chapter 7) account for damage resulting from the evolving microstructure and formation of cavities through state variables and require less parameters than parametric methods, proving great versatility in long-term creep curve modelling of power plant steels (Oruganti *et al.*, 2011; Gupta *et al.*, 2015).

2.1.2 Deformation mechanisms

The complexity of creep stems from the interlinked contributions from several competing deformation mechanisms as well as the variation of the dominant mechanism as a function of temperature and stress as established through Norton's law parameters (Subsection 2.1.1). One means of conveniently displaying the full spectrum of stress-temperature fields for which particular creep mechanisms dominate is the deformation mechanism map. Figure 2.2a shows such a map typical of ferritic-martensitic steel used in the power industry (redrawn from Ghoniem *et al.* (2013)). The vertical axis is stress normalised by room temperature Young's modulus E_{RT} and the horizontal axis is homologous temperature which is the temperature normalised by the melting temperature T_m. For pure iron, T_m is 1 800 K (Frost & Ashby, 1982).

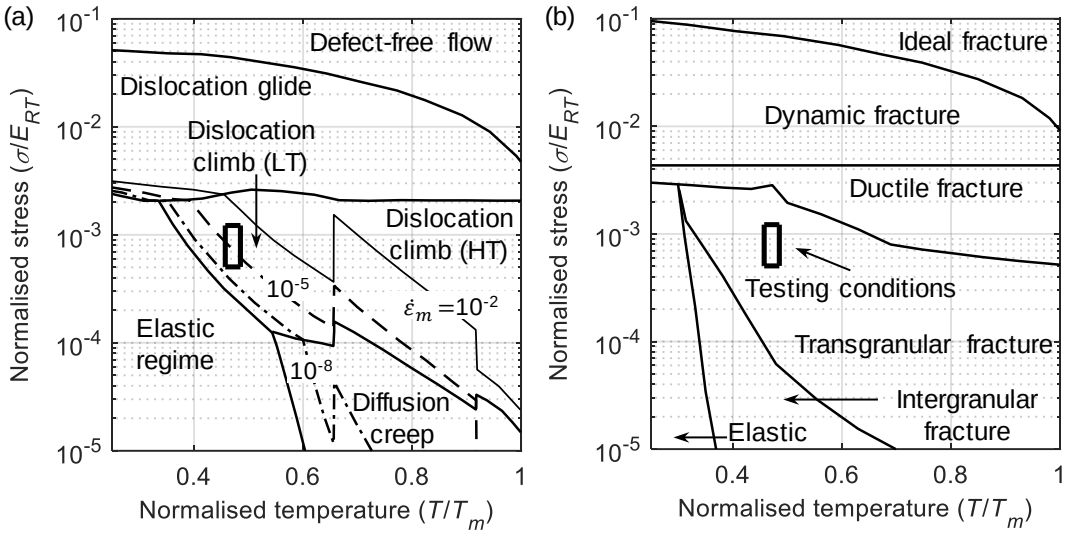

Figure 2.2: Typical (a) deformation mechanism map and (b) fracture mechanism map of power plant steels. The range of stress and temperatures employed in this study are highlighted. Note LT = low-temperature; HT = high-temperature. Redrawn from Ghoniem *et al.* (2013) and Shrestha *et al.* (2013), respectively

Developed by Ashby (1972), the map is constructed by equating pairs of the constitutive equations (special cases of Equation (2.1)) to define the boundaries of the fields. Within these fields, one mechanism contributes a faster strain rate than the others and results in a certain type of fracture as shown in Figure 2.2b (redrawn from Shrestha *et al.* (2013)) which is discussed in the next section. These mechanisms include crystal instability, grain boundary sliding, dislocation glide, dislocation creep and diffusional creep (Hosford, 2009:260). For further reading on creep mechanisms, consult the work by Ghoniem *et al.* (2013), Kassner (2009), Greenwood (2007) and Frost & Ashby (1982). Under the typical operating conditions of thermal power plants, diffusional and dislocation creep are the regimes that dominate creep deformation with the former mechanism prevailing at normal operating conditions (Ghoniem *et al.* 2013).

Diffusion and dislocation creep mechanisms are controlled by structural imperfections within the material lattice, including point, line and planar defects. Point defects include vacancies which are vacant lattice sites that were previously occupied by atoms. On the other hand, grain boundaries are forms of planar, interfacial defects that isolate two adjacent grains with

dissimilar crystallographic orientations (Callister, 2007:93). During the thermally activated diffusion creep regime at low stresses, atoms diffuse via vacancies either through the lattice bulk (Nabarro-Herring creep) or along grain boundaries (Coble creep), as shown in Figure 2.3a. This results in n equal to 1 for both regimes, Q equal to the lattice diffusion and grain boundary diffusion activation energy and C as inversely proportional to the square and cubic grain diameter, respectively.

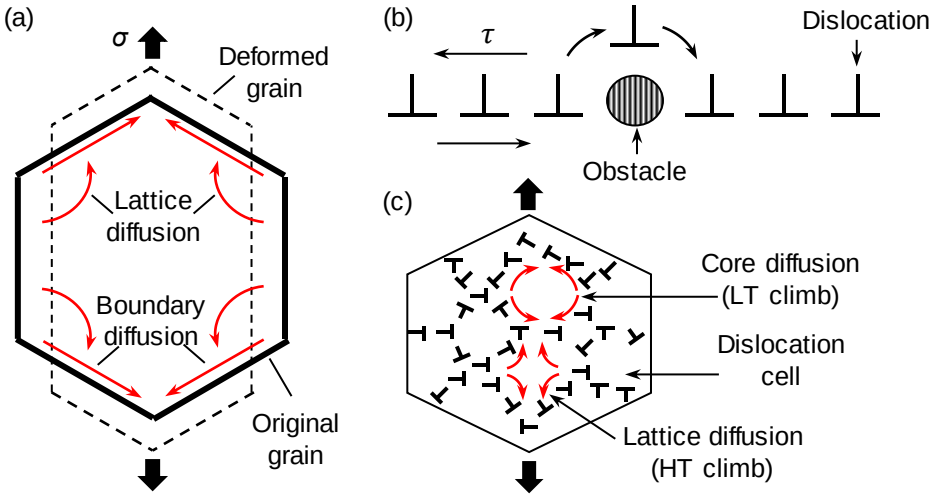

Figure 2.3: Creep controlled by (a) a diffusional mechanism and (b) dislocation climb either by (c) dislocation lattice or core diffusion. Red arrows indicate atomic motion. The applied shear stress is τ and the normal stress is σ

Lastly, dislocation lines are linear defects that result in a misalignment of lattice atoms and largely control the strength of metals. Plastic deformation in the dislocation creep regime is attributed to the motion of dislocations through the lattice in a process known as slip (Hosford, 2009:113). Creep rates from this mechanism are regulated by the rate at which the dislocations bypass inherent obstacles such as grain boundaries, precipitates, other dislocations and subgrain structures, as shown in Figure 2.3b. Most of the testing performed in this work is conducted within this regime. At higher temperatures, edge dislocations gain the ability to climb over obstacles as vacancies diffuse towards the defect through the lattice, illustrated in Figure 2.3c. Such high-temperature climb has n equal to 5 and Q equal to the lattice diffusion activation energy which is usually close to that of lattice self-diffusion in α-Fe at about 250 kJ/mol (Shrestha *et al.*, 2012). Low-temperature dislocation climb relies on dislocation core diffusion (Figure 2.3c), resulting in higher creep rates with n equal to 7 and Q equal to 60 – 70 % of the lattice diffusion activation energy at about 170 kJ/mol (Frost & Ashby, 1982).

2.1.3 Creep damage evolution and assessment techniques

During service, high-pressure steam pipework in power plants undergo degradation in creep resistance due to a variety of damage processes. These include the development of cavities and changes in microstructural elements, including precipitates and the tempered martensitic structure (Dobrzański *et al.*, 2011:260). Cavity damage development has long been related to lifetime exhaustion as illustrated in Figure 2.4 where damage is categorised into four classes that dictate maintenance actions. Insets are obtained from the VGB-TW 507 technical guideline

(Müsch *et al.*, 1992) for X20. After sustained exposure times, cavities nucleate at grain boundaries and within the matrix at carbides and inclusions (Wu & Sandström, 1995). Oriented cavities then develop at boundaries perpendicular and at 45° to the loading direction, followed by their coalescence to form microcracks. Near the end of component life, macrocracks develop before failure. At low stresses, creep cavitation and coalescence on grain boundaries results in brittle intergranular fracture as shown in Figure 2.2b. High stresses cause void nucleation and growth at inclusions, resulting in more ductile transgranular fracture (Abe *et al.*, 2008:351). A similar classification method is used by Eskom within its progressive inspection philosophy (Molokwane, 2013).

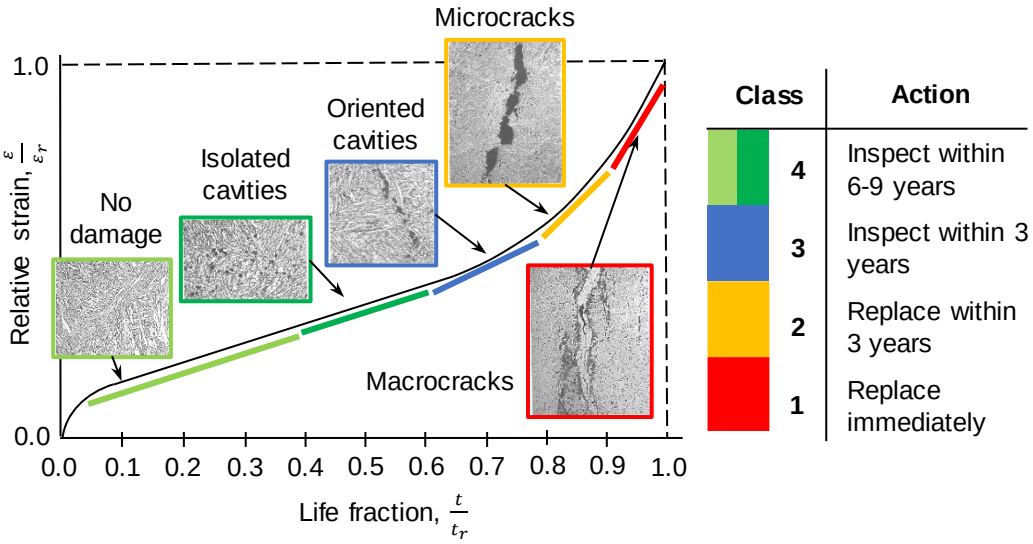

Figure 2.4: Creep damage development and assessment based on cavities. Insets from Müsch *et al.* (1992)

Traditionally, condition monitoring in power stations is done to establish inspection timing and support life management of critical components (Auerkari *et al.*, 2007). Surface replication is one of the most widely employed damage assessment techniques based on cavities and has been standardised for field examination such as in the ASTM standard E1351 (ASTM, 2002). The process involves applying a solvent-softened acetate film to a polished and etched piping surface. After evaporation of the solvent, the tape containing a negative image of the surface microstructure is removed and analysed under a light or electron microscope to calculate cavity densities. Such an approach is convenient for on-site examination due to its quasi-nondestructive nature and short preparation time. Due to the direct link between cavity density and creep strain (Eggeler *et al.*, 1989), this information is supplied to a remnant life model such as the one developed by van Zyl *et al.* (2005):

$$\frac{t}{t_r} = 1 - \left(1 - \frac{N_c}{N_r}\right)^{\lambda} \qquad (2.2)$$

where N_c is the cavity density at time t, N_r is the cavity density at rupture time t_r and λ is the creep ductility parameter.

Besides cavitation, additional damage processes can be defined in terms of microstructural evolution of subgrain, precipitates and dislocations. These processes are expanded on in Subsection 2.2.2. Microstructural scatter and material inhomogenieties (Gupta *et al.*, 2015), however, preclude the sole reliance on microstructural techniques for damage assessment.

When more advanced characterisation is required, post-exposure mechanical testing is done using conventional creep testing facilities as well as small-sample options such as SPCT (discussed in Appendix B). Conventional creep tests to measure creep deformation as a function of time have been standardised in ASTM E139 (ASTM, 2011a). These tests are usually conducted in uniaxial tension for ductile metals, under constant load and isothermal conditions. As indicated in Figure 2.5, a typical setup consists of a balance level that loads the specimen from a weight pan. The entire specimen, which is usually heated by a radiation furnace, must be raised to the testing temperature using feedback information from a thermocouple. Tests conducted until rupture of the specimen, often in the absence of accurate deformation measurements from extensometry, are termed stress-rupture tests, providing time to rupture and strain at rupture information. In determining the minimum creep rates, prolonged test periods of 10 000 h or longer are suggested by the ASTM standard E139 (ASTM, 2011a). For most of the existing creep data, however, tests range from 100 to 1 000 h, with data at longer times usually obtained from extrapolation (Straub, 1995).

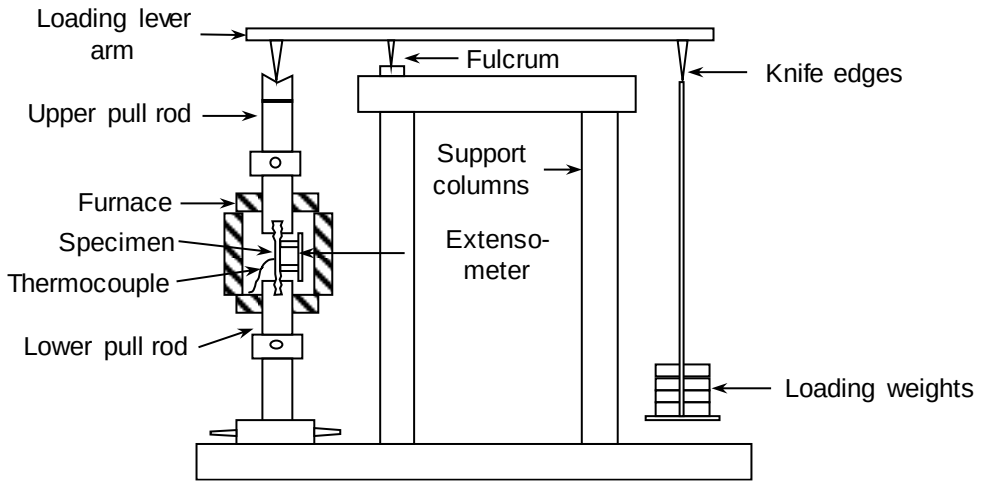

Figure 2.5: Conventional constant-load creep testing setup

One means of extrapolating creep data is the use of time-temperature parameters such as the commonly used Larson-Miller parameter $LMP = T(\log_{10} t_r + C_{LMP})$ where C_{LMP} is usually taken as 33 (Shrestha *et al.*, 2013). This parameter, derived from the Arrhenius rate equation, indicates a correlation between stress and time to rupture which could be used to predict rupture times at lower stress and temperatures (Penny & Marriott, 1995:207). Based on the considerable amount of scatter (about 15 %) typical of test data as well as the inability to capture microstructural evolution at longer testing times, careful consideration should be given to the use of LMP for remnant life prediction (Gupta *et al.*, 2015).

2.1.4 Unconventional creep testing methods

Due to the material intensive nature of conventional creep testing methodologies (such as those adopted by ASTM standards, for instance), plant engineers often adopt non-traditional

techniques for studying creep properties of ex-service materials. As this work was inspired by the same motivation, it is deemed appropriate to summarise previously developed creep characterisation techniques in this section. These testing methods range from small-sample testing (including subsized versions of conventional creep specimens, impression creep, small punch testing (SPT)) to constant-strain rate tests and accelerated testing. The main benefit of the small-sample category is that the low material requirements are suitable for "quasi-nondestructive" sample extraction which would not impact the operability of the component under investigation (Mathew *et al.*, 2016). The latter category brings about a time advantage.

2.1.4.1 Small-sample methods

Miniature versions of conventional test geometries most closely resemble the creep behaviour of full-sized conventional specimens, showing similar activation energies and stress exponents (Olbricht *et al.*, 2013). These test pieces, such as the one shown in Figure 2.6 with gauge diameters of 3 mm and gauge lengths of about 17.5 mm, are small enough to be extracted from scoop samples extracted from pipes. Although no major correlative efforts are required to compare small-sample data with standard testing, oxidation and differences in diffusion mechanisms are postulated to cause differences in key creep properties such as the rupture time (Olbricht *et al.*, 2013). For this reason, strict requirements are placed on the testing rigs in terms of loading, deformation measurement and providing an inert environment.

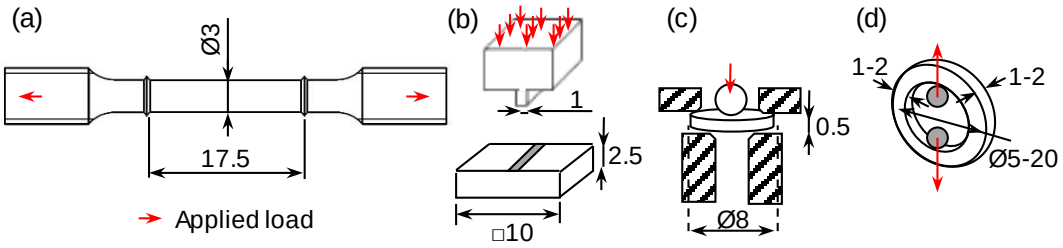

Figure 2.6: Small specimen geometries including (a) small-scale conventional, (b) impression creep, (c) small punch testing and (d) small ring types. All dimensions are in mm

Impression creep testing has been used extensively for creep deformation analysis since its invention in 1977 (Ali, 2014:33). This test involves the application of a constant load on a flat-ended indenter which, through the mechanism of creep, pushes into the surface of a square sample (Figure 2.6b) at elevated temperature. Details regarding the primary and secondary creep stages are resolved using this technique, with good correlations with minimum creep rates determined via standard means (Sun *et al.*, 2008). Besides the easy implementation of this test using standard creep testing equipment, the small sample dimensions ($10 \times 10 \times 2.5$ mm^3) allow measurement of creep deformation characteristics of heat-affected zones (HAZ) with some cases in literature predicting Type IV crack initiation in a steam header (Sun *et al.*, 2008). Sun *et al.* (2008) demonstrated that sequential application of stepped load and temperature on CrMoV steels can also be used to obtain multiple minimum creep rates from a single sample, further improving material efficiency. Tertiary creep behaviour and rupture times, however, are not measurable using this technique.

In a similar manner to impression creep testing, SPT specimens can be extracted from site-specific locations, such as welds, typically in the form of 8 mm diameter discs that are 0.5 mm thick, shown in Figure 2.6c. Creep testing involves high temperatures, an inert atmosphere and

the application of a constant load to a spherically ended indenter or ball as it is pushed into a thin disc clamped along its edges which consequently bulges into a recess until fracture (Mathew *et al.*, 2016). In this manner, the full creep curve (including tertiary) is generated in terms of load, displacement and time data. Originally developed in the 1980s to measure the post-irradiation mechanical properties of nuclear alloys from TEM-sized samples (Manahan *et al.*, 1981), SPT has seen increased use in the tensile (Madia *et al.*, 2013), fracture (Tshamano, 2017) and creep characterisation (Izaki *et al.*, 2009) of service-aged base and weld materials.

In spite of the ubiquity of SPT in creep behavioural studies, no finalised standardisation exists with recent attempts by the European Committee for Standardisation (CEN) focused on establishing a code of practice known as CWA 15627 (CEN, 2007). Furthermore, conversion of load-displacement output variables to stress-strain data required by creep analysis demands careful post-analysis procedures such as membrane stretching analytical models developed by Chakrabarty (1998) and numerical approaches such as finite element methods (Dymáček & Milička, 2009). The complexities of the evolving biaxial stress state, together with the sensitivities of results to geometrical variations (Komazaki *et al.*, 2017), disc clamping (Andrés & Dymáček, 2016), atmospheric conditions (Nakata *et al.*, 2016a) and indenter material factors (Hurst & Matocha, 2015), makes it difficult to relate results to standard uniaxial data.

Recently (Ali, 2014), there have been advancements in the development of a small ring creep testing geometry with dimensions as shown in Figure 2.6d (elliptical variations are also available). Such rings are easily machinable from small material samples and benefit from a simple loading setup whereby the load-line displacements between pins are measured over time. In contrast to other "stiff" small specimens, the geometry allows for relatively large equivalent gauge lengths that generate easily measurable deformations even at low strains typical of stresses and temperatures that are closer to in-service conditions (Hyde & Sun, 2009). Furthermore, a wide variety of materials can be tested with this technique, unlike those for impression creep where materials with creep strengths exceeding the indenter properties cannot be tested.

2.1.4.2 Other techniques

Apart from the small ring tests, most small-scale tests are conducted at elevated temperatures and stresses when compared to in-service conditions leading to shorter-term tests. Although it is well understood that extrapolation from these elevated conditions to component operating conditions results in the overestimation of component life (Subsection 2.1.3), the rapid turnaround required for making fast maintenance decisions during planned shutdowns often warrants accelerated creep testing of service-exposed materials. Amongst these methods are isostress accelerated, stress relaxation and constant-strain rate tests.

Isostress tests involve using elevated temperatures and constant stresses close to those encountered in service (< 100 MPa) as researchers have found that life fraction rules are more applicable for temperature-dependent extrapolations than stress-based extrapolations (Abe *et al.*, 2008:655). Such techniques have successfully demonstrated differences in rupture times between aged pipe materials from tests lasting less than 100 h (Regis & D'Angelo, 1989). Stress relaxation tests entail monitoring the decrease in stress over time of a specimen subjected to a constant total strain and elevated temperature. As elastic strains are converted into inelastic strains, the creep rate is obtained from the elastic modulus-normalised stress rate. Bose *et al.* (2004) showed that for tests lasting less than 7 h, this technique has produced rupture lives in

agreement with those determined traditionally for 9 % Cr steel and simulated similar microstructural evolution to long-term tests encouraged by higher activation energies. Finally, constant-strain rate tests at elevated temperatures produce stress-strain curves like those encountered in uniaxial tensile tests. Such curves have been successfully used to observe embrittlement in notched specimens of 9 % Cr turbine blades (Woodford, 2005) and to measure power-law constants of virgin and retired 12 % Cr steels (El Rayes & El-Danaf, 2017).

2.2 X20 steel for power plant applications

Throughout the 20th century, the advancement of plant efficiencies drove research efforts to develop creep strength-enhanced alloys for use in critical components in power plants subjected to ever increasing service temperatures. From these efforts, 9 – 12 % Cr ferritic-martensitic steels became widely employed for piping, tubing, headers and turbine forgings in larger power stations (Bendick *et al.*, 1993). Of these steels, X20 has been widely employed in SA and other countries due to its relatively high creep strength and microstructural stability (Jesper, 1985).

2.2.1 Brief history of 9 – 12 % Cr power plant steels

Following the rapid expansion of populations and industries with a concomitant rise in the demand for electricity, fuel conservation and reduction of CO_2 emissions over the past century, increased focus has been directed to improving thermal efficiencies of coal-fired power plants. Higher thermal efficiencies of fossil-fuelled, steam-powered plants can be achieved by elevating the temperature and pressure in the turbine units (Cengel & Boles, 2011). Figure 2.7 shows how the increase in operating conditions involved in subcritical to ultra-supercritical power stations paved the evolution of structural plant alloy developments throughout the past century (Abe, 2014; Ennis, 2014; Yin *et al.*, 2014).

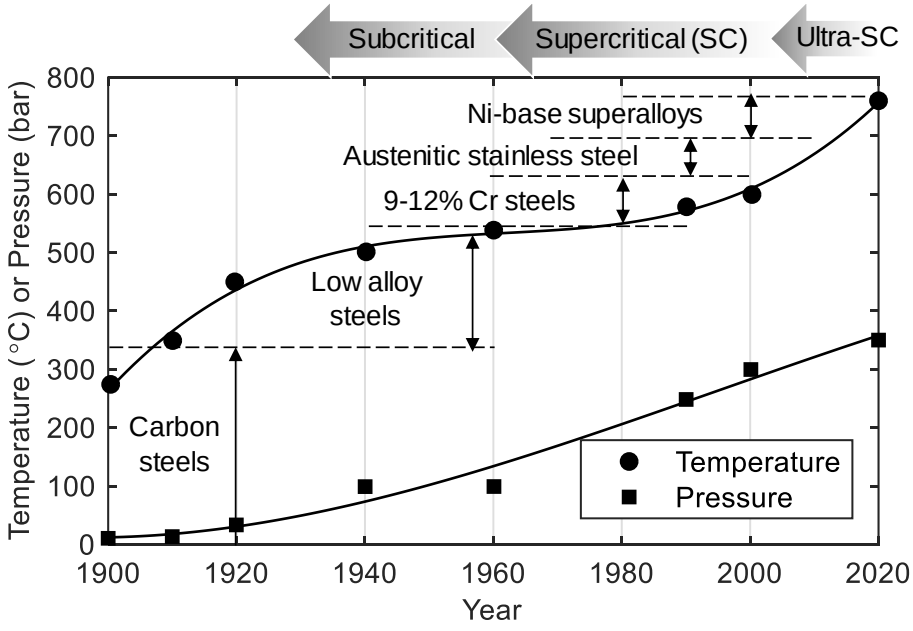

Figure 2.7: Development of power plant steels according to increases in operating temperatures and pressures. Redrawn from Abe (2014), Ennis (2014) and Yin *et al.* (2014)

This hierarchy of the alloy groups can best be explained by comparing their creep rupture strengths as summarised in Figure 2.8 (Abe, 2014; Ennis, 2014).

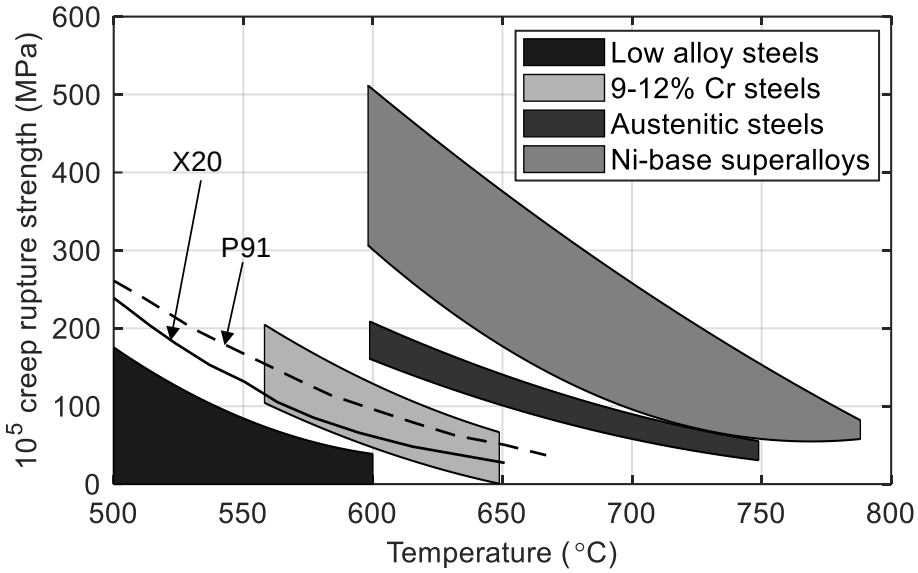

Figure 2.8: Creep rupture strength at 100 000 h versus temperature for various groups of power plant steels and alloys. Redrawn from Abe (2014) and Ennis (2014)

Of particular interest are the tempered martensitic-ferritic steels (TMFS) containing 9 – 12 % Cr as shown in Figure 2.7 and Figure 2.8. The development of 9 – 12 % Cr steels arose from a need for boiler and steam piping materials with enhanced creep and mechanical strength, corrosion and oxidation resistance, fracture toughness, high heat capacity and low thermal expansion coefficients as well as metallurgical stability under intensifying service conditions. One of the first TMFS steel alloys to find widespread application as steam pipelines and tubing in German steam plants in 1963 was the 12 % Cr steel X20 (with the 100 000 h creep rupture strength shown by the solid line in Figure 2.8) which was a 12CrMoV steel standardised for use in steam piping under DIN 17175 (Kalwa, 1985; EPRI, 2006). Since then, X20 has been employed in thermal power and chemical plant HTP components such as superheater and reheater tubing, boilers, main steam piping as well as turbine blades and encasings at temperatures up to 565 °C in Europe and other continents (Bakic *et al.*, 2014). Despite service histories of X20 exceeding 200 000 h with apparent slow rates of creep damage accumulation, carefully controlled procedures are required to avoid cracking of repair weldments of this material (Fleming *et al.*, 2000; Auerkari *et al.*, 2007). As a result, X20 was excluded from ASME regulations and was superseded by X10CrMoVNb9-1 (with the ASTM designation P91 for piping and T91 for tubing) in the 1970s which has improved creep strength (indicated by dashed line in Figure 2.8) and fabricability (Ennis, 2014).

The X20 steel, however, is currently relevant to fossil-fuelled power industry for several reasons. Firstly, this steel remains in use in aging coal-fired power stations across the world, including several subcritical power utilities in SA, as indicated by the map in Figure 2.9 adapted from Kalwa (1985). Secondly, the large capital expenditures associated with the construction of new power plants (using P91 and other more advanced creep-resistant steels) is often less economical than extending the life of existing plants (APEC, 2005). Furthermore, the early creep failures of P91 in newer plants when compared to X20 has been linked to increased

sensitivity of the precipitation hardening (discussed in Subsection 2.2.2) of the former steel to heat treatments (Auerkari *et al.*, 2007). This would suggest a benefit in the continuation of using X20 in existing (subcritical) fossil fuel power stations largely due to the vast knowledge accumulated of the steel behaviour over half a century of its use as well as its long performance history without appreciable creep damage (Jesper, 1985).

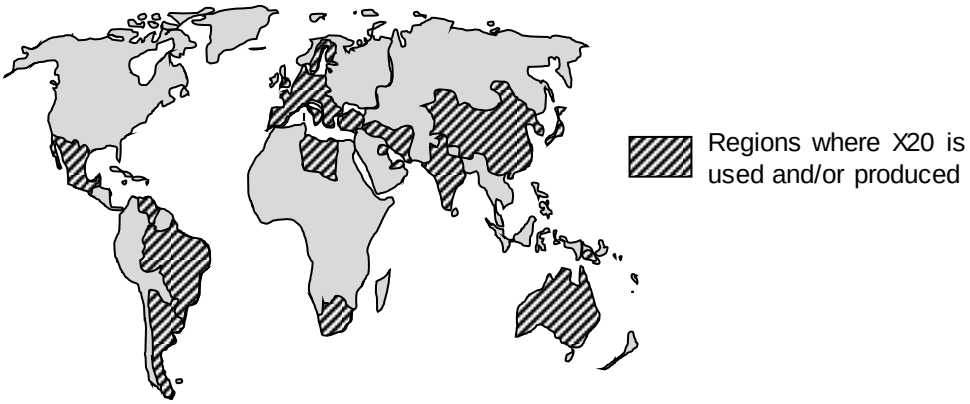

Figure 2.9: Regions where X20 was fabricated and/or employed in power plants. Adapted from Kalwa (1985)

2.2.2 Microstructural creep strengthening mechanisms

The creep strength of TMFS is linked to their underlying microstructural features. Following an austenising heat treatment at 1020 – 1070 °C and air cooling to less than 150 °C, the intermediate microstructure is brittle martensite which is then annealed at 730 – 780 °C to form tempered martensite with improved ductility (EPRI, 2006). Typically, the initial microstructure consists of martensitic laths secured with boundary $M_{23}C_6$ carbide precipitates (where M is mostly Cr, but can also be Ni, Mo and Fe). MX carbonitrides (where M is V or Nb and X is N or C) are smaller precipitates found within the grain interior along with high dislocation densities (Yan *et al.*, 2013). This is schematically illustrated in Figure 2.10.

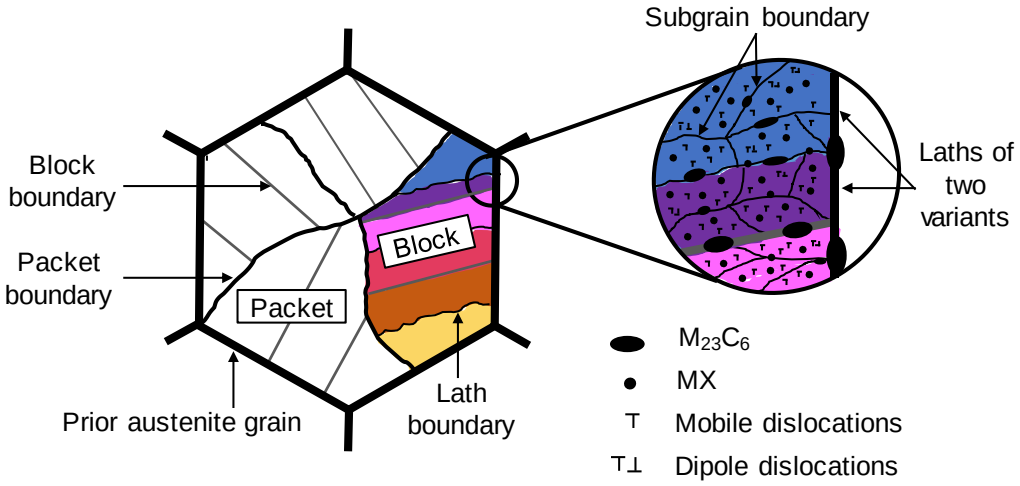

Figure 2.10: Schematic representation of the hierarchical as-tempered martensitic microstructure and precipitate distribution of X20

Classically, two sets of interlaced martensitic laths of two Kurjumov-Sachs (KS) variants with small misorientation between each other are arranged within blocks (Morris *et al.*, 2013). Three types of blocks (one for each Bain axis) in turn make up a packet and four packets (each of which shares a close-packed plane with a reference austenite plane) form a prior austenite grain. Each contribution of the mentioned microstructural features to the creep strengthening mechanisms of X20 and other TMFS will be discussed within three categories: substructure hardening; particle strengthening and solid solution strengthening.

2.2.2.1 Substructure strengthening

X20 microstructure features a high dislocation density (around 0.6×10^{14} m^{-2}) within the lath interiors resulting from the martensitic transformation of the steel (Pešička *et al.*, 2003) as shown in Figure 2.11a. Three types of dislocations are present, namely mobile dislocations, dipole dislocations and boundary dislocations (Yadav, Kalácska, *et al.*, 2016). Strength contribution due to dislocation hardening is given by (Abe, 2014):

$$\sigma_\rho = 0.5\, M_T\, G\, b \sqrt{\rho_m} \qquad (2.3)$$

where M_T is the Taylor factor (≈ 3), G is the shear modulus, b is the Burgers vector length and ρ_m is the mobile dislocation density. Dislocation hardening does not assist long-term creep strength due to recovery processes that occur at elevated temperatures. During creep, ρ_m decreases as dislocations are rearranged within laths into walls to form subgrain boundaries (as shown in Figure 2.11c) resulting in a lower strength contribution as indicated in Equation (2.3).

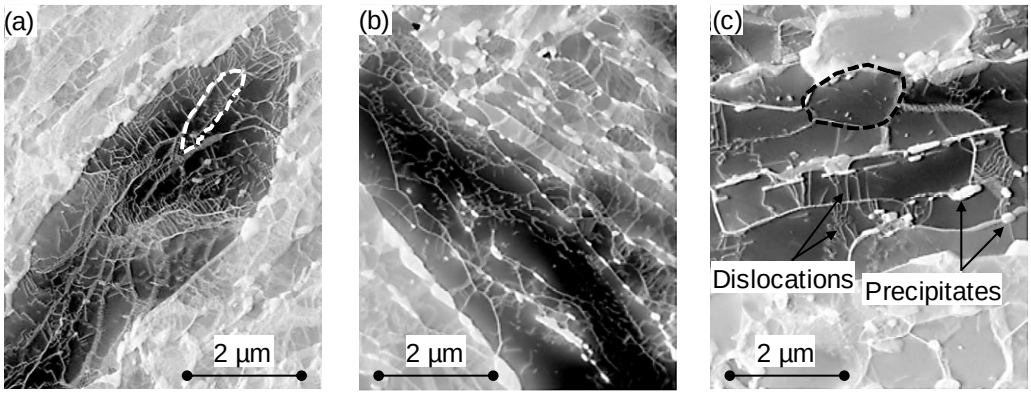

Figure 2.11: Micrographs showing the substructure of X20 (a) in an as-tempered state, (b) thermally aged at 139 971 h at 550 °C and (c) creep tested at 139 971 h, 550 °C and 120 MPa. A lath and subgrain is outlined in white and black in (a) and (c), respectively. Mobile dislocations are indicated in (c). Redrawn from Aghajani (2009)

Subgrains are fine grains with minor widths (from fitted ellipses) ranging from 0.2 to 0.7 µm that along with mobile dislocations contribute to substructure strengthening (Aghajani *et al.*, 2009). In Chapter 6, the term "micrograins" is adopted in lieu of "subgrains" in order to include subgrains with low (≤ 1°) misorientation angles with adjacent subgrains as well as micrograins with high misorientation angles (50° – 61°) with neighbouring micrograins (Pešička *et al.*, 2004).

Mobile dislocation density measurements made by Peŝiĉka *et al.* (2004) using transmission electron microscopy (TEM) on an X20 specimen subjected to primary creep revealed a decrease in creep rate during the primary stage that corresponded with an order of magnitude drop in free dislocation density. This reveals that within the creep regime, mobile dislocations are transporters of plastic deformation. Subgrain boundaries are key obstacles in absorbing these mobile dislocations and so are prominent contributors to creep strengthening in X20. Annihilation of mobile dislocations as they combine with dislocations within the subgrain boundaries results in recovery of the substructure. This recovery is manifested as a growth of subgrains with a concomitant reduction in total dislocation density and is especially evident when strain and stress is applied in addition to thermal aging as revealed by the exponential evolutional law proposed by Qin *et al.* (2003):

$$\ln S = \ln S_\infty + \ln \frac{S_i}{S_\infty} \exp\left(\frac{-\varepsilon_c}{k_s}\right) \qquad (2.4)$$

where S represents the minor width of the subgrain after creep exposure, S_i is the initial subgrain width, ε_c is the creep strain, k_s is a stress-dependent growth constant (~ 0.12) and S_∞ is the steady-state subgrain width given by $S_\infty = 10\,G\,b/\sigma$. Equation (2.4) suggests that strain is solely responsible for subgrain coarsening however during long-term creep the interaction between creep deformation and growth of precipitates is responsible for the loss in the pinning effect of subgrain boundaries (Yan *et al.*, 2013).

2.2.2.2 Precipitate strengthening

The ability to maintain a fine substructure is largely tied to the distribution of $M_{23}C_6$ particles along subgrain boundaries and dispersive MX particles within the grain interiors. $Cr_{23}C_6$ precipitates in X20 are about 65 – 130 nm in diameter and are the ideal size for pinning and preventing the migration of subgrain boundaries and the resultant growth of grains. Smaller VN particles, have diameters in the range of 35 – 70 nm and are effective in pinning mobile dislocations. Common precipitates in X20 are shown in Figure 2.12a (Danielsen *et al.*, 2007).

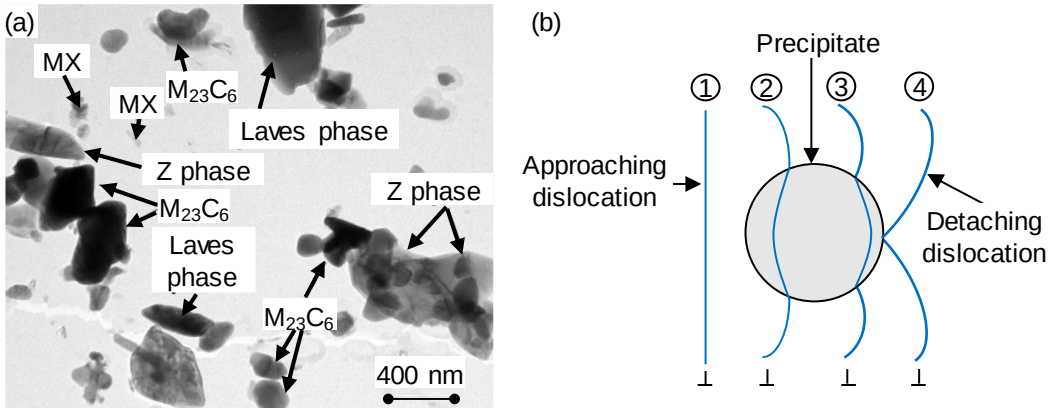

Figure 2.12: (a) Representation of the main precipitates in X20 steel and (b) a schematic of the mechanism of dislocation climb and detachment at a particle interface. Redrawn from Danielsen *et al.* (2007) and Zhao *et al.* (2018), respectively

Armaki *et al.* (2011) found that $M_{23}C_6$ carbides contribute a larger role in subgrain stability based on the close relationship between subgrain size and interparticle spacing. This is due to

the carbides exerting Zener pinning forces on the boundaries which is directly proportional to the volume fraction and inversely proportional to the particle size (Fedorova *et al.*, 2014). Coarsening of $M_{23}C_6$ occurs 10 times faster than for thermally stable MX, and together with agglomeration results in the loss of Zener pressure with the progress of creep (Kostka *et al.*, 2007; Prat *et al.*, 2010). Particle coarsening often occurs by the Ostwald ripening mechanism which is described by:

$$P^{np} - P_i^{np} = k_P t \tag{2.5}$$

where P and P_i are the mean particle diameters formed after time t and before testing respectively, np is an exponent depending on the diffusion mechanism and k_P is the growth coefficient that depends on the diffusion coefficient of atoms in ferrite (Maruyama *et al.*, 2001). In X20, $M_{23}C_6$ coarsens with np = 3 whilst MX diameters remain fairly stable during long-term creep (Aghajani, 2009).

Although significant creep strength enhancement is reported in 9 % Cr steels to come from finely dispersed MX particles, such an improvement is still under continual debate for 12 % Cr steels such as X20 (Hu & Yang, 2003; Aghajani *et al.*, 2009; Zhao *et al.*, 2018). Nonetheless, MX particles are known to pin dislocations via a detachment mechanism (illustrated in Figure 2.12b) that manifests as a threshold stress (Zhao *et al.*, 2018). The concept of a threshold stress was originally introduced to avoid the calculation of unreasonably high stress exponents and activation energies for creep (refer to Chapter 6) and is defined as the minimum stress required for creep deformation to occur at a specific temperature (Shrestha *et al.*, 2012). As mentioned in Chapter 6, this value is subtracted from the applied stress and is theoretically limited to a maximum value known as Orowan stress given by (Abe, 2014)

$$\sigma_{Or} = \frac{0.8\, M_T\, G\, b}{\lambda_P} \tag{2.6}$$

where the interparticle spacing λ_P of MX type particles can be calculated by (Holzer, 2010)

$$\lambda_P = \sqrt{\frac{\ln 3}{\pi\, N_V\, P} + P^2} - \frac{1.63}{2}\; P \tag{2.7}$$

where N_V is the number volume density. As the particles coarsen, there is a decrease in the number density and an increase in the diameters resulting in larger interparticle distances as predicted by Equation (2.7) and subsequently lower threshold stresses as indicated by Equation (2.6). This means that more of the applied stress is used to drive creep deformation, resulting in increased creep rates (El Rayes & El-Danaf, 2017).

In contrast to MX and $M_{23}C_6$ that form during tempering, Laves phase and Z phase are intermetallic and Cr-rich nitride compound phases, respectively, that precipitate during creep exposure and are largely detrimental to creep strength. The precipitation of Z phase, CrVN, degrades creep resistance through the dissolution of VX particles as Cr diffuses through the ferritic matrix to these particles (Kaibyshev *et al.*, 2010). Z phase particles have an initial size of 50 – 80 nm but coarsen at very fast rates to 200 nm during creep of 12 % Cr steels (Maruyama *et al.*, 2001; Danielsen *et al.*, 2013). Z phase transformation was found to reduce the expected lifetime by an order of magnitude in 12CrWMoCuVNbN tube steel in operation

in a Danish power plant where the increased Cr content accelerates Z phase precipitation (Hald, 2008). However, no evidence of this phase has been found in X20 tested at 550 °C and 120 MPa for 140 000 h (Aghajani *et al.*, 2009).

Similarly, Laves phase particles of type Fe_2Mo in X20 are large particles (> 200 nm) that form preferentially along lath and prior austenite boundaries due to the segregation of Si and Mo to these boundaries (Isik *et al.*, 2015). Due to the rapid coarsening of Laves phase (where $np = 4$ in Equation (2.5)), the ability to pin subgrain boundaries deteriorates with the time of creep exposure (Spigarelli, 2013). Furthermore, local enrichment of Si and P around $M_{23}C_6$ results in the preferential nucleation of Laves phase next to $M_{23}C_6$, increasing the effective particle size and decreasing the Zener pressure (Fedorova *et al.*, 2014; Isik *et al.*, 2015). As both these particles are hard, deformation gradients develop in the surrounding matrix during creep that initiate damage through cavity nucleation (Maddi *et al.*, 2016).

2.2.2.3 Solid solution strengthening

Precipitation of new phases as well as the coarsening of existing particles results in the depletion of alloying elements from the matrix. For instance, the precipitation of Laves phase and enrichment of $M_{23}C_6$ particles during growth results in the depletion of Mo whereas the precipitation of Z phase and growth of $M_{23}C_6$ deplete Cr levels (Bakic *et al.*, 2014). This results in the loss of solid solution strengthening and creep strength. Substitutional solute atoms such as Mo and Cr strengthen the material by lowering dislocation mobility through increasing the stress related to the drag of dislocations by solute clouds (Terada *et al.*, 2008). The backstress due to solid solution hardening is approximated by (Panait, Zielińska-Lipiec, *et al.*, 2010)

$$\sigma_{SS} = \frac{M_T \, \dot{\varepsilon}_m}{\rho_m \, b \, B} \tag{2.8}$$

where B is the dislocation mobility at the testing temperature. Some works (Hald, 2008; Panait, Zielińska-Lipiec, *et al.*, 2010) have found that the depletion of Mo due to Laves phase formation in some 9 – 12 % Cr steels is compensated for by the precipitation hardening offered by small Laves phase particles. However, when these particles grow larger than a mean size of 250 nm, they are unable to pin micrograin boundaries and the loss of solid solution strengthening causes a loss in creep strength (Li, 2006).

2.3 Image correlation techniques

Following the explosive development of computational power and digital image acquisition systems in the 1970s, DIC arose as an alternative experimental technique for noncontact deformation measurements across a broad range of fields. Since the invention of DIC, many improvements have been made to the technique, widening its applicability to many experimental challenges.

2.3.1 Basic principles and concepts

DIC is a photomechanical technique that was proposed in 1983 that extracts deformation data by analysing the grey intensity differences between a reference image of a material surface taken before loading and a sequence of images captured during loading (Sutton *et al.* 1983). Depending on the number of cameras employed in the image acquisition, DIC can be classified as either two-dimensional (2D) DIC or three-dimensional (3D) DIC. In order to avoid confusion

with volume deformation measurement using digital volume correlation (DVC), the term stereo-DIC is used in lieu of 3D DIC. The use of a single camera in 2D DIC restricts measurements to in-plane deformations on a planar surface, whereas out-of-plane measurements can be made of any curved object using two or more cameras in stereo-DIC (Sutton *et al.*, 2008). The operating principle of stereo-DIC is similar to planar DIC, with the exception that stereovision is employed.

A typical setup for stereo-DIC measurements of an object's surface is shown in Figure 2.13. Images of the specimen surface in different loading states are captured by two oriented cameras typically equipped with charged coupled device (CCD) image sensors. The imaged surface, which is illuminated by incoherent light sources, is often covered by a random pattern of speckles that follows the deformation of the underlying material. This pattern supplies the random greyscale distribution that acts as a bearer of displacement data and can either result from the material's natural surface features or can be applied artificially with paints or scratches, for example (Schreier *et al.* 2009:83).

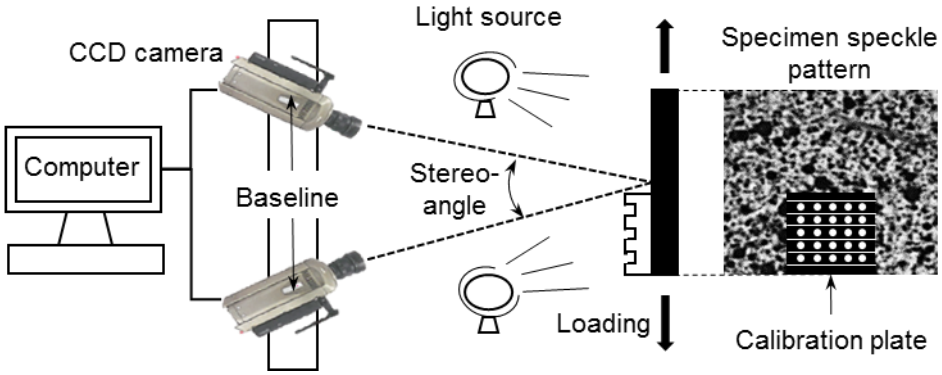

Figure 2.13: Schematic of a typical stereo-DIC setup. Adapted from Reu (2012)

In the subset-based or local DIC, the image comparison is made by correlating the greyscale intensities of a set of windows, termed subsets, throughout the reference and deformed images. As indicated in Figure 2.14a, a reference square subset of size $(2M + 1)^2$ pixels (where M is half of the subset width) with its centre located at point (x_0, y_0) and a discrete intensity field $F(x_i, y_j)$ is tracked by means of a correlation criterion in order to determine the central point $(x_0^{'}, y_0^{'})$ of its counterpart target subset in the deformed image with $G(x_i', y_j')$ as the intensity pattern (Pan *et al.* 2009). The in-plane displacements, $u_x(x_0, y_0)$ and $u_y(x_0, y_0)$, are then computed from the difference in locations between the reference and deformed subset centres (Pan *et al.* 2008). The subset centres form the points of intersection of a virtual grid, illustrated in Figure 2.14b, which spans the processed region (region of interest, ROI) of the images. These grid points are typically evenly spaced by a distance known as the step size, often alternatively expressed as a percentage of subset overlap. The displacement vectors are obtained at each subset centre across the tested surface within the ROI, as shown in Figure 2.14c, resulting in the term *full-field* deformation measurement.

2.3.2 Processing parameters

Apart from the subset and step size, other parameters that are defined either by the user or by the software package affect the processing flow. During loading, the specimen surface can

experience a combination of deformations including rigid body translation and rotation, normal extension and compression, and shear. For this reason, an originally square subset in the reference image assumes a distorted shape after deformation, as illustrated in Figure 2.14a. The mapping of the pixel point (x_i, y_j) in the reference subset to the corresponding point (x_i', y_j') in the target subset is achieved through so-called shape functions (Pan *et al.* 2009). Choosing a shape function requires consideration of the underlying deformation complexity, subset size and computational resources. Improper selection results in the inability to match subsets, which is known as decorrelation (Schreier *et al.*, 2009:88).

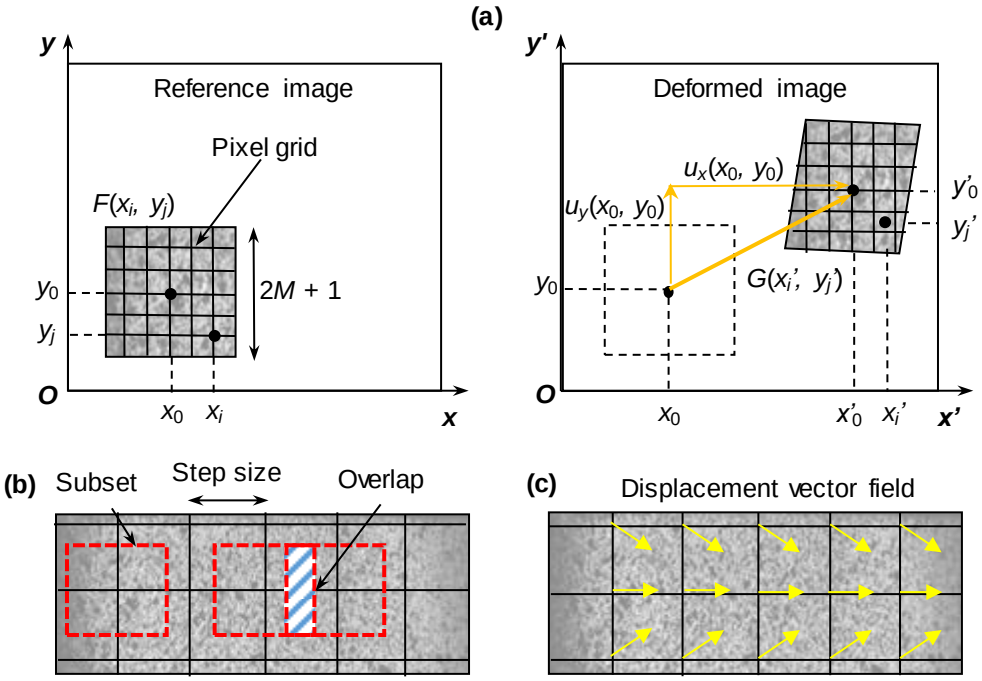

Figure 2.14: Illustrations of (a) subset tracking between a reference image and deformed image, (b) subset and step size definitions and (c) resulting displacement field

Typically, an affine transformation through a first-order shape function is employed (Schreier & Sutton, 2002):

$$x_i' = x_i + u_x(x_i, y_j) + \frac{\partial u_x}{\partial x}(x_i - x_0) + \frac{\partial u_x}{\partial y}(y_j - y_0) \qquad (2.9)$$

$$y_j' = y_j + u_y(x_i, y_j) + \frac{\partial u_y}{\partial x}(x_i - x_0) + \frac{\partial u_y}{\partial y}(y_j - y_0) \qquad (2.10)$$

where $i, j = -M{:}M$. For more complicated shape states of the target subset, higher order polynomial functions exist, such as second-order shape functions. Such functions improve systematic errors (accuracy) but suffer from a penalty of computational complexity and higher random error especially within smaller subset sizes (Schreier & Sutton, 2002; LaVision, 2017:76; Jones & Iadicola, 2018:53).

As evident from Equations (2.9) and (2.10) and the deformed subset in Figure 2.14a, the pixel point (x_i, y_j) may locate to a position (x_i', y_j') between discrete pixel values after deformation.

The actual continuous intensity pattern of the light reflected from an object's surface is discretised into several integer grey levels depending on the dynamic range of the CCD sensor and analog to digital converter. For a typical 12-bit camera system, the brightness levels vary from 0 to 4 095 representing the variation from the black to the white colour intensity (LaVision, 2017:16). In order to obtain the grey values at the subpixel positions, a surface interpolation fit reconstructs the sampled intensity distribution into a continuous representation (Pan *et al.* 2009). Various interpolation schemes are possible including bilinear, bicubic, bicubic spline, bicubic B-spline and biquintic B-spline interpolation (Chapra, 2008:379). The latter solution has been shown to minimise systematic error compared to lower-order versions (Baldi & Bertolino, 2015).

Finally, in order to assess the comparisons between the reference and deformed windows, a correlation criterion is necessary to match the intensity patterns between subsets. Several criteria are available in literature and are broadly categorised into two types based on their mathematical implementation (Schreier *et al.* 2009:96). The cross-correlation (CC) criterion is largely responsible for the digital image correlation name, whereas the sum of squared differences (SSD) criterion is mostly used due to its simple computation (Pan, 2011). The choice of correlation criteria is largely based on the ability to obtain an accurate correspondence between the reference and target subsets despite substantial changes in the greyscale distribution. In practice, intensity changes could be caused by uneven lighting, image blurring, specimen reflectivity variations due to strain and differences in camera angles in stereo setups (Tong, 2005). These variations can be represented as an offset b_i and scale $a_i\, G_i$ in lighting given by the photometric transformation $\phi(G_i) = a_i\, G_i + b_i$ where G_i is the grey intensity values at a point i within the deformed subset (Schreier *et al.* 2009:97).

If these variations are unaccounted for, large systematic errors could result from the mismatch in intensity distributions (Tong, 2005). Based on the consideration that a linear transformation involving both scaled and offset intensity variations could occur in a practical setting, the zero-mean normalised SSD (ZNSSD) and CC (ZNCC) criteria have been developed (Schreier *et al.* 2009:99). These criteria are often fixed for a given software package. For instance, the DIC processing software DaVis 8.4 used in this work performs correlation according to the ZNSSD criteria. The formulation of the ZNSSD criterion is given as

$$C_{ZNSSD} = \sum_i \left(\left(\frac{\sum \bar{F}_i \bar{G}_i}{\sum \bar{G}_i^2}\, G_i - \frac{\sum \bar{F}_i \bar{G}_i}{\sum \bar{G}_i^2}\, \bar{G} \right) - (F_i - \bar{F}) \right)^2 \qquad (2.11)$$

$$\bar{F} = \frac{\sum F}{2\,M+1}; \quad \bar{F}_i = F_i - \bar{F} \quad \bar{G} = \frac{\sum G}{2\,M+1}; \quad \bar{G}_i = G_i - \bar{G} \qquad (2.12)$$

where F_i is the grey intensity value at a point i in the reference subset.

The ZNSSD criterion attains its minimum at a value of 0 when perfect correspondence is attained between subsets. This minimisation involves resolving the parameters u, v, $\partial u_x/\partial x$, $\partial u_x/\partial y$, $\partial u_y/\partial x$ and $\partial u_y/\partial y$ from Equations (2.9) and (2.10) using an optimisation algorithm. A broad range of optimisation techniques are available for parameter extraction with the gradient-based Newton-Raphson method outperforming the initially developed coarse-fine approach in terms of computational efficiency and accuracy (Sutton *et al.* 1983; Bruck *et al.* 1989; Pan *et al.* 2009).

2.3.3 Stereovision correlations

Out-of-plane deformations are inevitable even in simple tension tests due to contractions caused by Poisson's effect, bending from grip misalignment, geometrical deviations from planarity of the specimen surface, expansion effects and specimen necking (Sutton *et al.*, 2008). The effect of out-of-plane rotations and translations on in-plane measurements is illustrated in Figure 2.15. In-plane strain errors are related to the quantity $\Delta Z/Z_o$, where ΔZ is the deviation from planarity and Z_o is the distance from the object to the pinhole aperture of the camera (Sutton *et al.*, 2008). Motivated by the limitation of 2D DIC for out-of-plane measurements, Helm *et al.* (1996) developed a stereo-DIC setup that accounted for out-of-plane displacements using viewpoint corrections for the different images from the pair of cameras. Since then, stereo-DIC has been refined for extensive use in experimental mechanics as a material characterisation tool particularly for specimens with curved geometries (Orteu, 2009).

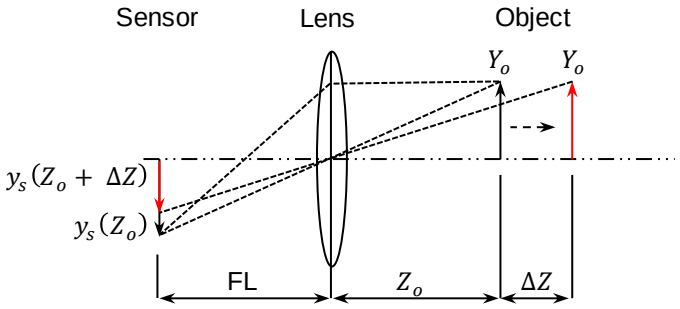

Figure 2.15: Effect of out-of-plane translations on 2D DIC measurements. Redrawn from Sutton *et al.* (2008)

Although the underlying principles of 2D and stereo-DIC are mostly identical, the calibration process, that converts the pixel dimensions of the object surface in the latter setup into real world coordinates to obtain metric displacement data, has added complexity. This can be achieved through a camera calibration process which involves extracting a combination of intrinsic and extrinsic camera parameters based on a simplified camera model (Ponce & Forsyth, 2003:129). The pinhole camera model, illustrated in Figure 2.15, is an ideal model based on perspective projection which is commonly applied to calibration algorithms (Lin & Sung, 2007; Schreier *et al.*, 2009:24). Calibration using this method involves determining intrinsic parameters including principle point pixel locations, focal length (FL), third-order and fifth-order lens distortion correction coefficients and a scaling factor for relating pixel dimensions to a metric value. Moreover, extrinsic parameters are related to the 3D translational and rotational positions of the cameras relative to each other. These parameters are obtained by a stereovision-combined technique which employs the use of a two-level precision calibration plate, as shown in Figure 2.13 (Schreier *et al.*, 2009:75). Alternatively, if distortion is present (from a glass window, for instance), a generic third-order polynomial mapping function is more appropriate. Such mapping requires full, coplanar and equidistant views of a calibration plate, as performed for the stereo-microscope in Chapter 8. Both calibration procedures are available in the LaVision processing software (LaVision, 2017:64).

When the multiple camera setup is not possible due to experimental constraints, such as the lack of space, several options are available for mitigating strain errors due to out-of-plane

motion (Hoult *et al.*, 2013). An experimentalist can increase the effective distance between the camera and object (Z_o in Figure 2.15) using a longer FL lens (as done in Chapter 7) or using a telecentric lens (Sutton *et al.*, 2008).

2.3.4 Resolution and accuracy

As is the concern with any new technology, the use of DIC as a deformation tracking tool requires an investigation into the resulting accuracy (bias) and resolution. Several aspects of the measurement chain (speckle pattern, interpolation, shape functions, stereo-angle, camera sensor, lens distortion, etc.) affect the suitability of DIC to capture strain gradients during a particular test. The user-defined subset and step size are arguably the most important parameters when considering this issue (Wittevrongel *et al.*, 2015). The selection of a subset size is based on assessing the trade-off between the noise floor and spatial resolution. Noise floor is the standard deviation of displacements measured during a self-correlation test in which images are correlated in the absence of any deformation (Wang *et al.* 2007). Although, theoretically, no deformation should be measured, background influences and camera noise result in non-zero displacement measurements. Spatial resolution refers to the minimum distance between independent measurement points. This corresponds to the subset size as abutting subsets use the intensity values of different pixels and remain independent (Reu, 2012).

Relatively large subset sizes allow an area to contain distinctive speckle features which uniquely identify the area with respect to other subsets, resulting in a low noise floor. As a general rule, each subset should ideally contain three speckle features that are each 3 – 5 pixels in size for adequate matching (Jones & Iadicola, 2018:54). A trade-off, however, exists between noise floor and bias caused by the low-pass filter effect of larger subset sizes. Small subsets provide improved spatial resolution and bias as they are more accurately discretised by shape functions, such as the first-order approximation used in the LaVision software (Pan *et al.* 2008). Smaller step sizes increase the density of data, which is useful in capturing high strain gradients and near-edge data. In general, the step size should be larger than 25 % of the subset size (Reu, 2012).

3 Hypothesis development

This chapter aims to discuss the methods introduced in Chapter 1 and described in Chapter 2 in relation to the objectives of the dissertation. The key outcome is the justification of technique choices as well as the delineation of the prime objectives from the project scope.

3.1 Motivation for selected methodologies

The techniques[6] described in this dissertation are aimed at the creep deformation measurement of thermal power plant steels. X20 steel was identified as a power station material that provided a suitable candidate for the experimental work conducted in this study. Although a wealth of creep, microstructural and cavity studies have been performed on this steel (most notably the report conducted under the Association of German Engineers by Straub (1995)), sparse attempts have been made to investigate the creep response of aged material. This 12 % Cr steel shares microstructural characteristics with its replacement 9 % Cr steel P91 but has been implemented on a broader scale and longer time period within SA stations for thick section components (Kalwa, 1985; Abe *et al.*, 2008:57). For this reason, X20 is readily available in various aged forms exceeding 10 years as utility maintenance engineers remove large sections of main steam piping for inspections, repairs and replacements.

X20, like other 9 – 12 % Cr steels, possess complicated microstructures with interacting features (Subsection 2.2.2) that evolve during creep exposure. Within progressive life management schemes, component life assessment has been guided mainly by two methods including direct measurements of the material degradation through microstructural investigation and indirect methods that include post-exposure mechanical tests (Dyson, 2000). It is therefore difficult to decouple mechanical behaviour from the underlying microstructure. From this position, electron microscopy techniques developed from the work of Marx (2019)[7] and tailored to the observation of X20 microstructure is employed to corroborate deformation behaviour.

Several techniques are available for creep loading of specimens, including conventional constant-load lever arm testing conducted in tension or compression, constant stress variations of creep testing and stress relaxation tests (Section 2.1). In order to preserve material, creep testing techniques have been selected based on the ability to accommodate variable stress or temperature profiles so that multiple creep curves can be obtained from a single test. For spatially varying temperature fields, resistance heating from a Gleeble thermomechanical simulator was utilised together with a specialised specimen geometry. A vacuum chamber prevents oxidisation and optical distortions resulting from convectional heat waves. Furthermore, fast feedback response from thermocouples and load cells makes this machine ideal for high temperature tensile tests. These tests are however less ideal for long-term testing due to machine availability and running costs. Using a specialised hourglass specimen geometry, a variable stress profile can be induced but with a constant temperature requirement. This is best achieved using a traditional constant tensile load creep testing setup together with a regular tube furnace from the standpoint of simplicity and suitability to long-term creep testing.

[6] A summary of all mechanical test methods and materials employed is provided in Appendix A.
[7] Interested readers can find more details regarding the microstructural evaluation techniques by consulting the doctoral work of Aghajani (2009) and Marx (2016, 2019).

However, high temperature strain measurement using conventional technology, such as strain gauges, is particularly challenging over spatially-changing temperature/stress fields due to their sizable footprints typically ranging from 3 to 6 mm (Hoffmann, 1989:38). Apart from these contact measurement techniques, experimentalists have recently resorted to optical techniques, such as laser-based interferometric methods as well as DIC, largely due to their contactless operation. Interferometric deformation data is typically obtained by analysing fringe patterns for the phase difference between light scattered from a deforming object surface (Pan *et al.* 2009). These methods, however, generally rely on carefully controlled laboratory conditions, specimen preparation and coherent light sources, which limits their suitability to conventional laboratory and field applications (Hild & Roux, 2006). Among the optical methods, DIC has recently found extensive applicability to full-field deformation measurements largely due to the emergence of commercial processing software, availability and relative low cost of computers and digital cameras as well as the simple experimental setup (Bornert *et al.*, 2009). In this work, DIC was selected due to its adaptability to high temperature testing, simple speckle pattern preparation and the ability to capture strain gradients resulting from nonuniform stress or temperature fields. Furthermore, DIC measurement is length-scale independent lending its versatility to different specimens with different geometries (Jones & Iadicola, 2018:1).

Within the field of power station maintenance, there is increasing interest in innovative, small-sample techniques for creep measurement including impression, small punch and small ring creep tests (Ali, 2014:34). Such techniques are especially useful when the material requirements for standard test specimen geometries cannot be met with the limited supply of aged steel or when site-specific analysis is required, such as for weld characterisation. Future work involving small punch creep testing is mentioned in the discussion chapter (Chapter 8) with reference made to Appendix B which explores the possibility of using small punch creep testing for creep measurement which is selected based on its compatibility with DIC strain measurement, whilst allowing all stages of the creep curve to develop. By contrast, impression creep testing excludes tertiary stage development and the indenter damages the speckle pattern on the deforming surface, making it unsuitable for visual observation through DIC (Mathew *et al.*, 2016).

3.2 Aims and objectives

This work is based on four core objectives that have been organised into individual stand-alone chapters using the chosen techniques highlighted in the previous section. This includes: the development of a technique for high temperature strain measurement across nonuniform temperature fields using DIC and testing the proposed method on basic mechanical properties of X20 (Chapter 4); an investigation of the extension of the technique to accelerated, constant-load creep testing (Chapter 5); application of the technique, together with microstructural analysis, to the damage assessment of various service-aged X20 steel (Chapter 6); the development of a DIC-based technique for medium-term creep testing using a variable stress profile on new and service-aged X20 and comparatively assessing damage parameters using damage mechanics modelling (Chapter 7). Although not a direct objective of the current study, a preliminary study related to the *ex situ* application of DIC to small punch creep testing is discussed in Chapter 8 (with reference to Appendix B) which forms part of the ongoing work in EPPEI's Material Science specialisation. These objectives are detailed below.

The first objective concerns the *experimental development of a single-specimen, high temperature DIC technique for measuring elastic properties from virgin X20 over a nonuniform thermal field*. This involves: overcoming sources of error associated with high temperature

DIC; design of a technique for generating variable temperature profiles across a specialised sample geometry using a Gleeble module; construction of a finite element (FE) model to investigate the influence of variable temperature on stress profiles; and formulating a numerical scheme for the combination of data streams to enable the extraction of elastic properties at several temperatures.

Once the high-temperature DIC setup is established, focus is attracted to accelerated creep testing. The second objective involves *the extension of the DIC technique to measurement of accelerated creep deformation curves over a nonuniform temperature field.* For this, focus is placed on applying the first objective to the creep testing of ex-service X20 that have been classified into original damage categories by the local power supplier. Due to the time constraint associated with Gleeble testing, stresses were selected to generate "accelerated" creep that allows full curve development under 10 h with some exceptions (see Chapter 5 for limitations on this method). This requires: revision of the FE model to include the effects of plasticity; an exploration into the effects of using a different specimen geometry; a comparison of DIC testing with conventional testing; a qualitative comparison of curves between different damage states; and a brief microstructural study on the effects of prior exposure and accelerated testing on starting microstructures.

Following this, the third objective involves verification of the technique as a damage assessment tool. The aim is the *creep damage assessment of various service-aged X20 using the DIC technique combined with advanced electron microscopy techniques.* This objective acknowledges the importance of coupling post-exposure mechanical testing with microstructural characterisation when assessing the damage state. As a result, the aim is to: identify microstructural parameters of the pre-test material that are most sensitive to the damage state; identify quantitative deformation-based parameters for comparative damage assessment; and critically compare the two methods in terms of their capabilities as diagnostic damage assessment tools.

Given the time limitations of Gleeble testing, experimental work is directed towards techniques that allow for longer testing times that might reveal differences in material behaviour otherwise not evident in short-term tests. The forth objective regards the *application of DIC to assess damage levels of ex-service X20 based on deformation measurement during medium-term*[8] *creep testing across a nonuniform stress field with a constant temperature.* This work builds onto the setup originally developed by Sakanashi *et al.* (2017) for spatially resolved measurement of creep curves across a stainless steel weldment. Aims include: adapting the basic setup through specimen geometry to generate a nonuniform stress field; development of a FE model to ascertain the distributions of stress; addressing the spurious strains caused by heat haze inherit to traditional tube furnaces and developing a strain-processing algorithm; measuring multiple creep curves during longer-term tests for new and different aged X20 states; comparing the DIC measurements with those of conventional strain monitoring methods; using a suitable continuum damage model to derive comparative damage parameters through a fitting approach on both accelerated and medium-term data; and performing a microstructural study to support damage findings.

[8] From here on, the phrase "medium-term" is used in lieu of "short-term" to describe creep testing of X20 with durations of less than ± 1 000 h. This is done to avoid confusion with "accelerated creep testing" performed in the second and third objectives. See Subsection 3.4.5 for terminology used.

3.3 Central hypothesis

Besides damage monitoring using surface replication conventionally employed by Eskom (Section 1.2), post-exposure mechanical tests (on service-aged X20) are often performed in the advanced stages of progressive inspection schedules with little regard given to material efficiency. This work aims to provide a framework for bridging this gap as stated in the core hypothesis:

> *Full-field deformation measurement methods can be used to aid in the creep damage assessment of ex-service X20 with various aging histories. This is done in a manner that preserves material economy and complements existing damage diagnosis tools for condition assessment of thermal power plant steels.*

3.4 Scope and project limitations

This work straddles across several engineering fields, including experimental mechanics, material science and image correlation, with an aim to assist in future endeavours of improved plant component life assessment. It is therefore necessary to demarcate the current project efforts from future missions for structural integrity management.

3.4.1 Image correlation error analysis

Several potential sources of errors exist within the measurement chain involved in image correlation including those associated with lighting, speckle patterns, optical aberrations and distortions, camera noise and calibration procedures (Schreier *et al.*, 2009:229-252). Due to the lack of standardised procedures for DIC error quantification, systematic and variance errors were collected for individual experiments according to the good-practice guidelines recently developed by the International DIC Society (Jones & Iadicola, 2018:57-62). Given the plethora of DIC software codes currently available, this work will focus mainly on the processing methods utilised by the commercial software package developed by LaVision (2017). No effort is made to alter the fundamental DIC software code other than user-defined parameters. Post-processing is performed using MATLAB[9].

3.4.2 Parent material

The application of techniques explored in this work are limited to parent thick-walled piping materials as opposed to weld regions, rotor blades or thin tubing. Focus is instead placed on developing the techniques on homogenous parent piping material, although an extension to welds is possible in future work (Chapter 8). The tests are conducted on grade X20 steel in the virgin state as well as in a creep damaged state, as categorised by Eskom as ranging from “low”, “medium” and “high” using a standardised replication technique (ASTM, 2002). Rotor material and tubing are more prone to creep-fatigue, corrosion or overheating effects (Bhadeshia *et al.*, 1998:228-230; Shibli, 2011:283-290), respectively, than creep as discussed in the following section.

[9] MATLAB release R2019a, The MathWorks Inc., Natick, MA, USA. Available: https://www.mathworks.com/products/matlab.html

3.4.3 Damage mechanisms

Damage mechanisms encountered by in-service components comprises a large subject. This work places emphasis on the characterisation of damage of X20 main steam piping steel solely due to creep processes. Other parallel high temperature damage processes such as environmental damage due to oxidation and corrosion are not considered. This is considered acceptable in thick-walled systems, such as the main steam piping examined in this study, where surface corrosion and oxidation and localised increases in temperature have smaller contributions to the overall damage than in internal boiler tubing for instance (Auerkari *et al.*, 2007). Transient effects of plant start-ups including fatigue and creep-fatigue are also excluded from the present study as they are more applicable to dynamic components, such as steam turbine rotor blades.

3.4.4 Long-term creep predictions

Due to the time sensitivities of a typical doctoral project, long-term creep testing (> 10 000 h) was deemed impractical and excluded from the current work. Instead, tests were conducted at significantly higher stresses and temperatures (within the low-temperature dislocation regime) than those typically applied in standard creep tests in order to provide a range of creep deformation curves within practical time periods. Nonetheless, the procedures described in standards ASTM E21 (ASTM, 2009) and E139 (ASTM, 2011a) were followed as closely as possible for the high-temperature tensile and creep tests, respectively. The majority of tests were limited to a maximum temperature of 600 °C which was chosen for several reasons: (i) to simulate the operating temperatures of main steam piping for both subcritical and supercritical coal-fired power stations; (ii) to induce high temperature DIC issues including surface radiation so that extension to higher temperatures is possible in future work; and (iii) in consideration for future testing of the replacement steel P91 which is typically operated at this temperature (Abe *et al.*, 2008:57). Furthermore, no attempt is made to extrapolate this relatively short-term data to service conditions due to the well-known errors arising from disregarding microstructural evolution during long-term exposures (Bolton *et al.*, 1980).

3.4.5 Accelerated creep, medium- and long-term testing

Given the variety of creep testing techniques available (Section 2.1), it is necessary to clarify what is meant by “accelerated creep testing” referred to in subsequent chapters and performed on the Gleeble machine. These tests involve the application of a constant load that results in initial stresses at or below the yield stress of the material at the maximum temperature (with minimum values of < 260 MPa at 550 – 600 °C as indicated by EPRI (2006)) so as to accelerate creep curve development within a reasonable time frame. Such tests would not normally be used for long-term predictions due to the potential introduction of dislocation densities upon initial plastic loading and the consequent change in inherent obstacle to creep (Abe *et al.*, 2008:277). As mentioned in the previous section, this work in no way uses these tests to predict long-term life. It is also expected that the plastic deformation associated with the high loads would have a lower effect on X20 due to the high initial dislocation density introduced during martensitic transformation. In this case, plastic deformation would aid in dislocation recovery through strain softening (Straub, 1995; Abe *et al.*, 2008:267).

Furthermore, these tests differ from “high temperature slow tensile tests” that involve the application of a constant strain rate (10^{-5} to 10^{-3}/s) as opposed to constant load (El Rayes & El-Danaf, 2017). In these tests, strain softening causes the true stress values to approach steady values and the resulting steady-state flow stress-strain rate relationship is used

as a replacement for minimum creep rate-stress relation obtained from constant-load tests (Abe *et al.*, 2008:267). From the standpoint of nonuniform temperature profiles in the current work however, applying constant strain rate over the entire gauge region is not possible and so such a test was not considered in this work.

This work adopts terminology based on the length of creep tests. “Accelerated creep tests” refer to tests that last for less than 10 h conducted at high stresses (> 150 MPa) whereas “medium-term” tests are conducted at intermediate stresses (100 – 150 MPa) that last in excess of 24 h but less than 1 000 h and are not usually conducted in a Gleeble setting. Instead, conventional creep testing machines that are adapted for interfacing with DIC are employed for the latter tests as explored in Chapter 7. Tests at low temperatures and/or stresses that continue in excess of 1 000 h are termed in this work to be “long-term” tests. An example of this is the 10^5 h tests conducted by Aghajani *et al.* (2009) on X20.

3.4.6 Component life prediction

Although the current work is motivated by the need for improved NDE methods for structural integrity assessments, it is not concerned with on-site application nor does it translate to accurate quantification of the remaining life of materials. Instead the DIC technique serves as a complementary method of comparative damage assessment between service-aged materials. Moreover, this is in line with the widely accepted sentiment that no single condition assessment technique satisfactorily describes the creep-exhaustion state of the material with the requisite safety margins demanded by modern plant engineers (Bhadeshia *et al.*, 1998:227).

4 High-temperature tensile property measurements using digital image correlation over a nonuniform temperature field

High-temperature testing presents many technical challenges for the accurate measurement of material properties. This chapter addresses these challenges through the development of an experimental DIC technique that is capable of measuring strains at temperatures up to about 900 °C. A demonstration of the accuracy of the technique is provided through the extraction of low strain-based (< 2 000 με) elastic properties at multiple temperatures from single test pieces of X20 steel. A maximum temperature of 600 °C was selected as it is the maximum temperature at which subsequent experiments were conducted (Subsection 3.4.4) and so this chapter addresses the first objective of the dissertation whilst providing a foundation for subsequent experiments. The chapter concludes with a short discussion about insight gained following the submission of the original manuscript to a journal.

This chapter is published in the *Journal of Strain Analysis for Engineering Design* (van Rooyen & Becker, 2018)[10] but is presented here in its pre-reviewed form (prior to reviewer input). A discussion on post-review considerations is included at the end of the chapter. The experimental technique was originally presented at a British Society for Strain Measurement (BSSM) conference (van Rooyen & Becker, 2015)[11].

Declaration by the candidate:

With regard to Chapter 4, the nature and scope of the author and co-authors is as follows:

Name	Email	Contribution	Extent (%)
M van Rooyen (candidate)	melzvanrooyen@sun.ac.za	Experimental design, completion of all tests and data analysis, streamlining of polynomial fitting code, writing and compilation of manuscript	95
TH Becker	tbecker@sun.ac.za	Beyond supervision and reviewing contributions, assisted in the conception and development of the polynomial fitting code for strain calculation	5

Signature of candidate: ……..[MvR][12]……..
Date: ……..2020/04/30……..

Declaration by co-authors:

The undersigned hereby confirm that:

1. The declaration above accurately reflects the nature and extent of the contributions of the candidate and the co-authors to Chapter 4,

[10] DOI link: https://doi.org/10.1177/0309324717752029
[11] Link to extended abstract: http://www.bssm.org/uploadeddocuments/Conference%202015/2015papers/A_3D-DIC_Method_for_High_Temperature_Application.pdf
[12] Declaration with signature in possession of candidate and supervisor.

2. No other authors contributed to Chapter 4 besides those specified above, and
3. Potential conflicts of interest have been revealed to all interested parties and that the necessary arrangements have been made to use the material in Chapter 4 of this dissertation.

Signature (see Footnote 12)	Institutional affiliation	Date
[TH Becker]	SU	2020/04/30

4.1 Introduction

Measurement of strain at elevated temperatures is essential for the extraction of temperature-specific (and in many instances, time-dependent) mechanical properties of materials employed in high-temperature environments. This is particularly of interest in the energy sector, where the life estimates of critical structures (such as steam pipelines), which operate at high pressures and temperatures for extended time periods, is vital.

Several methods exist for mechanical property characterisation at elevated temperatures from deformation information with conventional techniques being widely standardised. For instance, temperature-specific elastic moduli can be measured using the high-temperature tension testing procedure described in the ASTM standard E21 (ASTM, 2009) whereas time-dependent creep tests are detailed in ASTM E139 (ASTM, 2011a). Such traditional methodologies involve high-temperature strain measurement typically obtained from strain gauges and extensometers. Specialised versions of these devices are capable of strain measurement at temperatures over 1 000 °C, however suffer from limited spatial resolution and thermally induced errors (Hoffmann, 1989:52; Gregory & Luo, 2001). Furthermore, such strain measurements are averaged over a gauge length of several millimetres, necessitating a uniform temperature distribution across the device footprint. To obtain sufficient data to extract reliable material properties, parametric studies are required that focus on varying temperature. Extraction of material properties at several temperatures using traditional gauges requires several specimens and test runs. Multiple test runs can be expensive and time-consuming for determining creep properties of various materials that often involve testing durations in excess of 100 000 h (Haney *et al.*, 2009).

In contrast to classical methods, DIC is a modern noncontact measurement technique that provides a high spatial density of data through full-field measurement by optically tracking the deformation of a speckle pattern applied to the surface of a specimen (Sutton *et al.*, 1983). The respective strains can be obtained from the derivatives of the displacement data. In subset-based DIC, the recorded digital images are partitioned into groups of pixels known as subsets. Displacement maps between a reference image (taken before loading) and a deformed image are obtained with subpixel accuracy by correlating the greyscale values of the subsets' pixel collection (Ke *et al.*, 2011).

Several authors have successfully applied DIC to the property measurement of a wide variety of materials. For instance, elastic properties, such as Young's modulus and Poisson's ratio, have been established for animal arterial tissue (Zhang *et al.*, 2002), fabric (Hursa *et al.*, 2009) and steel weld zones (Touboul *et al.*, 2012). DIC has also been extended to obtaining fracture properties of materials. Becker *et al.* (2012) combined DIC displacement maps with finite element (FE) methods to establish *J*-integral values for nuclear graphite. The same principle was applied by Molteno and Becker (2015) to decompose the displacement fields to extract stress intensity factors for mode I, II and III fracture of a poly(methyl methacrylate) (PMMA)

thermoplastic material. Full-field data available from DIC has given rise to various inverse methods, notably the virtual fields methods (VFM), which have been developed to extract constitutive material properties from full-field strain data (Grediac *et al.*, 2006).

Extension of DIC to high temperature experiments however involves several challenges for successful deformation measurement (Swaminathan *et al.*, 2013):

1. The speckle finish must retain its contrast without debonding or burning off from the material surface, necessitating a thermally stable paint coating;

2. Excessive surface radiation at higher temperatures can lead to image saturation and decorrelation;

3. Convection currents caused by the test environment (such as in the air between a heated specimen and the DIC cameras) can optically distort the images, resulting in spurious measurements;

4. Oxidation of the material at high temperatures causes changes in the surface roughness and colour, which could deteriorate the speckle pattern contrast and alter deformation measurements.

Several authors have successfully measured material deformation and properties at high temperatures using DIC by overcoming these issues. (1) Heat-resistant speckle patterns consisting of ceramic coatings (Novak & Zok, 2011) and cobalt oxide paint (Pan *et al.*, 2011) have been utilised to measure the thermal properties of metals in excess of 1 200 °C. These coatings, however, have been reported to be relatively brittle, resulting in cracking of the paint and misrepresentation of the underlying material deformation at strains exceeding 0.5 % (Chen, Xu, *et al.*, 2012). Research conducted on the durability of speckle coatings allowing for relatively longer test durations (for example creep tests) is also limited. Sakanashi *et al*. (2017) monitored creep deformation over several weld zones for over 2 000 h at a uniform temperature of 545 °C using commercially available heat-resistant paint. (2) The issue of contrast loss due to blackbody radiation has been mitigated using monochromatic blue light to illuminate the specimen surface and subsequently filtering the reflected and emitted light using blue bandpass filters (Grant *et al.*, 2009; Novak & Zok, 2011; Pan *et al.*, 2011; Chen, Xu, *et al.*, 2012). (3) Techniques for minimising heat haze effects include mixing the air through an air knife (Novak & Zok, 2011) or a fan (Lyons *et al.*, 1996). These methods, however, could not eliminate strain errors due to air turbulence. On the other hand, the use of vacuum chambers (Grant *et al.*, 2009) effectively minimise heat haze as well as oxidation (4) of the specimen surface. Direct heating of the specimen through induction (Berke & Lambros, 2014) or resistance heating (Grant *et al.*, 2009) also prevents heating of the surrounding air.

Although DIC has been successfully applied to material characterisation at high temperatures of several materials (Grant *et al.*, 2009; Novak & Zok, 2011; Chen, Xu, *et al.*, 2012; Berke & Lambros, 2014), most studies report values that are averaged across a region of uniform temperature distribution in a manner similar to classical instruments. Limited attempts have been made to spatially vary a test parameter, such as temperature, and measure the displacement fields resulting from the heterogeneous material behaviour. The high spatial resolution offered by DIC allows deformation to be measured locally across nonuniform temperature fields. By taking advantage of the high spatial density of data, multiple material properties can be extracted from a single specimen. In the present work, a thermal gradient was

achieved through resistive heating from a Gleeble thermomechanical simulator: a common tool used for materials processing and characterisation simulations (Kardoulaki *et al.*, 2014).

This study describes a method that takes advantage of a spatially varying thermal field to extract temperature-dependent tensile properties during a single test run from a single specimen by using full-field surface strain and temperature measurement maps. The chapter begins by describing the experimental setup which employs a two-camera DIC system with blue colour filters, an infrared (IR) imager, white light-emitting diode (LED) illumination and a heat-resistant speckle coating. A parabolic temperature profile is generated through ohmic heating by a Gleeble tester, allowing strain measurements at various temperatures. The proposed methodology is validated by testing the temperature limit of the system in terms of displacement errors resulting from image saturation, investigating the stress state of the sample by means of an FE simulation and confirming the homogeneity of the microstructure within the measurement zone. Finally, by combining DIC strain measurements with full-field temperature readings obtained using an IR camera, the technique is demonstrated by extracting constitutive properties, specifically the Young's moduli and Poisson's ratios, of ferritic-martensitic X20 steel from tension tests with a peak temperature of 600 °C. These properties are well-established and depend on a high strain measurement sensitivity for their accurate determination, providing a good demonstration of the proposed setup's capability.

4.2 Experimental setup

The experimental setup comprised four elements that are schematised in Figure 4.1a: a thermomechanical loading system, an IR imager to measure full-field temperature maps, an optimised specimen geometry to allow for high temperature and strain gradients, and a two-camera DIC system with blue light filters and white lights to measure full-field displacement maps. Note that a Cartesian coordinate convention (indicated in Figure 4.1a) is used, where x aligns with the specimen's longitudinal axis and the loading direction, y is along the transverse width of the specimen and z refers to the out-of-plane direction. The origin was taken as the centre point on the sample surface. A photograph of the DIC setup positioned in front of the Gleeble viewing window is shown in Figure 4.1b.

4.2.1 Thermomechanical loading

Thermal and mechanical loading of the specimen during the high temperature test was performed using the tensile module of a Gleeble 3800 thermomechanical loading system. The specimen, housed within the vacuum chamber of the Gleeble module, was secured by water-chilled copper grips on either end and was visible through a 16 mm thick Pyrex borosilicate glass viewing window. Resistance heating of the specimen occurred by feedback control from a K-type (chromel/alumel) thermocouple welded to the centre of the gauge length. Heat conduction longitudinally along the specimen towards the cooled grips resulted in the development of a thermal gradient, which has been shown to be parabolic in shape (Walsh *et al.*, 1986; Norris & Wilson, 1999; Kardoulaki *et al.*, 2014). Heat haze and oxidation was minimised as the testing area was subjected to a vacuum of 44 Pa within a sealed chamber wherein mechanical loading was applied with a servohydraulic ram on one end of the specimen whilst force measurements were made by a strain gauge-based Interface Model 2450-20K load cell on the stationary jaw of the opposite specimen end with an accuracy of ± 0.10 % of the maximum applied load.

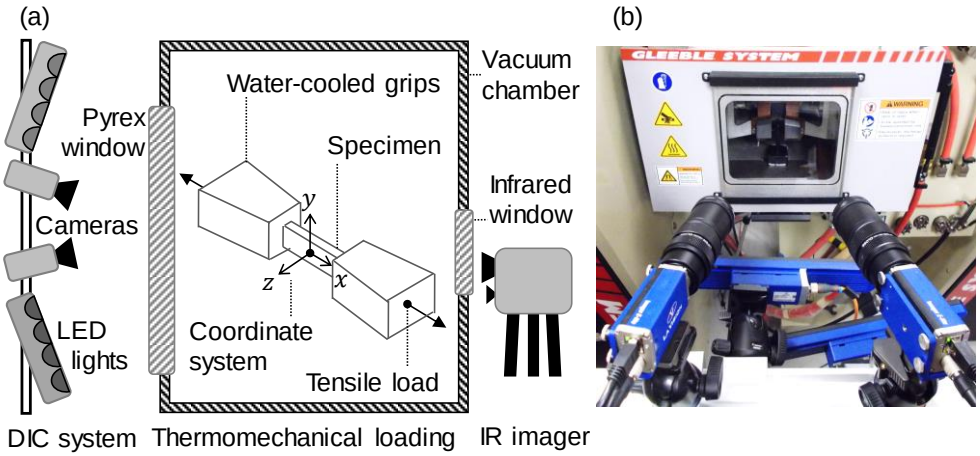

Figure 4.1: (a) Illustration showing the arrangement of the specimen in the Gleeble 3800 thermomechanical loading system relative to the IR and DIC imaging setup, together with the assumed coordinate system. (b) Photograph showing the DIC system positioned in front of the Gleeble vacuum chamber

4.2.2 Temperature measurement

The spatial resolution of temperature measurements offered by thermocouples is largely limited by the minimum distance required between adjacent weld beads, making it unsuitable for the high thermal gradients encountered in this study. IR thermography, on the other hand, allows a high density of temperature data to be recorded and complements full-field strain data (Chrysochoos *et al.*, 2010). In the present study, a Fluke Ti400 Thermal Imager was positioned on a tripod stand at the back of the Gleeble vacuum chamber where the back face of the specimen gauge region was visible through an IR spectrum view port. A uniform coating of matte black, heat-resistant paint was applied to enhance the emissivity of this sample surface. The setup detects IR radiation across the 7.5 to 14 μm spectral band with an accuracy of ± 2 °C at ambient temperature and a noise-equivalent temperature difference (NETD) of less than 0.05 °C at a 30 °C target temperature. An effective resolution of 60 × 15 pixels^2 across the gauge section was achieved. Spatial calibration of the IR images, by means of a 5 megapixel camera integrated within the thermal imager, resulted in a calibration factor of 1.4 ± 0.1 pixels/mm for an approximate 500 mm working distance (WD) and a field of view (FOV) of 230 × 170 mm^2. Full-field temperature measurements were obtained by applying a surface emissivity factor and a window transmission factor such that the highest apparent temperature agrees within 2 ºC of the control thermocouple reading. The assumption was made that the temperature recordings made from the back surface are equivalent to those at the location of the DIC measurements on the front of the specimen, i.e. thermal gradients in the z direction are considered negligible on accord of the relatively thin specimen thickness (2 mm) and insulation provided by the paint coatings.

4.2.3 Specimen geometry

The specimen geometry is shown in Figure 4.2. A $25 \times 10 \times 2$ $(x \times y \times z)$ mm^3 gauge section was selected to keep within the thermal capacity of the Gleeble as well as to maximise the effective pixel resolution across the gauge section. Furthermore, a reduced cross section results in a steeper thermal profile compared to uniform geometries, allowing properties to be determined for a greater variation in temperatures (Norris & Wilson, 1999).

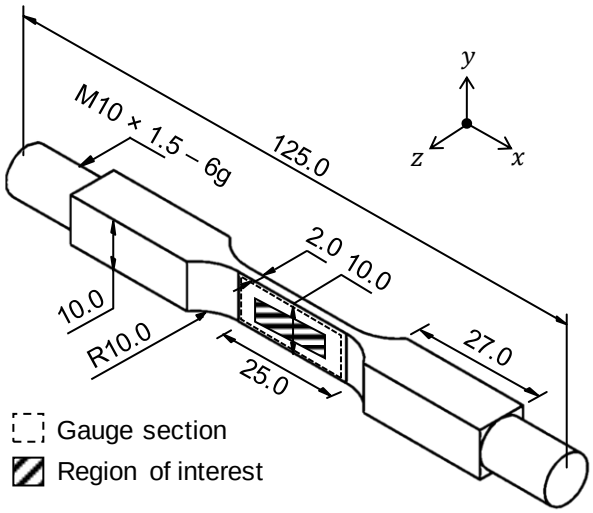

Figure 4.2: Gleeble specimen geometry with a 25 × 10 × 2 mm^3 gauge section. All dimensions are in mm

A linear-elastic, static analysis was implemented using ABAQUS/CAE ver. 6.15 comprising a three-dimensional model of the reduced gauge region. Full-field temperature map data, an example of which is shown in Figure 4.7b, is mapped onto the nodal positions of the FE mesh in x and y respectively. As assumed for the DIC strain analysis, temperature gradients in z (through the specimen thickness) are assumed constant. The model consisted of 62 000 C3D8 linear hexahedron brick elements and employed material properties (presented in Table 4.1) obtained from an online material database (Key to Metals AG, 2015).

Table 4.1: Temperature-dependent material properties of X20 steel employed in FE model (Key to Metals AG, 2015)

Temperature (°C)	20	200	300	400	500	600
Young's modulus, *E* (GPa)	218	206	198	190	180	167
Poisson's ratio, *ν*	0.290	0.302	0.309	0.316	0.323	0.330
Average coefficient of thermal expansion, (10^{-6} K^{-1})	10.3	10.9	11.3	11.6	12.0	12.2

The FE model aims to verify an assumed uniaxial stress state. Figure 4.3 shows the stress triaxiality ratio distribution along one half of the x and y direction centrelines. Clearly, not all data across the gauge section is suitable for property extraction. The stress triaxialities induced by steep thermal gradients in both x and y invalidate the assumption of a uniaxial stress state. Thus, a ROI was selected as a 20 × 5 (x × y) mm^2 area centred about the gauge section as indicated in Figure 4.2 and Figure 4.3. Within this region, temperatures in the y direction remained within 4 °C, resulting in triaxiality ratios near 0.33, typical of uniaxial tension tests.

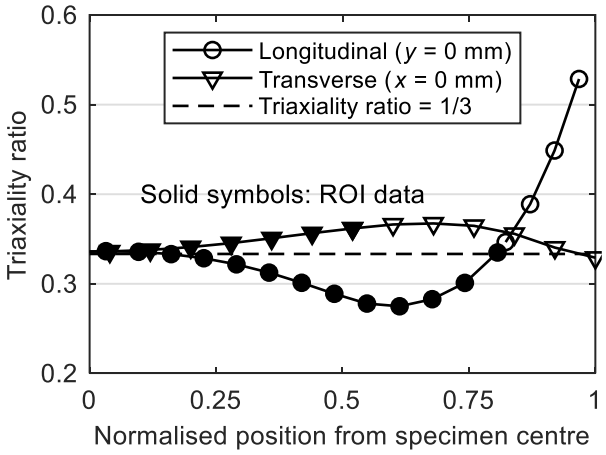

Figure 4.3: Triaxiality ratio along half of the gauge region in the x and y directions, indicating a near uniaxial stress state over the ROI

4.2.4 Full-field strain measurement

Full-field strain measurement maps were provided by DIC for which imaging was achieved with two LaVision Imager E-lite 12-bit (4 096 counts) cameras equipped with 5-megapixel Sony ICX625 CCD sensors. A two-camera system was employed to correct for in-plane displacement errors induced by out-of-plane motion resulting from specimen thermal expansion and contraction from Poisson's effects. To achieve a magnified view of the specimen gauge section, the cameras were paired with 75 mm TECHSPEC Double Gauss macro lenses. The imaging rig was positioned in front of the Gleeble vacuum chamber in such a manner to capture images of the specimen speckle pattern with an effective resolution of 1 000 × 400 pixels^2 across the gauge section. The setup was spatially calibrated by applying a camera pinhole model to fiducial markers on a specialised 30 × 30 mm^2 two-level calibration plate using DaVis 8.3. The camera-lens combination resulted in an image scaling of 40 pixels/mm for a 400 mm WD and a FOV of approximately 60 × 50 mm^2.

Displacement measurement background noise was quantified through a self-correlation test in which five consecutive images were recorded of the stationary specimen as a means of measuring the strain resolution. After applying central differencing to numerically differentiate the measured displacement fields, an average standard deviation of strain of 70 με at room temperature and 100 με at a stabilised temperature of 600 °C was obtained. Considering the relatively low elastic strains (< 2 500 με) expected in the tensile tests, these strain deviations would result in significant scatter owing to the direct differentiation of displacement maps involved in a central differencing approach (Yoneyama, 2016). Based on these considerations, a pointwise polynomial interpolation of surface displacements was used in lieu of central differencing and strains were subsequently calculated by differentiation of the fitted surface.

The choice regarding the order of the polynomial surfaces used is based on initial observations of the temperature fields measured by the IR camera (shown in Figure 4.7b). In the x direction, the temperature profile was parabolically shaped, whilst a subtle quartic distribution was evident in the y direction due to radiation losses. Both profiles were approximately symmetric with respect to the centre of the specimen. It is argued that, for the same stress states, strain profiles will be directly related to the temperature distribution; for the considered X20 material a linear dependence of elastic properties on temperature exists in the temperature range

investigated (EPRI, 2006; Key to Metals AG, 2015). This led to least-square fits of the displacement data using Equations (4.1) and (4.2). The respective strain maps were determined from the analytical derivatives of these displacement functions, resulting in quadratic and quartic functions in x and y respectively.

$$\begin{aligned} u_x = a_0x^3 + a_1x^2 + a_2x + a_3x^3y^4 + a_4x^3y^2 \\ + a_5x^2y^4 + a_6x^2y^2 + a_7xy^4 + a_8xy^2 \\ + a_9y^4 + a_{10}y^2 + a_{11} \end{aligned} \tag{4.1}$$

$$\begin{aligned} u_y = b_0y^5 + b_1y^3 + b_2y + b_3y^5x^2 + b_4y^5x \\ + b_5y^3x^2 + b_6y^3x + b_7yx^2 + b_8yx \\ + b_9x^2 + b_{10}x + b_{11} \end{aligned} \tag{4.2}$$

4.2.5 High-temperature setup

One of the main inputs to DIC strain measurement is high quality images of a speckle pattern on the surface of the deforming specimen. The imaging system was adapted to account for these issues, which include the speckle pattern and illumination design as follows.

To ensure a speckle surface of sufficient contrast and features, a matte white VHT Flameproof paint was applied as the base coat of the speckle pattern. This paint is composed of 10 % by weight titanium dioxide and amorphous precipitated silica dissolved in organic solvents, which has been successfully applied to displacement measurements up to 1 100 °C (Chen, Xu, *et al.*, 2012). Higher specimen strains can be measured as the paint ductility is similar to that of steel. Although a curing cycle is suggested for maximum contrast stability, initial tests found that the best coating ductility was achieved when the paint was subjected to a 30 min air cure.

At high temperatures, surface radiation introduces light at wavelengths shorter than 600 nm that saturate (excessively brighten) and narrow (reduce contrast) the light band of the CCD sensor. This reduces the quality of speckle pattern intensity distribution and can negatively affect subset correlation and hence displacement measurement accuracy. By isolating shorter wavelengths of about 440 nm (blue light) using a lens-mounted filter and by selecting an illumination source with a corresponding wavelength that provides a strong signal source at this wavelength, the radiated light was suppressed. This setup employed an illumination system consisting of two linear arrays of 12 white LEDs each that produce light with a radiometric power of 20 W, directed by 20° lenses. The LEDs have a peak relative radiant power at a wavelength of 443 nm, leading to the selection of Hoya B-440 filters. The filters have a maximum transmission of 47 ± 3 % at a wavelength of 440 ± 5 nm, confining the light band to around the peak LED output whilst remaining near the peak sensitivity spectral region of the Sony IXC625 CCD sensor. The combined filter-LED-CCD arrangement results in a wavelength peak at 440 nm, which significantly reduces the detected surface radiation at increased temperature. The respective response and transmittance curves are shown in Figure 4.4a.

To establish an upper temperature limit of the filter-illumination design, the point at which the thermal radiation overpowers the illumination and hence pattern contrast is significantly degraded must be determined. This involves theoretically calculating the specimen temperature at which the signal-to-noise ratio reaches unity (Novak & Zok, 2011). The presented approach provides a guideline for a filter-illumination design that can be adapted to experiment- and equipment-specific requirements. Experiment-specific values have been provided.

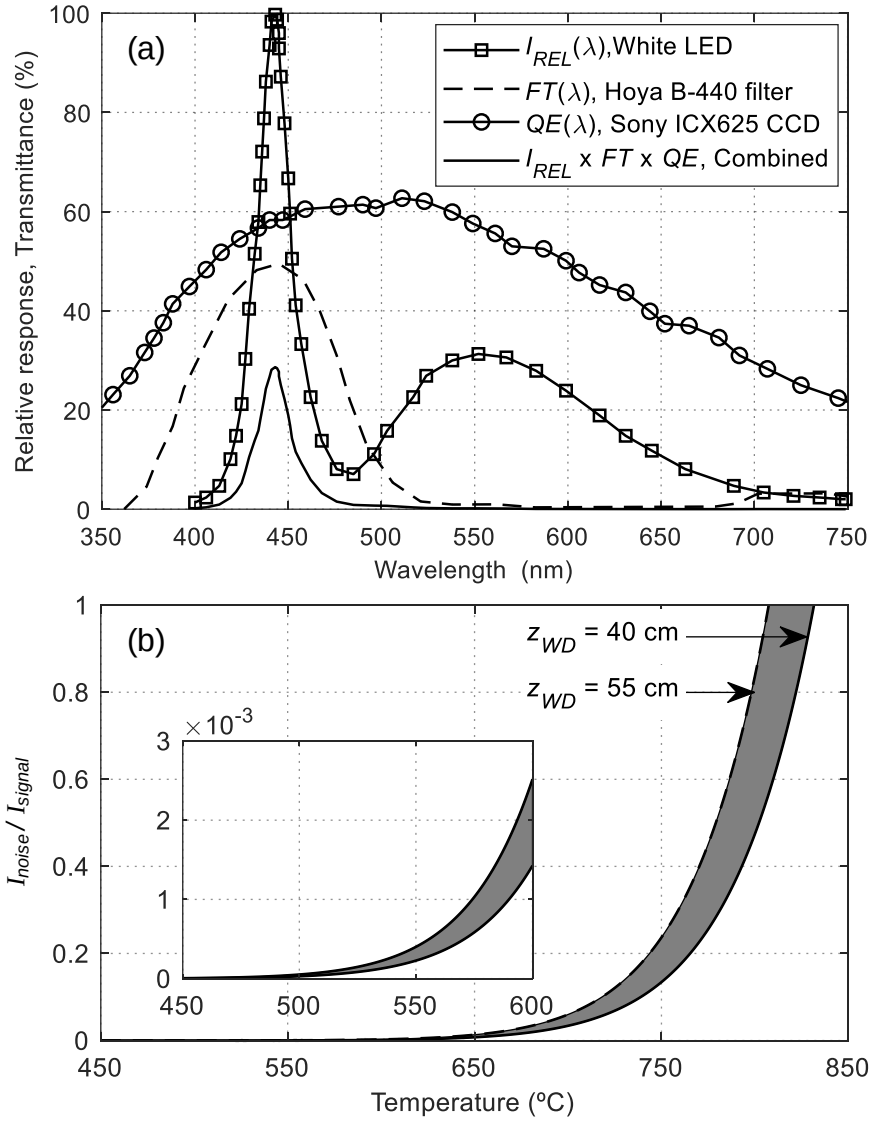

Figure 4.4: (a) Spectral properties of the colour filters, CCD sensor and lighting system in the DIC setup. (b) Calculated temperature limits of the filter-illumination setup for working distances between 40 and 55 cm

The signal intensity, I_{signal}, consists of the reflected LED light intensity that passes through the filter to the camera sensor. The intensity is computed by determining the irradiance L_e of the LED arrays, approximated as a point light source positioned at a working distance z_{WD} from the heated surface:

$$L_e = R_e \frac{F_{lens}\, P_{LED}}{\pi\,(r_i + z_{WD} \tan 0.5\alpha_{LED})^2} \tag{4.3}$$

where R_e is the reflectance (assumed to be unity), α_{LED} is the LED lens angle of 20°, P_{LED} is the total radiometric power of 40 W of the lights adjusted by an assumed lens correction factor F_{lens} of 0.85 and initial spot radius r_i of 1 cm (Novak & Zok, 2011). The signal intensity is calculated by multiplying the irradiance per solid angle of reflected light with the integral of

the combined effect of the filter $FT(\lambda)$, camera sensor $QE(\lambda)$, and relative radiant power of the LEDs $I_{REL}(\lambda)$:

$$I_{signal} = L_e \int_{\lambda=400\text{ nm}}^{600\text{ nm}} FT(\lambda) \times QE(\lambda) \times I_{REL}(\lambda)\, d\lambda \qquad (4.4)$$

The radiation noise I_{noise} is related to the spectral intensity of the emitted light as a function of the absolute temperature T and wavelength λ as specified by Planck's law for blackbody radiation:

$$I(\lambda, T) = \frac{2hc^2}{\lambda^5 \left(e^{\frac{hc}{\lambda kT}} - 1\right)} \qquad (4.5)$$

where c = 2.9979×10^8 m/s is the speed of light in a vacuum medium, h = 6.626069×10^{-34} J·s is Planck's constant and k = 1.38065 ×10^{-23} J/K is the Boltzmann constant. Similar to the signal intensity, the radiation noise is calculated by combining the blackbody radiation $I(\lambda, T)$ (Equation (4.5)), $FT(\lambda)$, and $QE(\lambda)$:

$$I_{noise}(T) = \int_{\lambda=400\text{ nm}}^{600\text{ nm}} FT(\lambda) \times QE(\lambda) \times I(\lambda, T)\, d\lambda \qquad (4.6)$$

The inverted signal-to-noise ratio, $I_{noise}(T)/I_{signal}$, estimates the maximum temperature at which the image of the speckle pattern becomes saturated and subset correlation is theoretically no longer possible. A plot of this ratio as a function of temperature at two extreme working distances (40 and 55 cm) that were encountered in the test setup is provided in Figure 4.4b. For this setup, the temperature range at which the ratio approaches unity is between 810 °C and 830 °C. It is noted, a prominently white speckle surface will ensure better reflectivity and therefore an improved signal-to-noise ratio.

4.2.6 Experimental procedure

The test procedure involves several processing steps of the data acquired from the setup detailed above. A summary of the steps involved in processing the various data streams are detailed in Figure 4.5 and include data acquisition, computation of strain, stress and temperature maps, synchronisation and extraction of material properties. Note that details regarding the material property extraction are presented in Section 4.4.

A preload force was applied to the specimen to improve the uniformity of the axial loading as well as contact at the specimen-grip interface for electrical and heat conduction. Subsequently, specimen heating occurred at a rate of 10 °C/s until the setpoint temperature was reached at the gauge section centre, followed by a 20 s dwell time to allow the temperature distribution to stabilise, before loading occurred.

DIC images are recorded at 1 Hz throughout the preloading, heating and loading stages using the LaVision DaVis 8.4 image acquisition software and was synchronised with the pulsed illumination using a LaVision Programmable Timing Unit. Thermal images were simultaneously captured, whilst the load, ram stroke and control temperature data from the

Gleeble is sampled at a rate of 20 Hz. The zero (reference) image for which the measured displacements are set equal to zero was captured at thermal steady-state, but prior to tensile loading. In this manner, thermal strains were excluded from the DIC dataset.

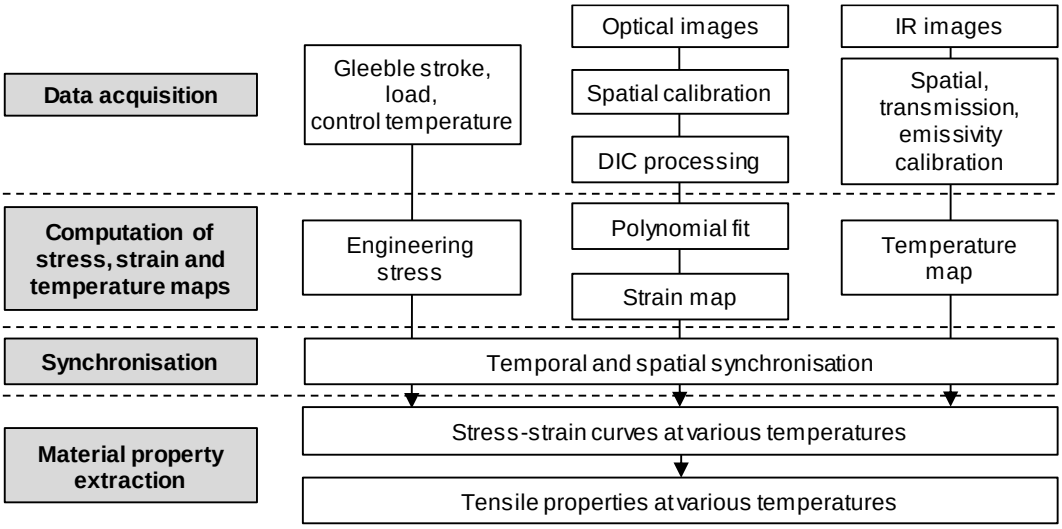

Figure 4.5: Data flow of proposed methodology

Strain, stress and temperature maps are computed using MATLAB 2016b. The respective data maps are stored in a gridded format defined by the DIC subset spacing. It was found that storing data in a regularised format allows for simple data synchronisation and computation of temperature-specific mechanical properties.

The current setup did not allow for automatic synchronisation between the three independent systems. For this reason, the data is manually aligned. Temporal matching is undertaken using the respective time stamps with a resultant error of 1 s. Spatial synchronisation between the displacement and temperature maps is undertaken by using MATLAB's linear interpolation function, *interp2*, centring data in the middle of the gauge section.

4.3 Methodology validation

Experimental validation of the developed methodology was performed from tests that assess the suitability of the various system components. This includes an assessment of the system temperature limit and the effects of heating on the speckle pattern contrast, a validation of the IR imager temperature readings as well as a FE validation of the displacement fit functions.

4.3.1 Temperature limit testing

To confirm the temperature limits estimated in Subsection 4.2.5, a specimen was gradually heated at 4.5 °C/s to a maximum temperature of 1 100 °C. As the specimen was heated, the hot zone resulted in a chemical reaction between the white base coat of the painted pattern and the underlying specimen metal (Chen, Xu, *et al.*, 2012). This resulted in a noticeable darkening of speckle features as the control temperature reached 900 °C, as shown in Figure 4.6a and b. Pattern contrast is degraded due to a reduction in spread of the grey level distribution (scale) and a shift to lower (darker) bit counts (offset) as shown in Figure 4.6b. In this experiment, it

was observed that the specimen surface began to glow at 900 °C, causing a grey scale distribution shift towards higher (lighter) bit counts as seen in Figure 4.6b. Based on visual inspection, the temperature limit of the filter-illumination combination appears to be around 900 °C, in near agreement with the theoretically determined limit of 810 °C to 830 °C.

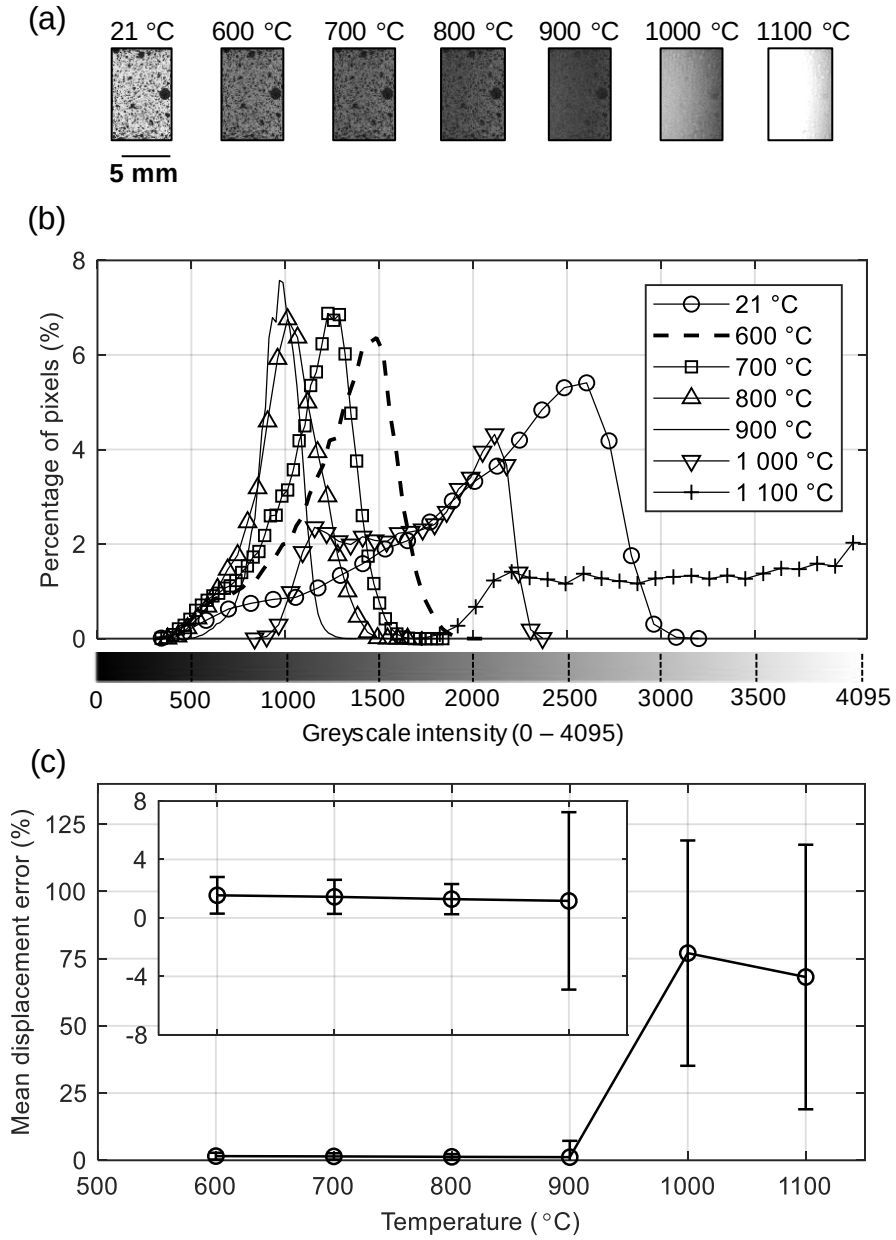

Figure 4.6: (a) Speckle pattern images taken at increasing temperatures (b) with corresponding grey level distributions. (c) Displacement error calculated at temperatures ranging from 600 °C to 1 100 °C

4.3.2 IR imager temperature measurement

In order to validate the temperature measurements, the IR thermal profiles along the specimen x-direction centreline ($y = 0$ mm) are plotted and compared to thermocouple readings in Figure 4.7a for several temperatures up to 1 100 °C. The full-field temperature map of the gauge

region as measured by the IR camera is shown in Figure 4.7b for a 600 °C set temperature. From the results, a parabolic temperature distribution in the x-direction can be observed, which agrees with findings by Walsh *et al*. (1986). On the other hand, y-direction profiles assume a quartic distribution as seen in Figure 4.7b. At 600 °C, a maximum temperature difference of 2 °C is measured between the full-field temperature map readings and the readings of four thermocouples spaced 2.50 mm apart, equating to an error of 0.3 %. This is within the measurement requirements of ASTM standards (ASTM, 2009, 2011a). Furthermore, the full-field temperature map shows a temperature range of 120 °C and a less pronounced 4 °C temperature range in the x-direction and y-direction respectively over the ROI. It was noted that the IR imager had difficulties in resolving temperatures near the specimen edges, however this was excluded from the ROI.

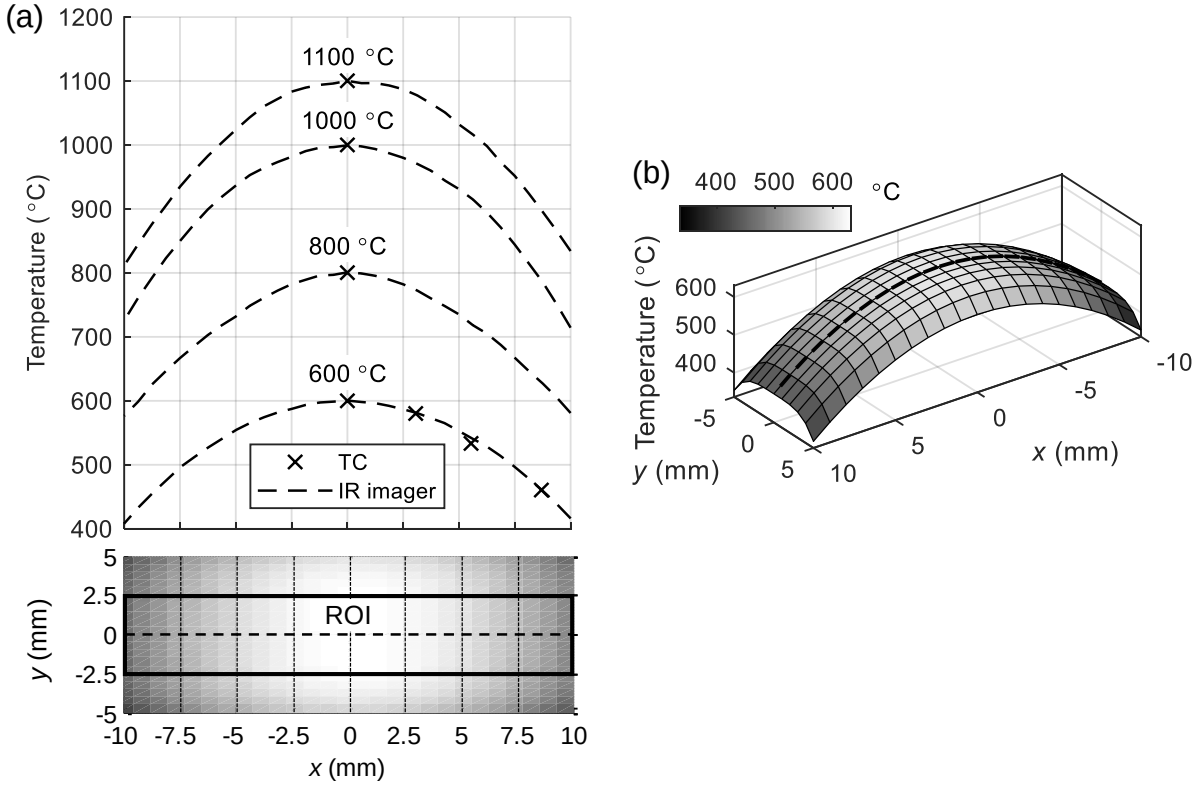

Figure 4.7: (a) Comparison between IR imager and thermocouple temperature measurements along the specimen centreline. (b) Temperature distribution recorded by IR thermography across the gauge region for a 600 °C set temperature. Additional thermocouple readings are shown for the 600 °C profile. The y = 0 mm centreline is shown as a dotted line

4.3.3 Displacement, strain and stress maps

DIC was performed using a quadratic displacement shape function and a sixth order spline grey level interpolation across the ROI using a subset size of 61 × 61 pixels^2 with a step size of 15 pixels. This equated to a subset size of about 1.5 mm. Using an Olympus GX51 optical microscope, speckle diameters were measured to range uniformly between 0.10 to 0.80 mm allowing between 10 to 25 speckles per subset. Employing a MATLAB GUI developed by Estrada and Franck (2015), an absolute displacement error of 7.5 µm was determined for a rigid

body translation of 0.5 mm, equating to a 1.5 % error. Following an increase in temperature however speckle pattern contrast decreases, which is known to have a direct effect on DIC accuracy (Estrada & Franck, 2015): as shown in Figure 4.6c, at 900 °C the displacement error lowers to 1.2 % despite the darkening of the paint. This is expected as a ZNSSD correlation criteria is used, which accounts for scaled and offset intensity variations (Schreier *et al.*, 2009). After image saturation, caused by radiation emission at temperatures over 900 ºC, a significant increase in error exceeding 77.1 % is observed.

Displacement maps can be seen in Figure 4.8a and b at an applied stress of 180 MPa for a 600 °C setpoint temperature. The polynomial fits (shown as surfaces) using Equations (4.1) and (4.2) resulted in an average RMSE of 1 µm and 0.8 µm and correlation coefficients R^2 of 0.99 and 0.92 for the u_x and u_y displacement measurements (shown as dots), respectively. Relatively larger residuals for the transverse deformation (about 30 % of maximum u_y) is attributed to the greater amount of noise present at low displacement values (within 2 µm in this case) (Grant *et al.*, 2009).

Normalised strain fields derived from the aforementioned polynomial-fitted displacement data and FE model along the specimen centrelines (y = 0 and x = 0 mm) are shown in Figure 4.8c and d respectively. Good agreement between the measured strain field profile and the FE results is shown with the greatest strain in x and y measured at the peak of the temperature profile, followed by a quadratic and quartic temperature drop in x and y, respectively. The normalised x-direction DIC strains demonstrate a 3.9 % average error with the FE results whereas the y-direction strains show a slightly higher error of 5.8 % as evident particularly outside the ROI ($|y|$ > 2.5 mm) owing to noisy displacement maps from which the fits were derived.

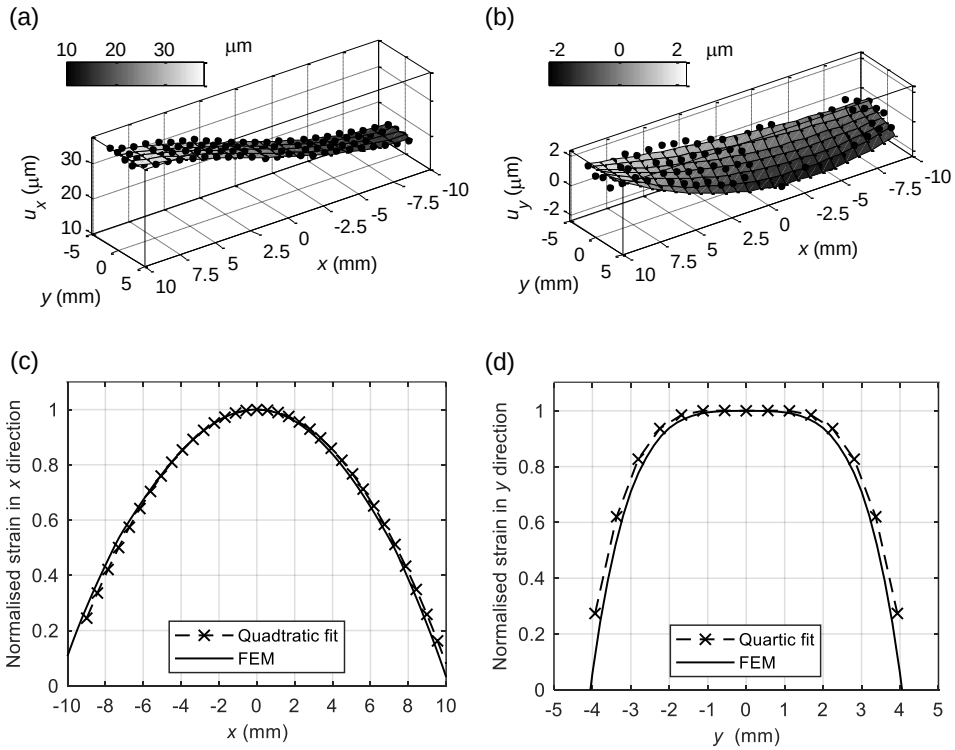

Figure 4.8: (a) and (b) Displacements measured at 180 MPa for a 600 °C setpoint, and (c) and (d) normalised measured and FE strain along the specimen centrelines in the *x* and *y* directions respectively

For all tests, engineering stress values were used as loading occurred within the elastic (low strain) regime of the material. Transverse strains however can be used to calculate true stress from the reduction in specimen cross-sectional area for testing at higher strains.

4.4 Tensile property extraction

The methodology was applied to extract the temperature-dependent tensile properties, namely Young's modulus and Poisson's ratio of X20 steel. X20 is a creep resistant, ferritic-martensitic steel and is commonly employed for steam piping, tubing and headers in coal-fuelled power stations (Bakic *et al.*, 2014). Component design for these applications relies on material property data obtained for a variety of temperatures, making X20 a good candidate material for demonstrating the proposed methodology.

4.4.1 Material composition and microstructure

The specimens are machined from virgin X20 piping in the geometry form shown in Figure 4.2. The nominal chemical composition of this steel as specified by the DIN 17175 (DIN, 1979) standard is given in Table 4.2.

Table 4.2: Nominal chemical composition of X20CrMoV12-1 in wt% (balance iron) (DIN, 1979)

C	Si	Mn	P	S	Cr	Mo	Ni	V
0.17-0.23	≤0.50	≤1.00	≤0.030	≤0.030	10.00-12.50	0.80-1.20	0.30-0.80	0.25-0.35

Microstructural heterogeneities caused by the temperature distribution will result in strain components that are not attributed to the loading condition alone. To rule out this effect, microstructural features were analysed post-test across the specimen centreline shown by the back-scattered micrographs in Figure 4.9a and b using a Zeiss MERLIN scanning electron microscope (SEM) with an accelerating voltage of 21.0 kV and magnification of 1 500×. The widths of subgrains within the martensitic lath structure were calculated using the line-intercept method as these fine features are more likely to coarsen within the time scale of a short high temperature tensile test as opposed to slower-growing precipitates (Eisenträger *et al.*, 2017). Near to the lower temperature end ($x \approx 10$ mm), widths of 0.85 ± 0.33 µm were measured, which did not differ from the 0.84 ± 0.37 µm measured at the location of highest temperature ($x \approx 0$ mm), indicating that property measurements can be made reliably across a region of uniform microstructure.

4.4.2 Elastic modulus and Poisson's ratio extraction

As a means of demonstrating repeatability of the setup, the specimen is mechanically loaded and unloaded three times at a rate of 25 N/s within the elastic range, allowing properties to be calculated from each cycle. The resulting stress-strain curves at sampling locations spaced 1 mm apart are shown in Figure 4.10a, where the solid lines are linear least-square fits to the unloading cycle data. Figure 4.10c shows the temperature-specific Young's modulus obtained from the gradient of the linear fit, compared to values reported by an online material database (Key to Metals AG, 2015). As expected, the elastic modulus decreases for an increase in temperature, with the lowest modulus of 171 GPa measured near the specimen gauge centre

where the temperature reaches a maximum of 600 °C. Compared to the database moduli, values derived from the unloading cycles agree within 10 %. It was found that measurements made from the loading cycles (shown as solid symbols) underestimated the strain rate-dependent Young's moduli especially at higher temperatures as the engineering strain rate was an order of magnitude lower than in the unloading cycles and loading possibly includes small amounts of plasticity (Eisenträger *et al.*, 2017).

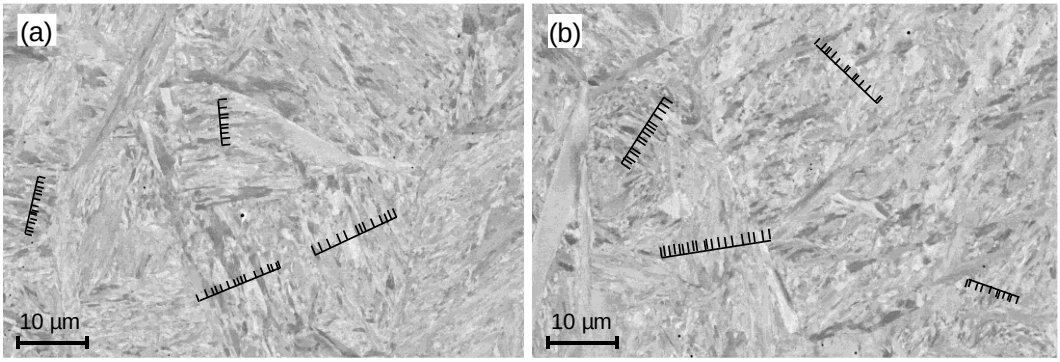

Figure 4.9: Micrographs showing subgrain width measured using the line-intercept method (a) at x = 0 mm and (b) at x = 10 mm

Similarly, the temperature-specific Poisson's ratio is calculated from a linear fit to the ratio of $-\varepsilon_y$ over ε_x as shown in Figure 4.10b. Figure 4.10d compares the obtained values to those reported in literature (indicated as a linear change from 0.32 to 0.33 from 480 °C to 600 °C). It is noted that a larger amount of scatter prevails in the measured ratios for both loading and unloading cycles due to a larger signal-to-noise ratio for the relatively small y displacement maps.

4.5 Conclusions

The presented methodology takes full-field measurement techniques to its advantage, providing temperature-dependent tensile properties from a single specimen. This is achieved, by synchronising full field strain, stress and temperature maps over a varying temperature field obtained by resistive heating using a Gleeble thermomechanical tester. It is shown that the assumption of a uniaxial stress state holds in the centre region of the specimen, and that Young's moduli and Poisson's ratios can be obtained from over a 120 °C range (for a peak temperature of 600 °C). This thermal range is especially useful for material characterisation of X20 for the power industry as it includes most of the service steam temperatures experienced in sub-,super- and ultrasupercritical power plants (Bakic *et al.*, 2014). Larger temperature variations can be achieved through the adjustment of the cross-sectional area of the specimen geometry (Norris & Wilson, 1999). Furthermore, literature values for elastic moduli are limited to temperatures of about 600 °C, with lower temperature limits (550 °C) available for tensile strength data. This methodology can potentially provide data up to 900 °C.

Future work involves employing the presented methodology to determine additional temperature-dependent material properties. For instance, the coefficient of thermal expansion can be determined from the same experiment, by setting the zero-displacement reference image to be at the beginning of the heating stage and setting external loads to zero. Time-dependent

properties such as creep can also be considered to further extract data from a single specimen. In this work, it was found that the setup could measure deformation during creep tests exceeding several hours without speckle pattern deterioration or hardware issues. It is seen that the presented metrology sets a framework for investigations that is aimed at characterising creep damage of aged power plant components.

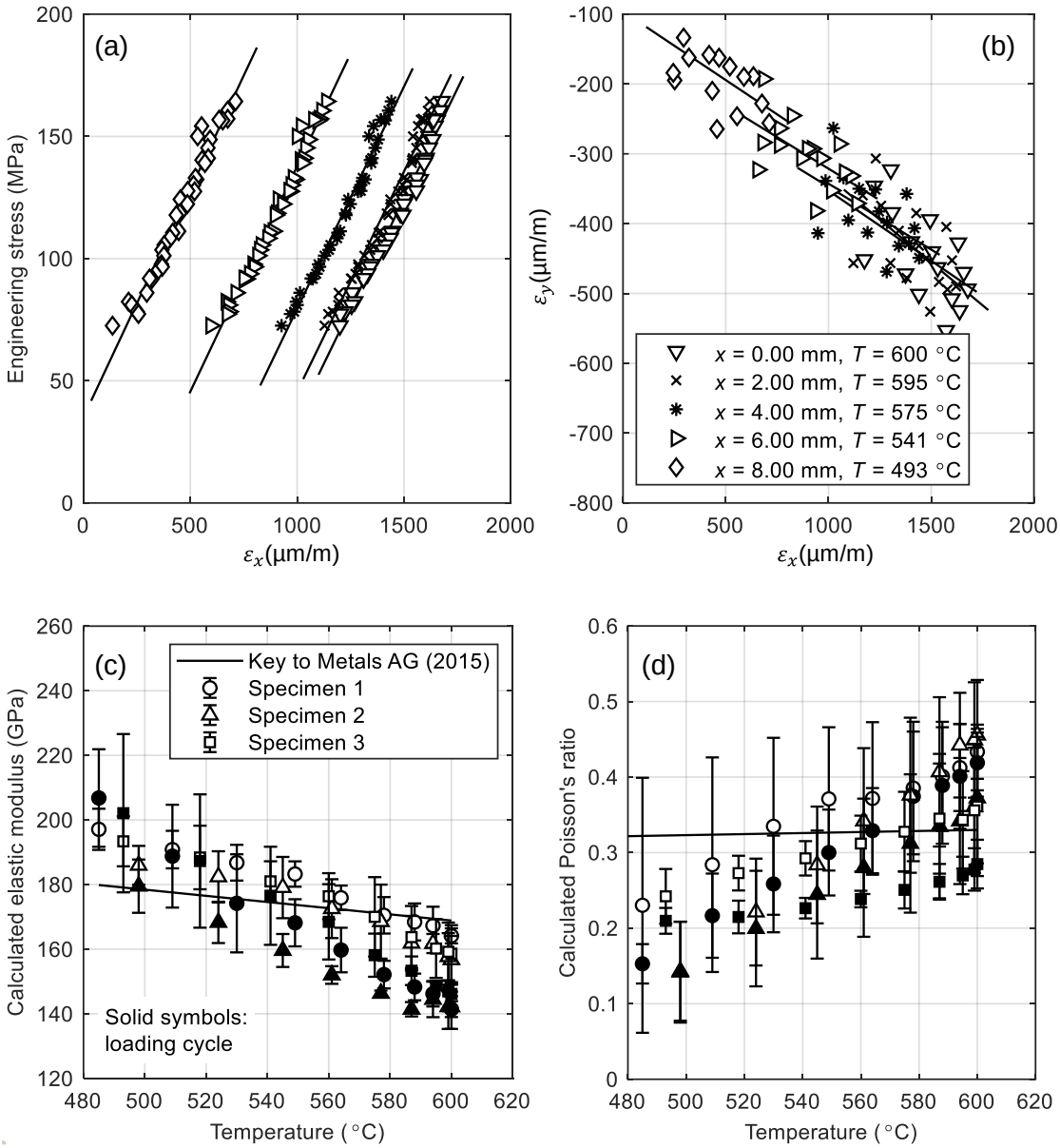

Figure 4.10: (a) Temperature-specific stress-strain curves for each unloading cycle with the legend given in (b) showing temperature-specific strain in *x* and *y* directions, (c) elastic moduli and (d) Poisson's ratios as a function of temperature for each sample (legend shown in (c)). Solid and clear symbols refer to the properties obtained from the loading and unloading cycles, respectively. Solid trend lines in (a,b) indicate linear fits to the unloading data. These trend lines are used to calculate elastic moduli and Poisson's ratios, respectively

Consideration of DIC accuracy at the low strain measurements, from which properties are measured, is of importance. A low signal-to-noise ratio can excessively skew property measurements, particularly those that consider strain in the *y* direction. In this work, polynomial fitting of the displacement data provided sufficient robustness against this. It is also important to investigate long-term aspects of camera and LED operation as well as speckle stability as these are directly linked to strain measurement accuracy.

4.6 Post-submission discussion

Following the development of the above-mentioned techniques, a few points of improvement were identified together with responses from reviewers. Firstly, this chapter did not consider the variation of true stresses across the specimen gauge on account of the thermal expansion resulting from a nonuniform temperature field using a FE model. Instead, the aim of the FE model was to indicate a range of validity of the uniaxial stress assumption across the gauge region. This is considered acceptable in the context of linear-elastic properties as the calculations of elastic moduli depend on the relative stress values $\left(E = \frac{\Delta\sigma}{\Delta\varepsilon_x}\right)$ as opposed to absolute values. In addition to the works mentioned in Subsection 4.1, Turski *et al.* (2009) demonstrated spatially resolved measurement of proof stress across weld zones of cross-weld samples using interferometric methods. In a similar manner to this work, Turski *et al.* (2009) assumed constant engineering stress across the ROI.

This is in contrast to creep tests in later chapters with an absolute dependence on stress values (notably, Equation (6.1)). Tighter control over the x-dimension of the ROI is required for the constant stress assumption in the case of elastic-plastic material property calculations. Calculation of true stress from transverse strains was also not done in this chapter on account of the relatively low stresses employed for tensile property extraction where differences between true and engineering stresses are small.

For testing in the plastic regime (such as for creep), the assumption of a linear relationship between the strain distribution and temperature profile (assumed for the derivation of elastic strain fields from Equations (4.1) and (4.2)) is not valid. To avoid systematic errors from fitting a higher-order polynomial to all strains within the ROI, a piecewise polynomial fitting approach is more appropriate. This is implemented in subsequent work related to creep testing.

5 Measurement of creep deformation of ex-service 12 % Cr steel using digital image correlation

This chapter expands the application of the technique developed in the previous chapter to accelerated creep tests. When applied to extreme conditions of ex-service X20 piping steels ("low" and "high" damage), multiple accelerated creep curves at temperatures ranging from 550 – 600 °C are measured from a single specimen for each material condition. On a comparative basis, the technique is shown to be a plausible form of damage assessment of ex-service X20 and serves as a suitable mechanical complement to the traditional void replica methodology. This is also backed by microstructural analysis through electron microscopy of the pre- and post-tested material, highlighting differences between the material states. Accordingly, this chapter addresses the second objective and serves as the basis for the subsequent chapter that applies this technique extensively.

This chapter is published in the *Journal of Strain Analysis for Engineering Design* (van Rooyen *et al.*, 2020)[13] and is presented here in its pre-reviewed form. A discussion on post-review considerations is included at the end of the chapter. The experimental technique was presented at a BSSM conference (van Rooyen & Becker, 2016a)[14] as well as at a South African Institution of Mechanical Engineering conference (van Rooyen & Becker, 2016b)[15].

Declaration by the candidate:

With regard to Chapter 5, the nature and scope of the author and co-authors is as follows:

Name	Email	Contribution	Extent (%)
M van Rooyen (candidate)	melzvanrooyen@sun.ac.za	Conceptualisation of paper, experimental design, completion of mechanical tests including DIC and hardness tests, DIC post-processing, processing of electron backscatter data, acquisition of backscatter electron images, statistical processing of microstructural data, writing and compilation of manuscript	90
TH Becker	tbecker@sun.ac.za	Beyond supervision and reviewing contributions, assisted with development of piecewise polynomial fitting code for strain calculation	2.5
JE Westraadt	johan.westraadt@mandela.ac.za	Provided access to electron microscopy facilities, draft review and microstructural data curation	2.5
G Marx	Geneveve.Marx@mandela.ac.za	Development of microstructural methodology, sample preparation and imaging (excluding backscatter electron images) and processing of concentric backscatter images	5

[13] DOI link: https://doi.org/10.1177/0309324720904517
[14] Link to extended abstract: http://www.bssm.org/uploadeddocuments/Conference%202016/2016%20papers/2-2_Becker2.pdf
[15] Conference website: https://www.saimeche.org.za/

Signature of candidate: ……..[MvR] ……..(see Footnote 12)
Date: ……..2020/04/30……

Declaration by co-authors:

The undersigned hereby confirm that:

1. The declaration above accurately reflects the nature and extent of the contributions of the candidate and the co-authors to Chapter 5,
2. No other authors contributed to Chapter 5 besides those specified above, and
3. Potential conflicts of interest have been revealed to all interested parties and that the necessary arrangements have been made to use the material in Chapter 5 of this dissertation.

Signature (see Footnote 12)	Institutional affiliation	Date
[TH Becker]	SU	2020/04/30
[JE Westraadt]	NMU	2020/04/30
[G Marx]	NMU	2020/04/30

5.1 Introduction

Damage monitoring of coal-fired power plant materials has garnered considerable interest in the past decade due to the need for extending the operating lifetimes of plants to meet the rising need for electricity. The lifetimes of critical components, which are subjected to high temperatures and loads during service times, are limited mainly by creep. Creep damage manifests as microstructural changes and the resultant deterioration of the inherent creep strength of the material, rendering the component unfit for continued safe operation. Considering the economic benefit of maintaining station components in existing aging fleets as opposed to the construction of new plants (van Zyl *et al.*, 2005), damage assessment techniques are of major practical significance to life monitoring and repair schedules used by plant operators to extend the operating life beyond the original design life.

In SA, the 12 % Cr tempered ferritic-martensitic steel with the DIN designation X20CrMoV12-1 (X20 hereafter) has been the workhorse material for the construction of thick-walled steam pipelines in coal-fired power stations for over half a century (Bakic *et al.*, 2014). Several researchers have investigated the creep strength (Auerkari *et al.*, 2007), microstructural properties (Aghajani *et al.*, 2009), deformation behaviour (Aghajani *et al.*, 2009; El Rayes & El-Danaf, 2017) and damage formation (Eggeler *et al.*, 1989) of X20. Although the understanding of X20 laboratory-generated properties is well-established, there is still a need for research into the response of ex-service power plant X20 to damage assessment techniques for life monitoring.

Traditionally, damage assessment on critical components is achieved by on-site metallographic analysis based on surface replication whereby the density of creep-induced flaws, such as voids and microcracks, are quantified. Although this technique is quasi-nondestructive, well-practiced on in-service samples (van Zyl *et al.*, 2005) and correlation has been found between the density and creep strain during creep tests on X20 (Parker, 2013), the technique suffers from several downfalls. In some cases, ex-service X20 components have displayed a lack of detectable voids at over 200 000 service hours, shifting damage classification to higher life fractions and closer to component failure (Trück *et al.*, 1991; Auerkari *et al.*, 2013). Subsurface

defects are not detectable by this method, with more invasive coring methods required to investigate damage distributions through the component thickness (Wedderburn *et al.*, 2012). Furthermore, replica preparation methods, the presence of inclusions as well as coalescence of cavities nearing the end of the component life result in apparent voids that lead to incorrect damage assessments (Sposito *et al.*, 2010).

When it is practical to remove sufficient material, post-exposure mechanical tests are conducted for damage evaluation of X20 steel, including hardness measurements (Straub *et al.*, 1997; Aghajani *et al.*, 2009), room temperature tensile tests (Bakic *et al.*, 2014), impact toughness tests (Hu & Yang, 2004; Bakic *et al.*, 2014), high temperature tensile tests (Straub *et al.*, 1997; El Rayes & El-Danaf, 2017) and creep rupture tests (Hu *et al.*, 2008). Although hardness measurements are quasi-nondestructive and can be applied to small amounts of material, Hu *et al*. (2008) found that hardness was insensitive to the damage state of ex-service X20. This is further complicated by batch-to-batch differences in heat treatments which influences strength properties of X20, making it difficult to pinpoint effects of prior exposure (Straub *et al.*, 1997). Furthermore, traditional creep testing (as outlined in ASTM E139 (ASTM, 2011a) for instance) often requires a constant temperature profile over a gauge length of a specimen. Each stress and temperature testing condition involves a new specimen and therefore such testing requires large amounts of material. For this reason, together with the long-term testing times (> 100 000 h) (Aghajani *et al.*, 2009) required to emulate the diffusional creep mechanisms that occur during service, conventional creep tests are not ideal for the damage assessment of service-exposed X20 which is often in limited supply.

Recent advancements in the field of digital image correlation (DIC) have claimed numerous benefits for material testing. DIC is a photomechanical technology in which deformation is measured by tracking a unique speckle pattern applied to a test subject surface (Schreier *et al.*, 2009). A region of interest (ROI) is divided into specified subregions known as subsets whose collection of pixel intensities is tracked across subsequent images of a surface during loading. The spatial resolution of DIC is determined by the camera setup, speckle detail and subset size settings, making it possible to collect a higher density of deformation data over the same footprint of conventional extensometry and strain gauges (Schreier *et al.*, 2009; Sakanashi *et al.*, 2017).

Literature presents few examples of application of DIC to creep deformation measurement. Narayanan *et al.* (2017) measured creep strain at 700 °C of notched Inconel 617 samples using DIC together with linear variable differential transducers (LVDTs). Similarly, creep fracture properties of alloy IN800 was measured from DIC-obtained deformation maps together with finite element methods (FEM) by Liu *et al.* (1998). Leplay *et al*. (2015) overcame the difficulties associated with classical extensometry in measuring asymmetrical creep strains of a ceramic at 1 350 °C using DIC. Within the power generation industry, DIC has shown potential for combination with online strain monitoring systems for life assessment of high-temperature piping systems (Morris *et al.*, 2007).

Very few attempts have been made to use the full-field property of DIC in combination with spatially varying temperature, stress and material properties during creep testing. Sakanashi *et al*. (2017) used DIC to track creep deformation across different weld zones of 316H stainless steel using a single specimen, highlighting the material efficiency offered by this technique. In the authors' previous work (van Rooyen & Becker, 2018), DIC was successfully used to measure elastic properties at several elevated temperatures from a single specimen subjected to a thermal profile generated through the resistive heating from a Gleeble thermomechanical testing rig.

In this work, a DIC-based experimental technique is used to measure the accelerated creep deformation behaviour of virgin and ex-service X20 with varying levels of damage. A varying thermal profile is applied using a Gleeble machine whilst DIC images are captured of a heat-resistant speckle pattern applied across a specimen gauge region. Higher stresses (close to the yield strength of X20 at temperature) and higher temperatures (550 – 600 °C) are used to accelerate creep curve development within a time frame practical to Gleeble testing (< 10 h). The aim is to investigate the feasibility of using this technique to assess the damage level of service-exposed X20 with different conditions of exposure. Quantitative microscopy is also performed to corroborate the observed deformation behaviour and to establish the effects of testing. To the best of the authors' knowledge, no previous attempt has been made to collect creep properties over a varying temperature field using DIC.

This chapter first discusses the materials and experimental method, including temperature and stress determination. The elevated temperature behaviour of X20 in various damage states and the resulting microstructural properties are presented in Section 5.3, followed by a short discussion on the plausibility of accelerated creep testing using DIC as a technique for damage evaluation.

5.2 Experimental materials and methods

5.2.1 Materials and specimen geometry

In the current study, specimens were machined along the longitudinal direction of virgin and service-exposed X20 main steam pipe sections with internal diameters of 255 ± 5 mm and wall thicknesses of 35 ± 1 mm. Two different ex-service X20 states that were previously characterised for damage according to void densities measured from surface replication were investigated in this work. Low damage material (60 – 90 cavities/mm^2) was exposed to 545 °C operating temperatures at pressures of 17 MPa for about 130 000 h whereas the high damage material (220 – 690 cavities/mm^2) was subjected to operating temperatures of 543 °C and pressures of 18.1 MPa for approximately 156 000 h. Table 5.1 shows the alloying elements of the piping materials measured using spectrographic analysis.

Table 5.1: Chemical composition of virgin and two different ex-service X20CrMoV12-1 steels in wt% (balance iron)

Material	**Elements**								
	C	**Si**	**Mn**	**P**	**S**	**Cr**	**Mo**	**Ni**	**V**
Virgin	0.21	0.19	0.58	0.015	0.004	11.6	0.88	0.76	0.25
Low	0.19	0.36	0.63	0.013	<0.005	11.7	0.91	0.67	0.32
High	0.17	0.20	0.59	0.015	<0.005	11.6	0.94	0.71	0.34

Two variations in specimen geometry were considered in order to investigate the effect of different stress and temperature profiles (as discussed later). The first geometry is standard for Gleeble specimens and consists of a 10 × 10 mm^2 cross-sectional area whilst the second geometry has a gauge region with a 10 × 2 mm^2 cross-sectional area. The specimen geometries are respectively named square and flat specimens with dimensions shown in Figure 5.1. The

coordinate system in Figure 5.1b where *x* is the longitudinal loading direction and *y* is the transverse direction is used from hereon.

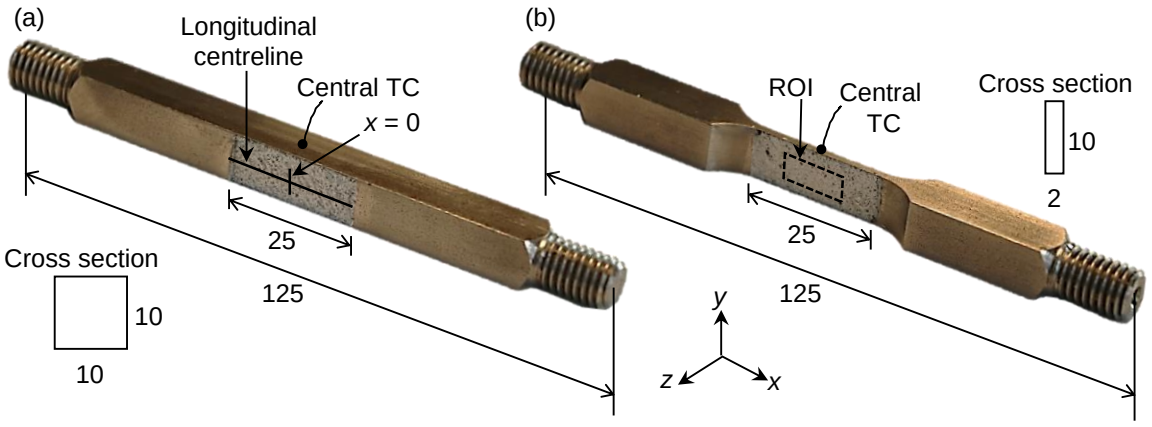

Figure 5.1: Geometry of the (a) square and (b) flat cross section specimens. Coordinate system is shown in (b). All dimensions are in mm. TC = thermocouple. ROI = region of interest

5.2.2 Gleeble-DIC testing

Accelerated creep testing was performed using an arrangement presented in the authors' previous work (van Rooyen & Becker, 2018) and is briefly summarised here along with setup differences. X20 specimens were loaded within the vacuum chamber of a Gleeble 3800 thermomechanical testing system as shown in Figure 5.2. Resistive heating was controlled by feedback from a K-type thermocouple welded to the specimen centre (shown in Figure 5.1) which regulated temperatures within 2 °C. Conduction heat loss from the specimen centre to water-cooled grips resulted in a nonuniform thermal field. Full-field temperature measurement was made using a Fluke Ti400 infrared (IR) camera on the rear of the specimen which was coated in a heat-resistant matte black paint. Following temperature stabilisation after 30 s, the force was increased from a pre-load to a maximum value which is maintained within 0.10 % during accelerated creep testing in load control.

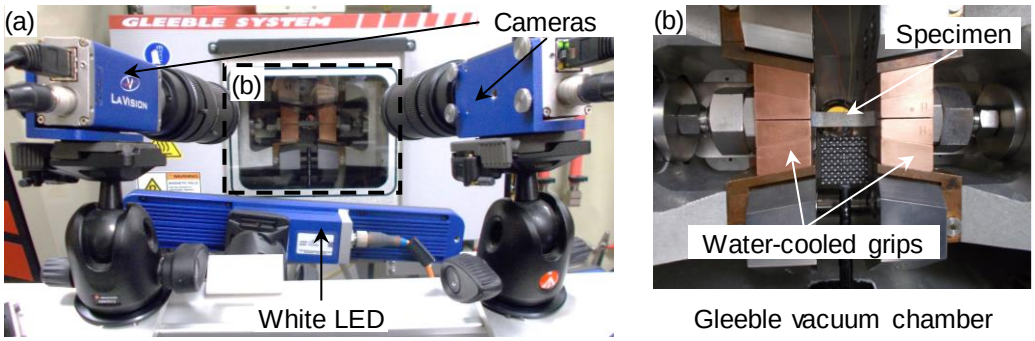

Figure 5.2: Photograph of the (a) DIC setup positioned in front of the loaded specimen in the (b) Gleeble vacuum chamber

Table 5.2 highlights the main DIC hardware elements involved in this study. During testing, images were recorded by a two-camera LaVision setup positioned in front of the Gleeble vacuum chamber viewing window as shown in Figure 5.2a. The cameras were paired with macro lenses and blue filters which along with high-powered white light-emitting diodes (LEDs) functioned together to suppress surface radiation at high temperatures. A speckle pattern was applied to the 25 × 10 mm^2 ($x \times y$) gauge region of the specimens using heat-resistant, black spray paint on a white base (shown in Figure 5.1).

Table 5.2: DIC hardware details

Camera	LaVision Imager E-lite 12-bit, 5 MP CCD cameras
Image resolution	2 058 × 2 456 pixels^2
Lens	75 mm TECHSPEC Double Gauss macro lenses
Aperture	f/4
Field of view	50 × 60 mm^2
Magnification factor	42 pixels/mm
Stand-off distance	400 mm
Image acquisition rate	0.1 Hz
Lighting	Pair of LaVision white linear units consisting of 12 LEDs each, 20 W, 6 500 K colour temperature
Patterning technique	White VHT heat-resistant base coat with corresponding black speckles applied via spray can
Pattern feature size (average)	0.07 – 0.2 mm (3 – 8 pixels)

5.2.3 Conventional creep testing

As a means of verifying the accelerated creep technique, conventional creep tests were conducted according to ASTM E139 (ASTM, 2011a) using a 11,1:1 single lever creep testing machine. The round specimen geometry consisted of a 5.65 mm diameter and 28.25 mm gauge length. A three-zone tube furnace was used to heat the specimen and the temperature was maintained within 2 °C across the specimen gauge as monitored by three K-type thermocouples. Displacement was measured using two LVDTs fixed to the specimen through an extensometery setup. Accelerated tests at 600 °C were conducted at engineering stresses of 250 MPa for the virgin X20 and medium-term tests were conducted at 140 MPa for virgin and ex-service X20.

5.2.4 Temperature and stress determination

Previous investigations (Walsh *et al.*, 1986; van Rooyen & Becker, 2018) have shown that the Gleeble specimen geometry has a direct influence on the resulting temperature distribution and

consequently the stress distribution. Figure 5.3a compares the two temperature profiles (averaged across four tests) as measured by the thermal imager longitudinally along a specimen centreline (indicated in Figure 5.1a) for each geometry type at a setpoint temperature of 600 °C. Note $x = 0$ is taken to be the location of maximum temperature – located close to the central thermocouple. For both geometries, the longitudinal temperature profiles can be represented by a second-order polynomial (Walsh *et al.*, 1986). A more gradual quartic profile (< 5 °C within ±2.5 mm) was observed for the transverse directions. Flat geometries produced a steeper thermal gradient due to a higher surface area-to-volume ratio which reduces the dominance of conduction in the specimen heat flow (Walsh *et al.*, 1986). Throughout testing, the thermal profile remains within 2 °C of the initial stabilised profile.

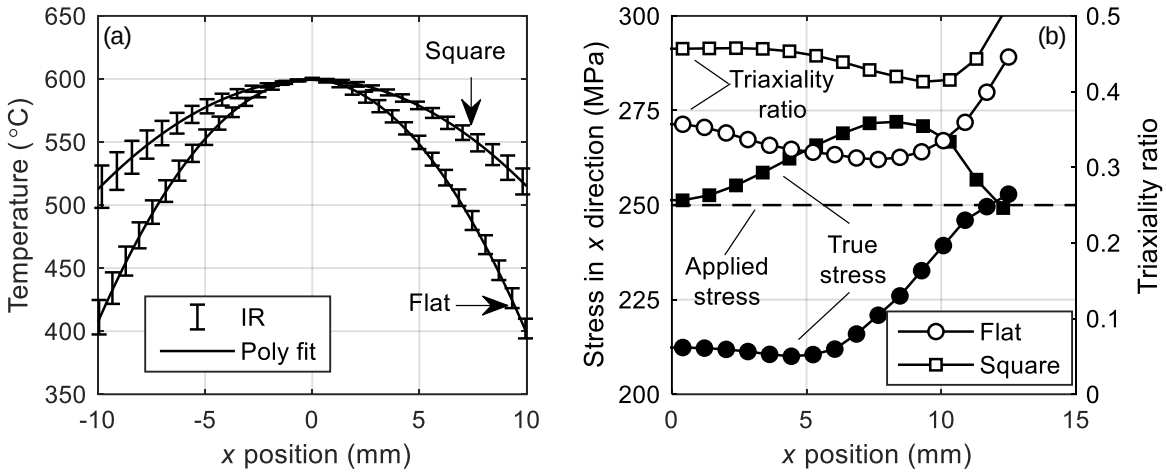

Figure 5.3: (a) Temperature profile along the longitudinal centreline of the flat and square geometries as measured by the IR imager. (b) Variation of the true longitudinal stress component and triaxiality ratio along the longitudinal centreline of the flat and square geometries at a 250 MPa applied stress

Differences in thermal profiles will also influence the stress distribution of each specimen geometry. To investigate this effect, a finite element (FE) elastic-plastic model was created for each geometry gauge region. Using ABAQUS 2017 FE analysis code, a mesh consisting of 62 000 and 50 400 eight node linear brick (C3D8) elements were assigned to flat and square geometries, respectively. The full thermal distribution measured for each geometry using the IR imager was applied to the geometry through a predefined temperature field. Considering that the applied engineering stresses used in testing was close to the reported yield strength of X20 (< 260 MPa at 600 °C), deformation plasticity had to be considered using a Ramberg-Osgood (RO) law. RO parameters (Table 5.3) at several temperatures were determined from stress-strain data using DIC during a tension test that used the same setup as described in this paper. Elastic and thermal parameters can be found in van Rooyen and Becker (2018).

The longitudinal true stress distribution along one half of the specimen surface centreline ($y = 0$) is shown in Figure 5.3b along with the stress triaxiality (ratio of hydrostatic stress to von Mises stress) (Wen *et al.*, 2016) for each geometry type at an applied (engineering) stress of 250 MPa. Longitudinal true stress profiles for both geometries differ from the applied stress of 250 MPa. This is a direct result of the nonuniform thermal expansion resulting from the temperature field. Lower true stresses (≈ 210 MPa) are experienced by the flat specimens when compared to the square versions. This can be attributed to the steeper thermal profile that results in higher

compressive thermal stresses that take up the applied tensile stress. Unlike the square geometry with relatively high stress triaxialities (≈ 0.46), triaxiality ratios determined from the flat specimens at $x = \pm 5$ mm are closer to 0.33, indicating uniaxiality in the stress distribution. Although not shown here, *y*-direction stress triaxiality at $x = 0$ was found to be within 1 % of the *x*-direction values within ± 2.5 mm due to the uniformity of temperature in this direction. Based on these findings, flat samples were employed for accelerated testing using a ROI of 10×5 $(x \times y)$ mm^2 centred on the gauge area (shown in Figure 5.1b) for DIC processing equating to a temperature variation of 550 °C to 600 °C. Only the deformation measured at 600 °C of the square specimen was included for comparison at higher stresses. In all cases, the average true stress is quoted.

Table 5.3: RO parameters values as a function of temperature employed in the FE analysis.RMSE = root-mean-square-error

Temperature (°C)	Yield stress (MPa)	Exponent	Yield offset	RMSE (MPa)
600	295	7.27	1.14	5.84
590	304	9.07	1.12	4.82
580	313	10.86	1.09	3.01
570	322	12.66	1.07	3.93
560	331	14.45	1.04	5.56
550	340	16.25	1.02	2.44

5.2.5 Processing of DIC data

Displacement maps were obtained by processing the recorded images in the LaVision DaVis 8.4 correlation software using key processing parameters in Table 5.4. A ROI of 10×5 $(x \times y)$ mm^2 centred on the gauge area was selected for strain calculation to remain within the uniaxial stress region as established above. Self-correlated tests (correlation of images at no load) at 600 °C revealed similar spatial and temporal strain noise floors as calculated according to iDICs guidelines (Jones & Iadicola, 2018). By setting the reference DIC image to coincide with when the maximum constant load is reached, only creep strains were included whilst elastic, plastic and thermal components were excluded.

Subsequently, a piecewise quadratic polynomial surface fit was applied to the DIC displacement data using MATLAB 2019a across a window size of 7 data points. Strain maps were obtained from the derivative of the displacement fits. At various x-positions (corresponding to different temperatures as shown in Figure 5.3a) the reported strain values are the average values across the y-direction of the ROI. This allowed scatter to be minimised in comparison with strains approximated from central differencing of displacements which was found to be as high as 250 με from self-correlation tests. Creep strain rate is obtained by applying a Savitzky-Golay filter to the creep strain-time data using the derivative of a quadratic polynomial regression fit over a sliding window size of 30 points. This method overcomes the scatter and negative strain rates that result from the MATLAB *gradient* function as shown in Figure 5.4.

Table 5.4: DIC software parameters

Software	LaVision DaVis 8.4
Subset size	61 pixels (Gaussian-weighted)
Step size	15 pixels
Subset shape function	Second-order
Matching criterion	Zero-normalized sum of squared differences (ZNSSD)
Interpolant	Sixth-order spline
Region of interest (ROI)	5 × 10 ($x \times y$) mm^2 centred about highest temperature location
Strain window	7 data points
Virtual strain gauge size	151 pixels (3.6 mm)
Strain derivation	Derivative of piece-wise quadratic surface fit to displacements
Post-filtering of strains	Temporal moving-average spanning 30 points (300 s)
Displacement noise floor (x direction)	Spatial: 2.9 μm (0.12 pixels), Temporal: 3.0 μm (0.13 pixels)
Strain noise floor (x direction)	Spatial: 109 μm/m, Temporal: 103 μm/m

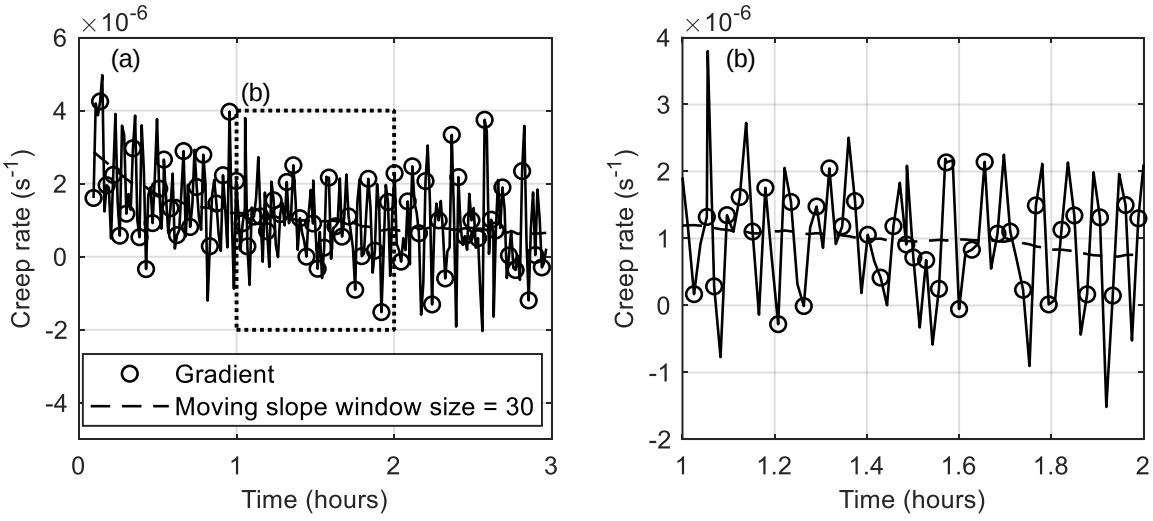

Figure 5.4: (a) Evolution of creep strain rate (at 200 MPa nominal stress) over time calculated from the gradient of creep strain over time and using a moving slope second-order polynomial regression fit. Details are highlighted in the magnified image in (b)

5.2.6 Microstructural analysis

The current setup ensures that grip regions are not strained or subjected to high temperatures. The grip regions are therefore reflective of the initial state of the material before testing. Microstructural characterisation was made on the high and low damaged samples in the grip and subsequently in the gauge (near the 600 °C location) regions using electron microscopy techniques developed in Marx (2019). Void density was investigated by a JEOL JSM 7001F field emission gun scanning electron microscope (FEG-SEM) in backscatter (BS) mode (15 kV accelerating voltage, 0.27 nA probe current and 9.9 mm working distance) on bulk specimens prepared with a final polishing step of 0.25 μm colloidal silica. Subgrain and precipitate details are analysed using a FEI concentric backscatter (CBS) detector on a FEI Heloios NanoLab DualBeam 650 focused ion beam (FIB) SEM (5 kV, 0.20 nA and 4 mm). Atomically heavier precipitates were identified as brighter features on these micrographs.

Qualitative information regarding dislocation density and substructure was observed on 3 mm diameter electro-polished discs using a JEOL JEM 2100 LaB6 scanning transmission electron microscope (STEM) at a 200 kV accelerating voltage operated in annular dark field (ADF) mode. For quantitative analysis, MIPAR image processing software (Sosa *et al.*, 2014) was used as described in Marx (2019). Electron backscatter diffraction (EBSD) maps are acquired using a Nordlys HKL system on the FEG-SEM with a 0.2 μm step size using settings optimised for X20 (Marx, 2019). Grain size analysis was conducted using the MTEX 5.2 MATLAB R2019a toolbox (Bachmann *et al.*, 2010) using a half quadratic optimisation filter with a 1.3° boundary preservation. Grains smaller than 3 pixels^2 were excluded.

5.3 Results

5.3.1 Effect of temperature on deformation

In order to demonstrate the repeatability of this experimental procedure, the strain at temperatures symmetrically located about the maximum temperature of the parabolic thermal profile is compared. This would confirm that the stress encountered within the ROI is uniform and that the deformation behaviour is similar at the symmetric temperature locations. As shown in the error bar plots of Figure 5.5 for low damage X20 at 236 MPa, the variation in accelerated creep strain and rate between the two locations of identical temperature is small, demonstrating good repeatability within a single sample. Strains are within 4×10^{-4} and creep rates are within 8×10^{-8}/s between the two locations. Larger errors are noted at lower temperatures (< 550 °C) due to the smaller strains that evolve at these temperatures as well as the higher scatter in the lower temperature measurements (Figure 5.3a).

Figure 5.6 shows the difference between low and high damage X20 material in terms of the creep strain and rate evolution over time at several temperatures. Higher creep strains and faster creep rates are observed for the high damage material compared to the low damage counterpart. Shorter rupture times and more evolved creep curves are also noted for the high damage state. At lower temperatures (~ 550 °C), only the primary creep stage is evident for both damage states and larger scatter is noted in the creep rate curves which is again attributed to the higher variability of the thermal profile at lower temperatures.

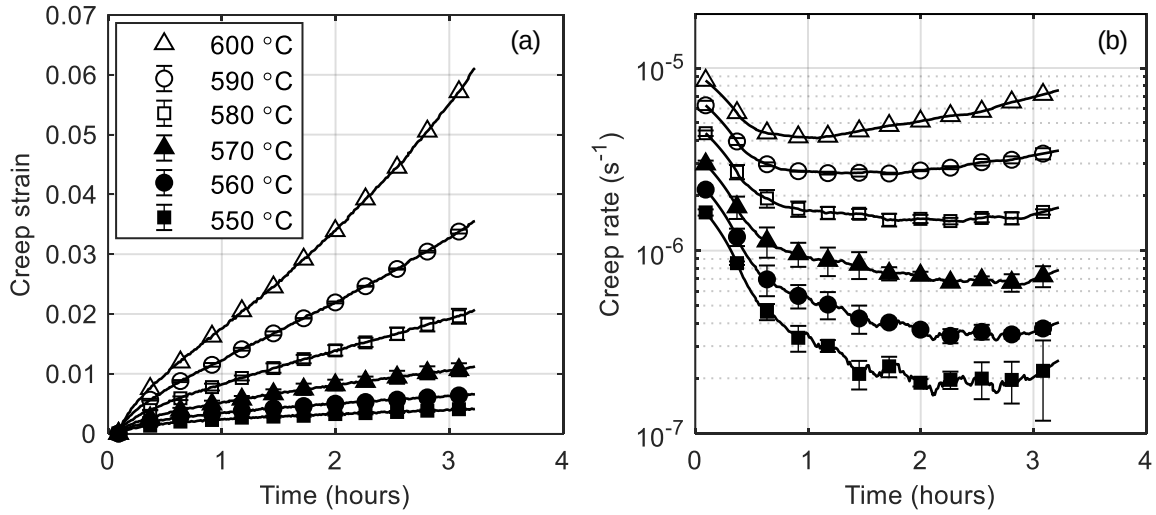

Figure 5.5: (a) Creep strain-time and (b) creep rate-time plots for low damage X20 at 236 MPa averaged at temperatures symmetrically about the maximum temperature of the quadratic thermal profile. Error bars indicate the variation in measurements between the two locations

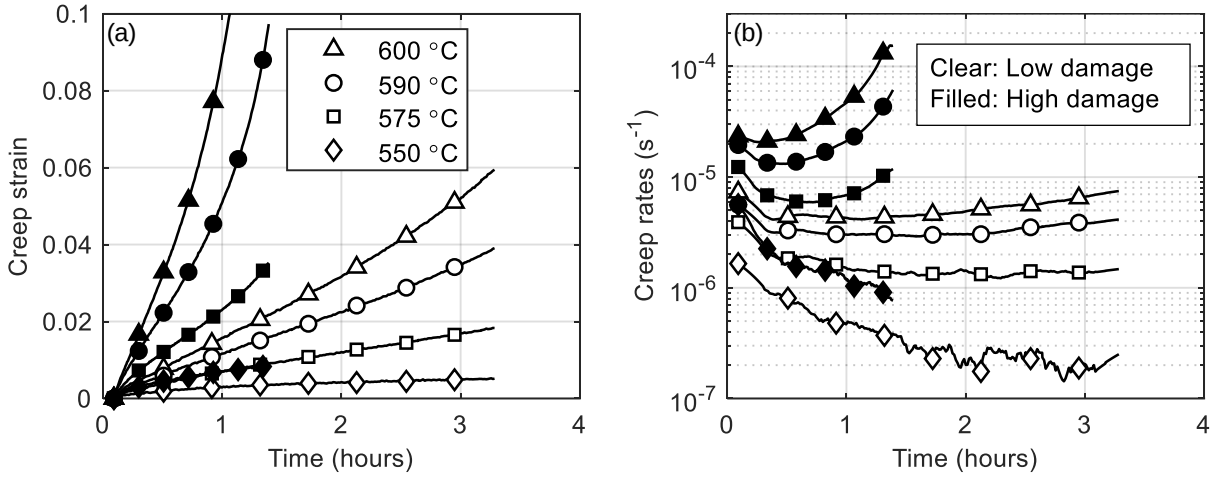

Figure 5.6: Comparison of (a) creep strain and (b) creep rate vs. time of low and high damage X20 at several temperatures and 223 MPa (clear and filled symbols, respectively)

5.3.2 Effect of stress on deformation

Accelerated creep curves at several stresses measured at 600 °C for low and high damage material are compared in Figure 5.7. Curves measured from square specimens are included and indicated with (S) next to the corresponding legend entry in Figure 5.7a. Higher creep rates are noted for the high damage material across all stress states. Considering that the high damage material does not demonstrate a typical creep rupture curve at stresses greater than 257 MPa as shown in the inset in Figure 5.7b, well-defined minimum creep rates are best observed between the low and high damage material within the 159 MPa to 236 MPa stress range. It should also

be highlighted that although the creep strain curve of the low damage material at 236 MPa lies above the curve at 223 MPa (Figure 5.7a), similar creep rates are shown for the two stresses (Figure 5.7b). This highlights the importance of comparing creep rates in addition to creep strains when considering damage comparisons. One possible explanation for the similar creep rates at the two different stresses is the heterogeneous nature of microstructural and damage features across the sampled pipe volume, which is suggested by the large variation in hardness at different positions in the low damage pipe (211 – 231 HV using a 1 kg load).

5.3.3 Comparison with conventional testing

As a validation of the technique in alignment with conventional creep testing, two different tests were conducted on virgin X20. One test was conducted using the Gleeble-DIC setup and square geometry at a maximum temperature of 600 °C (at the specimen centre) and engineering stress of 250 MPa as described in this work. Using a conventional creep testing rig with average deformation measured using LVDTs, another test was conducted on a standard specimen geometry at a uniform temperature of 600 °C at 250 MPa engineering stress. Strain rate from the latter test is calculated using the MATLAB *gradient* function. Figure 5.8 compares the creep curves from the two tests. Good agreement is apparent between the DIC strain and LVDT measurements (over a gauge length of 28.25 mm). Deviation between the curves occurs within the tertiary regime, although this can be attributed to plastic instabilities, such as necking and void formation (Sakanashi *et al.*, 2017). Furthermore, the DIC technique fails at high strains (> 15 %) that causes the speckle pattern to flake off the specimen surface (Figure 5.8b) and decorrelation to occur. Although not demonstrated here, strains of up to 35 % have been successfully measured before paint flaked off from the flat specimen geometries. This is considered the strain limitation of the proposed DIC technique.

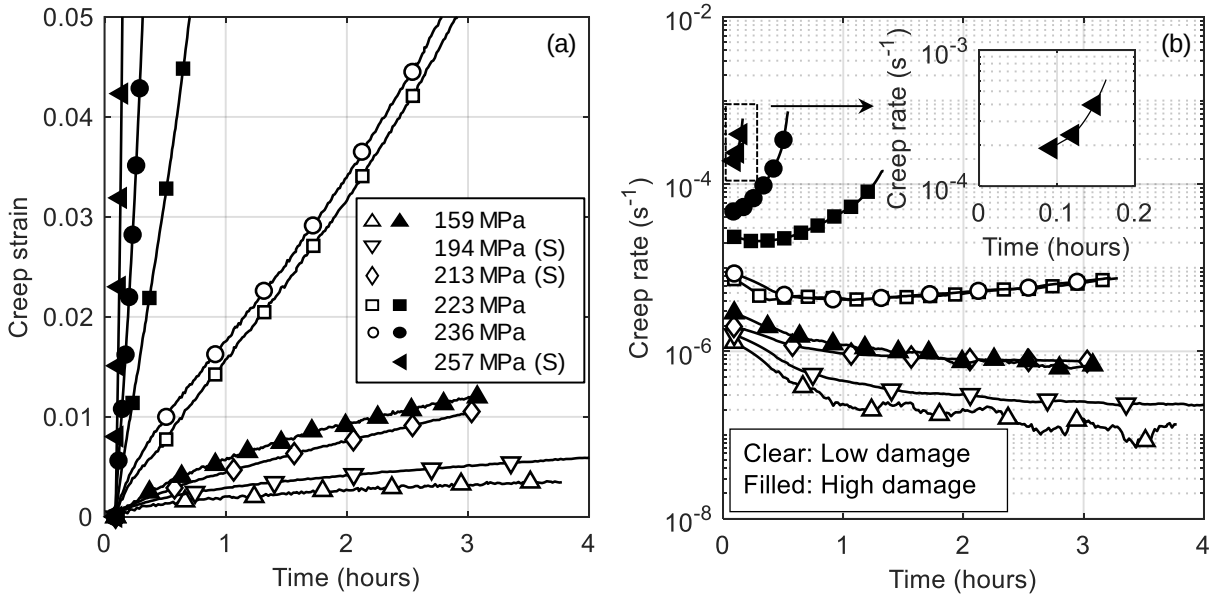

Figure 5.7: Comparison of (a) creep strain and (b) creep rate vs. time of low and high damage X20 at several stresses and 600 °C (clear and filled symbols, respectively). Curves measured from square specimens are indicated with (S) in the legend in (a)

The creep curves measured from conventional tensile creep tests conducted at 140 MPa engineering stress and 600 °C on the virgin and ex-service material are shown in Figure 5.9.

High damage X20 displays faster creep rates and shorter rupture times in agreement with the shorter, high-stress Gleeble-DIC tests.

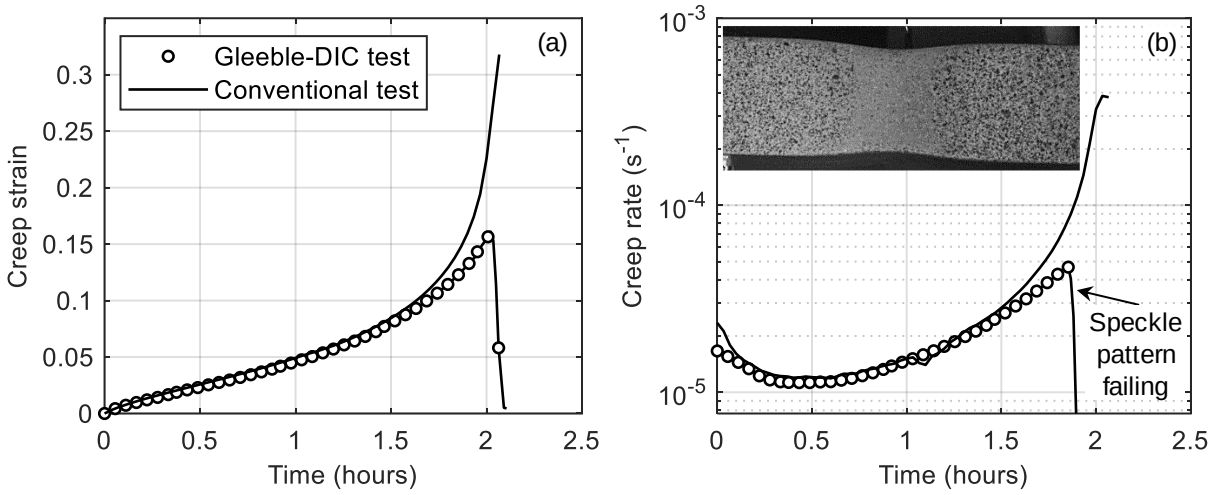

Figure 5.8: (a) Creep strain-time and (b) creep rate-time curves at 600 °C and 250 MPa engineering stress for virgin X20, comparing strain measurements made by Gleeble-DIC at the square specimen centre and by LVDTs over the gauge length of a conventional creep specimen. A faded speckle pattern which causes erroneous strain readings is shown in the inset in (b)

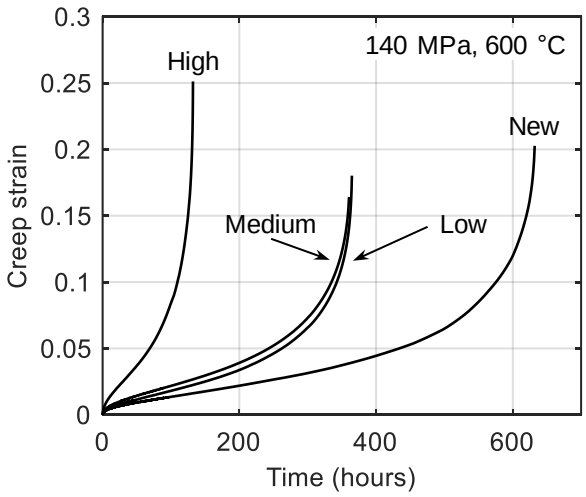

Figure 5.9: Evolution of creep strain of virgin and ex-service X20 during conventional creep tests at 140 MPa and 600 °C[16]

5.3.4 Microstructural investigation

The microstructural differences in terms of subgrain size and precipitate distributions are qualitatively shown in the BS-SEM images in Figure 5.10 for the gauge (223 MPa, 600 °C) and

[16] Figure 5.9 has been modified from the original submission to include medium X20 data. This is purely for convenience for discussions in Section 8.3.

grip regions of the low and high damage material. Both material states show small subgrains (< 1 µm width) outlined with stringers of two different precipitates. Large and low volume fraction (< 1 %) Laves phase (Fe_2Mo) particles are shown on some boundaries along with smaller and higher volume fraction (> 5 %) $M_{23}C_6$ (where M = Cr, Fe) carbides.

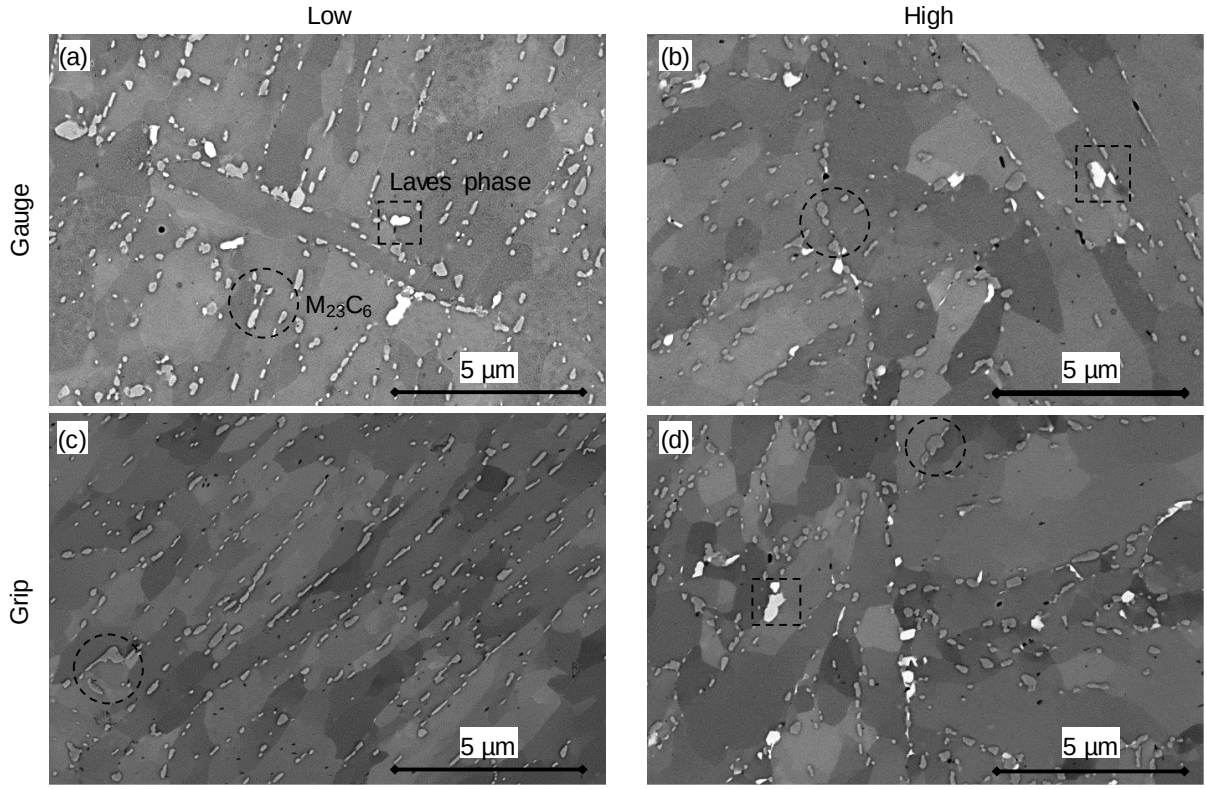

Figure 5.10: BS-SEM images of the gauge (a,b) and grip (c,d) regions of low and high damage X20, respectively. Subgrain and precipitate details are shown with lighter features corresponding to Mo-rich Laves phase (examples shown in square outlines) and darker particles are Cr-rich $M_{23}C_6$ particles (circle outlines)

Table 5.5 summarises the mean size and volume number densities of the precipitates measured in the grip and gauge regions of the ex-service material along with 95 % confidence intervals. Although no differences are qualitatively obvious between the gauge and grip regions of each material condition, the high damage material displays a higher amount of Laves phase and larger and more globular Cr-carbides when compared with the low damage counterpart. Larger precipitates that are spaced further apart result in the deterioration of creep strength due to the reduced ability to pin dislocations (Aghajani *et al.*, 2009). The precipitation and growth of Laves phase is also linked to solid solution depletion of Mo and weakening of the matrix (Aghajani *et al.*, 2009). Table 5.5 also indicates the cavity density measured from BS-SEM images which agree with the supplier's surface replica results reported in Subsection 5.2.1. The cavity density increases to 488 voids/mm^2 near fracture in the high damage material.

The distribution of subgrain size (calculated from the short width of fitted ellipses to segmented grains in BS-SEM images) compared between the grip and gauge regions of the low and high damage materials are shown in Figure 5.11. A lognormal distribution is apparent for the subgrain sizes with the high damage material displaying a higher frequency of larger subgrain

sizes (> 2 µm) indicating a higher extent of subgrain growth. Subgrain growth is obvious in the low damage material following testing as shown in Figure 5.11a. Interestingly, minor differences are found between the gauge and grip regions of the high damage material as shown in Figure 5.11. This can be attributed to dynamic recrystallisation that occurs near the necked and ruptured end of the low and high damage material, respectively, that results in a higher frequency of smaller subgrains. Furthermore, the image segmentation technique employed in identifying individual subgrains in the BS-SEM images is especially susceptible to errors resulting from similar threshold values between neighbouring subgrains with minor misorientation differences (Marx, 2019).

Table 5.5: Precipitate diameters and volume number densities as measured in the grip and gauge region of the low and high damage X20 tested at 600 °C and 223 MPa

Material	Region	Laves phase		$M_{23}C_6$	
		Size (nm)	Volume number density (μm^{-3})	Size (nm)	Volume number density (μm^{-3})
Low damage (≈ 100 cavities/ mm²)	**Grip**	-	0	182 ± 12	16.8 ± 4.7
	Gauge	264 ± 51	0.4 ± 0.4	197 ± 13	16 ± 1.7
High damage (≈ 270 cavities/ mm²)	**Grip**	212 ± 40	1.9 ± 0.7	196 ± 2	13.8 ± 1.3
	Gauge	246 ± 27	1.5 ± 0.5	210 ± 20	11.3 ± 3.4

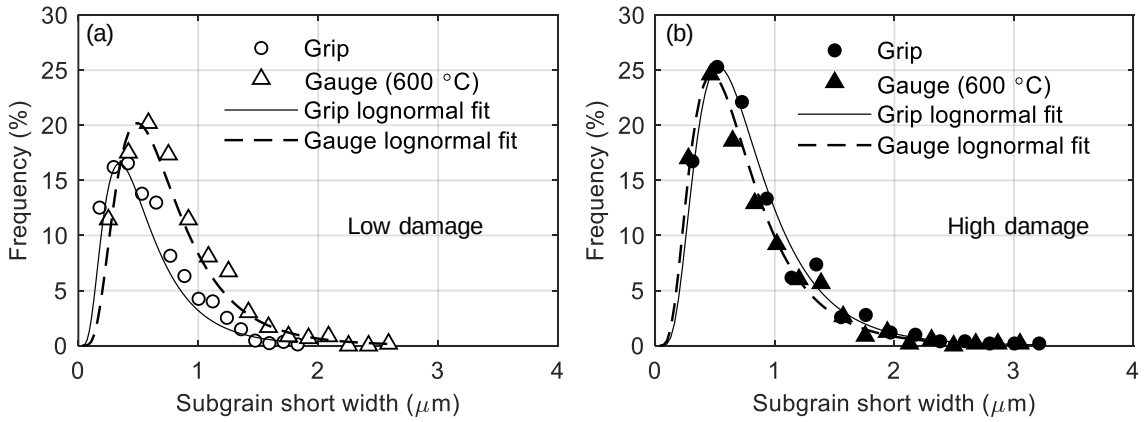

Figure 5.11: A comparison of the subgrain size distribution between the grip and gauge regions (at 600 °C and 223 MPa) in the (a) low and (b) high damage X20

As a complement to the subgrain size calculation from BS-SEM images, EBSD was employed. The advantage of EBSD subgrain calculation is the improved sampling statistics gained from the large amount of grains within a single map. Typical inverse pole figure (IPF) maps of the

gauge and grip regions of each ex-service state are shown in Figure 5.12. Subgrains reconstructed with boundary misorientations of at least 5° are outlined. This threshold boundary angle was chosen in consideration of the angular resolution limitation of orientation mapping techniques, which is typically 0.5 – 2° (Humphreys, 2004). Subgrain widths are measured from the short axis of ellipses fitted to grains outlined within 245 × 184 μm^2 sized EBSD maps and results are shown in Figure 5.13 alongside BS-SEM measurements with 95 % confidence intervals measured from the lognormal distributions (Olsson, 2005). Subgrain sizes appear to grow in the unruptured, low damage gauge region compared to the grip region. Comparing BS-SEM and EBSD measurements from the high damage material, growth is registered using the latter technique in the gauge region. This is potentially due to the EBSD filtering procedure that removes refined, dynamically recrystallised grains with higher misorientation angles from the gauge region (Xu *et al.*, 2019). Subgrain growth kinetics for X20 suggested by Straub (1995) also suggests that larger initial subgrain sizes (such as those in the high damage material) have a lower driving force to grow to stabilised values at high stresses, resulting in less subgrain growth for the same strain.

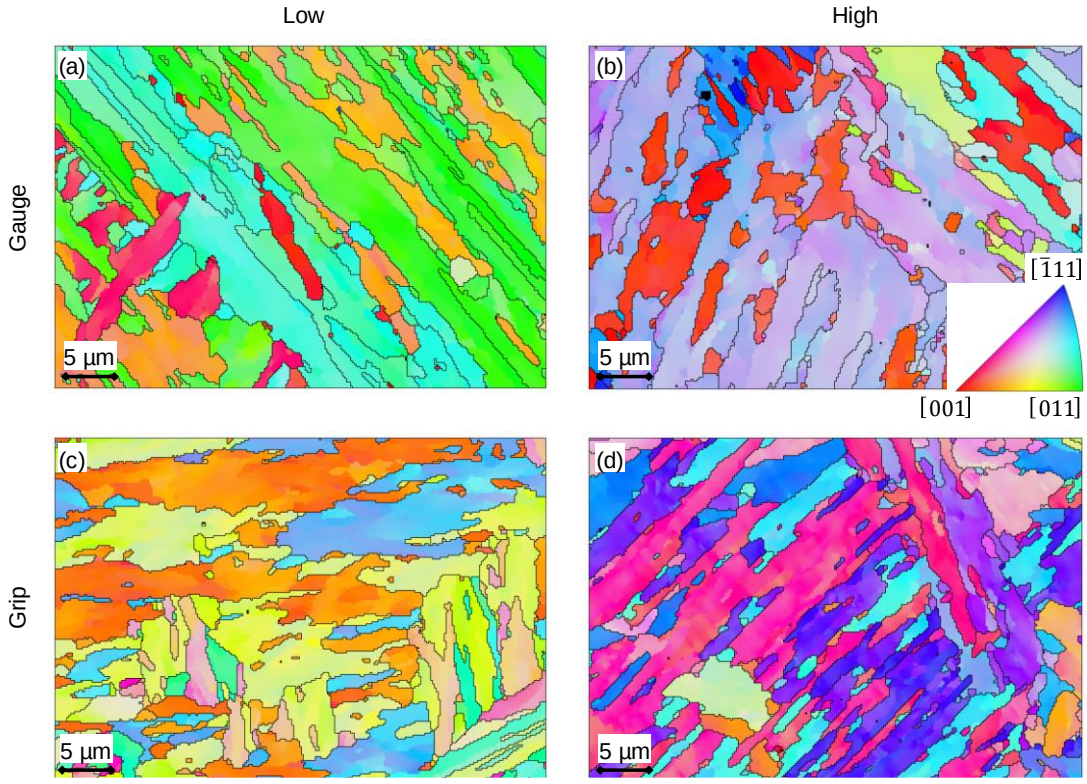

Figure 5.12: IPF maps for the (a,b) gauge and (c,d) grip regions of the low and high damage X20, respectively. Boundary misorientations of greater than 5° are outlined

Substructure details are more clearly seen in the ADF-STEM images of the grip and gauge regions of low and high damage material in Figure 5.14. Qualitatively, less dislocations are evident in the gauge regions (Figure 5.14a and b). This could be due to the grain orientation dependence of the visibility of dislocations at specimen positions that do not satisfy the two-beam condition as well as due to the heterogeneity of grain features (Marx, 2019). The short duration of the creep tests would also not result in a notable decrease in dislocation density, as shown in studies by Pešička *et al*. (2010). Evidence of some substructure recovery within the

gauge regions is noted from dislocation pile-ups on subgrain boundaries (indicated with arrows in Figure 5.14a and b) that would encourage subgrain growth (Pešička *et al.*, 2010; Benaarbia *et al.*, 2018). Less pile-ups are noted in the ex-service grip regions as dislocations would have been swept away from diffusion processes during service aging. Minor qualitative differences are seen between the low and high damage materials, with the latter displaying a higher number of grains with low dislocation densities.

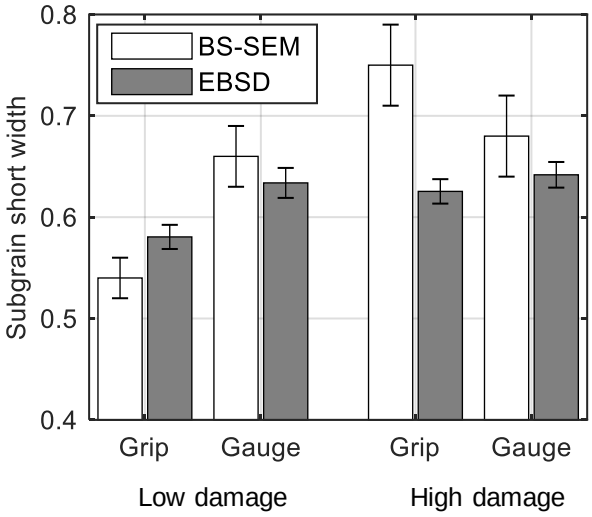

Figure 5.13: Comparison between subgrain size of the low and high damage material measured from BS-SEM and EBSD images of the gauge and grip regions. 95 % confidence intervals are shown in the error bars

5.4 Discussion

The presented DIC technique allows multiple accelerated creep curves to be measured from a single specimen subjected to several temperatures. As the Gleeble-DIC setup is better suited to short testing times, the technique is ideal for accelerated creep testing lasting less than 10 h and for strains less than 35 %.

Accelerated creep tests conducted in this work are at relatively high stresses (159 – 257 MPa at 550 – 600 °C) compared to traditional, long-term creep tests for X20 (such as the 140 000 h creep test conducted at 120 MPa and 550 °C in (Aghajani *et al.*, 2009)). With reference to deformation mechanism maps for typical ferritic-martensitic steels used in the power industry, the current testing conditions fall within the dislocation creep regime (Ghoniem *et al.*, 2013). This is suggested by Figure 5.14 for instance, where dislocation movement is evident from dislocation-denuded subgrains, dislocation pile-ups and subgrain growth in the gauge regions. Even within the short time frame of testing, the high and low damage material still display characteristic features of typical creep curves for ferritic-martensitic steels (including a transient stage, a minimum creep rate and a tertiary stage if tested until rupture) (Abe, 2015).

Subgrain and precipitate differences between the grip and gauge regions resulting from the testing may be small in view of the large scatter associated with microstructural measurements. In order to isolate test-driven microstructural differences from nonuniform microstructural features between the grip and gauge regions of the low and high damage X20, an unpaired *t*-

test assuming unequal variances was conducted using a 0.05 threshold probability on the precipitate data in Table 5.5 and subgrain data in Figure 5.13. The *t*-test parameters are summarised in Table 5.6 and show that no precipitate growth (observed from precipitate sizes) and no precipitation of new phases or agglomeration of existing phases (observed from the number densities) occurs following testing. This is reasonable considering the short testing times and slow evolution rates associated with precipitates (Aghajani *et al.*, 2009). Subgrain sizes, however, were found to be statistically different following testing, indicating growth driven by dislocation creep mechanisms.

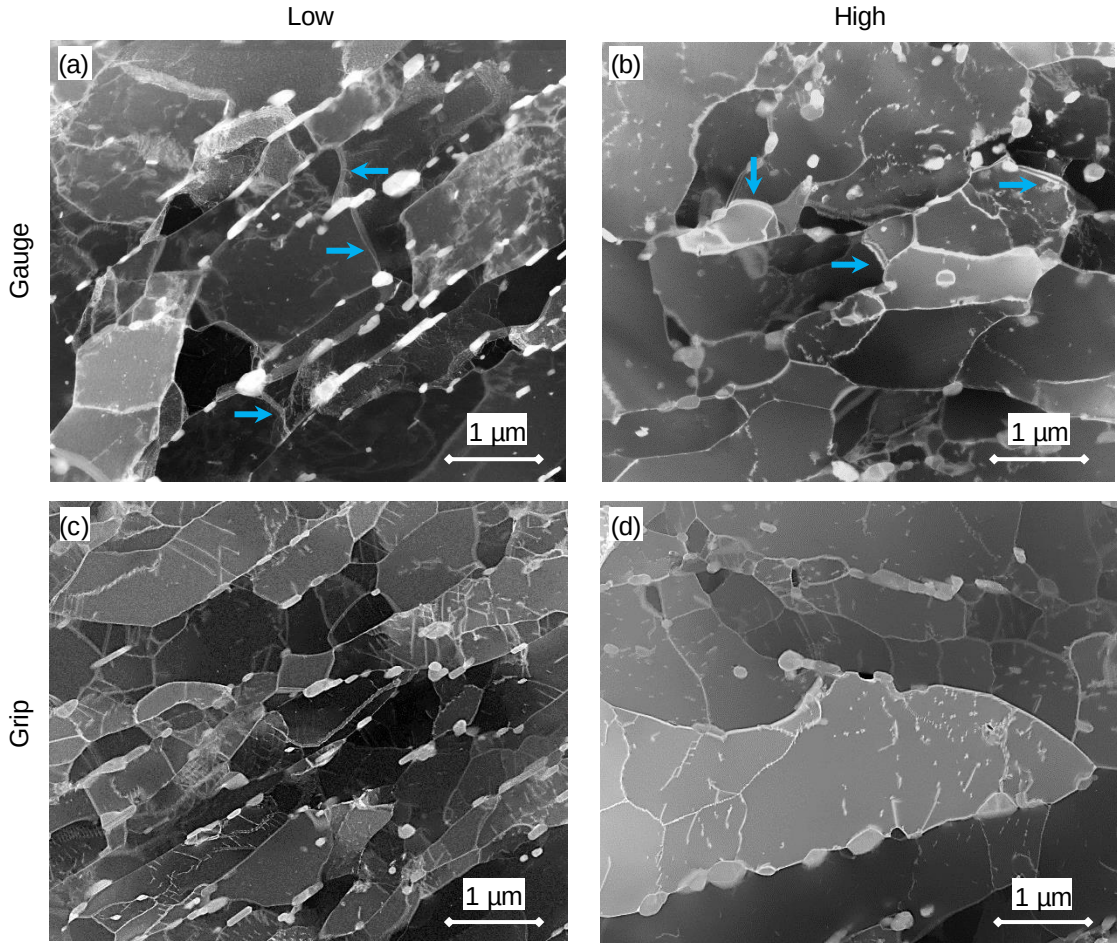

Figure 5.14: ADF-STEM for the (a,b) gauge and (c,d) grip regions of the low and high damage X20, respectively. Arrows in (a) and (b) show dislocation pile-ups at subgrain boundaries

It should be noted however, that these tests are not intended for remnant life extrapolation calculations due the large errors in predictions resulting from mechanism changes at lower stresses. Instead, differences in the creep deformation curves and creep rates can be used as distinguishing factors between ex-service materials and can complement existing methods for damage characterisation. The embrittlement of the high damage material, for instance, is evident from the short rupture times and fast creep rates. These differences are largely tied to the differences in void densities between the two materials, although some evidence of precipitate and subgrain coarsening was also evident from BS-SEM images and EBSD maps (Table 5.5 and Figure 5.13) for the high damage material when compared with the low damage

counterpart. Despite the short nature of the DIC-based tests (Figure 5.6), the comparative deformation behaviour between low and high damage X20 agrees with medium-term tests (Figure 5.9). Based on these grounds, the technique developed in this work is a suitable tool for damage assessment. In the authors' previous work (van Rooyen *et al.*, 2019a), the DIC technique was shown to isolate differences in ex-service materials that were otherwise not obvious from void density characterisation. This highlights the potential benefit to plant operators who wish to make faster repair or replacement decisions during plant shutdowns by making use of the higher density of data that can be measured from a single specimen within a shorter time frame using DIC.

Table 5.6: Parameters used in the statistical assessment of relevant microstructural differences between the grip and gauge regions of ex-service X20 using an unpaired *t*-test with a threshold probability of 0.05

Microstructural feature	Degrees of freedom	*t* statistic	*p* value	Difference statistically relevant ($p < 0.05$)?
Low damage				
$M_{23}C_6$ size	5.93	2.23	0.0762	No
$M_{23}C_6$ density	3.91	0.451	0.683	No
Laves phase size	-	-	-	-
Laves phase density	3.00	2.67	0.0759	No
Subgrain size (BS-SEM)	5.23	6.66	0.00116	Yes
Subgrain size (EBSD)	8630	199	~ 0	Yes
High damage				
$M_{23}C_6$ size	3.09	1.74	0.181	No
$M_{23}C_6$ density	4.12	1.83	0.141	No
Laves phase size	5.32	1.75	0.140	No
Laves phase density	5.72	1.25	0.267	No
Subgrain size (BS-SEM)	6	2.47	0.0481	Yes
Subgrain size (EBSD)	12 000	72.9	~ 0	Yes

Future work involves applying continuum damage mechanics models to DIC-based accelerated tests as well as medium-term tests to extract microstructurally related damage parameters (Oruganti *et al.*, 2011; Sakanashi *et al.*, 2017). Such parameters can be used as a comparative baseline for damage characterisation of ex-service steels.

5.5 Conclusions

The aforesaid study has led to the following conclusions:

- The developed Gleeble-DIC technique can extract multiple accelerated creep curves at several temperatures from a single specimen of X20 steel.
- Thinner specimens result in a uniform stress distribution and a higher range of temperatures (550 – 600 °C) within a ROI. Only the strains measured from the position of the highest temperature (600 °C) of the thicker specimens can be used due to stress variations over the specimen gauge region.
- The DIC results compare well with those obtained using LVDTs in traditional creep setups, although speckle pattern paint flaking places an upper limit on the measurable strain.
- No effect of the accelerated testing was noted in the precipitate distributions when comparing the grip and gauge regions.
- Subgrain size measurements based on BS-SEM and EBSD shows grain growth after testing. Some dynamic recyrstallisation near the ruptured end of the high damage material was noted.
- The Gleeble-DIC technique can be used in the comparative damage assessment of service-exposed X20 and is a suitable complement to standard damage characterisation techniques.
- When applied to ex-service X20 with different operating conditions, the technique can identify the steels with higher damage levels (with higher cavity densities) based on the accelerated creep strain and creep rate curves.

5.6 Post-submission discussion

Following the development of the above-mentioned techniques, a few points of improvement and insights were identified from reviewers' responses. As "damage assessment" is referred to frequently in this work, it is considered important to distinguish what it means within the context of this chapter. Revisiting Section 1.2, damage in this work refers to weakening of the material as a result of creep exposure, including microstructural deterioration, mechanical property (creep resistance and hardness) degradation and intergranular decohesion resulting from cavity development. Traditional definitions are more commonly associated with the latter concept and relates to the original classification system employed by the power plant supplier based on cavity density measurement from metallographic replicas. In a mechanical sense, "damage assessment" is adopted to refer specifically to differences in creep strain and rate curves observed between the material states as shown for example in Figure 5.6 and Figure 5.7.

Full-field analysis is therefore aimed at the measurement of creep strain and rates as relative mechanical damage indicators. These are seen as indirect measures of the effect of higher physical damage (higher cavity densities) in the damaged material. This differs from full-field studies on the effects of physical damage on strain accumulation as done by Hild *et al.* (2015), for instance. Detection of pipe subsurface defects (size > 10 mm) using DIC-measured strain fields by Morris *et al.* (2007) is not applied in this work as the micron-sized cavities are not resolvable by the spatial resolution of the current setup[17].

[17] The reader is referred to Molteno (2017) for studies related to DIC measurements of flaw and crack development.

Comparison of creep curves and rates between material states is a qualitative process and the need for quantitative measures is necessary especially when similar damage states are considered (viz. low and medium damage states). Chapter 6 attends to this insight through the inclusion of the creep data of a non-extreme damage state (medium damage) and quantitative mechanical damage analysis through the calculation of model-based threshold stresses, stress exponents, activation energies and Zener-Hollomon parameters. These parameters are calculated from minimum creep rates in the secondary creep regime, relegating the priority of speckle pattern longevity issues within the tertiary region (demonstrated in Figure 5.8).

Similarly, differences in microstructural features between ex-service materials also inspire a quantitative comparison in Chapter 6, although this chapter primarily focuses on the microstructural differentiation between gauge and grip regions to identify the effects of testing. This is useful in Chapter 7 where the selection of damage evolution equations is made based on the observed changes in microstructural features. Microstructural differentiation between ex-service states, on the other hand, is possible from the grip (pre-tested) regions alone as indicated in Chapter 6. Furthermore, metallographic methods should be expanded from the current work to include analysis of MX and Z phase precipitates as previous studies suggest their role in the creep resistance of 12 % Cr steels (Cipolla *et al.*, 2010).

6 Creep damage assessment of ex-service 12 % Cr power plant steel using digital image correlation and quantitative microstructural evaluation

The previous chapter was concerned with applying DIC to accelerated creep testing to extract several creep curves from single samples of virgin and ex-service X20 across a variable temperature profile. This chapter involves the application of this method to the damage characterisation of ex-service X20 with three different levels of operating conditions as characterised for damage previously by the local power utility by means of surface replication ("low", "medium" and "high" damage). This form of damage characterisation is combined with damage indicators related to key microstructural factors revealed through electron microscopy. In this regard, this chapter addresses the third objective as outlined in Section 3.2.

This chapter is published in the *MDPI Materials* journal (van Rooyen *et al.*, 2019a)[18] and has been presented here in its pre-reviewed form. A discussion on post-review considerations is included at the end of the chapter. This work has also been presented at the 56th Congress of the Microscopy Society of Southern Africa (van Rooyen *et al.*, 2019b)[19].

Declaration by the candidate:

With regard to Chapter 6, the nature and scope of the author and co-authors is as follows:

Name	Email	Contribution	Extent (%)
M van Rooyen (candidate)	melzvanrooyen@sun.ac.za	Conceptualisation of paper, experimental design, completion of all mechanical tests including DIC tests and hardness testing, DIC post-processing, processing of electron backscatter and transmission Kikuchi diffraction data, acquisition of backscatter electron images, statistical processing of microstructural data, figure preparation and visualisation, writing and compilation of manuscript	90
TH Becker	tbecker@sun.ac.za	Beyond supervision and reviewing contributions, assisted with development of the piecewise polynomial fitting code for strain calculation	2.5
JE Westraadt	johan.westraadt@mandela.ac.za	Provided access to electron microscopy facilities, draft review and microstructural data curation	2.5
G Marx	Geneveve.Marx@mandela.ac.za	Development of microstructural methodology, sample preparation and imaging (excluding backscatter electron images), processing of concentric backscatter and EFTEM images	5

Signature of candidate: ……..[MvR]……..(see Footnote 12)

[18] DOI link: https://doi.org/10.3390/ma12193106
[19] Link to extended abstract: http://www.microscopy.co.za/nmmu-form/abstracts/abs-van457.pdf

Date: ……..2020/04/30……

Declaration by co-authors:

The undersigned hereby confirm that:

1. The declaration above accurately reflects the nature and extent of the contributions of the candidate and the co-authors to Chapter 6,
2. No other authors contributed to Chapter 6 besides those specified above, and
3. Potential conflicts of interest have been revealed to all interested parties and that the necessary arrangements have been made to use the material in Chapter 6 of this dissertation.

Signature (see Footnote 12)	Institutional affiliation	Date
[TH Becker]	SU	2020/04/30
[JE Westraadt]	NMU	2020/04/30
[G Marx]	NMU	2020/04/30

6.1 Introduction

The reliable operation of thermal power stations is largely tied to the material integrity and life management of critical components. As these components are subjected to high operating temperatures and stresses over extended service times (> 20 years), the material properties are degraded through several processes, including creep. Within the power industry, the tempered martensitic-ferritic 12 % Cr steel known as X20CrMoV12-1 (X20 hereafter) under DIN designation is well-known. Considered a vintage alloy in the 9 – 12 % Cr steel group, X20 has been in service as main steam piping in coal-fired power plants for over 60 years (Bakic *et al.*, 2014). However, there is continued interest in this steel as it is currently in use in about half of the power stations in SA and, in some cases, has outperformed its replacement P91 (X10CrMoVNb9-1) in terms of damage accumulation (Auerkari *et al.*, 2013).

Several methodologies are available to characterise creep damage (Bhadeshia *et al.*, 1998; Sposito *et al.*, 2010). These methods commonly focus on two closely related aspects, namely, (i) the creep deformation or strength behaviour (revealed through mechanical testing) and (ii) microstructural and damage evolution (revealed through metallographic methods).

There have been various approaches to characterising the extent of material degradation in X20 and other 9 – 12 % Cr steels through mechanical testing. Masuyama (2009) proposed a creep life fraction model based on the reduction of hardness displayed by interrupted creep samples of 9 % Cr steel. Such hardness drop is in turn linked to microstructural components such as the reduction in dislocation density resulting from stress-driven subgrain growth, an increase in creep cavity density (Panait, Bendick, *et al.*, 2010) and coarsening of carbides (Hu *et al.*, 2015). Although this method allows practical degradation assessment during service of power plant steels, hardness measurements are sensitive to material processing parameters and heterogeneous microstructural features (Straub *et al.*, 1997; Masuyama, 2009).

High temperature tensile tests have revealed a decreased strength and ductility of exposed X20, although the property differences can be concealed by different initial heat treatments (Straub *et al.*, 1997; Hu & Yang, 2004). El Rayes and El-Danaf (2017) found that constant-strain rate tensile tests at elevated temperatures revealed minor differences between the

deformation mechanisms of retired and as-produced 12 % Cr steel through the calculation of stress exponents and activation energies after correcting for the influence of threshold stresses. These stresses arise from the attractive force between MX carbonitride particles and detaching dislocations and are themselves dependent on material degradation through the coarsening of precipitates (Shrestha *et al.*, 2012; Zhao *et al.*, 2018). Typically, however, the creep rate-controlling mechanisms of 9 – 12 % Cr steels are often investigated by means of conventional creep testing rigs which involve long testing times (> 10 000 h) due to the slow creep rates associated with diffusional creep mechanisms experienced at service conditions.

Traditional tests use single samples at a single uniform temperature and can be costly due to the heating requirements of traditional furnaces as well as continuous monitoring required for strain measurement. Furthermore, an average strain measurement is obtained using conventional equipment such as strain gauges and LVDTs. As a result, only one specimen can be used to simulate one stress and one temperature condition at a time.

With the increasing popularity of digital image correlation (DIC) as a strain measurement tool for material testing, deformation data can be collected in a full-field manner (Sutton *et al.*, 1983). This noncontact technique correlates the deformation of a speckle pattern on a loaded material surface using digital image recording, resulting in a deformation map from which a strain map can be derived. Spatial resolution for DIC-measured displacements is determined by the size of interrogation windows (or subsets) that make up the region of interest (ROI) and are usually on the order of 10 – 100 pixels (Wittevrongel *et al.*, 2015). Sakanashi *et al.* (2017) extended the use of DIC to measure creep deformation spatially across a stainless steel weldment. In the authors' previous work, DIC was successfully used to measure tensile properties of X20 at several elevated temperatures from a single specimen subjected to a thermal gradient using resistive heating in a thermomechanical simulator (van Rooyen & Becker, 2018).

It is clear that the mechanical properties of ex-service 9 – 12 % Cr steels are closely related to their microstructural stability during long-term creep exposure. The most commonly practiced damage surveying method is replica metallography that monitors creep cavity density which can be directly linked to remnant material life (Ankit, 2009). However, this technique suffers from several limitations (Sposito *et al.*, 2010): it is restricted to the surface of the pipe only; void formation from the replica preparation results in spurious measurements; an incorrect judgment of damage can result from an apparent reduction in void density due to coalescence nearing the end of component life; and other forms of microstructural degradation can mask the effects of cavity growth (Panait, Bendick, *et al.*, 2010). In some cases (Auerkari *et al.*, 2013), X20 piping has not manifested damage in terms of creep cavitation up to 200 000 h of service exposure, requiring an alternative means of microstructural damage assessment.

Microstructural investigations are therefore necessary, and focus is usually placed on three main microstructural barriers to creep deformation, namely, micrograins (including subgrains), second-phase precipitates and dislocation networks. Long-term (> 130 000 h) creep tests on X20 have revealed a coarsening of $M_{23}C_6$ carbides, precipitation of Mo-rich Laves phase, a reduction in dislocation densities and concomitant coarsening of subgrains using scanning electron microscopy (SEM), transmission SEM (TEM) and electron backscatter diffraction (EBSD) (Pešička *et al.*, 2003; Aghajani *et al.*, 2009). There have been few attempts, however, to compare the changes of the microstructural details in ex-service material in a quantitative manner. Hu *et al.* (2015) proposed the change in the Cr:Fe ratio in carbides with operating time to be an index of life depletion for X20 superheater tubes. Straub *et al.* (1997) found little difference between the dislocation density, subgrain size and cavity density of creep-exposed

tube compared to an initial melt, although a coarsening of precipitates was identified, quantitatively demonstrated later by Hu *et al.*(2004) using TEM on extraction replicas. Other investigations (Hu *et al.*, 2008) of ex-service X20 displayed a lack of creep cavitation but a reduction in subgrain-interior dislocation densities. This suggests that certain microstructural features are more suitable indicators of creep damage than others. Indeed, some microstructural or creep cavity distribution factors are more sensitive indicators of damage as the rate of damage development varies depending on the extent of life exhaustion (Dobrzański, 2005).

Due to the complexity of creep in 12 % Cr steels, it is not clear what microstructural-based technique is best suited to the damage assessment of ex-service material. By using accelerated creep tests (< 10 h testing time) and exploring the exposure-driven microstructural features that explain the resulting deformation behaviour in a comparative manner between X20 with varying levels of pre-existing damage, a consensus can be reached on the most prominent damage indicators. This work in no way attempts to use accelerated testing (at higher stresses) to extrapolate to the service conditions of the piping material (at lower stresses) due to the difficulty in accounting for the stress-state sensitivities of damage micromechanisms (Bolton *et al.*, 1980). Instead, the deformation behaviour at accelerated conditions is used as a means of assessing the loss of creep resistance between the material states. By using the developed DIC technique (van Rooyen *et al.*, 2020), material requirements are reduced as multiple deformation curves at several temperatures can be conveniently measured from a single specimen. The present work therefore aims to assess the creep damage of various ex-service X20 piping material in a comparative manner using a combination of post-exposure mechanical deformation tests and microstructural evaluation.

A Gleeble thermomechanical simulator allows the generation of a near-parabolic shaped temperature profile longitudinally across the specimen through resistive heating. Multiple accelerated creep curves are in this way generated from a single specimen and are captured by DIC. Following testing, previously explored (Marx, 2016; van Rooyen *et al.*, 2020) electron microscopy techniques were employed to holistically classify the damage levels of the tested samples across various microstructural indicators, including: boundary character from EBSD; substructure (dislocations and micrograins) and large precipitate details using concentric backscatter (CBS) SEM, dislocation density details from an annular dark field scanning TEM (ADF-STEM); and smaller precipitate morphology identified by energy-filtered TEM (EFTEM).

In what follows, a brief description of the materials, selection of specimen geometry and experimental procedure for the DIC testing and microstructural study is supplied. This is followed by a presentation of the accelerated creep behaviour, hardness measurements and comparison of microstructural elements. Finally, a discussion is provided linking the two types of damage assessment, offering a conclusion on the plausibility of the DIC technique and suggested microstructural features as damage indicators.

6.2 Experimental details

6.2.1 Materials

The chemical composition of the virgin X20 as measured by inductively coupled plasma, optical emission spectroscopy and combustion analysis is given in Table 6.1.

Table 6.1: Alloying elements of X20 used in this study in wt% (balance iron)

C	Si	Mn	P	S	Cr	Mo	Ni	V
0.21	0.19	0.58	0.015	0.004	11.6	0.88	0.76	0.25

Operating conditions of the ex-service material are given in Table 6.2. EXL, EXM and EXH stand for "low", "medium" and "high" damaged ex-service X20 material, respectively, as categorised by replica-based cavity density measurements. In the interest of brevity, these abbreviations will be used in the remainder of this chapter.

Table 6.2: Details of investigated service-exposed X20

Ex-service material designation	Reported operating temperature (°C)	Reported operating pressure (MPa)	Service time (h)	Cavity density from replicas (mm^{-2})
EXL	545	17.0	130 000	60 – 90
EXM	545	19.4	130 000	~ 200
EXH	543	18.1	156 000	220 – 690

6.2.2 Specimen geometry

Test specimens were machined from virgin and ex-service X20 main steam piping sections provided by a local power utility with internal diameters of 255 ± 5 mm and wall thicknesses of 35 ± 1 mm. All specimens were oriented axially with respect to the pipe orientation as shown in Figure 6.1a and are located close to the pipe outer diameter. Previous investigations (van Rooyen & Becker, 2018; van Rooyen *et al.*, 2020) have shown that the Gleeble specimen geometry has a direct influence on the resulting temperature distribution and consequently the stress distribution. In this work, the selected specimen geometry has a 2 × 10 mm^2 (shown in Figure 1b) cross-sectional area that differs from the traditional 10 × 10 mm^2 Gleeble specimen, respectively called flat and square specimens. Results from square specimens were included for comparative purposes[20]. Note the coordinate system in Figure 6.1b where x is the longitudinal loading direction and y is the transverse direction. For both geometries, the x-direction temperature profiles can be represented by a second-order polynomial (Walsh *et al.*, 1986).

For the microstructural analysis, 3 mm diameter discs were wire cut from specimens at three locations: from the grips; near the gauge centre (corresponding to the maximum temperature of 600 °C) and at an offset of about 5 mm from the centre (subjected to about 550 °C) as indicated in Figure 6.1b.

6.2.3 Accelerated creep test setup

The specimens were tested in the vacuum chamber of a Gleeble 3800 thermomechanical loading system using a technique (van Rooyen & Becker, 2015, 2018) previously presented by

[20] See Section 6.5 for a discussion on data from square cross section specimens

the authors. Resistive heating through feedback control from a K-type thermocouple spot-welded to the specimen centre (see Figure 6.1b) resulted in a temperature profile that decreases quadratically from a maximum in the specimen centre towards the water-cooled grips along the specimen axis. The full-field temperature map was measured by a Fluke Ti400 infrared (IR) camera on the rear specimen surface which was coated with a highly emissive and heat-resistant black paint. The quadratic temperature profile varied from 600 °C in the centre (x = 0) to about 550 °C symmetrically over 5 mm. Due to the inherent Gleeble setup, the grips were subjected to room temperatures and minimal strain and are thereby considered to represent the pre-tested bulk material.

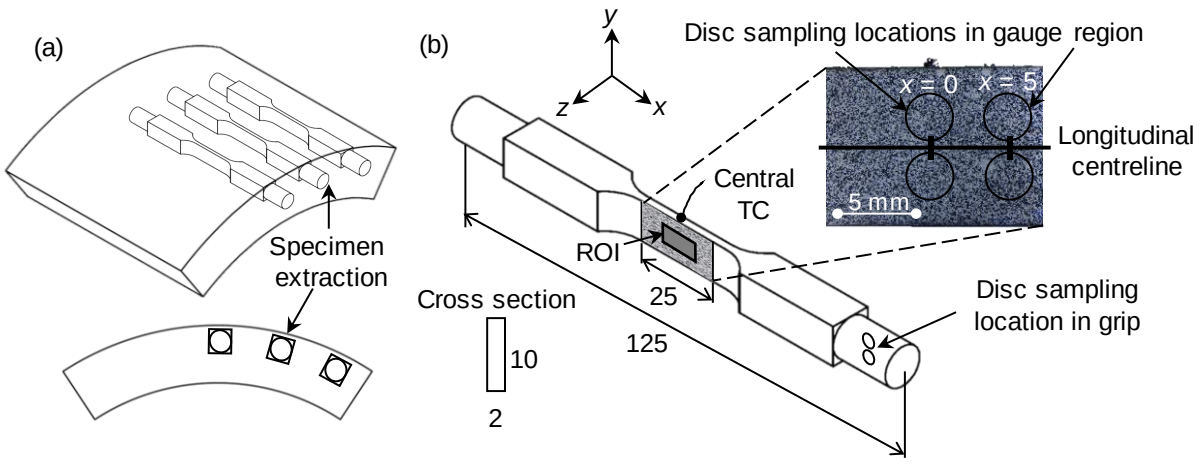

Figure 6.1: Illustration of the (a) sampling scheme in piping material and the (b) selected geometry for accelerated creep tests as well as the location of the disc specimens extracted for microstructural analysis of the gauge and grip regions. All dimensions are in mm. TC = thermocouple. x = 0 indicates the specimen centre

The thermal profile will influence the distribution of stress in the specimen gauge region as a direct result of nonuniform thermal expansion. To investigate this effect, a finite element (FE) elastic-plastic model was created for the gauge region using ABAQUS 2017 FE software with further details presented in van Rooyen *et al.* (2020). Figure 6.2 reveals the distribution of stresses in the loading direction at an applied (engineering) stress of 250 MPa, showing a narrow region centred about the gauge region within which the stress remains near-uniform.

By calculating the longitudinal variation of stress triaxiality (ratio of hydrostatic stress to von Mises stress) (Wen *et al.*, 2016) over this region as summarised in Table 6.3, the stress distribution can be analysed for its alignment with the ideal uniaxial stress condition. A ROI of 10 × 5 (x × y) mm^2 centred on the gauge area was selected for DIC processing as the triaxiality values within this area are near 0.33, which is typical of uniaxial stress states. The actual stress range in the ROI is also reported in Table 6.3. Hereafter, the average actual stress σ_x over the ROI is reported.

Displacement measurement maps were obtained by a two-camera LaVision DIC system consisting of 5 megapixel 12-bit cameras paired with 75 mm macro lenses that resulted in a 60 × 50 mm^2 field of view (FOV) and 40 pixel/mm image scaling. After the temperature field had stabilised, specimens were subjected to a constant load whilst images of a heat-resistant speckle pattern painted over the 25 × 10 mm^2 gauge area (as shown in Figure 6.1b) were

recorded through the vacuum chamber viewing window at a rate of 0.1 Hz. Blue colour filters and high-powered white LEDs were used to suppress surface radiation noise.

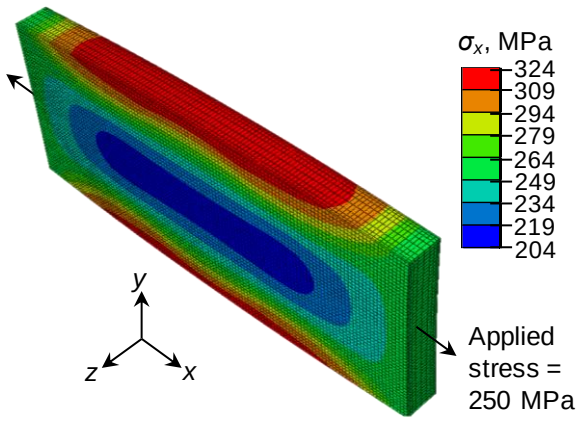

Figure 6.2: Distribution of x-direction stresses (σ_x) from an FE analysis of the flat specimen gauge region at an applied stress of 250 MPa

Table 6.3: Range of actual stress and triaxiality ratios over ROI at three applied stresses

Applied stress (MPa)	Actual stress range σ_x (MPa)	Triaxiality ratio range
200	145-150	0.315-0.350
250	210-212	0.321-0.357
260	224-228	0.321-0.357

Analysis of images captured during testing was performed using the LaVision DaVis 8.4 correlation software over the ROI with a 61 pixel^2 subset size with a 15 pixel overlap that resulted in a software-estimated spatial resolution of 0.4 mm and strain accuracy of 0.05 %. Subsequently, a piecewise quadratic polynomial surface fit was applied to the DIC displacement data using MATLAB 2019a across a window size of 7 data points. Creep strain rate was obtained by applying a moving average filter to the creep strain-time data over a sliding window size of 30 - 40 points. Further details surrounding the DIC technique is provided in van Rooyen *et al.* (2020). Creep strain measured at a position within the ROI of the specimen gauge section is therefore associated with a specific temperature as measured by the IR imager and an average longitudinal stress with near-uniaxial triaxiality ratios as calculated from FE analysis.

Following testing, Vickers hardness measurements were made along the longitudinal direction of the flat specimen gauge regions and on the grips using a 1 kg load and 10 s holding time according to ASTM E834 (ASTM, 2012).

6.2.4 Deformation mechanism regime

Accelerated creep testing in this work was conducted at actual stresses ranging from 145 to 260 MPa and with temperatures ranging from 550 to 600 °C. Given this range of testing stresses and temperatures, it may be worthwhile to elucidate the most likely dominant mechanism using

deformation mechanism maps. As literature pertaining to map construction for virgin X20 is scarce and almost nonexistent for service-exposed materials, approximate maps were used here based on deformation modes encountered by a similar ferritic-martensitic steel namely F82H (Ghoniem *et al.*, 2013) for the range of normalised temperatures and stresses used in the current work. Based on these mechanism maps, it is expected that accelerated creep tests will be within the low-temperature dislocation climb regime with creep rates varying from 10^{-5}/s to 10^{-3}/s.

6.2.5 Microstructural examination

Bulk specimen discs were sectioned from the tested samples (at locations indicated in Figure 6.1b) and polished to a 0.25 µm colloidal silica finish. Backscatter electron SEM (BS-SEM) was employed to measure initial cavity densities of the untested pipe sections using ImageJ (Johannes *et al.*, 2012) image processing software whilst subgrain details of the gauge samples were qualitatively analysed. In order to isolate the largest differences in damage features, the EXL and EXH material was selected for more qualitative TEM, STEM and transmission Kikuchi diffraction (TKD) study. Subsequently, thin foils were prepared from the discs using a Struers TenuPol-5 twin-jet electropolisher (5 % $HClO_4$ solution; 21 – 30 V; -20 °C).

Subgrains, $M_{23}C_6$ carbides and Laves phase precipitates were investigated using a CBS detector fitted to a FEI Helios NanoLab DualBeam 650 focused ion beam (FIB)-SEM operated at a 5 kV accelerating voltage, 0.20 nA probe current and 4 mm working distance (WD). Identification of MX precipitates was facilitated using Cr and V elemental maps acquired with the three-window method using EFTEM with a GATAN Quantum GIF fitted to a JEOL JEM 2100 LaB_6 TEM (200 kV and 10 mRad collection angle). Subgrain size analysis was realised with MIPAR (Sosa *et al.*, 2014) image analysis software by measuring the short widths of the grains from the minor axes of fitted ellipses. Precipitates were identified based on the brightness variations in the CBS-SEM images which are directly linked to the atomic number of constituent elements. Due to sectioning of the $M_{23}C_6$ carbides and Laves-phase precipitates in the thin foil specimens, stereological corrections were applied to correct for smaller measured diameters (Gokhale, 2004; Holzer, 2010). Qualitative details regarding the distribution of dislocations in the X20 substructure was revealed through ADF-STEM on the same TEM used for the EFTEM analysis with inner and outer detector angles of 18 ± 5 mrad and 47 ± 5 mrad, respectively.

As it is challenging to distinguish between different grain boundaries using imaging techniques alone, the boundary character of subgrains is also studied through EBSD using a Nordlys HKL system of a JEOL JSM 7001F field emission gun (FEG) SEM using settings of 15 keV, 4 nA, 22 mm WD and 0.2 µm step size. This step size enables the identification of individual subgrains (with short widths varying from 0.7 – 1.2 µm (Aghajani *et al.*, 2009)) in a statistically significant manner. In accordance with the definition provided by Peŝiĉka *et al.* (2004), the term "micrograins" is used hereafter and refers to the finest features of tempered martensite ferritic steels that consist of subgrains (with misorientations ~ 1°) and small grains with high misorientation angles with adjacent small grains (here restricted to 2 – 5° misorientations). This differentiation is needed due to the angular resolution limitations of orientation mapping which can result in spurious subgrain measurements (Panait, Zielińska-Lipiec, *et al.*, 2010).

Post-processing on the EBSD data was performed using the MTEX 5.2 MATLAB R2019a toolbox (Bachmann *et al.*, 2010). Prior to processing of EBSD data for micrograins size analysis, noise removal was achieved through a half quadratic optimisation filter with a smoothing parameter of 0.2 and edge preservation was assured for boundaries above a 1.3° misorientation to retain relatively low-angle boundaries. Grains were constructed with a 1.5° boundary misorientation and only grains larger than 5 pixels^2 (about 0.64 µm^2) were

considered. No noise removal was performed for misorientation analysis to prevent smoothing over subgrain boundaries.

EBSD furthermore allows the reconstruction of prior austenite grains into packets which are subdivided into blocks consisting of laths each typically formed from two different variants. A MTEX-based prior austenite reconstruction graphical user interface using a Markov clustering algorithm with an inflation power of 1.6 was used to identify block, packet and prior austenite grain boundaries (PAGB) (Nyyssönen *et al.*, 2018).To resolve micrograins more accurately, TKD was combined with energy dispersive X-ray spectroscopy (EDS) using an Oxford X-Max EDS SDD detector. A step size of 0,03 µm allows for improved spatial resolution, together with settings of 30 kV, 4 nA, 10 mm WD and 20° specimen tilt.

6.3 Results

6.3.1 Accelerated creep deformation

Creep strain-time curves at several temperatures at a 250 MPa applied stress for virgin X20 are shown in Figure 6.3a. Good repeatability in measurements is indicated by minor differences between the two specimens which is better demonstrated by the variation of the logarithm of creep rate with time plotted in Figure 6.3b. At higher temperatures (> 580 °C), the curves consist of a primary creep stage with a decreasing creep rate followed by a secondary stage with a minimum creep rate turning point leading into accelerating rates caused by specimen necking in the tertiary stage. As the temperature decreases, the creep strains and rates decrease. For this reason, curves at temperatures below 580 °C remain within the primary stage for the virgin material.

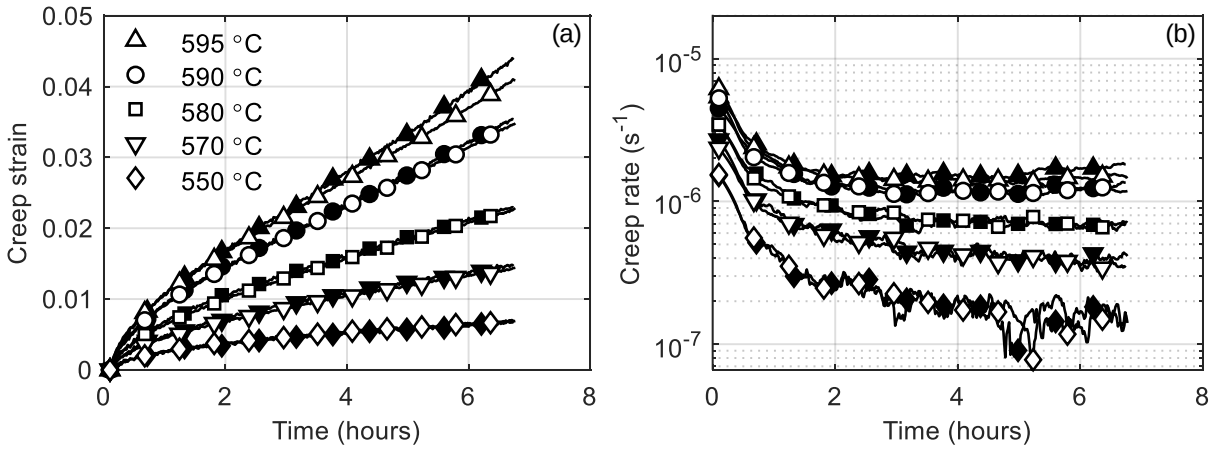

Figure 6.3: Evolution of accelerated (a) creep strain and (b) creep rate over time for two different virgin X20 specimens at several temperatures (clear and shaded symbols)

A comparison between the creep behaviour of various degrees of service-exposed and virgin material at different temperatures is shown in Figure 6.4. Generally, higher strain rates are observed for the service-exposed material resulting in more pronounced creep curve stages. This implies that the secondary creep stage is reached sooner with the same testing conditions as for virgin material. At 600 °C, the highly aged material displays a tertiary-dominated creep curve and ruptures within 1 h of testing. At temperatures below 575 °C, creep strains remain

within the primary stage for all material states as evident from the lack of a turning point in Figure 6.4c for 550 °C. Highlighted are the accelerated creep rates when comparing EXL and EXM, which is discussed later. Variations in creep strain and creep rate with stress of the virgin (a) and service-exposed material (b-d) are shown in Figure 6.5. For comparison, standard square Gleeble specimen data is included as solid symbols. Creep rates increase with stress, with EXL and EXH displaying increasingly higher strains and rates when compared to virgin material.

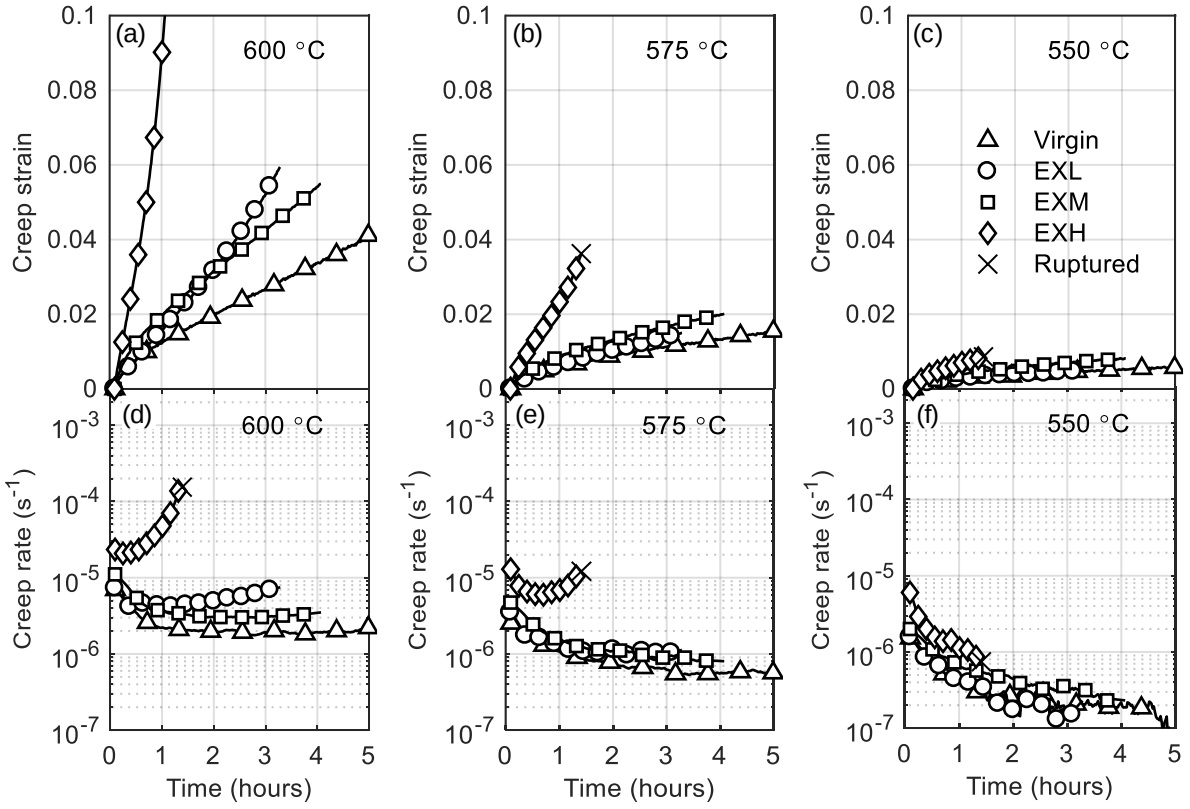

Figure 6.4: Comparison between the creep strains ((a)-(c)) and creep rates ((d)-(f)) of virgin and service-exposed material at 600 °C, 575 °C and 550 °C for an applied stress of 250 MPa for column 1,2 and 3 respectively. Legend is given in (c)

6.3.2 Longitudinal hardness profiles

Figure 6.6 shows that service-exposed material and virgin material demonstrate a decrease in hardness towards centre of the specimens near the maximum temperature of 600 °C. Compared to the grip hardness, the drop in gauge hardness is attributed to the material age (Masuyama, 2009). Similarly, a difference between EXL and EXM hardness readings is highlighted.

6.3.3 Microstructural characterisation

The microstructural characterisation is predominantly based on the EXL and EXH states that theoretically should identify the largest difference in microstructural features. Some reference is made to EXM, as previously highlighted. Its relevance is discussed later.

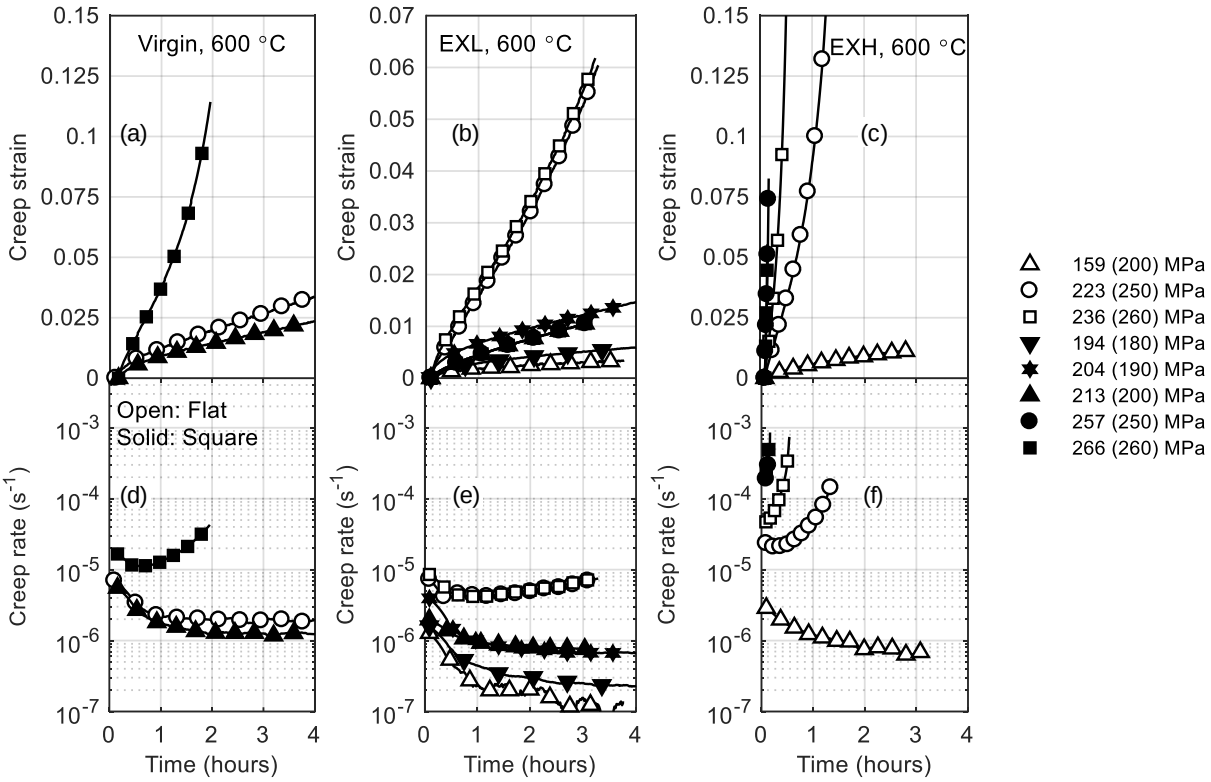

Figure 6.5: Creep strain and creep rate curves for virgin ((a) and (d)), EXL ((b) and (e)) and EXH ((c) and (f)) material at 600 °C and various stresses. Open and solid symbols refer to the flat (2 × 10 mm^2) and standard square (10 × 10 mm^2) geometries respectively. True stresses are reported (with applied stress in brackets) in the legend

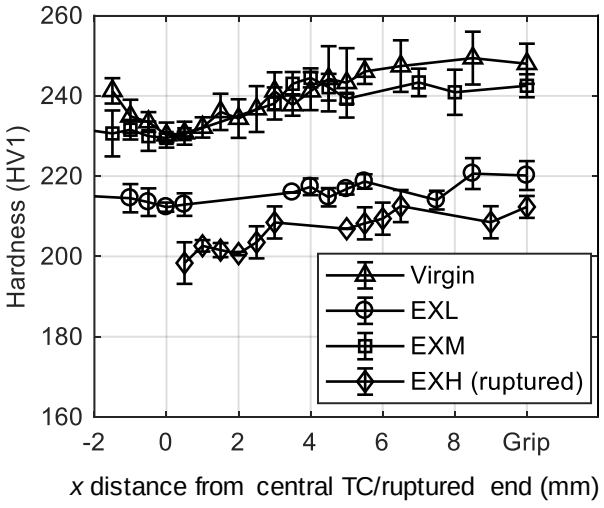

Figure 6.6: Variation of hardness with distance from the central thermocouple for the virgin, EXL and EXM material and with distance from the ruptured end of the EXH material

6.3.3.1 Comparison of cavity distributions

BS-SEM images at 400× magnification taken on ex-service material pipe offcuts were subjected to a threshold adjustment in ImageJ after which cavities with an equivalent circle diameter ($ECD = \sqrt{4 * A_c/\pi}$) larger than 0.1 µm but less than 5 µm were counted. This allows a direct comparison with surface replication results acquired using optical microscopy with limited spatial resolution whilst excluding large pores from which inclusions have been removed during specimen preparation (Eggeler *et al.*, 1989; Straub *et al.*, 1997; van Zyl *et al.*, 2005). Qualitative differences in cavity distributions (shown as black speckles), large precipitates (white speckles) and micrograins can be identified in 2000× magnification SEM micrographs in Figure 6.7 together with measured cavity details.

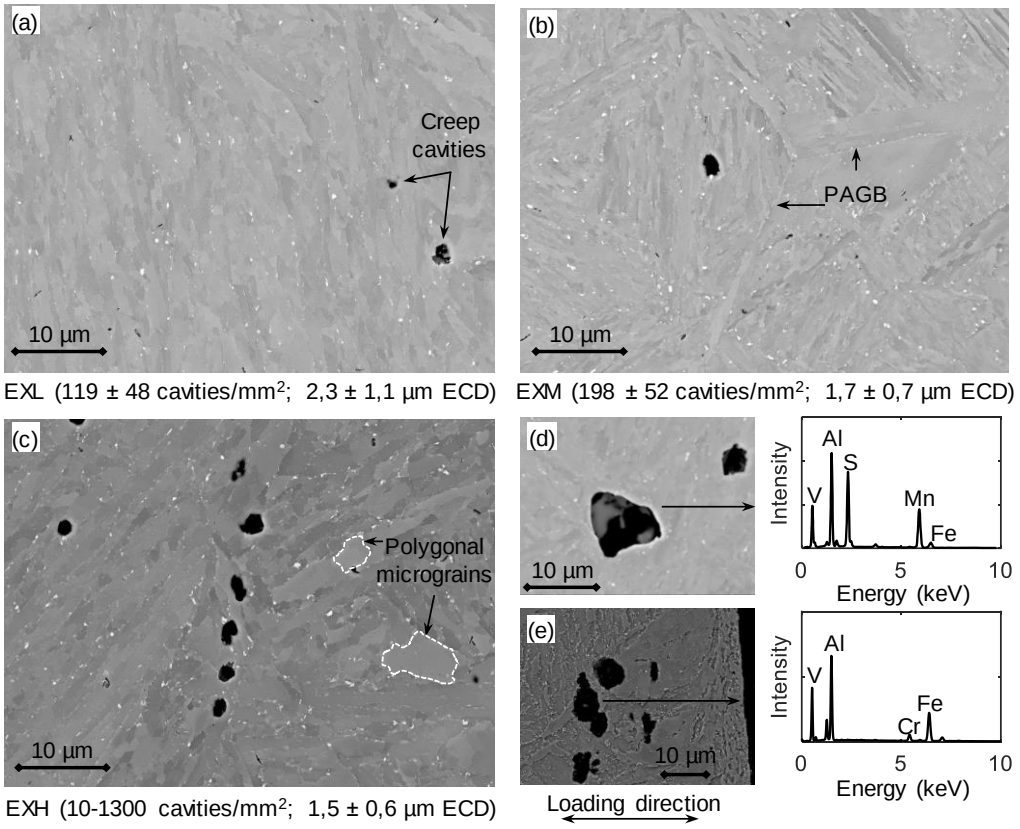

Figure 6.7: BS-SEM images showing micrograins and voids in (a) EXL, (b) EXM and (c) EXH material. Large inclusions in (d) EXL material are shown by EDS to contain Al and Mn and are also located (e) near the ruptured end of the EXH material

Although not shown here, the cavity sizes are lognormally distributed. Interestingly, larger cavity sizes were measured for EXL than EXM and EXH – suggesting delayed cavity growth in the latter material possibly due to production from a different melt having differences in virgin material void sizes and the presence of inclusions as nucleation sites (Straub *et al.*, 1997). Some large voids (> 10 µm) in the EXL material are associated with inclusions as suggested by EDS analysis in Figure 6.7d to be MnS and Al_2O_3 (Straub *et al.*, 1997). Larger void sizes could also partly explain the lower hardness measured for EXL compared to EXM. However, in agreement with replica results, a wide range of cavity densities are recorded in the EXH material. Unlike in work reported by Aghajani *et al.* (2009), the service-exposed material did

not demonstrate significant cavitation on PAGBs in this orientation (one of which is indicated in Figure 6.7b). Instead, large intragranular cavities appear to be more common, mostly nucleating at large inclusion particles and coarse precipitates on micrograin boundaries. An example of a cavity chain is shown for the EXH material in Figure 6.7c, which has the potential, with further creep exposure, to grow and merge to form microcracks as has occurred due to inclusions after accelerated creep testing at 223 MPa in Figure 6.7e (Eggeler *et al.*, 1989).

6.3.3.2 Boundary character from EBSD

Figure 6.8a and c show the inverse pole figure (IPF) maps for the grip regions of EXL and EXH specimens, respectively. No significant differences were observed between the grip and gauge regions. Prior austenite reconstruction of the data allows the determination of packet, block and PAG boundaries as shown in Figure 6.8b and d for EXL and EXH, respectively. Boundaries of micrograins are difficult to distinguish from block boundaries due to the sampling size used for EBSD analysis (0.2 µm step size whilst the aged micrograin widths < 0.8 µm (Sonderegger *et al.*, 2008)). However, as shown in the reconstructed maps, focus is placed on differences between block (red outlines), packets (blue) and continuous PAGB (thick black).

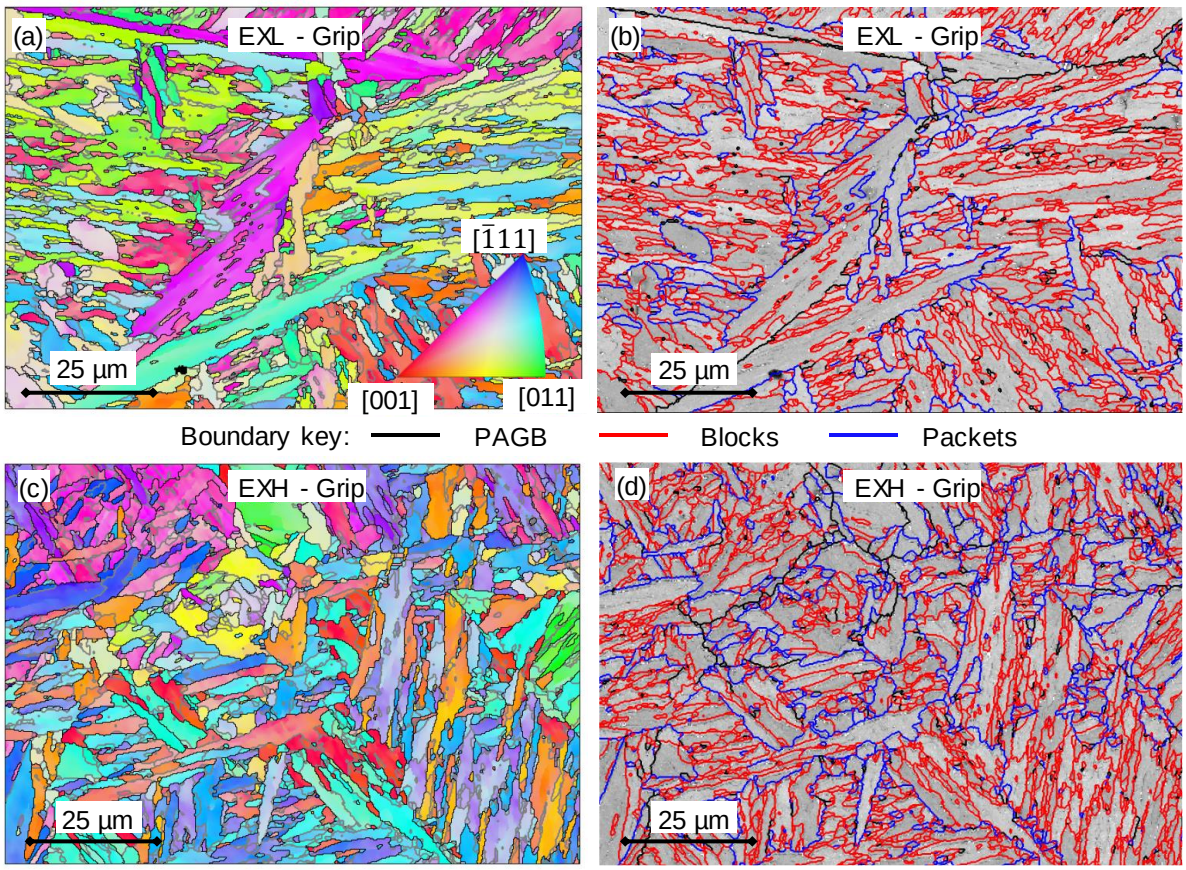

Figure 6.8: IPF maps of the tested (a) EXL and (c) EXH grip regions where the colouring identifies the crystallographic directions parallel to the sample normal (*z* direction) according to the colour key given in (a). Boundaries of > 1.5° misorientations are outlined. These maps are used to reconstruct block (red), packet (blue) and PAGB (thick black) boundaries in (b) and (d) respectively

As suggested by work of Payton *et al.* (2012), the extent of creep exposure can be identified by considering the densities of micrograin, block and packet boundaries (length per unit area), which is summarised in Table 6.4 for the EXL and EXH material.

Table 6.4: Comparison of boundary length per unit area of prior austenite grain constituents between EXL and EXH

Material	Boundary density (μm^{-1})		
	Micrograin	**Block**	**Packet**
EXL	1.39 ± 0.05	1.10 ± 0.01	0.30 ± 0.06
EXH	1.47 ± 0.05	1.13 ± 0.02	0.40 ± 0.01

From this analysis, EXL demonstrates a decrease in micrograin, block and packet boundary density compared to EXH, suggesting higher damage accumulation in the former material through migration of boundaries and grain growth. Micrograin boundary analysis using EBSD however is subject to possible error due to many virtual grains being detected from small misorientations between sub-block boundaries that are within the angular resolution of the EBSD technique (Payton *et al.*, 2012). A strong variant texture was also noted in the sampled PAG (possibly due to the pipe processing of the material (Tak *et al.*, 2009)) where variants 1-6 occurred more frequently than other variants, resulting in the increased detection of block boundaries.

The misorientation of grain boundaries can also be used as an indicator of creep damage between the material states (Aghajani *et al.*, 2009). A comparison of the low-angle (< 5°) misorientation distributions between EXL and EXH grip regions is shown in Figure 6.9. An increase in subgrain (< 1°) boundaries is noted for the EXH grip material over the EXL material. Increased creep exposure has been found by Aghajani *et al.* (2009) to cause the same result however it must be emphasised that any measurement of subgrain boundary misorientation (< 1°) is subject to scrutiny given that the angular resolution of traditional EBSD setups range from 0.5 – 2 ° as indicated in Figure 6.9 (Humphreys, 2004). Nonetheless, the increased frequency in subgrain boundaries supports the higher micrograin boundary density (Table 6.4) noted in the EXH material. No significant differences in misorientation angles are noted above about 1.5° for the EXL and EXH material.

Further investigation was conducted using high resolution TKD orientation maps shown in Figure 6.10 and Figure 6.11 taken from near the centre of the gauge region and location of the maximum temperature of 600 °C (labelled “0 mm” for EXL and “1.5 mm from rupture” for the ruptured EXH specimen), 5 mm offset from the highest temperature location (at approximately 550 °C) and from the grips of the EXL and EXH tested samples, respectively. TKD maps were used to investigate another means of assessing creep damage as proposed by Fujiyama *et al.* (2009) for high Cr steels involving analysis of kernel average misorientation (KAM) which is the average misorientation angle measured over a kernel of pixels surrounding each measurement point.

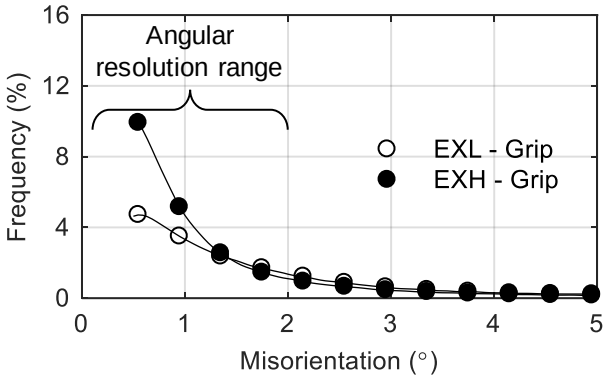

Figure 6.9: Distribution of misorientation angles (< 5°) in EXL and EXH showing a higher frequency of subgrain (< 1°) boundaries in EXH grip material

The value is related to intragranular misorientation gradient and consequently establishes regions of orientation differences associated with a dense collection of dislocations present in subgrain boundaries and is sensitive to EBSD step size. Grain orientation spread (GOS) has also been employed (Fujiyama *et al.*, 2011) as a means of damage assessment that is independent of the step size and is the average misorientation of each point in a grain from the grain average orientation. This indicator has been reported to be more sensitive to strain accumulation within grain interior than KAM methods yet is susceptible to differences in grain sizes. KAM maps using a kernel size of 9×9 pixels^2 (0.24×0.24 µm^2) are shown in Figure 6.10(d,e,f) and Figure 6.11(d,e,f) together with maps of GOS in Figure 6.10(g,h,i) and Figure 6.11(g,h,i) calculated with a 5° boundary threshold at the three locations, respectively. The arrows in the KAM maps (Figure 6.10d and Figure 6.11d) point out examples of boundaries or locations of high densities of dislocations that are not identified as subgrain boundaries (< 1.5°) in the corresponding orientation maps (Figure 6.10a and Figure 6.11a).

Average KAM and area-weighted average GOS values calculated from each location of EXL and EXH specimens are shown in Figure 6.12a and b, respectively. As Fujiyama *et al.* (2009) found that mean KAM values decrease with increased creep exposure and correlates with a decrease in dislocation density and subsequently hardness, it can be concluded from Figure 6.12 that EXH demonstrates higher damage accumulation possibly due to competing processes of migration of micrograin boundaries during grain growth and increase in frequency of subgrain boundaries which is also manifested as a reduction in hardness as shown in Figure 6.6. Interestingly, the highest GOS and KAM values are noted at the 5 mm location for the EXL material. Seeing as the 5 mm sampling location experiences primary creep (see Figure 6.4c), we expect a large reduction in dislocation densities as any remaining free dislocations migrate to subgrain boundaries in this regime (Pešička *et al.*, 2004).

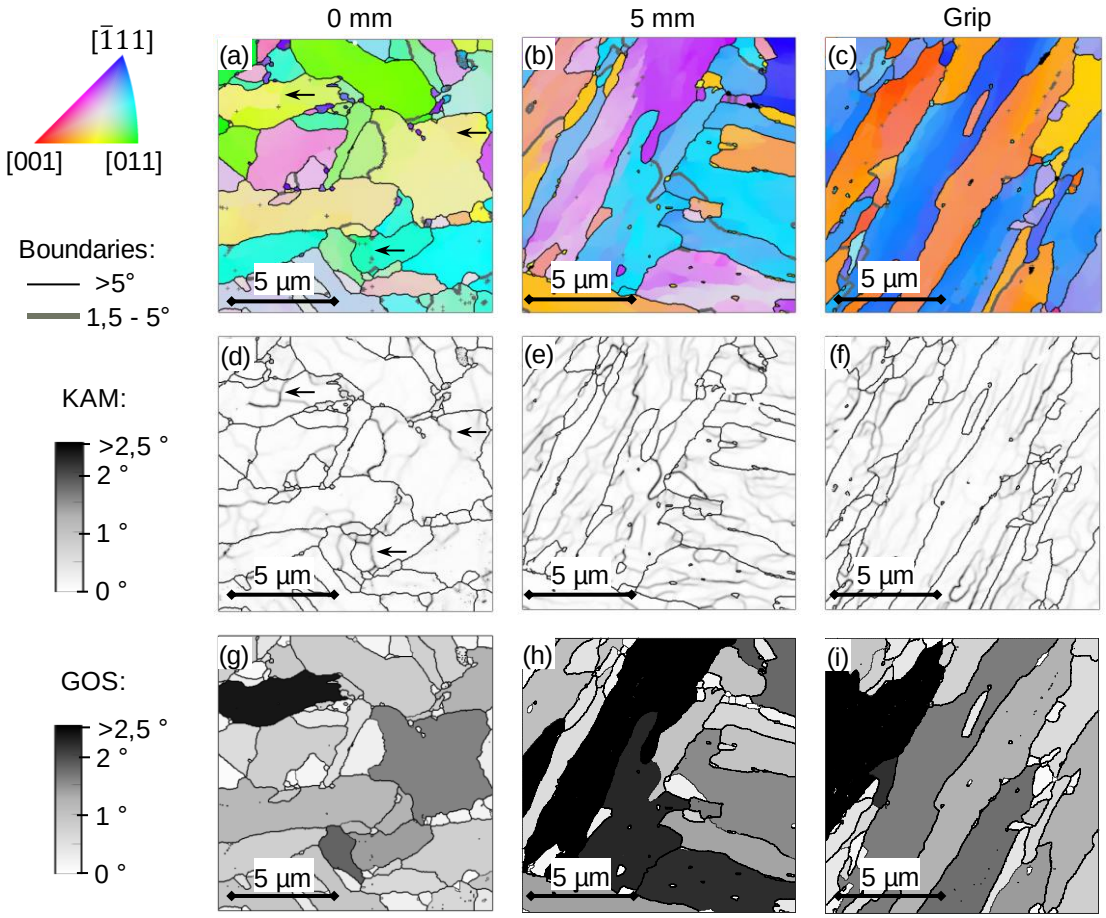

Figure 6.10: (a-c) IPF maps showing crystal orientations relative to the sample normal according to the colour key (top left), (d-f) KAM maps and (g-i) GOS maps of areas at 0 mm and 5 mm from the maximum temperature gauge region and at the grip of the EXL material, respectively

Subgrains are, however, pinned by carbides (which are later shown to be more closely spaced in the EXL material). This causes the internal strain of the grains to increase which is represented by higher KAM and GOS values in the EXL material at this location. A strong inflection point is noted in the creep curve of EXL at the 0 mm location (see 223 MPa curve in Figure 6.5e) similar to that reported for a 15Mo3 material in Szabó (2004). This corresponds with a low GOS value at 0 mm which corresponds to the relief of the internal strain. The EXH material seems to overall have lower KAM and GOS values which suggests that little resistance is offered in terms of pinning of dislocations by carbide distribution that would normally increase the internal strain.

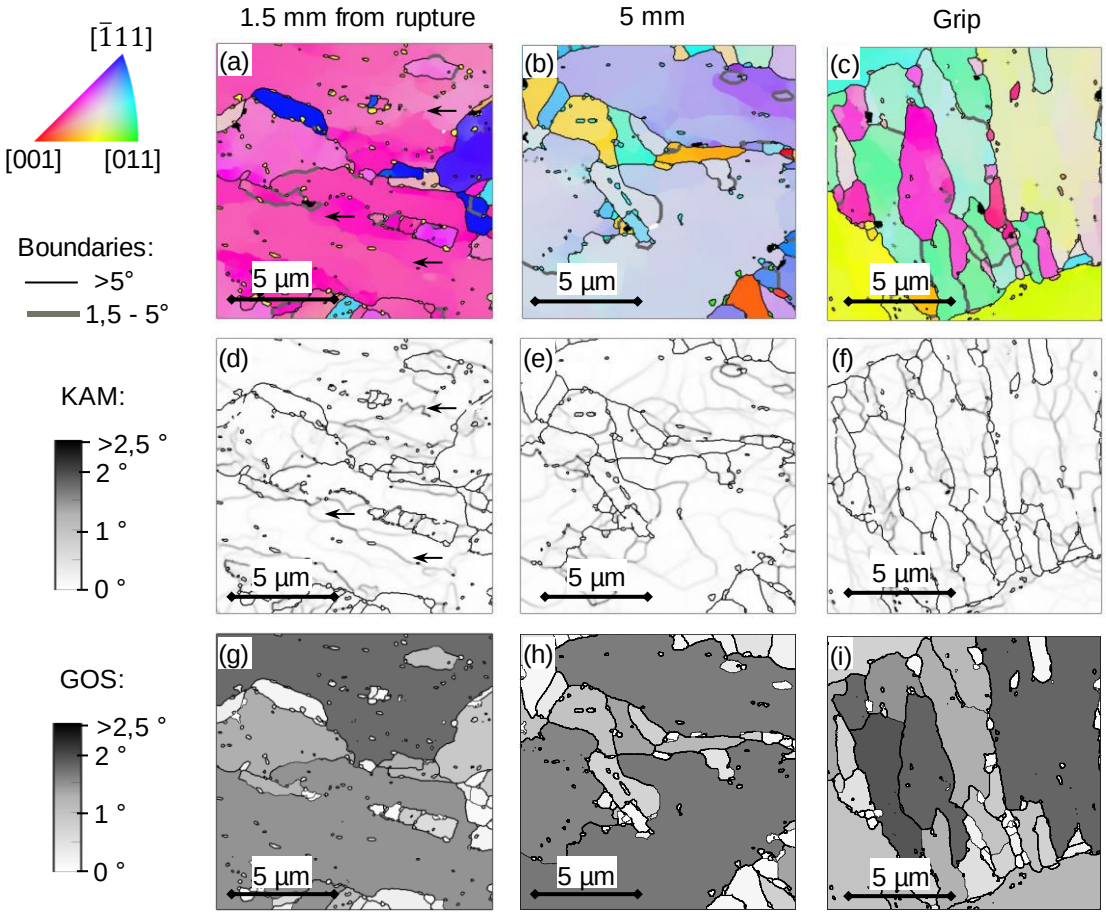

Figure 6.11: (a-c) IPF maps showing crystal orientations relative to the sample normal according to the colour key (top left), (d-f) KAM maps and (g-i) GOS maps of areas at 0 mm and 5 mm from the maximum temperature gauge region and at the grip of the EXH material, respectively

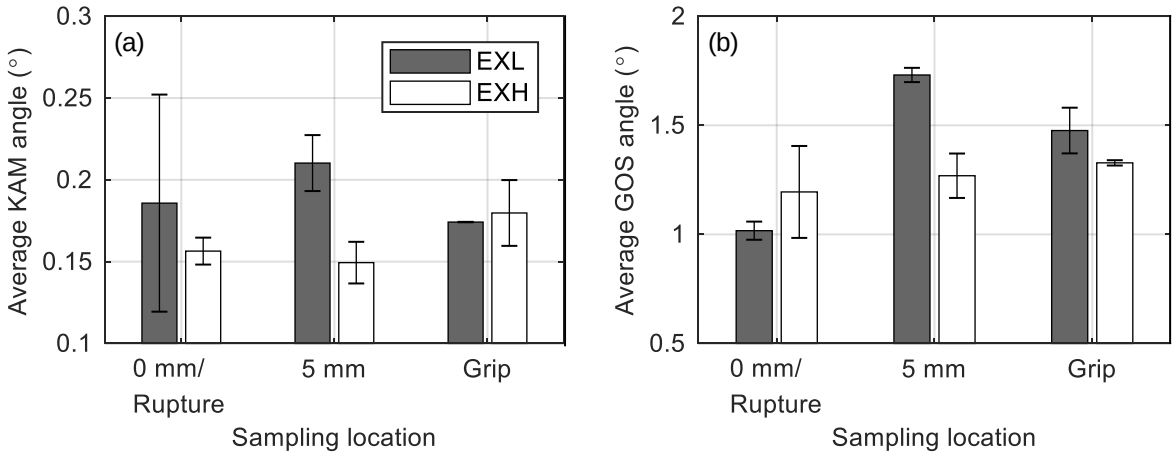

Figure 6.12: Average (a) KAM and (b) GOS angles for EXL and EXH material at various sampling locations in the specimen gauge regions

6.3.3.3 Grain size analysis

Qualitative comparison of micrograin sizes can be seen in the BS-SEM images in Figure 6.7(a-c) which suggest EXH has larger, polygonal-shaped grains than the EXL and EXM material. This is as a result of the well-documented effect of micrograin coarsening that occurred during creep exposure in service and serves as a microstructural indicator of creep damage as larger grains offer less pinning resistance to mobile dislocations (Mitsuhara *et al.*, 2016). Figure 6.13 shows BS-SEM images using a CBS detector at a 10 000× magnification revealing micrograins speckled with precipitates (see Subsection 6.3.3.4).

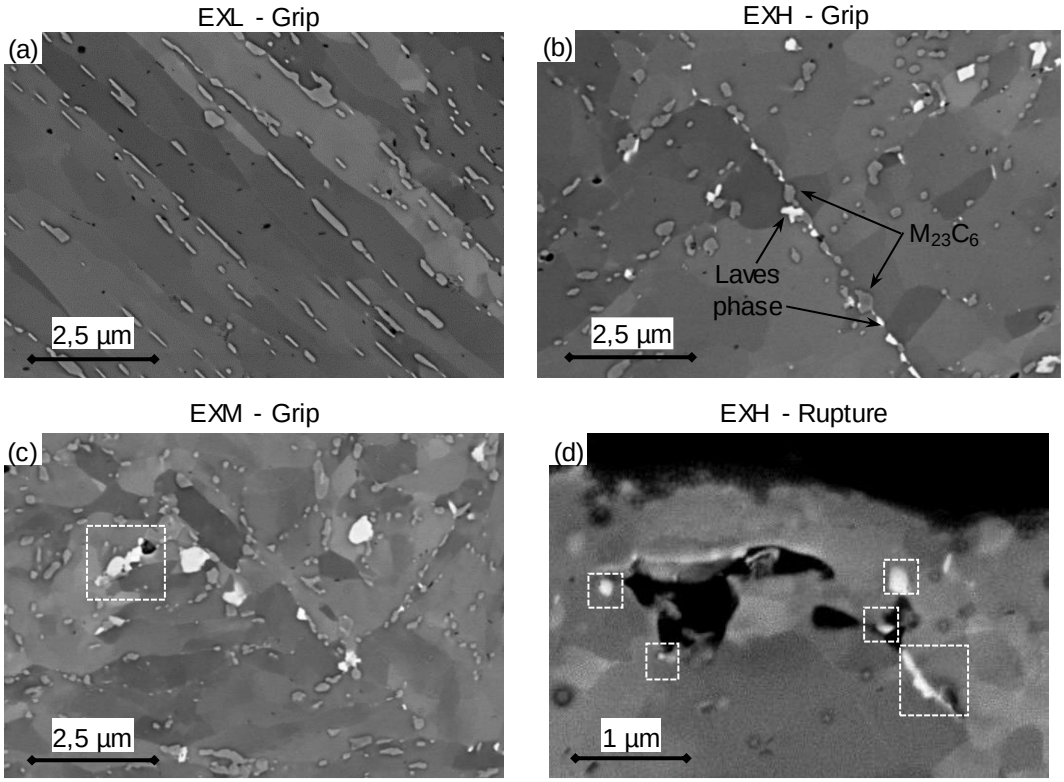

Figure 6.13: CBS-SEM images of (a) EXL, (b) EXH and (c) EXM grip regions and (d) EXH rupture regions. $M_{23}C_6$ and Laves phase particles can be preliminarily identified in the images based on the local brightness of features. Laves phase particles are found adjacent to large voids near the (d) rupture surface of EXH as outlined in white squares

Table 6.5 summarises the measured micrograin short widths measured from BS micrographs and reconstructed from EBSD data with a threshold of 5° (Kinoshita *et al.*, 2011). Micrograins are on average larger in the EXH material than the materials with lower service exposure when considering the BS-SEM micrographs, although the differences are subtler from EBSD analysis. This suggests that micrograin growth is only detected at less than 5° misorientations as the growth of subgrains with low-angle boundaries is one of the main contributors to creep damage. However, this is difficult to detect due to subgrain boundary misorientations (~ 1°) that are within the angular resolution of the EBSD technique. Relatively large micrograin sizes in the EXL material also supports evidence of a decrease in boundary density (Table 6.4). The tendency to more equiaxed grains is evident from the larger micrograin shape factors (ratio of minor to major ellipse axis) in EXH and EXM in comparison to EXL which is also substantiated by the observation of polygonised grains (Figure 6.13b and c).

Table 6.5: Comparison of average micrograin width measured from CBS-SEM and EBSD maps between EXL, EXM and EXH materials (95 % confidence indexes are provided)

Specimen	EXL grip (BS - 936 grains EBSD - 5144 grains)	EXM grip (BS – 1013 grains)	EXH grip (BS - 551 grains EBSD - 5666 grains)
Micrograin width from CBS-SEM (µm)	0.54 ± 0.02	0.60 ± 0.02	0.75 ± 0.04
Shape factor from CBS-SEM	0.52 ± 0.18	0.57 ± 0.18	0.57 ± 0.19
Micrograin width from EBSD with boundaries > 5° (µm)	0.65 ± 0.01	-	0.67 ± 0.01

6.3.3.4 Precipitate analysis

Typically, two main types of precipitates form in X20 following heat treatment: $M_{23}C_6$ carbides (where M = Cr, Fe, Mo) and VX carbonitrides (where X = C, N). Service creep exposure promotes the morphology evolution of these particles through diffusion processes and also results in the formation of new Laves phases $(Fe,Cr)_2(Mo)$ which leads to a reduction in solid solution and precipitation strengthening of the material (Aghajani *et al.*, 2009). Besides differing in chemical composition, $M_{23}C_6$ and Laves phase particles have been reported (Dimmler *et al.*, 2003; Tuma & Kosec, 2007) to be larger (with diameters ranging from 200 – 400 nm) than the VX counterparts and so can be identified through resolutions typical to CBS-SEM imaging along with the micrograin detail as shown in Figure 6.13. VX particles, however, are too small (< 100 nm) to be identified from CBS-SEM images and are instead captured by EFTEM analysis.

Several precipitates are seen decorated along micrograin boundaries in Figure 6.13 with varying degrees of brightness based on their constituent atomic numbers. Seeing as the atomic numbers of Mo and Cr is 42 and 24 respectively, it is expected to identify Laves phase and Cr-rich $M_{23}C_6$ particles from BS map features with corresponding brightness levels with the former being the brightest (Figure 6.13b for example). An overlay of EDS maps over TKD band contrast maps in Figure 6.14a indicates that Laves phase are concentrated regions of Mo which also correspond to regions of Si as shown in Figure 6.14b. This is in agreement with Isik *et al.* (2015) and Aghajani *et al.* (2009) who found that Si promotes Laves phase nucleation.

The EXL material demonstrates stringers of $M_{23}C_6$ particles (notably Figure 6.13a) along micrograin boundaries which appear more broken up in the EXM and EXH material (Figure 6.13b and c). Evidence of cavity growth near larger Laves phase particles was found in EXM (as seen in Figure 6.13c outlined by a white square) and EXH. Specifically, large voids surrounded by Laves phase clusters were noticed near the rupture surface of an EXH specimen in Figure 6.13d. Figure 6.14 also indicates that Laves phase predominantly nucleates adjacent to Cr-rich carbides and along micrograin boundaries. The mean particle diameter, volume number density and interparticle spacing (Holzer, 2010) of $M_{23}C_6$ and Laves phase particles are

compared in error bar plots in Figure 6.15a and b, respectively. Although no differences are expected between the grip and gauge regions on account of the short nature of the accelerated creep tests, the heterogeneous distribution of low-fraction precipitates (in particular Laves phase) require analysis of both regions to quantify the precipitate details more holistically.

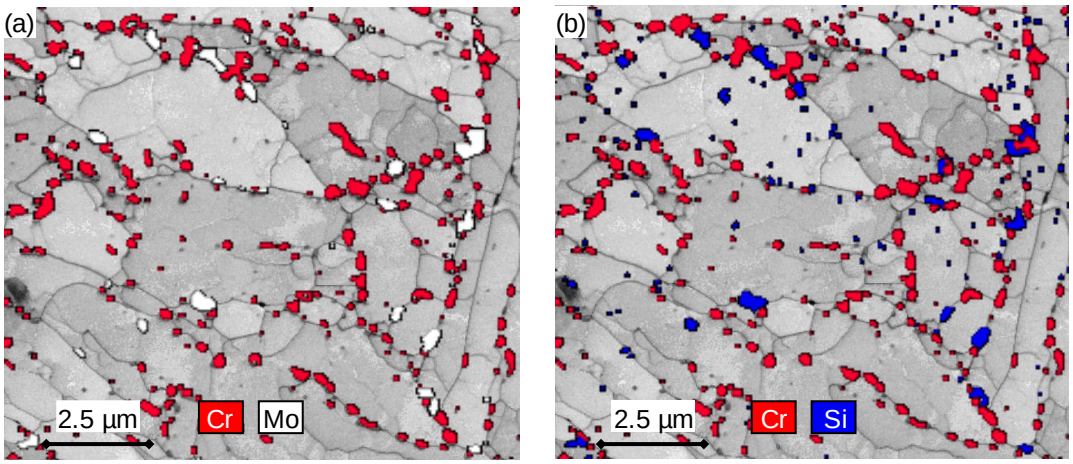

Figure 6.14: EDS maps of (a) Cr and Mo and (b) Cr and Si overlaid over TKD band contrast maps in EXH material, indicating the location of carbides (Cr) and Laves phase particles (Mo and Si) along micrograin boundaries

From these measurements, three main conclusions can be drawn. Firstly, EXH on average demonstrates larger $M_{23}C_6$ particles, spaced further apart with a lower number density. This manifests in a weakening of the pinning effect of micrograins by precipitates (as later deduced from the ADF-STEM micrograph in Figure 6.17b which shows an increased presence of interior precipitates and loss of the close distribution of particles along boundaries present in EXL shown in Figure 6.17a). Secondly, little difference is found between particle parameters in the grip and gauge region given the short durations of the accelerated creep tests and the slow rate of diffusion-related precipitate growth under creep conditions (Aghajani *et al.*, 2009; van Rooyen *et al.*, 2020). In fact, any differences can be attributed to the heterogeneous nature of microstructural features throughout the pipe material. It must be noted, however that no Laves phase was found in the sampled grip region of the EXL material suggesting a less frequent presence of this particle in EXL. Indeed, similar Laves phase interparticle spacings were measured in the EXM and EXH materials. Lastly, a higher number density and smaller interparticle spacing of $M_{23}C_6$ particles is found in the EXM material. A source of error comes from falsely identifying Z phase (CrVN) as $M_{23}C_6$ particles although the effect on these measurements is considered negligible on account of the low Z phase fractions present in X20 (Aghajani *et al.*, 2009).

Composite Cr (green) and V (red) EFTEM maps are shown in Figure 6.16 for EXL (a,b) and EXH (c,d) gauge and grip regions, respectively. The VX particles appear to be dispersed in the matrix with no preferential alignment as evident for the larger Cr-rich particles. Extraction of VX particle parameters from thin foil samples using this technique is challenging due to the degradation of the signal-to-noise ratio from the iron matrix (most notably in Figure 6.16a) as well as the low sample density. However, small differences between the EXL and EXH materials are still evident in the calculated parameters shown in Figure 6.15c. Most notably, coarsening of VX particles with a concomitant increase in interparticle spacing and decrease in

number density is found in the EXH material compared to the EXL counterpart. However, differences in the gauge region are not as obvious. It has been suggested that since no significant changes in VX precipitate morphology is found during long-term creep testing of X20, these particles play a smaller role than $M_{23}C_6$ precipitates in micrograin stability (Aghajani *et al.*, 2009; Armaki *et al.*, 2011). Z phase particles are highlighted in the EXH gauge region (Figure 6.16c) identified as overlapping regions of the Cr and V maps. Observation of this phase suggests that EXH shows increased dissolution of the creep strengthening VX particles due to the growth of large Z phase particles, resulting in decreased creep strength and increased creep damage (Zhao *et al.*, 2018).

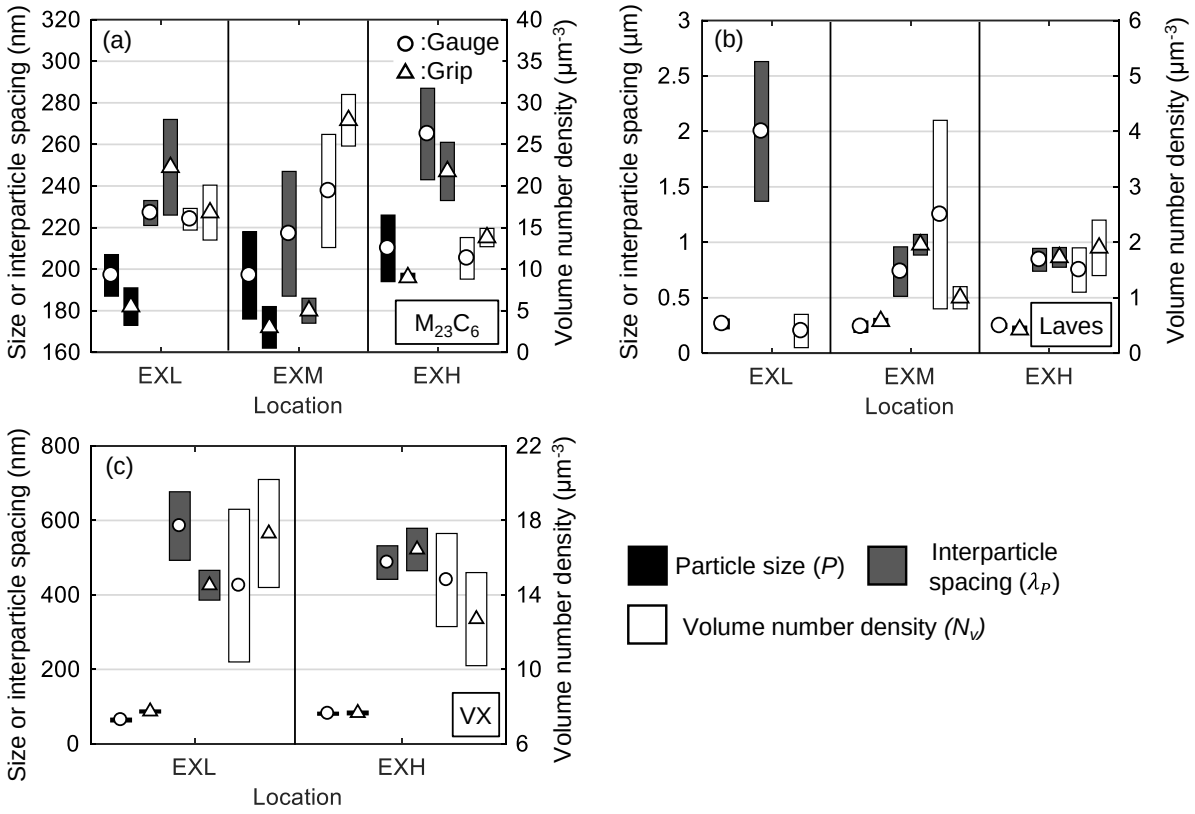

Figure 6.15: Error bar plots of particle diameter, interparticle spacing and volume number density of (a) $M_{23}C_6$ (EXL - 2570, EXM - 2467, EXH – 2560 particles), (b) Laves phase (EXL - 40, EXM - 226, EXH – 364 particles), and (c) VX precipitates (EXL - 348, EXH – 345 particles) in the gauge (circles) and grip (triangle) regions of the EXL and EXH material

6.3.3.5 Dislocation density and substructure

Qualitative differences in dislocation densities and substructure is shown in ADF-STEM micrographs in Figure 6.17a and b for EXL and EXH grip regions, respectively. A heterogeneity in micrograin-interior dislocation densities is noted in the EXL material with some micrograins displaying a higher concentration of dislocations than others. Lower densities are noted in the larger micrograins in the EXH material. The presence of larger and more polygonised grains shown in Figure 6.17d in the EXH state reinforces previous observations (Table 6.5).

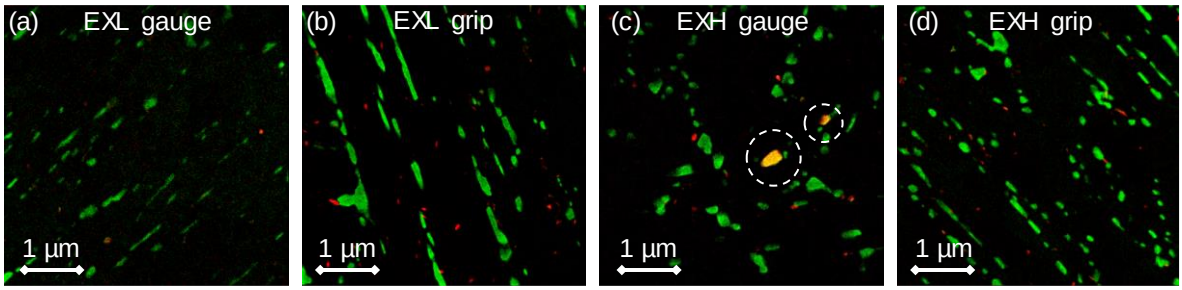

Figure 6.16: Composite Cr (green) and V (red) elemental maps obtained from EFTEM of (a,b) EXL and (c,d) EXH gauge and grip regions, respectively. Z phase particles are indicated by the circle outlines in (c)

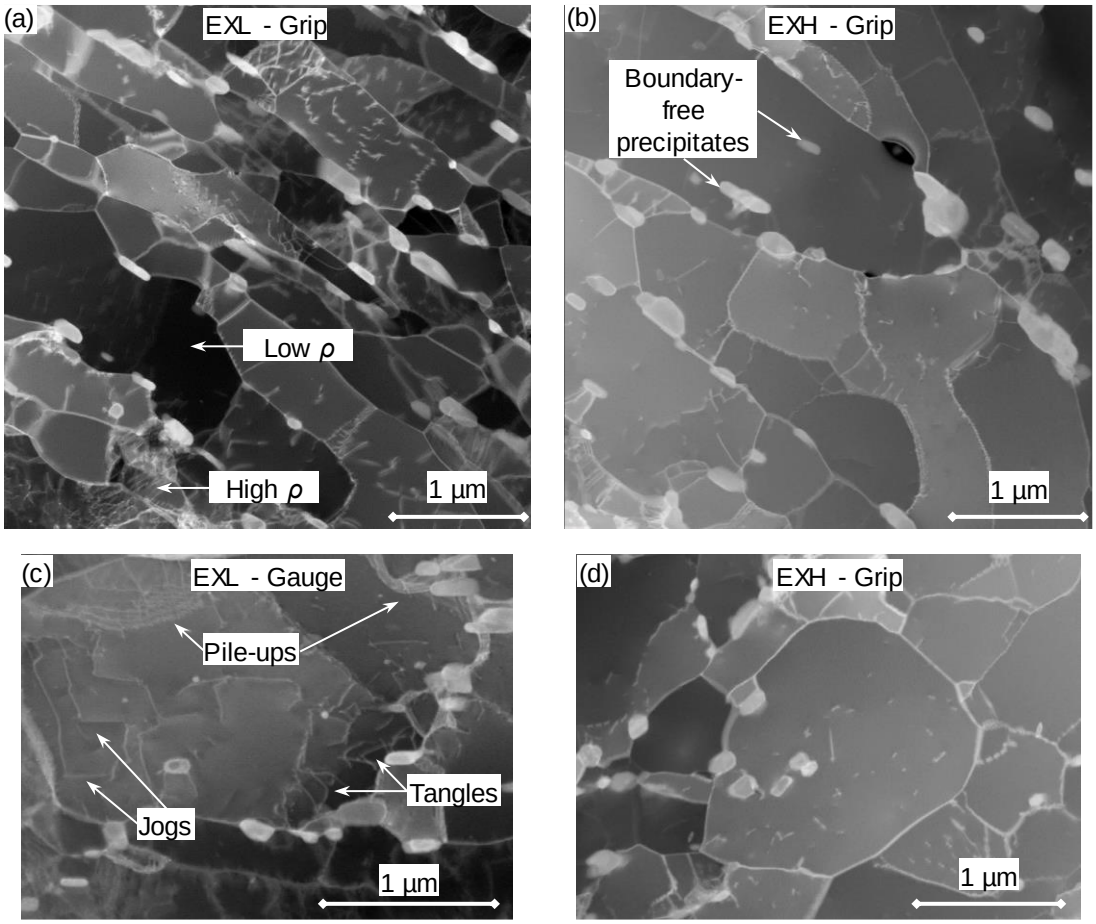

Figure 6.17: ADF-STEM micrographs of (a) EXL, (b) EXH grip regions, (c) various dislocation interactions at the gauge centre of EXL material and (d) an equiaxed micrograin in the EXH grip region. Regions of high and low concentrations of dislocations ρ are indicated in (a)

Comparisons between the respective grip and gauge regions of the EXL and EXH material states reveal substructure and damage features representative of different mechanisms. Prior to testing (best represented by the grip regions), microstructural features reflect the pre-existing

effects of the diffusional creep regime typically encountered in service conditions in power plants (Ghoniem *et al.*, 2013). Following accelerated creep testing (represented by the gauge microstructures), tangles, pile-ups and jogs of dislocations are evident in both material states yet are more common in the EXL material as indicated in Figure 6.17c due to higher dislocation densities within micrograins. Pile-ups are evident at some micrograin boundaries and at large precipitates. These interactions are not noted as extensively in the grip regions, which suggests that testing is within the dislocation climb deformation regime as suggested by changes in gauge microstructures (Benaarbia *et al.*, 2018).

6.4 Discussion

6.4.1 Influence of cavity damage

The impact of the difference in cavity damage can be observed by the shorter rupture times, high strain rates and tertiary-dominated character of the EXH accelerated creep curves (Figure 6.5c), lending credence to the use of cavity density as a damage class indicator (Dobrzański, 2005). The effect of the high number of cavities on the creep rupture mode can be observed through the calculation of creep damage tolerance factor $\lambda_D = \varepsilon_r/(\dot{\varepsilon}_m t_r)$ where ε_r is the strain at rupture, t_r is the time to rupture and $\dot{\varepsilon}_m$ is the minimum creep rate. Values around $\lambda_D = 1$ indicate relatively brittle failure modes or failure without tertiary creep whereas values in excess of 2.5 indicate a combination of plastic deformation from necking, transgranular cracking and microstructural degradation (for $\lambda_D > 5$) (Shrestha *et al.*, 2013). For the current accelerated creep tests, the factor was found to be around 3 – 3.5 for EXH and ~ 4 for the virgin material. Similar trends in degradation of creep ductility were observed by Roy *et al.* (2013) for ex-service P-22 alloy. The lower λ_D value suggests that damage due to loss of cross section and transgranular crack growth from plastic deformation is more likely to occur in EXH than the virgin material in the current accelerated tests due to the presence of closely spaced cavities. Evidence of this is shown in Figure 6.7e where large connected cavities with traces of Al inclusions were found to coalesce perpendicular to the loading direction near the ruptured surface of an EXH specimen at 600 °C and 223 MPa.

Moreover, cavities associated with large Laves phase particles were found in the EXM and EXH material, suggesting a correlation of higher cavity densities with higher Laves phase number densities in a similar manner to that presented by Zhang *et al.* (2017) on F91 steel. As EXL is expected (from replica analysis) to outlive EXM material, the current findings suggest that other microstructural features besides cavity density are responsible for the accelerated creep rates of EXL.

6.4.2 Calculation of deformation mechanism parameters

As temperature and stress is varied in traditional creep experiments, deformation mechanisms at which creep deformation takes place also alters. For instance, at low stress levels at high temperatures, the rate-controlling mechanism is usually diffusional creep (Shrestha *et al.*, 2012). In accelerated creep testing (conducted at intermediate stress and temperature levels), dislocation creep is assumed to dominate based on observations in similar particle-strengthened steels. A typical description of dislocation creep rate behaviour is given by the Bird-Mukherjee-Dorn (BMD) expression modified for threshold stress (Shrestha *et al.*, 2012):

$$\dot{\varepsilon}_m = A_M \frac{D_o E b}{kT} \left(\frac{\sigma_x - \sigma_o}{E}\right)^n \exp\left(-\frac{Q}{RT}\right) \quad (6.1)$$

where $\dot{\varepsilon}_m$ is the steady-state creep rate (minimum creep rate in the case of 9 – 12 % Cr steels), A_M is a mechanism-dependent constant, E is the temperature-dependent Young's modulus, k is the Boltzmann constant, b is the Burgers vector, R is the universal gas constant, σ_x is the average longitudinal stress as established by FEM, T is the applied temperature in Kelvin, D_o is the diffusivity frequency factor, Q is the mechanism-dependent activation energy, n is the stress exponent and σ_o is the threshold stress.

Different deformation mechanisms are elucidated by the values of the parameters Q and n. Additionally, σ_o can also be investigated as a point of comparison between the two aged materials. σ_o is theorised to be necessary to account for the stress required to overcome departure side pinning of dislocations on incoherent particles (Zhao *et al.*, 2018). Without the stress adjustment, high stress exponents and physically impossible activation energies above the value for bulk diffusion in α-Fe are calculated (Shrestha *et al.*, 2012).

By following the procedure laid out by Shrestha *et al.* (2012) to determine Q, n and σ_o using the modified BMD relation, mechanism differences (if any) can be identified between EXH and EXL material. Various models (Shrestha *et al.*, 2012) developed to predict the stress value show a dependency on precipitate size and interparticle spacing. As the microstructural investigation in Subsection 6.3.3.4 has revealed, EXH and EXL possess different precipitate morphologies which will theoretically manifest in different threshold stress values.

Determination of activation energy requires the variation of minimum creep rate with temperature. The DIC technique used in this work allows for the measurement of accelerated creep curves at multiple temperatures from a single specimen within a uniform stress field. From each curve the minimum creep rate was extracted and plotted on a semi-logarithmic plot in Figure 6.18 for each material state at 233 MPa. As deduced from the gradients of each plot, Q appears to be approximately equal between all materials. Prior to threshold stress correction, an activation energy of 335 ± 33 kJ/mol for EXL and 311 ± 43 kJ/mol for EXH is revealed across the different stress states. These values exceed the activation energy for bulk diffusion in α-Fe (240 kJ/mol) (Shrestha *et al.*, 2012). Similarly, n values were calculated to be 10.2 ± 0.7 for EXL and 11.4 ± 0.3 for EXH across the investigated temperature range. The nearly parallel curves in Figure 6.18 signify that no change in deformation mechanism occurs over the range of testing conditions and materials. Such relatively high values for the BMD parameters, however, indicate that compensation for threshold stress is necessary.

Threshold stress correction was performed using the procedure outlined in Shrestha *et al.* (2012) that involves plotting the creep rates to the power of an assumed inverse stress exponent against modulus-normalised applied stress. The exponent n was varied between 3 (viscous glide), 5 (high temperature dislocation climb via lattice diffusion) and 7 (low-temperature dislocation climb via pipe diffusion) until the best fit is obtained for all temperatures, and the temperature-dependent σ_o is then obtained from the intercept of the best-fit curve with the stress axis at a zero creep rate value. For both EXL and EXH materials, stress exponents of 7 achieved a correlation coefficient of ≥ 0.98 suggesting that dislocation climb via pipe diffusion is the dominant deformation mechanism. Similar results were found for virgin and retired X20 investigated by El Rayes and El-Danaf (2017). Based on the resulting exponents, σ_o values of approximately 78 – 84 MPa and 69 – 78 MPa were calculated for EXL and EXH respectively

at temperatures ranging from 600 – 575 °C. This suggests that EXL demonstrates only slightly higher resistance to dislocation climb of precipitates than the EXH counterpart.

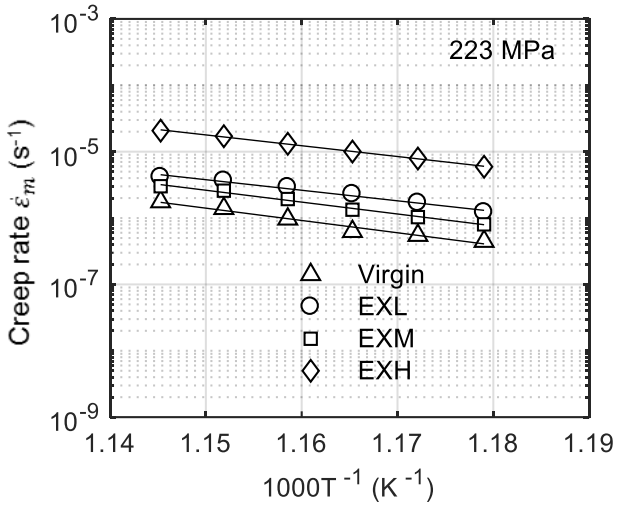

Figure 6.18: Logarithmic creep rate versus inverse temperature plots for all material states at 223 MPa

In order to relate the experimental σ_o with the measured particle distributions, a model prediction developed by Arzt *et al.* (1986) is employed, given in Equation (6.2) using a Taylor factor of 2.73 to convert from shear to normal stresses:

$$\sigma_o = 2.73G\frac{b}{\lambda_p}\sqrt{1-k_A^2} \qquad (6.2)$$

This model considers the detachment stress involved in freeing dislocations from the particle-dislocation attraction to be synonymous with the threshold stress and was recently shown by Zhao *et al*. (2018) to work well in predicting creep rates at intermediate stresses for Grade 91 ferritic steels. The model variables and constants are given in Table 6.6, including the interparticle spacing associated with the VX particles measured in this study. As $M_{23}C_6$ are considered to stabilise micrograin boundaries, VX particles dispersed within the grain matrix are the main obstacles to dislocation motion and are therefore employed in this model. Using this model, values of 97 (71) MPa and 79 (85) MPa were predicted using interparticle spacing values measured for VX precipitates from EXL and EXH grips (gauge values are supplied in brackets), respectively.

It is evident that the increased precipitate diameters and consequently longer interparticle spacing in EXH has resulted in a lower threshold stress than for the EXL material. Lower values predicted from gauge measurements in the EXL material is due to higher amount of scatter present in these EFTEM-based measurements (seen in Figure 6.15c). Although EXH demonstrated close agreement with the calculated values, the model overestimated the threshold stress for EXL compared to the experimental results. This could be due to several reasons including measurement scatter due to the lack of particle statistics associated with small EFTEM sampling windows and difficulty in determining the model constants (Arzt & Rosler, 1988). There is also evidence that VX particles play a smaller role compared

to $M_{23}C_6$ on creep strength enhancement (Aghajani *et al.*, 2009). The same model, however, cannot be applied to $M_{23}C_6$ precipitates as dislocation climb kinetics are altered with smaller interparticle spacing to radius ratios (Arzt & Wilkinson, 1986). Despite this, however, both the model and analytical method indicate a greater weakening of the particle-strengthening effect in EXH as opposed to EXL. Evidence of the prevailing dislocation-particle interaction is shown in Figure 6.19a for the EXL material where dislocations are trapped by closely spaced particles. On the other hand, a larger spacing between precipitates as well as the increased presence of large (> 0.25 µm diameter) Laves phase particles in EXH material offers less resistance to dislocation migration as shown in Figure 6.19b.

Table 6.6: Model inputs for the equation of threshold prediction by Arzt *et al*. (1986)

Symbol	Description	Value	Reference
G	Shear modulus at 600 °C	63.5 GPa	EPRI (2006:5.1-5.3)
b	Burgers vector	2.5×10^{-10} m	Aghajani *et al.* (2009)
λ_p	Average interparticle spacing of VX precipitates	585[21]/426 nm – EXL gauge/grip 487/522 nm – EXH gauge/grip	Subsection 6.3.3.4
k_A	Detachment factor model constant	0.3	Shrestha *et al* (2012)

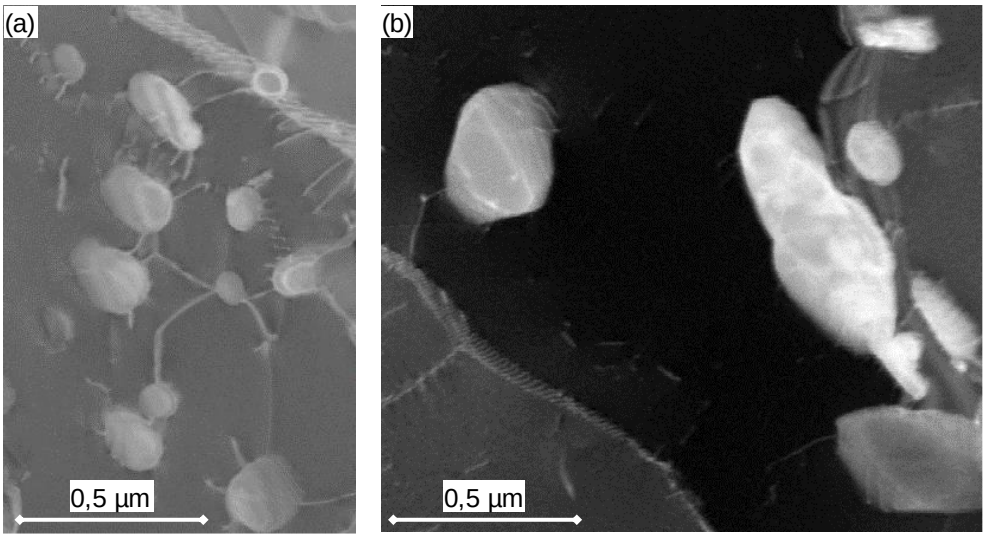

Figure 6.19: ADF-STEM images showing (a) multi-particle pinning of dislocations by $M_{23}C_6$ particles closely spaced together in the EXL material and (b) dislocations bypassing larger precipitates spaced further apart in the EXH material

[21] Large scatter is evident in VX interparticle spacing measurements from EFTEM micrographs

Following threshold stress correction, the activation energies and stress exponents were calculated as shown in Figure 6.20. Data from lower temperatures (< 575 °C) were excluded for the following analysis as creep curves failed to reach the secondary creep stage within the testing time, which is evident by a lack of minimum points in Figure 6.4f. Further verification of the stress exponent of 7 is obtained by using the threshold stress previously calculated in a double logarithmic plot of minimum creep rate versus normalised effective stress in Figure 6.20a where the gradient is calculated as 7.13 ± 0.02 and 6.92 ± 0.02 across all temperature values for EXL and EXH, respectively.

Activation energies were calculated from three modulus normalized effective stress ($\frac{\sigma_e}{E} = \frac{\sigma_x - \sigma_o}{E}$) of 5.4 × 10^{-4}, 9.1 × 10^{-4} and 9.9 × 10^{-4} and were found to be 159 ± 4 kJ/mol and 171 ± 4 kJ/mol for EXL and EXH, respectively (Figure 6.20b). Calculated energy values for EXL and EXH are close to 60 % of the theoretical value of lattice self-diffusion in α-Fe (0.6 × 250 kJ/mol = 150 kJ/mol) which is expected for low-temperature climb as a governing mechanism in which pipe diffusion of atoms occurs through dislocation cores (El Rayes & El-Danaf, 2017).

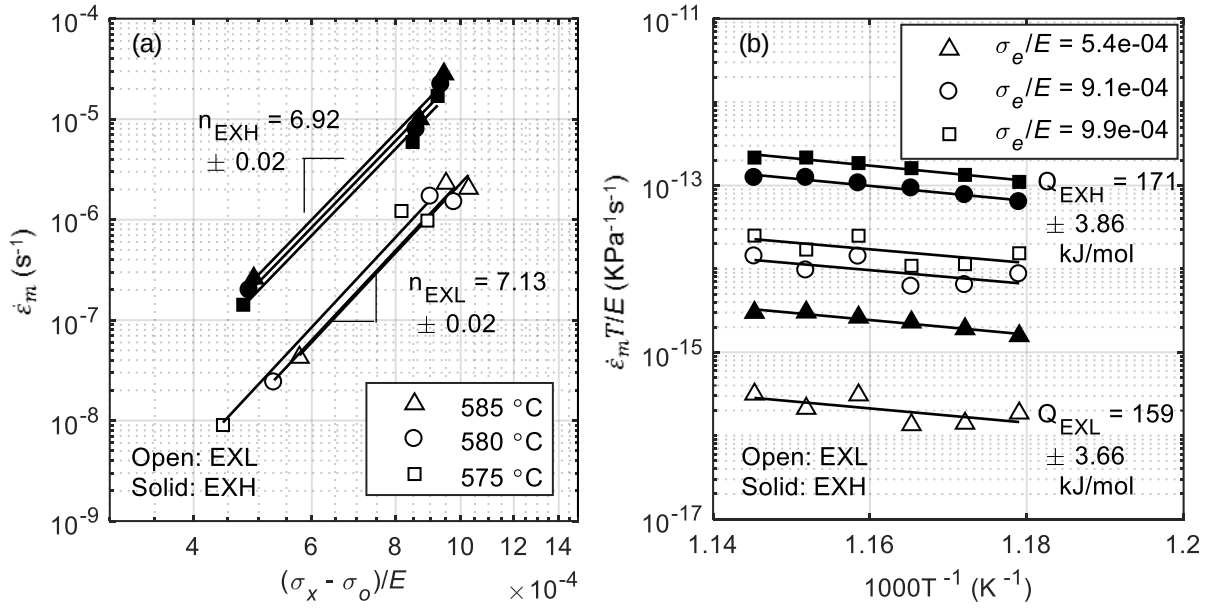

Figure 6.20: (a) Calculation of stress exponents from log-log plot of minimum creep rate versus normalised effective stress. (b) Calculation of activation energies for EXL and EXH at three modulus compensated stresses (open and solid symbols, respectively)

As a final comparison between the two aged materials, the data for each condition is collected onto a single reference plot as shown in Figure 6.21 using the Zener-Hollomon parameter (El Rayes & El-Danaf, 2017):

$$Z = \dot{\varepsilon}_m \exp\left(\frac{Q}{RT}\right) = A\left(\frac{\sigma_x - \sigma_o}{E}\right)^n \qquad (6.3)$$

where A is the Zener-Hollomon constant. Data from both EXL and EXH each fall onto a straight line on the double logarithmic plot the gradient of which corresponds closely with the stress exponents previously calculated in Figure 6.20a and are represented by equations of

$1.31 \times 10^{25} \left(\frac{\sigma_x - \sigma_o}{E}\right)^{6.97}$ and $4.47 \times 10^{26} \left(\frac{\sigma_x - \sigma_o}{E}\right)^{6.91}$ for EXL and EXH, respectively. These results are similar to findings by El Rayes and El-Danaf (2017) for as-produced and ex-service 12 % Cr steel using hot tensile tests. Z values from a single stress state for the EXM material lies close to the EXL data, stemming from similar creep rates between the two material states. This implies that the Z parameter obtained using the proposed accelerated creep technique can be used to establish the relative damage between service-exposed X20 as an alternative to other techniques, such as hardness testing, that would otherwise not reveal a difference in damage.

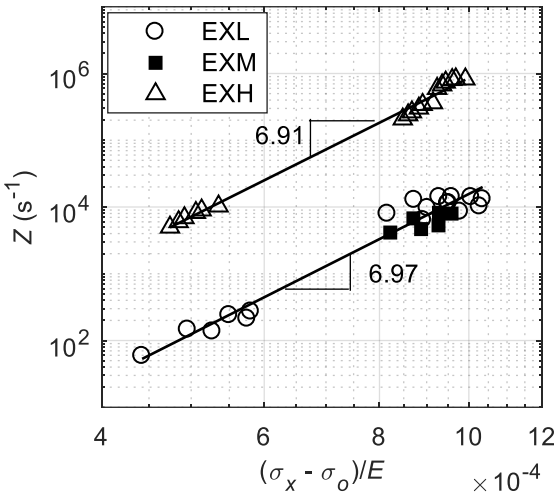

Figure 6.21: Plot of Zener-Hollomon parameters of EXL and EXH materials. A single stress state for EXM is included for comparison with EXL

6.4.3 Comparison between mechanical and microstructural damage indicators

This technique has proven that differences in levels of damage of service-exposed material can be identified using both mechanical testing methods based on DIC and microstructural analysis. The mechanical testing-derived parameters, specifically the Zener-Hollomon parameter, are shown to be a simpler indictor of damage in comparison to microstructural factors which are often more complicated to analyse. This is due to the complex interactions between precipitates and micrograin coarsening (Figure 6.13); dislocation pinning and precipitates (Figure 6.19); dislocations and micrograin boundaries (Figure 6.17c); and between different types of precipitates (Figure 6.14 and Figure 6.16). Slow evolution of some microstructural features, depending on the point of life exhaustion, result in subtle differences between ex-service materials (as shown for characteristic boundary features and EBSD-based micrograin size in Table 6.4 and Table 6.5, respectively) and further exacerbates the difficulty of using microstructural analysis as a form of damage measurement (Dobrzański, 2005). There is high scatter associated with the microstructural statistics possibly due to different starting microstructures, alloy compositions for the EXL and EXH material and spatial heterogeneity of some microstructural features. For instance, the difference in misorientaion indicators, such as KAM and GOS, is not as obvious if untested material at the grips were analysed – indicating that the testing manifests differences between EXL and EXH in the gauge regions. Finally, it should be noted that small window analysis is very sensitive to nonuniform spread of microstructural features in the sampled field, resulting in large standard deviation values as shown in Figure 6.12.

In this case, the close similarity in damage between EXL and EXH was initially revealed through hardness measurements (Figure 6.6). Interestingly, the EXL hardness measurements are lower than those for the EXM specimen and closer to that of EXH, both of which have higher cavity densities. The lower hardness can thus be attributed to features of microstructural degradation (such as larger micrograins and/or precipitates) similar to that displayed by EXH rather than due to the presence of cavities (Panait, Bendick, *et al.*, 2010).

Based on these grounds, key mean microstructural parameters are compared via unpaired *t*-testing with a 0.05 significance value to indicate statistically significant differences between EXL, EXM and EXH grip regions in Figure 6.22 using values of the latter region as a baseline. Mechanical-based parameters, such as BMD equation parameters, threshold stresses and Zener-Hollomon pre-exponentials *A*, are also included along with the traditional means of damage assessment using cavity densities.

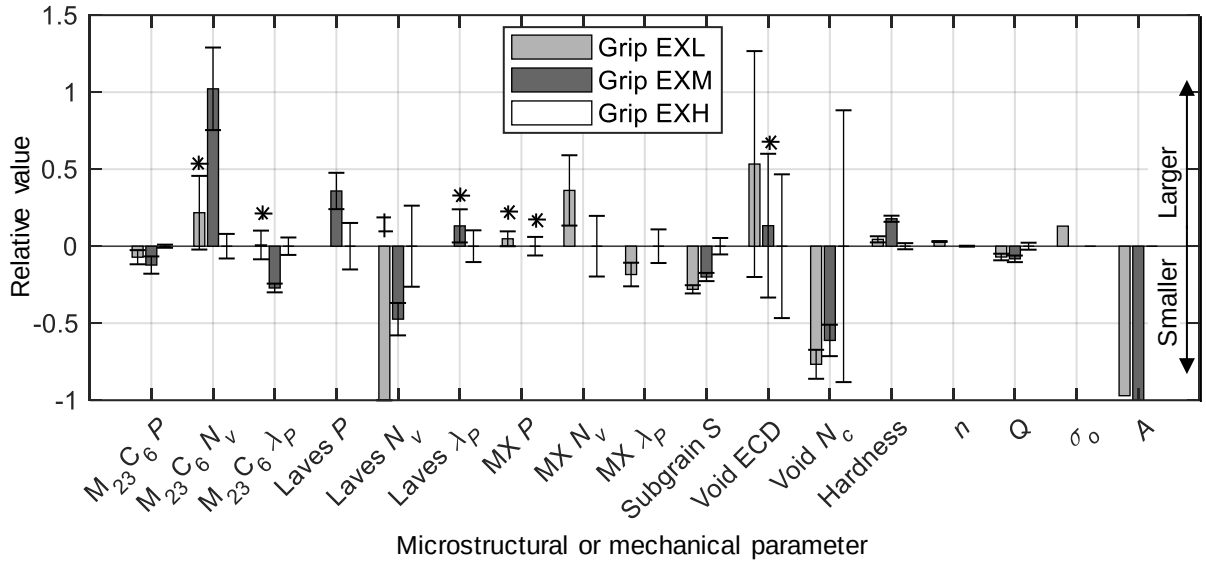

Figure 6.22: Relative differences in microstructural parameters indicating damage using the EXH grip region as a baseline. Note: P = particle diameter, S = minor micrograin diameter, N_V = particle volume density, λ_P = interparticle spacing, N_c = cavity area density, n = stress exponent, Q = activation energy, σ_o = threshold stress, A = Zener-Hollomon pre-exponential. Asterisks (*) indicate features that are not statistically different from the baseline. ‡ indicates that no Laves phase was recorded in the EXL grip region

The most prominent differences in microstructural damage indicators is noted in micrograin width (measured from BS-SEM) as well as the precipitate distribution, specifically Laves phase (between EXL and EXM/EXH) and $M_{23}C_6$ (between EXM and EXL/EXH). Micrograin width shows increasingly coarser, polygonised grains with damage level, correlating somewhat with cavity density measurements. With no significant amounts of Laves phases observed in the EXL grip, one contributing factor to increased damage in EXH is the solid solution depletion of Mo and Cr due to the formation of Laves phase ($(Fe,Cr)_2Mo$) and growth of $M_{23}C_6$ carbides. This effect appears to outweigh any potential benefit gained from particle strengthening (Aghajani *et al.*, 2009). The relative ability of different precipitates to pin micrograin boundaries is established by considering their respective normalised Zener pinning pressure,

given as $P_z/\gamma = 3f/P$ (Fedorova *et al.*, 2014) where P_z is the Zener pinning pressure, γ is the boundary surface energy per area, f is the particle volume fraction and P is the particle diameter. In the EXH gauge region, $M_{23}C_6$ and Laves phase precipitates result in an average normalised pressure of 0.74 and 0.13 μm^{-1}, respectively. The corresponding values in the EXL gauge region are 0.97 and 0.045 μm^{-1}, respectively. Therefore, Laves phase is shown to be ineffective in pinning micrograins, providing a 5 – 20 times smaller pinning pressure compared to $M_{23}C_6$ particles. Additionally, as Laves precipitation is known (Isik *et al.*, 2015) to often occur adjacent to $M_{23}C_6$ particles (also found in this work in Figure 6.13b and Figure 6.14), the Zener pinning pressure responsible for micrograin boundary pinning is reduced as the effective precipitate size increases. Such clustering has also been found in previous research to cause a reduction in yield strength of the material especially when particle sizes exceed 0.2 µm (similar to sizes obtained in this study) (Li, 2006). Although it has been shown that solid solution depletion of Mo takes a minor role in overall creep damage in some 9 – 12 % Cr steels (Aghajani *et al.*, 2009), it is considered here together with larger micrograin sizes to be the principle difference between EXL and EXH besides cavity density. Traces of Z phase found in the EXH material could also suggest higher damage levels than in EXL, although no conclusions can be drawn from the small amount observed.

The deformation resistance of EXM revealed from the deformation tests, however, cannot be explained in the same manner as it has similar Laves phase interparticle spacing to that of EXH. Instead, a dense $M_{23}C_6$ particle distribution is the only feature investigated that explains the enhanced strength of EXM with P_z/γ values of 1.29 μm^{-1} in the grip region. Previous investigations (Aghajani *et al.*, 2009; Armaki *et al.*, 2011) emphasised the hardening effect of these carbides from stabilising the substructure and pinning boundaries. These microstructural results together with the deformation measurements therefore suggest that EXM has a similar amount of remnant creep strength as EXL, despite the higher category of damage based on cavity density. This highlights the benefit of exploring alternative damage indicators, such as the Zener-Hollomon parameter and precipitate densities, in the assessment of service-exposed X20. Creep strain and rate data used in this work as well as microstructural statistics are provided in an online repository (van Rooyen, 2019).

6.5 Post-submission discussion

During the revision process, concern was raised regarding the limited stress ranges used to calculate the stress-dependent creep parameters, including the threshold stresses and stress exponents (Figure 6.20a). On account of the limited supply of the long-term service-exposed material, only two stress ranges using the flat specimen geometries were originally considered. As a demonstration of the versatility of the technique and in response to the aforementioned concern, additional square samples were included in the calculation of stress-dependent parameters. A brief discussion of the post-submission findings is provided here.

6.5.1 Parameter calculation using square data

Inclusion of the square geometry involved the extraction of stresses using the FEM model discussed in Subsection 6.2.3 at the locations of the respective temperatures. Square geometry data at nominal engineering stresses ranging from 180 MPa to 250 MPa were included as shown in Figure 6.23a and b for calculation of σ_o and n respectively with these data points specifically identified by arrows. By including the square geometry data, σ_o values of approximately 75 – 85 MPa and 85 – 90 MPa were calculated for EXL and EXH, respectively. As illustrated in Figure 6.23a, there is an overlap in threshold stress values when considering the square data.

This suggests that, within experimental and microstructural scatter associated with Equation (6.2), no clear differences in threshold behaviour can be identified between these two ex-service states. This finding is similar to that of Singh (1995) who found a mild difference of 12 MPa in σ_o between virgin and 100 000 h service-exposed boiler Cr-Mo steel. Nonetheless, evidence of the role of $M_{23}C_6$ particles in dislocation entrapment is shown in Figure 6.19, suggesting that these carbides serve a greater strengthening role than the VX precipitates considered in traditional threshold investigations (Shrestha *et al.*, 2012).

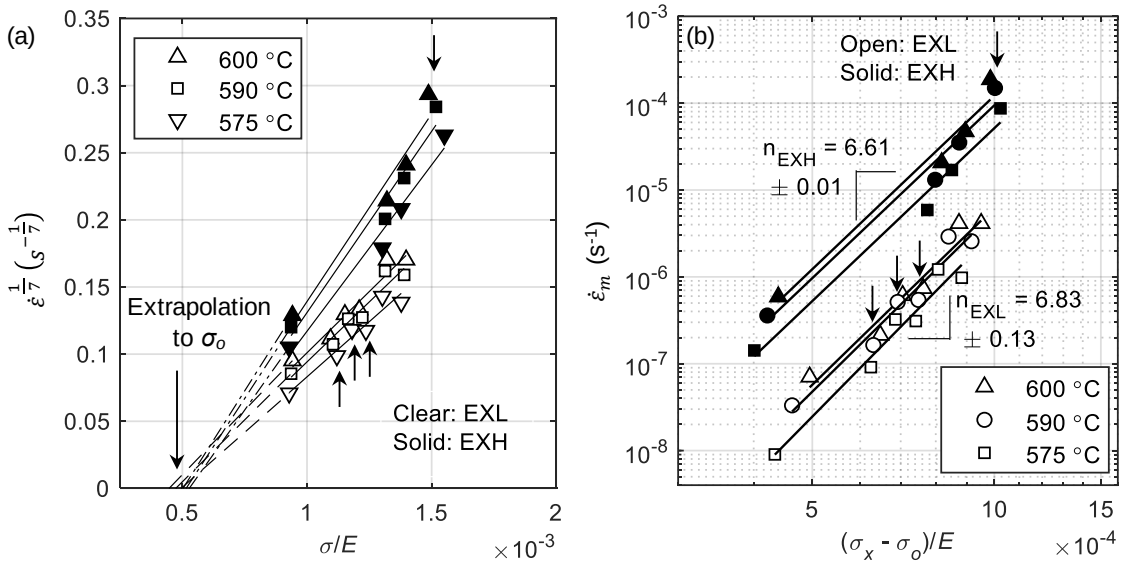

Figure 6.23: Calculation of (a) threshold stresses and (b) stress exponents for EXL and EXH using flat and square specimen data. Square data points are identified by arrows

As indicated in Figure 6.23b, stress exponent calculations were found to be 6.61 ± 0.01 and 6.83 ± 0.13 across all tested temperature values for EXL and EXH, respectively. This is in close agreement with the predicted stress exponent of 7 for the low-temperature dislocation creep regime. Zener-Hollomon parameter calculation with the included square data resulted in values represented by $2.56 \times 10^{24} \left(\frac{\sigma_x - \sigma_o}{E}\right)^{6.72}$ and $1.53 \times 10^{26} \left(\frac{\sigma_x - \sigma_o}{E}\right)^{6.61}$ for EXL and EXH, respectively. As previously found in Figure 6.21, higher Zener-Hollomon values are found for the EXH state than for EXL.

6.5.2 Limitations of current technique

The main limitation in the current analysis is that each stress condition requires a separate specimen. This means that any stress-based analysis (such as for determining stress exponents and threshold stresses) is specimen intensive. In keeping with the requirement for ex-service material economy in power plant applications, however, the current work, which employs variable temperature profiles, is better suited to temperature-based calculations (such as for activation energies and Zener-Hollomon parameters). Using the current testing parameters, no notable difference is evident between the ex-service materials in terms of stress-based parameters. For this reason, less onus is placed on these parameters as a method of damage characterisation using this technique. Although beyond the scope of the current study, Chapter 7 introduces a DIC technique that integrates a variable stress profile with a constant temperature profile on a single specimen. In contrast to the current work with variable temperature profiles

at a single stress state, such tests are better suited to the material-efficient calculation of stress exponents and threshold stresses as opposed to temperature-based calculations (such as activation energy). The conclusions in the following section are framed with respect to these post-submission findings.

6.6 Conclusions

The presented work allows for the comparative damage assessment of ex-service (EXL, EXM and EXH – low, medium and high damaged) X20 piping material by comparing the deformation behaviour of the material states through DIC-based mechanical testing and applying advanced electron microscopy to elucidate the link with microstructural features. Both techniques correlate well when considering the Zener-Hollomon parameter and Laves phase and carbide distributions. In summary, the following conclusions are highlighted:

- Multiple accelerated creep curves at several temperatures ranging from 550 – 600 ºC are extracted from single samples of virgin and ex-service 12 % Cr steam piping steel using the full-field capabilities of DIC. Increasingly higher creep strains and rates were measured for virgin, EXM, EXL and EXH material, respectively.
- Orientation mapping revealed higher boundary densities, higher frequencies of small angle (< 1º) boundary misorientation angles and smaller KAM and GOS values for the EXH material. Micrograin sizes determined from EBSD were found to be very similar between the two materials, whereas BS-SEM identified larger, near-equiaxed grains in the higher damage materials.
- An increase in the mean $M_{23}C_6$ size and Laves phase size and spacing was noted in the EXH material and no Laves phase was found in the sampled EXL grip region. Differences in the VX precipitate distributions were subtle.
- Following threshold stress correction using the BMD formulation, stress exponents of 7 and activation energies of 159 ± 3.66 and 171 ± 3.86 kJ/mol similar to that of pipe diffusion were calculated for the EXL and EXH material, respectively, pointing to low-temperature dislocation climb as a potential deformation mechanism. Lower threshold stresses computed using microstructural means suggest that EXH material has a reduced ability to pin dislocations as is also identified qualitatively by dislocation-denuded micrograins and coarse precipitates in ADF-STEM analysis. Creep-based analytical calculations suggest similar threshold stresses between the EXL and EXH material within experimental scatter.
- Higher Zener-Hollomon values were found for EXH compared to the EXL and EXM, serving as a reliable damage indicator based on DIC measurements. Extensive reduction in solid solution strengthening and pining of precipitates through Laves phase and $M_{23}C_6$ coarsening is suggested as the main form of microstructural degradation of EXH over the other material states. Slower creep rates, relatively low Zener-Hollomon values and dense $M_{23}C_6$ distributions for the EXM material suggest a remnant creep life close to that of EXL, despite the higher cavity density count and resulting damage category.

Future work utilising the full-field capabilities of DIC opens the possibility of measuring multiple creep curves at multiple stresses using a specialised geometry during traditional creep testing at constant temperature (Sakanashi *et al.*, 2017). This will allow comparative damage identification from ex-service material across different deformation mechanism regimes through the more convenient calculation of stress exponents and threshold stresses from a single specimen.

7 Creep damage parameter extraction from 12 % Cr steel using digital image correlation

The following chapter focuses on performing DIC-based damage characterisation using variable stress profiles in addition to the variable temperature profiles (as discussed in the previous chapter). Instead of conventional creep equations, however, this chapter uses damage evolution relationships through continuum damage mechanics (CDM) modelling as a damage diagnostic tool. In a similar manner to the previous chapter, damage evaluation is achieved both through strain-based modelling as well as microstructural analysis of ex-service X20 with varying levels of cavity damage.

This chapter has been submitted to the *International Journal of Damage Mechanics*. CDM and DIC aspects of this paper have also been presented at the 12th International Conference on Advances in Experimental Mechanics hosted by BSSM (van Rooyen & Becker, 2017)[22].

Declaration by the candidate:

With regard to Chapter 7, the nature and scope of the author and co-authors is as follows:

Name	Email	Contribution	Extent (%)
M van Rooyen (candidate)	melzvanrooyen@ sun.ac.za	Conceptualised paper, performed all Gleeble-based testing, performed variable stress tests of new and high damage (high cavity density) X20 at 150 MPa, performed all hardness measurements, processed all experimental DIC data, collected and processed micrographs, performed finite element simulations and CDM modelling, compiled and performed final edits of manuscript	90
TH Becker	tbecker@ sun.ac.za	Beyond supervisory and reviewing roles, assisted with optimising CDM code; reviewed manuscript; and suggested core idea	5
AN Forsey	alex.forsey@ open.ac.uk	Designed original experimental setup, performed low and medium X20 variable stress tests at 150 MPa, developed demosaicing code and reviewed manuscript	5

Signature of candidate: ……..[MvR]……..(see Footnote 12)
Date: ……..2020/04/30……

Declaration by co-authors:

The undersigned hereby confirm that:

1. The declaration above accurately reflects the nature and extent of the contributions of the candidate and the co-authors to Chapter 7,

[22] DOI link: http://www.bssm.org/uploadeddocuments/Conf 2017/2017 papers/98_Melody_Van_Rooyen_formatted.pdf

2. No other authors contributed to Chapter 7 besides those specified above, and
3. Potential conflicts of interest have been revealed to all interested parties and that the necessary arrangements have been made to use the material in Chapter 7 of this dissertation.

Signature (see Footnote 12)	Institutional affiliation	Date
[TH Becker]	SU	2020/04/30
[AN Forsey]	OU	2020/04/30

7.1 Introduction

As coal-fired power stations approach their design lifetimes, plant operators demand improved creep damage assessment techniques for critical component materials. Main steam piping steels commonly used in older generation plants, such as the 12 % Cr steel X20CrMoV12-1 (X20 hereafter), exhibit complicated degradation mechanisms which involve interacting microstructural factors. The creep strength resistance of X20 and other 9 – 12 % Cr tempered martensitic-ferritic steels stems from a fine substructure with dense dislocation structures stabilised by fine precipitates, such as MX carbonitrides and $M_{23}C_6$ carbides (Aghajani *et al.*, 2009). Adding to the complexity of X20 microstructure, plant service exposure drives the evolution of thermodynamically unstable features including the coarsening of subgrains, recovery of dislocations, coarsening of precipitates as well as the development of new precipitates such as Laves and Z phase.

The past half-century has seen the promulgation of several damage assessment techniques for power engineering alloys, prompted by the efforts to extend thermal power plant operability. Such methods include, amongst others, physical assessments, such as hardness measurements, as well as creep constitutive relations (Cardoso *et al.*, 2015). Such relations encompass single-creep-stage predictions, such as the description of minimum creep rates through Norton's power law (Abdallah *et al.*, 2014), rupture life predictions such as the Larson-Miller parameter (Larson & Miller, 1952) as well as full-curve descriptions including the θ-projection and Ω models (Kim *et al.*, 2011). Decreases in Vickers hardness measurements have been employed as crude empirical assessments of the remnant life of low- and high-alloy CrMo steels through correlation with time-temperature relations such as the Larson-Miller parameter (Masuyama, 2009; Cardoso *et al.*, 2015). However, these methods have limited applicability to service-exposed materials due to their inability to account for the aforementioned microstructural intricacies (Gupta *et al.*, 2015). Some improved creep relations have also demonstrated difficulty in isolating differences between service-aged materials. In the authors' previous work (van Rooyen *et al.*, 2019a), for instance, insignificant differences were found between ex-service X20 states in terms of precipitate-dependent threshold stress calculation using a modified power law relation despite large differences in the corresponding creep curves. Classical creep models also do not universally capture the different creep mechanisms that dominate as the material state, testing temperature and stress conditions are altered. Parameters, such as activation energy and stress exponents, have been found (El Rayes & El-Danaf, 2017; van Rooyen *et al.*, 2019a) to be insensitive to the state of material exposure and so do not lend themselves as effective damage indicators.

Prompted by the need to simulate evolving microstructural damage in creep modelling, continuum damage mechanics (CDM) was originally developed as a tool for lifetime predictions. CDM models provide a framework whereby several coupled damage laws phenomenologically track the evolution of microstructural and cavitation factors during creep

through the inclusion of sets of dimensionless damage parameters. The advantage of physically based CDM methods is the adaptability of these damage descriptors to physical microstructural characterisation through electron microscopy, allowing the entire creep curve to be modelled within creep regimes with different loading conditions and operating mechanisms (McLean & Dyson, 2002).

A large body of literature has centred around the application of CDM to 9 – 12 % Cr steels which evolved from the works of Dyson and McLean (Dyson & McLean, 1998; Dyson, 2000; McLean & Dyson, 2002) who pioneered the incorporation of several damage parameters into the fundamental hyperbolic sine creep rate equation which lies at the root of CDM. Since then, research has adapted various combinations of these damage parameters with most of the approaches specifically focusing on long-term creep modelling of power plant alloys. For 10 % Cr steels, Kadoya *et al*. (1997) proposed a model containing a combination of MX particle coarsening, dislocation accumulation and Mo solute depletion (due to Laves phase Fe_2Mo precipitation) damage parameters to predict creep strain-time curves for lives in excess of 6 000 h. This model was later adapted by Semba *et al.* (2008) who recognised that a dislocation recovery damage parameter is more appropriate for tempered martensitic-ferritic steels and included this as an indirect means of accounting for subgrain coarsening in the modelling of 9 % Cr steel. The model formulation was later expanded in work by Basirat *et al.* (2012) to include a cavitation damage parameter. However, the authors did emphasise the technical challenges associated with quantifying dislocation densities required by a dislocation-based creep model.

There has also been evidence in literature (Yin & Faulkner, 2006; Aghajani *et al.*, 2009; van Rooyen *et al.*, 2019a) to suggest that instead of MX growth, the main particle damage parameter in X20 steel is related to the coarsening of subgrain-pinning (intergranular) $M_{23}C_6$ precipitates. This was recently implemented in the multi-precipitate CDM model developed by Christopher and Choudhary (2019) in modelling long-term creep of Grade 91 steel. Besides thermal induced coarsening, straining has also been shown to accelerate the growth kinetics of precipitates. A strain component is included in a particle damage evolution law by Murchú, *et al*. (2017), who revealed that such an approach does not improve parameter correlation in short-term tests but does become significant when considering creep strain contributions across weld regions (Murchú *et al.*, 2019). Instead, the need for subgrain damage evolution was identified.

Oruganti *et al.* (2011) focused on essential microstructural factors that contribute to creep degradation in CDM modelling of 9 – 10 % Cr steels, including subgrain and particle coarsening. One of the overarching benefits of this model is the reduction in the number of fitted parameters to 12, of which 9 are physically bounded. Even more parameters can be combined under certain testing conditions such as for isothermal testing. Furthermore, this work was one of the first efforts to directly model subgrain growth as a damage parameter which is considered vital to X20 modelling due to the sensitivity of this parameter to aging through service exposure (Aghajani *et al.*, 2009; van Rooyen *et al.*, 2019a).

Literature is currently sparse in terms of the application of CDM to service-exposed power alloys. Dyson and Osgerby (1993) and later McLean and Dyson (2002) applied CDM models to service-exposed 1Cr0.5Mo steel through adjustment to two non-damage parameters. More recently, efforts have been made to capture elements of creep degradation of P9 steel subjected to different heat treatments through the comparison of fitted microstructural rate constants (Christopher & Choudhary, 2018). Little attempt has been made to date, however, to explore how damage parameters vary between undamaged and service-aged material.

The most prominent reason for this lack of exploration is the large material requirement for datasets to input to CDM models as different stress or temperature states are necessary for curve fitting and there is often large scatter associated with creep datasets (Dyson, 2000; Yin & Faulkner, 2006). Service-exposed steel is often in limited supply and can only be removed in small sections from repaired components during planned station maintenance periods (Gupta *et al.*, 2015). Measuring multiple creep curves at several temperatures and stresses using conventional creep rigs typically requires multiple specimens and substantial amounts of material, making the CDM approach less feasible for modelling ex-service steels. There has been little attempt to interface CDM with modern image correlation methods that presently lie at the heart of full-field experimental mechanics, let alone the application to service-exposed power engineering alloys.

Digital image correlation (DIC) has seen vast applications in the past decade in the field of material characterisation. In contrast to conventional deformation measurement solutions such as extensometers, DIC allows full-field measurement of displacement by spatially tracking unique speckle features within subset windows discretised from sequential digital images (Schreier *et al.*, 2009). Previously, the authors' have developed a technique for obtaining multiple tensile (van Rooyen & Becker, 2018) and creep (van Rooyen *et al.*, 2019a) curves at different temperatures from single specimens of ex-service X20 using DIC and spatially varying thermal fields generated by resistance heating. Sakanashi *et al*. (2017) measured long-term creep curve development across the complex microstructural zones of welded stainless steels from single test pieces within a conventional creep testing rig interfaced with DIC. The high spatial density of deformation measurement points obtainable through DIC satisfies the material economy required by mechanical testing of ex-service X20.

This work aims to use a novel specimen design in combination with 2D DIC (DIC using a single camera) to measure multiple creep curves from single specimens of ex-service X20 material for damage parameter extraction. The paper begins with a description of this experimental procedure that involves a waisted specimen geometry (Muyupa *et al.*, 2017) to develop a spatially varying stress profile across the specimen gauge length. Load and heat are applied using a weighted lever arm mechanism and three-zone tube furnace within a traditional creep setup, whilst deformation is tracked using a single digital camera through a furnace viewing window. The resulting creep curves are supplied to a CDM model adapted from Oruganti *et al.* (2011) in order to calibrate baseline parameters from virgin material and consequently extract initial-state damage parameters from ex-service X20. A comparative assessment of the fitted parameters between material states is coupled with microstructural analysis to confirm the damage levels of the tested ex-service X20.

7.2 Experimental procedures

7.2.1 Materials and specimen design

The material selected for this work is virgin and service-exposed X20 steel supplied in the form of 34 mm thickness piping offcuts from a local power utility. Conventional damage assessment involving cavity counting through surface replication was employed to categorise the ex-service X20 with various levels of service exposure. High damage X20 has the highest cavity density (200 – 700 cavities/mm^2) with an approximate service time of 18 years at 543 °C operating temperature and 18.1 MPa operating pressure. Medium (200 cavities/mm^2) and low (60 – 90 cavities/mm^2) X20 have been in operation for 15 years at 545 °C at 19.4 MPa and 17 MPa, respectively. Further details regarding the chemical composition of materials are

provided in van Rooyen *et al.* (2019a). In the interest of brevity, the as-received and service-exposed materials will be referred to as virgin and low, medium and high damage X20, respectively, with their severity of damage directly linked to their cavity counts.

A schematic of the waisted specimen dimensions (in mm) is provided in Figure 7.1a and the location of the sample extraction (using wire cutting) relative to the piping geometry is shown in Figure 7.1b. The reference coordinate system illustrated in Figure 7.1a is used in the remainder of this work, with the y direction aligning with the loading direction and x direction corresponding to the width dimension.

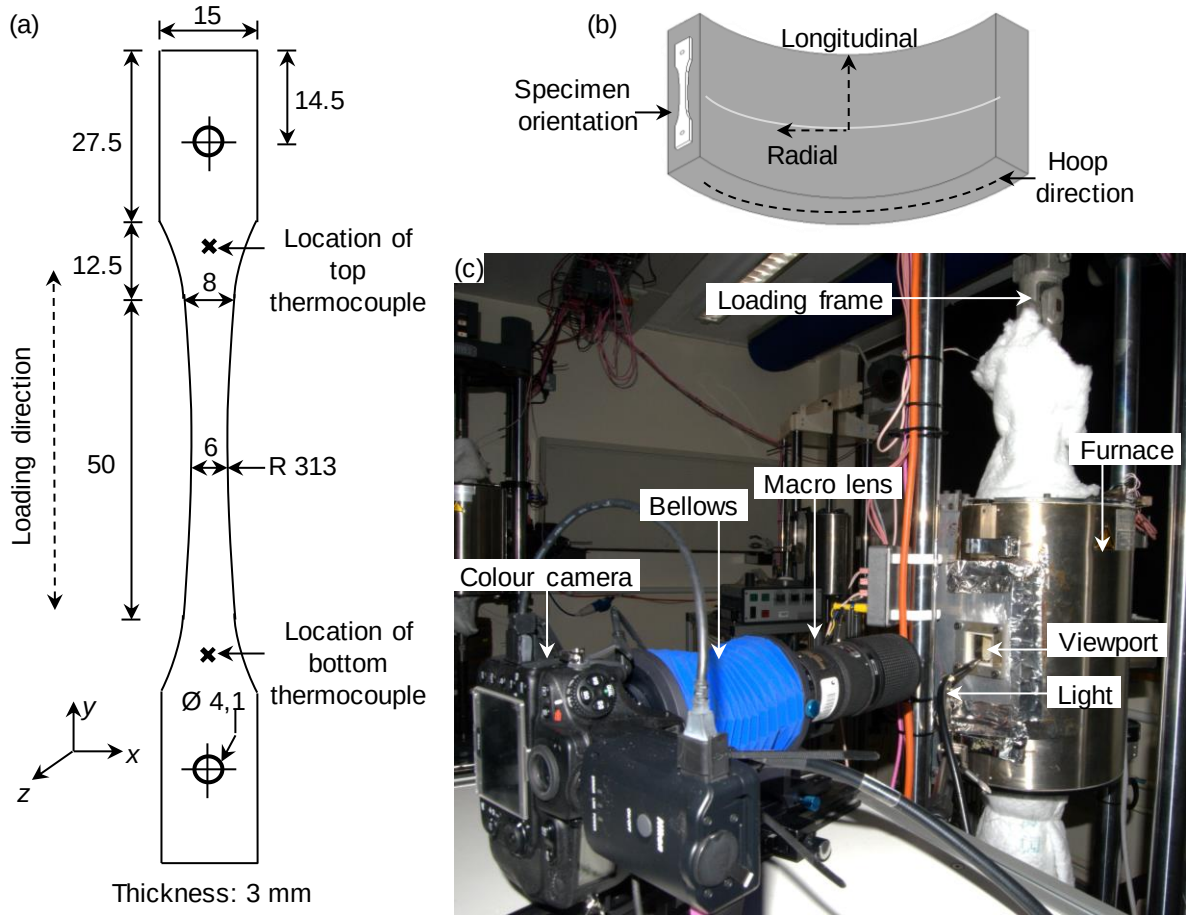

Figure 7.1: (a) Waisted specimen geometry and (b) the orientation of extracted specimen with respect to pipe section geometry. The camera setup relative to the creep testing rig is shown in (c). All dimensions are supplied in mm. The chosen coordinate system is shown in (a)

7.2.2 Digital image correlation creep testing setup

A photograph illustrating the main components of the setup is shown in Figure 7.1c, including the DIC hardware components summarised in Table 7.1. Briefly, a Nikon D810 digital single-lens reflex (DSLR) colour camera with a complementary metal oxide semiconductor (CMOS) sensor is placed approximately 250 mm in front of the specimen which is located within a three-zone furnace (Severn Thermal Solutions) modified to include a high optical quality sapphire viewing window with an approximate width of 20 mm and height of 40 mm. The perimeter of

the viewport is sealed to diminish the effects of heat haze currents in the distortion of the DIC images. A Nikon Nikkor 200 mm micro f4 IF-ED macro lens is fitted to a Novoflex Ballpro bellows mounted with a 100 mm extension to increase magnification and close-focus capabilities at the required working distance. The specimen, which is loaded within the furnace by a standard 10:1 lever arm loading frame, is illuminated by a single 1/4-inch diameter fibre optic light triggered by the built-in flash of the camera manually set to fire at its maximum illumination setting.

Table 7.1: Hardware details for DIC setup

Camera	Nikon D810 DSLR colour camera
Image resolution	4912 × 7360 pixels^2
Lens	Nikon AF micro-Nikkor 200 mm f4 IF-ED macro lens
Aperture	f/16
Field of view	27 × 40 mm^2
Magnification factor	184 pixels/mm
Stand-off distance	250 mm
Image acquisition rate	1 every 5 – 10 min
Patterning technique	White VHT heat-resistant base coat with corresponding black speckles applied via spray can. Furnace-cured according to manufacturer's instructions*
Pattern feature size (range)	8 – 14 pixels (0.04 – 0.08 mm)

*Refer to Subsection 7.2.4: Image correlation processing

Heating was performed in air and temperature was measured by two N-type thermocouples placed outside the 50 mm gauge region of the specimen as shown in Figure 7.1a. Specimen temperature was controlled through manual adjustment of the setpoints of the three zones of the furnace. The difference between the two thermocouples was maintained within 2 °C after about a 24 h saturation time according to the ASTM E139 (ASTM, 2011a) standard for creep testing. Following this, load was applied through gradual weight loading until a calibrated mass is reached (within ± 0.1 kg) and a constant load was maintained. The load was chosen in order to generate the desired maximum stress at the specimen centre. This maximum stress is quoted to differentiate between tests with different loads. Depending on the anticipated test duration, images were captured once every 5 min or 10 min. Further details regarding the setup can be found in Sakanashi *et al.* (2017). Conventional creep testing was conducted as outlined in van Rooyen *et al.* (2020).

7.2.3 Stress determination

The 50 mm gauge region of the specimen is an hourglass shape with a large curvature allowing width variation from 6 mm at the centre to 8 mm symmetrically at 25 mm (effective gauge length). For the initial stress distribution analysis, a linear-elastic finite element (FE) analysis was performed using the ABAQUS ver. 2017 software. A symmetric model (about the x axis) was constructed from 6 080 linear hexahedron (C3D8) elements meshed to have a higher density near the high stress region at the gauge centre. Young's modulus, Poisson's ratio and thermal expansion coefficients at 600 °C were obtained from Straub (1995). A constant temperature field was applied across the model (simulated as the region between the thermocouple and gauge centre) whilst a load is applied in the form of a uniform pressure at the largest width near the grip of the specimen that is equivalent to the load applied in the creep testing rig. Figure 7.2a shows the resulting y-direction stress, σ_y, distribution.

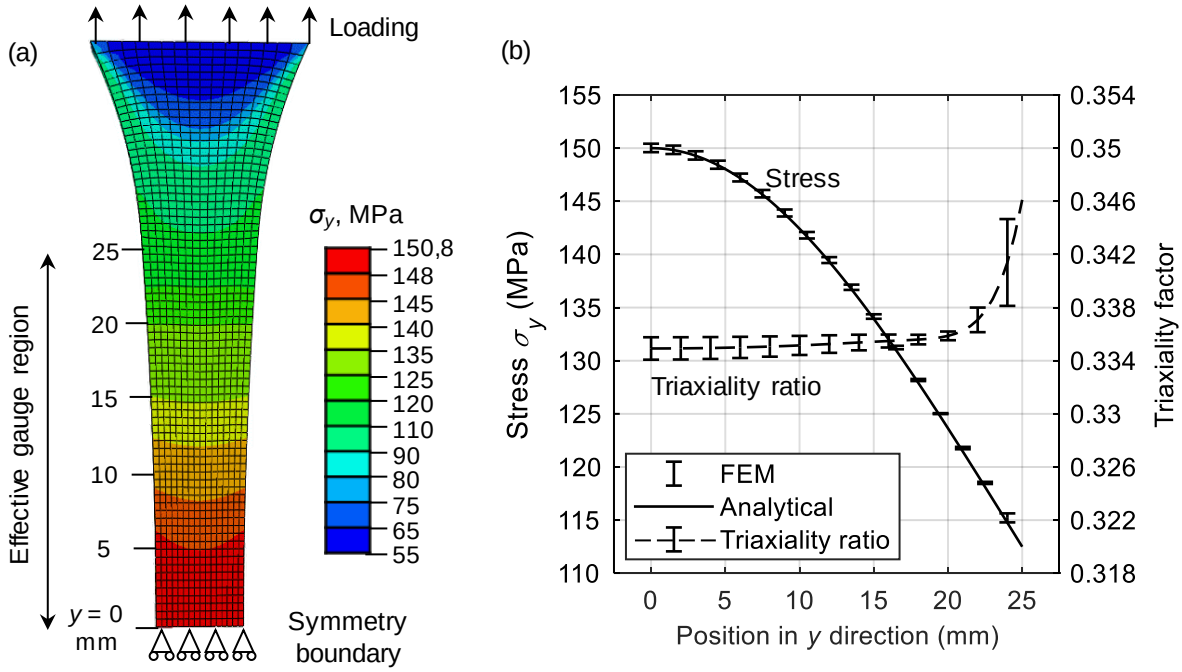

Figure 7.2: (a) Symmetrical FE model of waisted specimen geometry showing the distribution of y-direction stress in the x-y plane during initial loading. (b) Variation across the half the gauge length of y-direction stress averaged across the specimen width along with the analytical predictions and triaxiality factors

The analytical representation of the y-direction stress σ_{ya} in MPa is provided as:

$$\sigma_{ya} = \frac{F}{2t_z\left(0.5w_i + R_c - \sqrt{R_c^2 - y^2}\right)} \tag{7.1}$$

where y is the vertical distance from the thinnest width w_i = 6 mm at y = 0 mm, R_c = 313 mm is the curvature radius of the hourglass shape, t_z = 3 mm is the specimen thickness and F is the applied force in N. FE-calculated stress is in good agreement (within 0.5 %) with the stress based on Equation (7.1) as shown in Figure 7.2b, despite the lack of consideration for thermal expansion on the original dimensions of the specimen. This is evident from the slight

(< 0.1 mm) shift of the FEM stresses to the right of the analytical curve. An assessment of the triaxiality factor (ratio of hydrostatic stress to von Mises equivalent stress) as shown in Figure 7.2b indicates that a uniaxial stress state with an ideal factor of 0.33 is approached within the gauge region with a slight increase encountered at $y \geq 15$ mm adjacent to the sharper radius of the grip region. For this reason, the vertical dimension of the ROI selected for DIC processing is -15 mm $\leq y \leq$ 15 mm centred about the minimum width (or maximum stress) position.

7.2.4 Image correlation processing

The images from the colour camera require a demosaicing technique to convert the Bayer colour filter arrays into a monochromatic equivalent suitable for correlation algorithms. Forsey and Gungor (2016) proposed a bilinear polynomial and bicubic spline interpolation demosaicing algorithm and demonstrated similar accuracy and aliasing to monochromatic images using the same cameras as employed in this study. MATLAB R2019a was employed to implement the demosaicing methods to convert raw files generated by the camera (.NEF) into 16-bit, uncompressed, tagged image file formats (.TIFF) which were supplied to the LaVision DaVis 8.4 software for DIC processing.

Self-comparison tests in which images are taken of a stationary speckle pattern and compared was performed to assess a suitable demosaicing algorithm and subset size for this study. These images were taken after temperature saturation at 600 °C prior to loading and are not subjected to any post-processing steps so as not to mask any differences between the demosaicing procedures. The bilinear and bicubic interpolation algorithms are compared in Figure 7.3a and b in terms of mean (vertical) displacement error and standard deviation from a zero-displacement situation, respectively. This was done across several subset sizes each with a step size of 10 pixels. Bias from the zero-displacement measurement (Figure 7.3a) decreases with an increase in subset size (Schreier *et al.*, 2009). This is due to the larger subsets acting as low-pass filters that minimise spatially varying displacement errors resulting from heat haze effects (Jones & Iadicola, 2018; Jones & Reu, 2018). At subset sizes ≥ 101 pixels or 0.54 mm, the correlation windows overlap the spatial frequency of the heat haze errors, leading to an enhanced smoothing effect.

Only about a 0.01 μm increase in accuracy is noted for the bicubic method over the bilinear version whereas a small (< 0.005 μm) improvement in standard deviations of displacements is noted for the bilinear method. Based on this analysis and the recent work of Baldi (2018) who found algorithms with a smaller spatial span to produce lower variance errors in displacements, the computationally faster bilinear interpolation algorithm was selected for subsequent processing. A subset size of 61 pixels was selected as it will result in similar accuracy and variance to larger subsets but with better spatial resolution as noted from Figure 7.3a and b.

A speckle pattern was applied to the specimen surface consisting of a basecoat of heat-resistant white VHT Flameproof paint followed by a black VHT speckle application via a spray can. After 3 h of drying, the specimen was cured at 121 °C for 30 min followed by cooling for 30 min, which was subsequently repeated at 204 °C and 343 °C. Sakanashi *et al.* (2017) demonstrated the durability of this pattern application technique during creep testing at 545 °C for over 2 000 h. The average speckle measured using ImageJ (Johannes *et al.*, 2012) ranged from 8 – 14 pixels which allowed for a minimum of three speckle features per subset size for an assumed 50 % feature density as recommended by iDICs (Jones & Iadicola, 2018). By overlaying a grid of 61 × 61 pixel^2 squares onto a typical speckle pattern in Figure 7.3c, it is evident that each independent subset contains a suitable distribution of speckles.

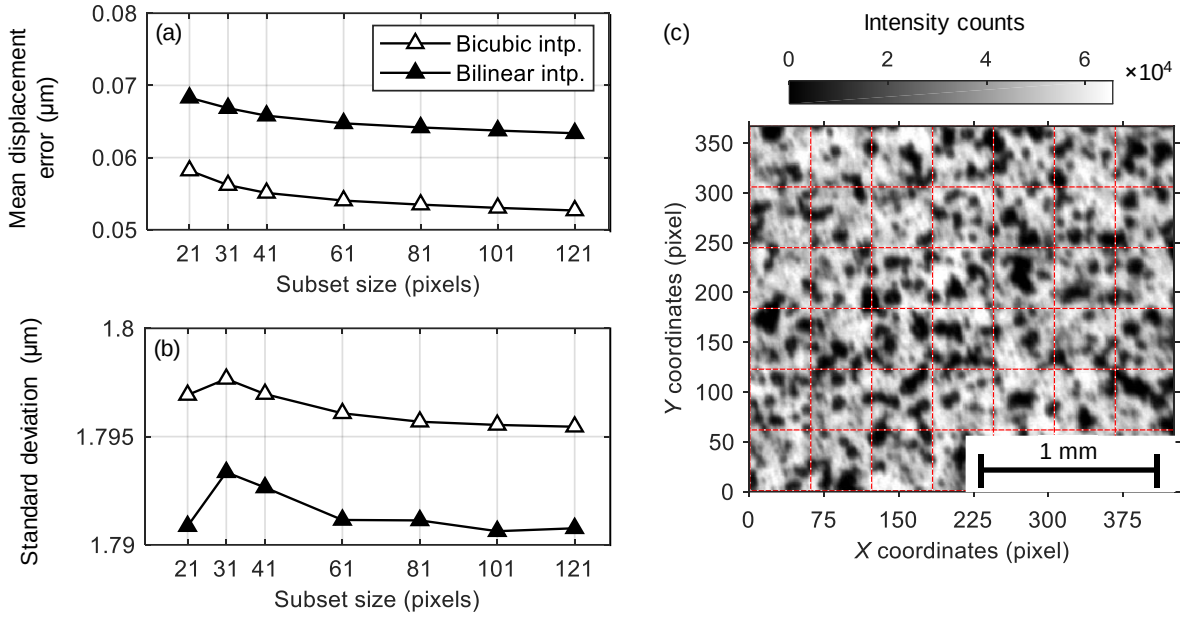

Figure 7.3: Variation of (a) mean displacement error and (b) standard deviation with subset size for bicubic and bilinear demosaicing methods. (c) Typical speckle pattern overlaid with chosen window size

7.2.5 Displacement and strain calculation

Following the colour-to-monochrome image conversion using the bilinear demosaicing algorithm, images from the creep tests were processed using LaVision DaVis 8.4 by setting the starting (reference) image to occur after temperature saturation and loading. This ensures that only creep strains are included in the analysis. Correlation was performed using a subset size of 61×61 pixels^2 and a step size of 10 pixels. Additional DIC calculation parameters are provided in Table 7.2.

Following the procedure of Sakanashi *et al.* (2017), strains were derived from the DIC displacements using a piecewise bilinear polynomial least-squares fit with window sizes spanning the specimen width (excluding 0.5 mm from the edges) and 11 data points in the y direction. Heat haze effects are noted from the horizontal, vertical and checkered pattern bands in the ε_x, ε_y and ε_{xy} strain fields, respectively, in Figure 7.4a. To eliminate these effects spatially, a low-pass filter with a normalised passband frequency of 0.01 (as identified by fast-fourier transform analysis) is applied to the strain fields, as shown in Figure 7.4b. Creep strain-time curves are obtained along the gauge length of the specimen by averaging the ε_y values across the width of the ROI at each y position for each image. Temporal noise evident in the creep strain-time curves affects strain rate calculations and was addressed by smoothing through a moving average based on a Savitzky-Golay filter with a quadratic polynomial fit over a window of 30 points.

Under the assumption of an isotropic Poisson's ratio, the strains through the thickness ε_z are set equal to ε_x strains averaged across the specimen width and thereby the instantaneous cross-sectional area and true stress field can be calculated along the gauge length.

Table 7.2: DIC analysis parameters

Software	LaVision DaVis 8.4
Image filtering	Bilinear demosaicing algorithm (Sakanashi *et al.*, 2017)
Subset size	61 pixels (0.33 mm)
Step size	10 pixels (0.054 mm)
Subset shape function	Affine
Matching criterion	Zero-normalized sum of squared differences (ZNSSD)
Interpolant	Sixth-order spline
Region of interest (ROI)	5 × 30 ($x \times y$) mm^2 centred about smallest width
Strain window	11 data points
Virtual strain gauge size	161 pixels (0.88 mm)
Strain derivation	Derivative of piecewise bilinear fit to displacements (Sakanashi *et al.*, 2017)
Post-filtering of strains	Spatial low-pass filter, temporal moving-average spanning 30 points (2.5 – 5 h depending on test length)
Displacement noise floor (y direction)	Spatial: 1.79 μm (0.33 pixels), Temporal: 0.80 μm (0.14 pixels)
Strain noise floor	ε_y: 122 (spatial), 142 (temporal) μm/m ε_x: 429 (spatial), 1216 (temporal) μm/m

7.2.6 Microstructural study and hardness measurements

Considering that different damage mechanisms can result in the same creep curve shape in the context of CDM (Dyson & McLean, 1998), microstructural characterisation was done in order to identify the evolution of core parameters investigated in the Oruganti *et al.* (2011) model as well as the potential for inclusion of other damage mechanism parameters (such as cavities). A detailed description of the pre-test microstructure of the virgin and ex-service X20 employed in this study is supplied elsewhere (van Rooyen *et al.*, 2019b, 2020). Post-test microstructural analysis was performed in order to characterise the effect of testing on subgrain sizes, precipitate and cavity distributions in the gauge and grip regions. Specimens were polished to a 0.25 μm colloidal silica surface finish. A Zeiss MERLIN field emission gun scanning electron microscope (SEM) operating in mixed backscattered electron (BSE) and secondary electron mode (with the former comprising 80 % of the signal) was used to observe cavity distributions using an accelerating voltage of 20 kV, probe current of 11 nA and a working distance of 9.5 mm. The signal mixing allowed cavities to be distinguished from darker precipitates based on the preferred expulsion of secondary electrons from the cavity edges (edge effect)

(Yadav *et al.*, 2015). ImageJ software was used to quantify density and size distributions of cavities larger than 1 µm in diameter at a ×500 magnification. Subgrain short widths were measured using the line intercept method (Aghajani *et al.*, 2009) on ×4000 SEM images. Approximately 20 line intercepts were made using ImageJ for each location.

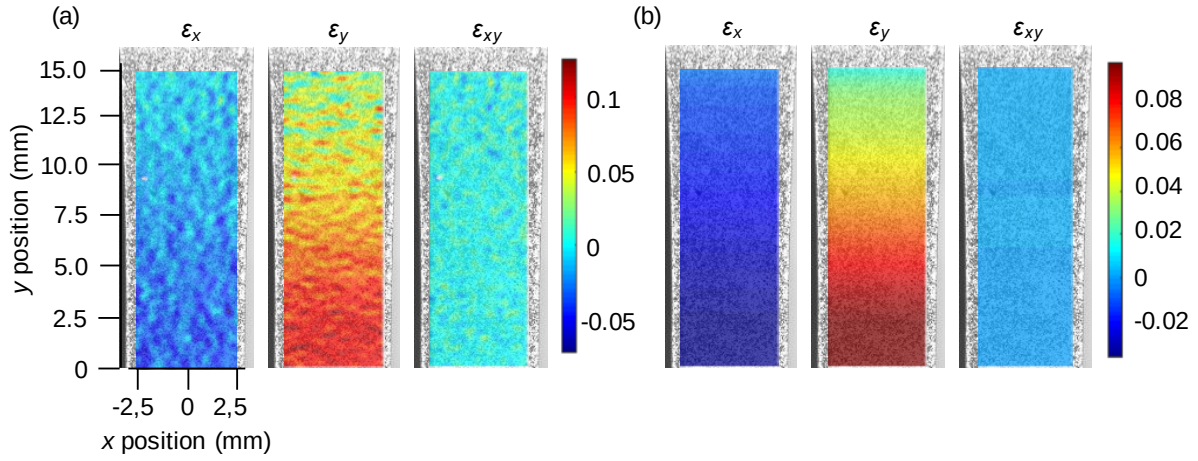

Figure 7.4: Evidence of the (a) spatial effects of heat haze on strains which are (b) removed using a low-pass filter

Following this, the samples were electropolished using a Struers Lectropol-5 at 20 V, 20 °C and a 5 % perchloric acid solution to produce a surface suitable for precipitate analysis using a JEOL JSM-7001F Schottky emission SEM using settings of 5 kV accelerating voltage, 4 nA probe current and 10 mm working distance. This detector allows different precipitates to be distinguished based on differences in image brightness proportional to the respective atomic weight of the constituent particle elements (Marx, 2019). The advanced image processing software MIPAR version 3.0 (Sosa *et al.*, 2014) was utilised to quantify the different precipitate morphologies based on a thresholding routine. Further details pertaining to the microstructural analysis can be found in van Rooyen *et al.* (2019a).

Vickers hardness measurements were made on the mechanically polished gauge regions along the loading direction as well as in the grip regions using a Buehler MicroMet 6030 tester with a 1 kg load and 10 s holding time.

7.3 Model formulation

The creep model employed in this work is based on the CDM formulation developed by Oruganti *et al.* (2011). This selection was made on the basis of simplicity and the inclusion of key microstructural parameters (subgrains and precipitates) relevant to the creep strength of X20 (van Rooyen *et al.*, 2019a).

7.3.1 Basic equations

The CDM model employed is represented by the collection of coupled differential equations below.

$$\dot{\varepsilon} = \varepsilon_0' \exp\frac{-Q}{RT} \sinh\left(\frac{\sigma(1 - H^*(1 - D_S))}{\sigma_{ro}(1 - D_P)(1 - D_c)}\right) \tag{7.2}$$

$$\dot{\sigma}_{ro} = K_1\left(1 - \frac{\sigma_{ro}}{K_2}\right)\dot{\varepsilon} \tag{7.3}$$

$$\dot{D}_S = \frac{\dot{\varepsilon}(1 - D_S)^2}{S_i}\left(K_{S1} + K_{S2}\exp\left(\frac{-Q_S}{RT}\right)\right) \tag{7.4}$$

$$\dot{D}_P = \frac{(1 - D_P)^4}{P_i^3}\left(K_P \exp\left(\frac{-Q_P}{RT}\right)\right) \tag{7.5}$$

$$\dot{D}_C = \frac{k_N}{\varepsilon_r}\dot{\varepsilon} \tag{7.6}$$

$$\dot{\sigma} = \sigma\dot{\varepsilon} \tag{7.7}$$

The fundamental creep law in Equation (7.2) relates the creep strain rate $\dot{\varepsilon}$ to stress σ and temperature T by tracking the evolution of the state variables including the reference stress σ_{ro}, the subgrain D_S and precipitate D_P damage parameters shown in Equations (7.3–7.5), respectively. For modelling constant-load creep curves, the stress rate Equation (7.7) must be coupled with the preceding model equations.

The characteristic creep constant ε_0' is a scaling parameter which mainly affects the modelled minimum creep rate and depends on the initial dislocation density, subgrain and precipitate volume fraction (Semba *et al.*, 2008) as well as matrix solute diffusivity of Mo (Kadoya *et al.*, 1997). This constant is associated with the Arrhenius relation $\varepsilon_0' \exp\frac{-Q}{RT}$ where R is the universal gas constant and Q is the creep activation energy. The reference stress σ_{ro} is a measure of the strengthening mechanisms offered by dislocation-particle interactions and, in many CDM formulations, is treated as a constant related to the Orowan particle bypass stress.

Primary creep is represented by an evolution of σ_{ro} in Equation (7.3) which phenomenologically models the evolution of dislocation structures to be in equilibrium with the applied stress until a steady value of K_2 is reached at a rate of K_1. This differs from other CDM models that represent the primary hardening through evolution of the normalised kinematic backstress H as the stress redistributes between the soft steel matrix and hard precipitates (Ion *et al.*, 1986). In the Oruganti model, the maximum value of normalised kinematic backstress H^* is fixed at a constant value that depends on the initial subgrain S_i and high-angle block B_i widths (Oruganti *et al.*, 2011; Xiao *et al.*, 2019):

$$H^* = 0.26\,(1 - \nu)\frac{\lambda_{M23C6}^{4/3}\theta^{1/3}}{b^{1/3}S_i} + \frac{K''}{\sqrt{B_i}} \tag{7.8}$$

where ν is the Poisson's ratio, λ_{M23C6} is the average spacing of $M_{23}C_6$ precipitates, θ is the average subgrain misorientation in radians, b is the Burgers vector magnitude (= 2.48×10^{-10} m for body-centred phases (Callister, 2007)), and K'' is a constant.

7.3.2 Damage parameters

The tertiary regime is modelled through the damage parameters and their evolutionary equations. The subgrain coarsening damage parameter is given as:

$$D_S = 1 - \frac{S_i}{S} \tag{7.9}$$

where S is the subgrain short width at a point in time. Equation (7.4) gives the rate equation for D_S where $K_{S1}$and K_{S2} are the strain and thermally activated components, respectively, of subgrain coarsening and Q_s is the associated activation energy. The weakening effect of the migration of subgrain boundaries is modelled through the decrease of the backstress parameter H^* by multiplication of $(1 - D_S)$ in Equation (7.2).

The damage term related to precipitate coarsening is a function of the initial particle diameter P_i and final particle diameter P:

$$D_P = 1 - \frac{P_i}{P} \tag{7.10}$$

The Ostwald ripening law based on volume diffusion control (Yadav, Sonderegger, *et al.*, 2016) leads to the rate equation of D_P in Equation (7.5) where Q_P and K_P refer to the particle growth activation energy and pre-exponent constant, respectively. Previous research underlined the importance of $M_{23}C_6$ carbides in maintaining the creep strength of X20 by hindering subgrain boundary migration, highlighting the need to include the relevant coarsening parameters in the damage modelling of such materials (Aghajani *et al.*, 2009; van Rooyen *et al.*, 2019a)

Besides microstructural deterioration parameters, physical damage in the form of creep cavitation has long been reported for X20 particularly at low stresses (Trück *et al.*, 1991; Parker & Siefert, 2018), leading to consumed life estimation of in-service components based on cavity density measurements from replica metallography (van Zyl *et al.*, 2005). Based on this line of thinking, a creep-constrained cavity nucleation-controlled damage parameter D_C is added to the Oruganti model in Equation (7.2). Dyson (2000) proposed a linear relationship between D_C and strain, resulting in the rate Equation (7.6) where ε_r is the failure strain and k_N is a parameter approximately related to the area of cavitated boundaries before failure and has a maximum value of 1/3 (McLean & Dyson, 2002). The relationship of D_C with cavity densities of N_c and diameters d_c is given as (Wu & Sandström, 1995; Dyson & McLean, 1998):

$$D_C = \frac{\pi {d_c}^2 N_c}{4} \tag{7.11}$$

In reality, both void growth and cavitation takes place (as noted in the gauge regions in Figure 7.9), requiring combined creep constrained cavity growth and growth-constrained cavity nucleation damage equations that prove to be complex when defining for high stresses within the transgranular fracture regime (Perrin & Hayhurst, 1996; Dyson & McLean, 1998; Lin *et al.*, 2005). For the sake of simplicity in the optimisation routine, Equations (7.6) and (7.11) are employed to simulate cavity damage.

7.4 Experimental results

7.4.1 Validation of strain measurements

Two methods were employed to confirm the validity of the DIC measurements. The first method aims to demonstrate the fidelity of the strain measurement with respect to symmetrical positions and hence stresses about the maximum stress condition at $y = 0$ mm. This is demonstrated in the error bar plot of creep curves in Figure 7.5a for new X20 at a 150 MPa maximum stress and 600 °C at several positions (correlated with engineering stresses σ_y) along the gauge length. There is good agreement between the symmetrically located creep curves although a more robust comparison is made between the creep rates at the symmetric locations as shown in Figure 7.5b, indicating scatter in the order of 10^{-8}/s at stresses lower than 140 MPa. At lower strains and rates, measurements become more susceptible to baseline error and heat haze effects. This is also evident in the true stress σ_{yt} variation shown in Figure 7.5c due to the dependence on ε_x which is subject to higher errors (Table 7.2). The rate of longitudinal true stress evolution is calculated in Figure 7.5d from the constant volume assumption $\dot{\sigma}_{yt} = \sigma_{yt}\dot{\varepsilon}$ (as considered in Equation (7.7)) which is applied in constant-load damage mechanics prior to tertiary necking (Christopher & Choudhary, 2019).

Secondly, DIC creep strains are compared with strains measured using traditional linear variable differential transducers (LVDTs) during conventional creep testing at a single temperature and stress. Creep curves at the stress corresponding to the nominal stress applied in the conventional setup were obtained by linearly interpolating the DIC strain fields at y positions that were correlated with the location of the required stress in the FEM model. Comparisons between both virgin and high damage X20 conventional and DIC creep tests for stresses at off-centre and central locations within the DIC specimen gauge region is presented in Figure 7.6. In general, higher creep rates and shorter rupture times are noted for the ex-service X20 than the virgin material as shown through comparisons between Figure 7.6d and e. At 110 MPa (Figure 7.6f), high damage X20 demonstrates similar creep resistance to the virgin counterpart at 140 MPa (Figure 7.6e).

DIC and LVDT strain measurements correlate well (< 10 %) within the primary and secondary regimes. At off-centre stresses, however, DIC strains accelerate into the tertiary regime earlier than for the conventional tests as necking is regulated by the highest stress condition at the specimen centre. For this reason, tertiary regimes show better alignment when comparing DIC strains measured at stresses at the gauge centre with conventional tests at the corresponding stresses. A relatively small difference in failure times is noted in Figure 7.6c and f. This is attributed to sample-to-sample microstructural variability (Yin & Faulkner, 2006) and/or the accelerated necking caused by stress concentrations at the smallest width location of the DIC test specimens. However, it is not possible to rule out this being an effect of the measurement process.

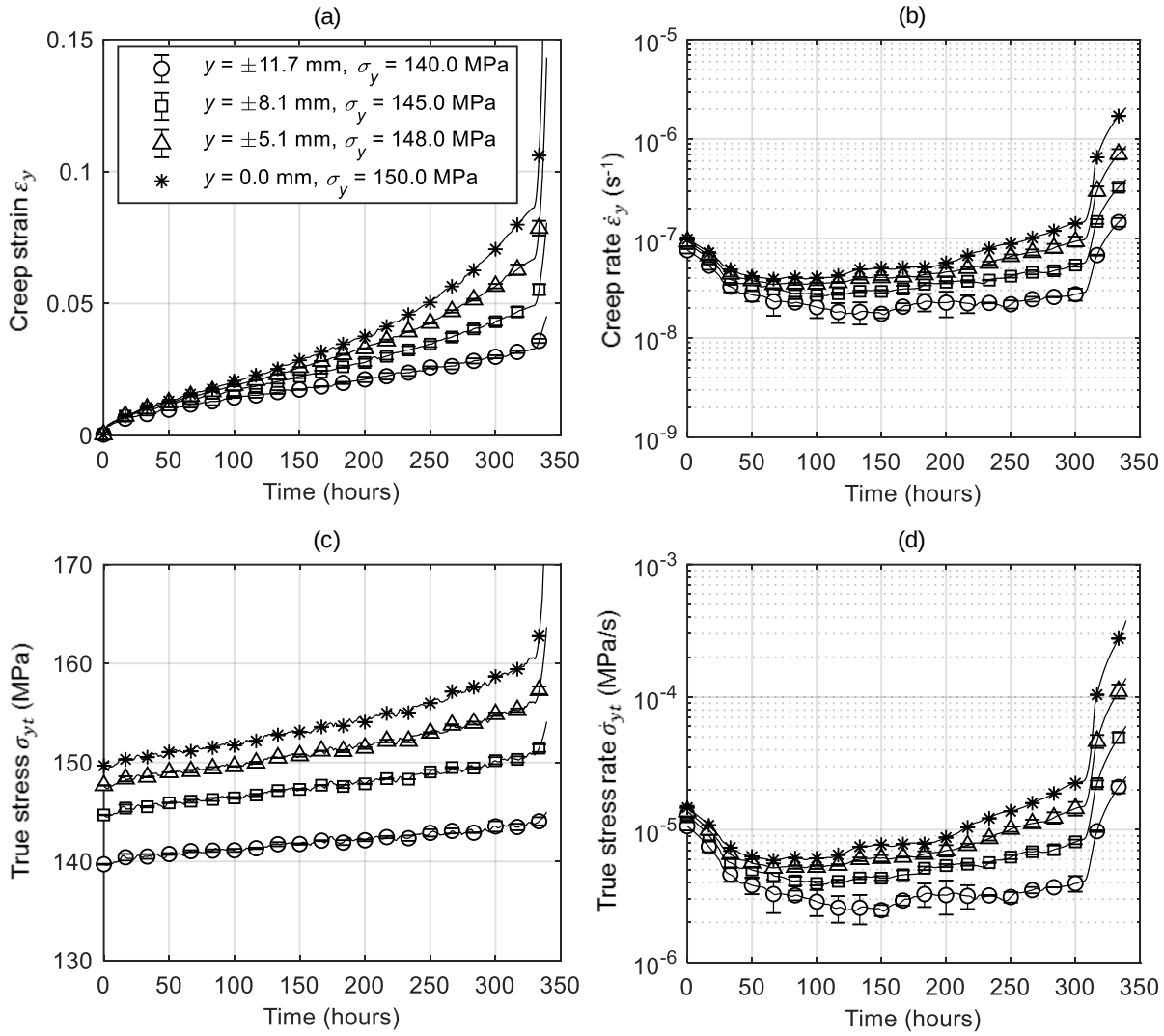

Figure 7.5: Plot of (a) creep curves, (b) creep rates, (c) true stresses and (d) true stress rates over time at several symmetrical positions (stresses) for virgin X20 at 600 °C

7.4.2 Microstructural and hardness development

The BSE-SEM images in Figure 7.7 show examples of subgrain and precipitate differences between virgin (a,b) and high damage X20 (c,d) grip and gauge (near fracture at the smallest width) regions, respectively, of specimens tested at 150 MPa and 600 °C. All specimens fractured at the smallest width of the waisted geometry. Typical $M_{23}C_6$ particle clusters and Laves phase precipitates are highlighted in Figure 7.7a and d, respectively. Quantitative comparisons of subgrain short widths and precipitate diameters at three approximate distances from the ruptured end (0 mm, 5 mm and 10 mm) within the gauge and grip regions for virgin material and low, medium and high damage X20 is shown in Figure 7.7e and f, respectively.

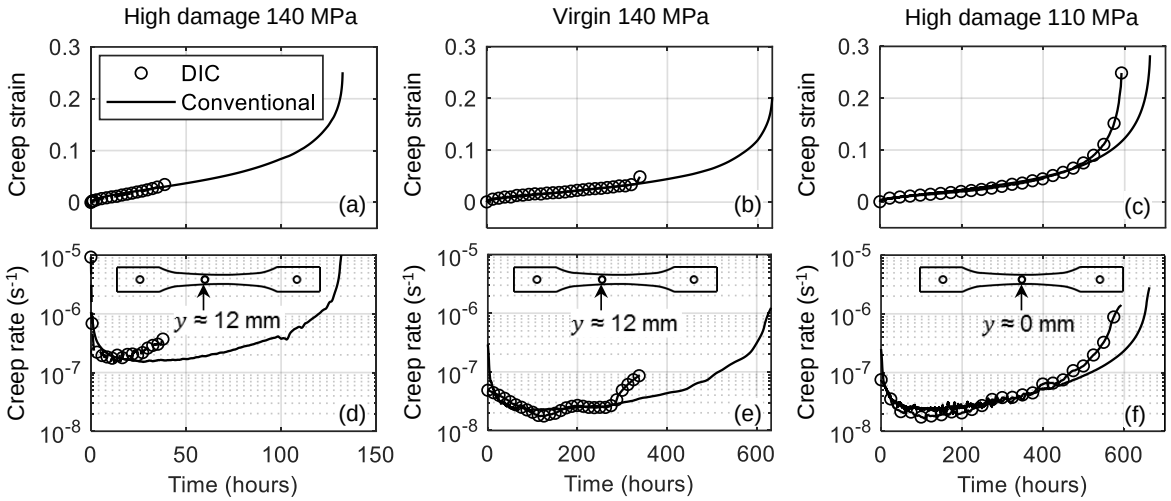

Figure 7.6: (a-c) Creep strain and (d-f) rate curves for virgin and high damage X20 at 600 °C comparing DIC measurements at (a-b, d-e) off-centre and (c,f) central stresses with measurements from LVDTs in a conventional creep test

It is necessary to note the differences between the pre-tested and post-tested (gauge and grip) material states in order to justify the damage evolution framework. This comparison is qualified through an unpaired *t*-test with a 0.05 significance value with statistically different values marked by arrows in Figure 7.7e and f. Subgrain growth is evident between the grip and gauge regions of all four material states, with the largest grains evident in the high damage material. Contrary to expectations, subgrain sizes similar to virgin X20 are observed in the medium damage X20 that are finer than the low damage analogue. It should also be noted that increased subgrain growth occurs at higher stresses closer to the smallest width of the specimen geometry (y = 0 mm in Figure 7.2). Larger $M_{23}C_6$ carbides are noted in the high damage material with a lower volume density (13.2 ± 1.2 μm^{-3} in the grip region) than in the virgin material (33.6 ± 3.0 μm^{-3}), suggesting particle growth during extended service times. Compared to the pre-test conditions, particle diameters are on average 18 % and 7 % larger in the gauge region for the virgin and high damage X20 tested at 150 MPa, respectively. Within microstructural scatter, however, it is conjectured that precipitate coarsening has a lower contribution to the damage evolution equations than subgrain growth especially for short duration tests (< 50 h for the high damage 150 MPa, 600 °C test). Furthermore, pre-tested high damage X20 displayed sparsely distributed (1.9 ± 0.5 μm^{-3}) Laves phase particles with diameters on the order of 0.2 – 0.3 μm. Following testing, there is no statistically significant growth or nucleation of Laves phase apart from the 5 mm gauge location which can be attributed to microstructural inhomogeneity evident from the large scatter in Laves diameters in Figure 7.7f. Trace amounts of small Laves phase particles were noted in the tested virgin material.

The relationship between hardness and longitudinal position along the gauge length of the tested specimens is depicted in Figure 7.8 with decreasing values measured for virgin, medium, low and high damage X20, respectively. It is clear that hardness decreases from the pre-tested values towards the higher stress regions near the ruptured end which correlates with the higher strains encountered within these regions (as seen in Figure 7.5a) that drive subgrain growth and precipitate evolution as demonstrated by Figure 7.7e and f, respectively (Endo *et al.*, 2003). Additionally, a greater softening effect is noted for a lower stress as shown in Figure 7.8 for the 110 MPa (max.) test compared to the 150 MPa (max.) test for the high damage material. This

subgrain-hardness correlation was proposed by Hino *et al.* (2013) to be an indicator of life-consumption ratio of laboratory-tested X20 steel with subsequent extensions to ex-service steels by Cardoso *et al*. (2015).

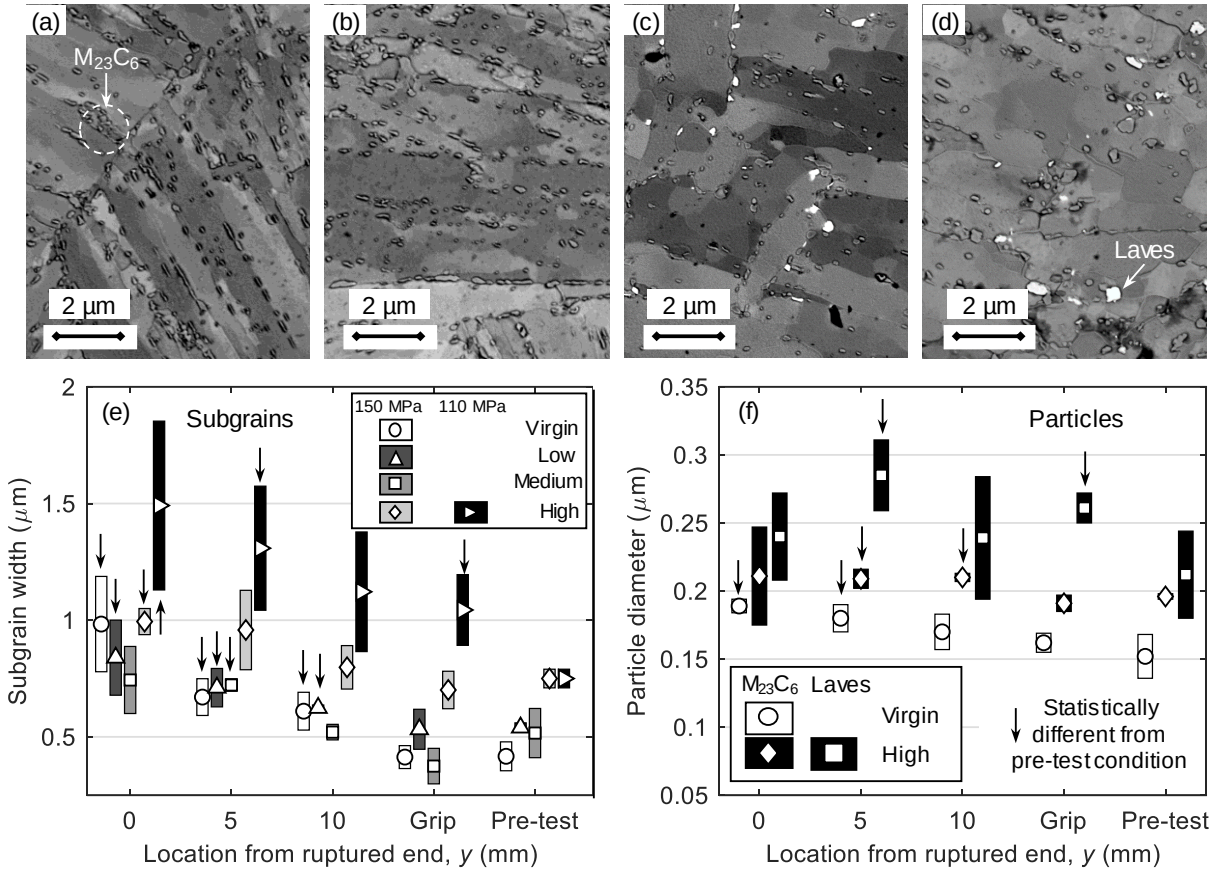

Figure 7.7: BSE-SEM images of (a,b) virgin and (c,d) high damage X20 grip and gauge regions, respectively, of specimens tested at 150 MPa and 110 MPa and 600 °C used to measure the average (e) subgrain width and (f) diameters of $M_{23}C_6$ and Laves phase particles at locations from the ruptured surface in the gauge and grip regions. Measurements that are statistically different from the pre-test condition are based on a 95 % confidence interval are indicated with arrows

Variation of cavity area densities over several longitudinal locations in the waisted specimens of virgin and high damage X20 is shown in Figure 7.9a. Note that in all cases there is an increase in cavity density towards the ruptured end (high stress) regions of the specimens. Interestingly, similar increases in densities are measured in the virgin and high damage X20 at 150 MPa (max.) despite the former test having fewer pre-test cavities and lasting almost 10 times longer (Figure 7.6a and b). This is possibly due to the linear dependence of cavity density on strain and the potential coalescence of existing voids in the high damage material that results in lower apparent cavity densities (Eggeler *et al.*, 1989). At lower stresses (at 110 MPa max.), the high damage X20 develops higher cavity densities towards the ruptured end with cavities that are on average 2 and 4 times larger in diameter than those within the 150 MPa (max.) virgin and high damage specimens, respectively, as shown in Figure 7.9b. This is in agreement with similar studies on 11 % Cr steels by Gupta *et al*. (2013) and suggests significant cavitation and cavity growth in the high damage, low stress test compared to the higher stress tests

(Parker & Siefert, 2018). However, it should be noted that freshly nucleated cavities have diameters in the order of < 1 μm (Yadav *et al.*, 2015) and so have been excluded from the current analysis. This is because both pre-existing and large creep cavities (> 1 μm) in the ex-service materials have been shown to be principle contributing factors to failure at the relatively high stresses employed in this study (Yadav *et al.*, 2015; Parker & Siefert, 2018).

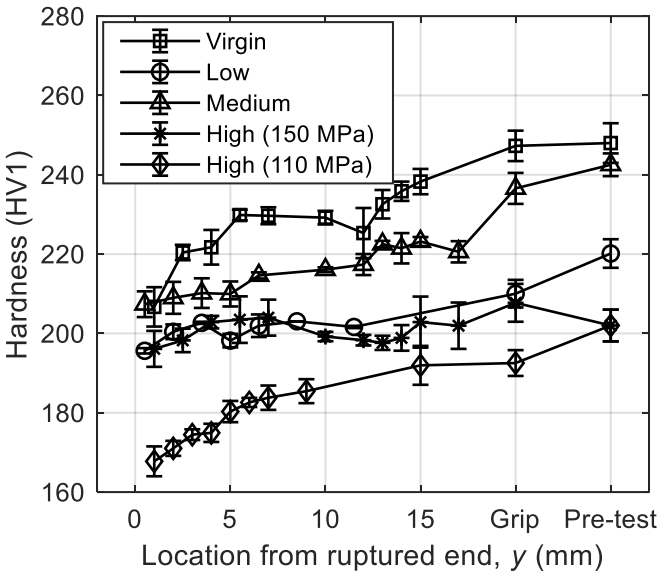

Figure 7.8: Hardness as a function of longitudinal distance from the ruptured end of the virgin and ex-service X20 waisted specimens

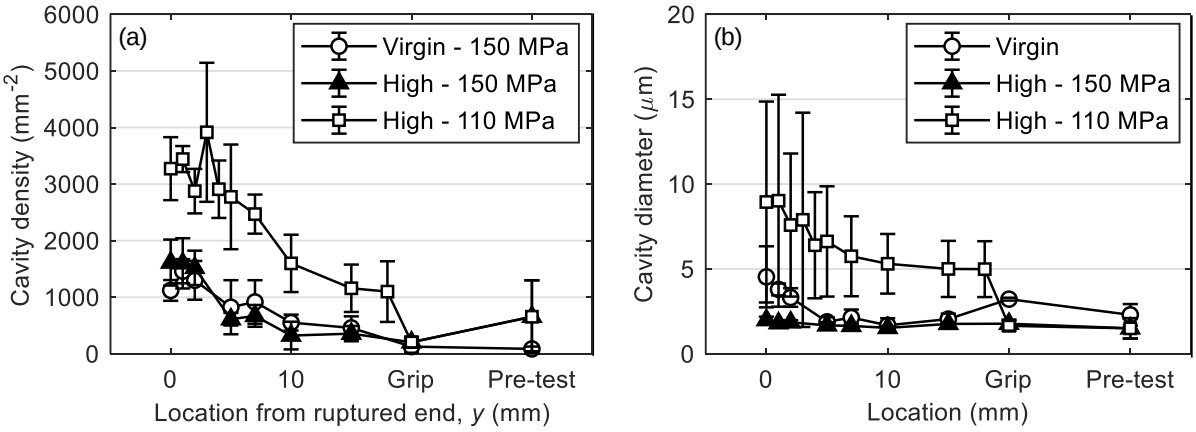

Figure 7.9: Plot of (a) cavity (diameter > 1 μm) density and (b) cavity diameter versus longitudinal distance from ruptured end of virgin and high damage X20 waisted specimens

7.4.3 Sources of input creep curves

Several sources of creep curves from various test types are employed in this work for input to the CDM models as summarised in Table 7.3. Data types are categorised according to their

durations and subdivided according to their methodologies. For the sake of brevity, a consistent naming convention is used for each data stream as indicated in Table 7.3.

Table 7.3: Summary of different test types for measuring creep curve data

Naming convention	Accelerated		Medium-term	
Duration; Stress range	< 10 h; High stress, > 200 MPa		24 – 1000 h; Intermediate stress, 100 – 150 MPa	
Subcategory	Variable temperature	Conventional	Variable stress	Conventional
Methodology	Several curves at several temperatures (575 – 600 °C) from single specimen using DIC and Gleeble	Single curve from single specimen at temperature and stress condition using ASTM E139 standard and LVDTs (ASTM, 2011a)	Several curves at several stresses (100 – 150 MPa) from single specimen using DIC and waisted specimen geometry	Single curve from single specimen at temperature and stress condition using ASTM E139 standard and LVDTs (ASTM, 2011a)
Source	van Rooyen *at al.* (2020)		Current work	

7.5 Model calibration

The baseline model parameter set (all model parameters apart from damage parameters) is determined for virgin X20 using a combination of an optimisation routine applied to DIC-measured creep curves from medium-term, variable stress tests (examples in Figure 7.5a), medium-term conventional data as well as literature values and published microstructural data.

Table 7.4 summarises the values for fixed baseline parameters. Using values of λ_{M23C6} = 180 nm (Marx, 2019), υ = 0.29 (EPRI, 2006), θ = 1° (Pešička *et al.*, 2004), $K'' = 3.34 \times 10^{-4}\sqrt{m}$ (Oruganti *et al.*, 2011), B_i = 9 µm and S_i = 420 nm (measured from this work) in Equation (7.8), a value of $H^* \approx 0.30$ is calculated. The activation energy for creep is considered the sum of volume diffusion (250 kJ/mol) and jog formation (50 kJ/mol) components: Q = 300 kJ/mol (Yin & Faulkner, 2006; Hore & Ghosh, 2011). Q_S is reported (Oruganti *et al.*, 2011; Stracey, 2016) to be similar to that of self-diffusion within solid solution strengthened iron. For the purpose of this study, the value of 285 kJ/mol is used which is approximately equivalent to the activation energy for the diffusion of Mo within an α-iron matrix (Nitta *et al.*, 2002). Q_P (and initial estimates of K_P) is obtained by applying a least-squares linear fit of the logarithmic of the Ostwald ripening law in Equation (7.12) to thermal coarsening data of $M_{23}C_6$ carbides (Straub, 1995) in X20 as indicated in Figure 7.10a. Time is denoted as t.

$$\frac{P^3 - P_i^3}{t} = K_P \exp\left(\frac{-Q_P}{RT}\right) \tag{7.12}$$

Table 7.4: Summary of initial estimates, bounds and optimised values of baseline parameters

Material parameter and units	Initial estimates	Searching bounds	Final parameters	Source for initial estimates
Fixed parameters				
H^*	0.30	-	0.30	Equation (7.8)
Q, kJ/mol	300	-	300	Yin & Faulkner (2006), Hore & Ghosh (2011)
Q_S, kJ/mol	285	-	285	Nitta *et al* (2002)
Q_P, kJ/mol	225	-	225	Straub (1995), Figure 7.10a, Equation (7.12)
k_N	0.1	-	0.1	Dyson (2000)
S_i, m	0.42×10^{-6}	-	0.42×10^{-6}	Current work
P_i, m	152×10^{-9}	-	152×10^{-9}	Current work
Optimised parameters				
ε_0', s^{-1}	1.3×10^{7}	$1 \times 10^{5} – 1 \times 10^{9}$	7.59×10^{6}	Straub (1995), Murchú *et al* (2017) Figure 7.10c
K_1, Pa	6.5×10^{9}	$0.1 \times 10^{9} – 10 \times 10^{9}$	3.72×10^{9}	Shear modulus at 600 °C (EPRI, 2006)
K_2, Pa	13.6×10^{6}	$6 \times 10^{6} – 15 \times 10^{6}$	12.7×10^{6}	Straub (1995), Murchú *et al* (2017), Figure 7.10c
K_{S1}, m/s	140 < σ < 150 MPa: 2.6×10^{-6} (Adjusted) σ > 200 MPa: 1.27×10^{-8}	$1 \times 10^{-8} – 1 \times 10^{-5}$	2.58×10^{-6}	Aghajani (2009), Oruganti *et al.*(2011), Figure 7.10b
K_{S2}, m/s	3.1×10^{11}	$1 \times 10^{10} – 1 \times 10^{11}$	5.35×10^{10}	Aghajani (2009), Oruganti *et al.*(2011), Figure 7.10b
K_P m^3/s	7.6×10^{-15}	$1 \times 10^{-15} – 1 \times 10^{-14}$	4.81×10^{-15}	Straub (1995), Figure 7.10a, Equation (7.12)

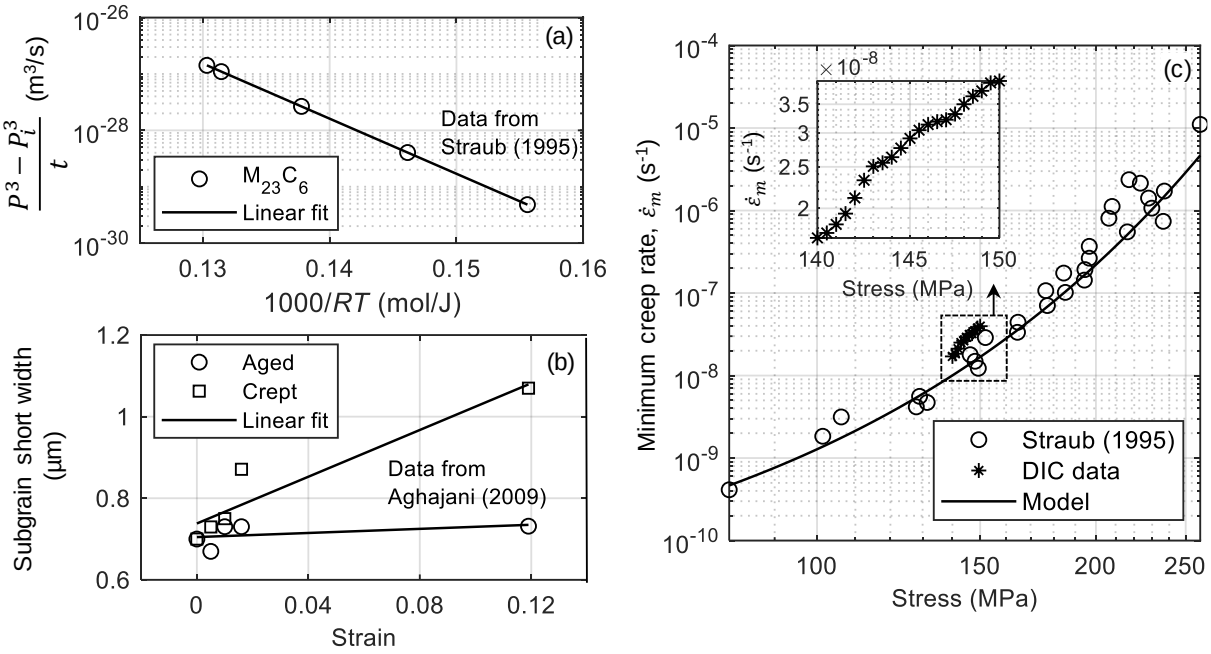

Figure 7.10: Identification of initial estimates of constants in the damage mechanics model using (a) $M_{23}C_6$ carbide coarsening data from Straub (1995), (b) subgrain coarsening data from Aghajani *et al.* (2009) and (c) minimum creep rate versus nominal engineering stress plots from this work (inset) and from Straub (1995). Symbols and solid lines represent data and fit predictions, respectively

For cavity damage evolution, a value of 0.1 was fixed for k_N which corresponds to the reduced constraint of cavity growth at relatively higher stresses encountered in this work (Dyson, 2000).

The second half of Table 7.4 summarises the initial estimates of baseline parameters selected for optimisition. Initial guesses of the subgrain parameters, K_{S1} and K_{S2}, are obtained using the linear least-squares fitting procedure outlined by Oruganti (2011) on subgrain evolution data from Aghajani *et al.* (2009) of creep strained and aged X20, respectively, during long-term creep tests at 550 °C and 120 MPa. The data and fits are shown in Figure 7.10b. Initial estimates of ε_0' are calculated using the method of Murchú *et al.* (2017) by using nonlinear least-squares fitting of $\dot{\varepsilon}_m = \varepsilon_0' \exp(-Q/RT) \sinh(\sigma(1-H^*)/S_o)$ to the X20 minimum creep rate data of Straub (1995) at 600 °C, as shown in Figure 7.10c. The optimised value of S_o is equivalent to the Orowan particle bypass stress and is used as the initial guess of K_2. K_1 is in the order of the shear modulus of X20. Parameter searching bounds are mostly taken from Oruganti *et al.* (2011) for 9 – 10 % Cr ferritic steels, whilst some bounds were expanded to account for the different creep behaviour of the 12 % Cr steel X20.

Optimum values of the baseline material parameters (ε_0', K_1, K_2, K_{S1}, K_{S2}, K_P) were calculated using an optimisation routine. This iterative methodology consists of minimising an objective function following the numerical integration of the coupled differential Equations (7.2) to (7.7) using a fourth-order Runge-Kutta *ode45* (Shampine & Reichelt, 1997) solver in MATLAB R2019a. A constant value of 0.2 was assumed for ε_r in order to terminate the integration of Equation (7.2), which corresponds to the smallest ductility measured in this work for virgin X20 and dictates the maximum value of D_c in Equation (7.6). In the present analysis, the

normalised least-square strain error is employed as an objective function (Christopher & Choudhary, 2018):

$$F_{min} = \sum_{j=1}^{n_c}\left(\sum_{i=1}^{n_p}\left(\frac{\varepsilon_i^{Pred} - \varepsilon_i^{Exp}}{\varepsilon_i^{Exp}}\right)^2\right) \tag{7.13}$$

where ε_i^{Pred} and ε_i^{Exp} is the model-predicted and experimental strain, respectively. The total number of points in a creep curve is represented by n_p and n_c is the total number of curves. Optimised parameters are iteratively developed from the initial guesses with the aim to minimise the value of Equation (7.13) via a Nelder-Mead simplex algorithm (Lagarias *et al.*, 1998) employed by the MATLAB *fminsearch* function. Convergence on the best fit is achieved when the change in parameter and objective function values between successive iterations is less than the tolerance of 1×10^{-6}.

In a similar manner to the approach of Oruganti *et al.* (2011), parameters were optimised using different stages of the creep curve. The primary creep parameters (ε_0', K_1, K_2) are optimised from the curves in Figure 7.5a up to a strain of 3.5 %. This cut-off strain was chosen on the basis of the microstructural analysis in Figure 7.7e and f, which shows that smaller subgrain widths and precipitate diameters are expected at $x > 10$ mm when compared to higher stress regions in the specimen gauge area. This suggests reduced subgrain and particle coarsening below the strain cut-off which corresponds to the highest strain encountered at the stress of about 140 MPa at this location (Figure 7.5a). These primary regime values were then fixed as the remainder of the curves before the final acceleration to fracture (for instance, 3.5 % < ε_c < 9 % at 150 MPa in Figure 7.5a) is used to calculate the subgrain parameters (K_{S1}, K_{S2}). Given the slow precipitate coarsening rates (Christopher & Choudhary, 2018), the final precipitate parameter (K_P) is determined from the remainder of the 150 MPa curve (ε_c > 9 %) and from the 140 MPa conventional creep curve in Figure 7.6b. Table 7.4 summarises the searching bounds and final optimised parameters.

Figure 7.11a compares the medium-term experimental data (symbols) and the corresponding CDM model response (solid line) for the DIC-measured creep curves of the waisted specimen at several stresses. Data and model predictions for the 140 MPa conventional creep test are also included. Good agreement is noted between the model predictions and the DIC experimental data, including the conventional creep curve at 140 MPa. This demonstrates the ability of the current model to simulate medium-term (< 1 000 h duration) creep curves.

At higher stresses and shorter durations typical of accelerated tests, however, the model underestimates the time to rupture as shown in Figure 7.11b for a conventional creep test at 250 MPa and 600 °C. This is most likely due to the change in dislocation climb mechanism from general to local at higher stresses (Christopher & Choudhary, 2019) or due to the stress dependence of the evolution of internal structures. Straub (1995) and Qin *et al.* (2003) demonstrated that the steady-state subgrain size is inversely proportional to stress. Under the assumption of the aforementioned stress-dependent subgrain growth mechanism, an updated K_{S1} was optimised from the conventional creep curve at 250 MPa and 600 °C and given in Table 7.4. The adjusted model results in an improved fit as shown in Figure 7.11b.

In order to demonstrate the ability of the adjusted model to simulate creep data at higher stresses and at different temperatures, the adjusted model was applied to accelerated, variable temperature creep curves measured using DIC from a single specimen. As indicated in

microstructural analysis performed in previous work (van Rooyen *et al.*, 2020), particle coarsening was ignored for these short duration tests ($\dot{D}_P = 0$). The comparison of the model predictions and experimental creep strain and creep rate curves is shown in Figure 7.11c and Figure 7.11d, respectively. A satisfactory match (within 5 % for secondary regime) is apparent between the model and experimental strain barring the primary regions and the tertiary region at 600 °C. Differences within the tertiary regime are still minor considering typical scatter of factor 2 encountered within rupture life measurements (Yin & Faulkner, 2006). As seen from Figure 7.11d, however, the secondary creep regime is reasonably captured by the adjusted CDM model.

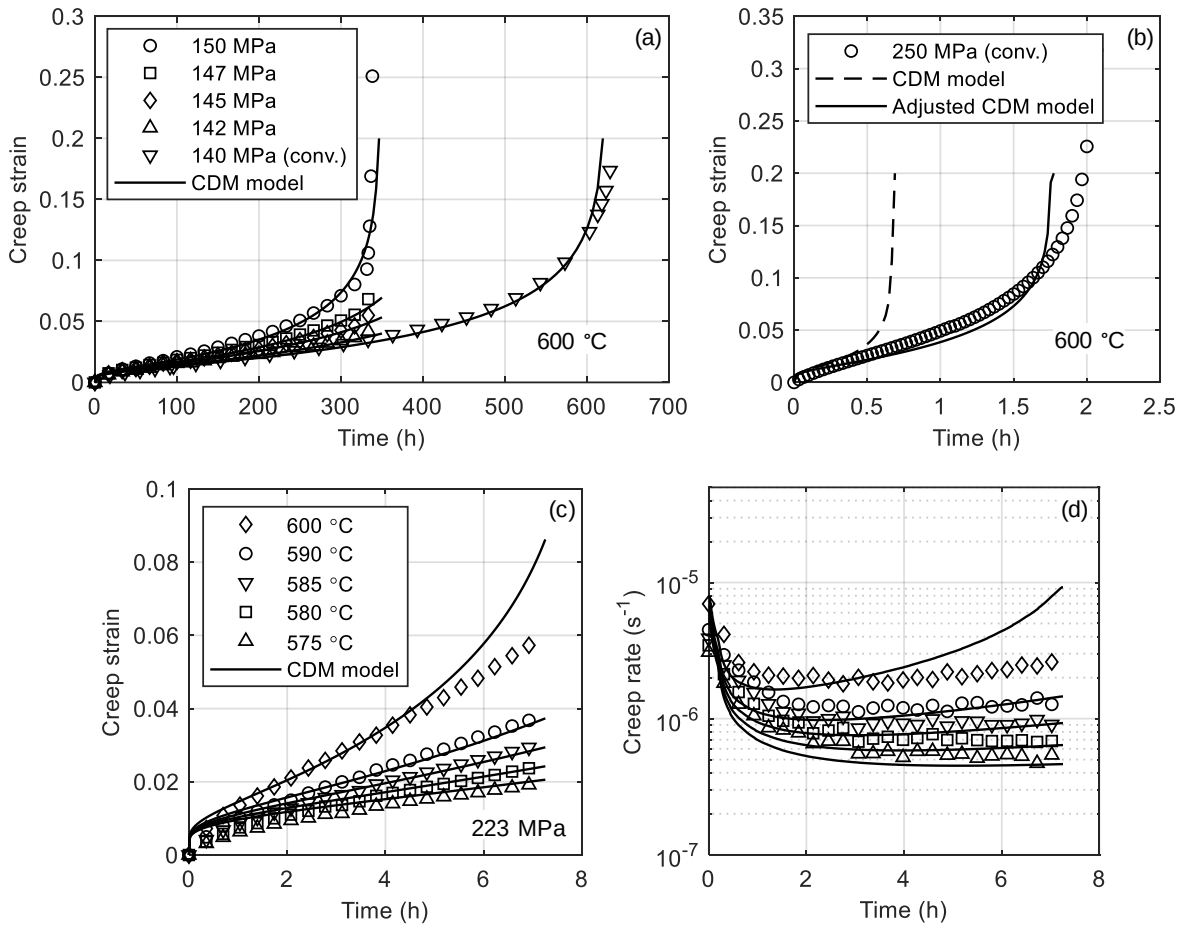

Figure 7.11: Comparison of CDM model predictions and experimental data of virgin X20 from (a) medium-term, variable stress data including a conventional test at 140 MPa, (b) accelerated, conventional test data with adjusted model parameters and (c) accelerated, variable temperature test data with corresponding (d) creep rates

7.6 Damage parameter extraction

Thus far, this paper has demonstrated DIC measurements of creep curves from single specimens of virgin X20 for the calibration of a CDM model. The applicability of the DIC technique and model can be expanded to the creep damage investigation of ex-service X20 by applying the calibrated model and fitting initial values of selected damage parameters (D_S, D_P, D_C) to DIC-measured creep curves of low, medium and high damage X20. The proposed method considers

baseline parameters (Table 7.4) to remain constant (within a restricted stress range) whilst initial damage parameters are considered to vary between ex-service states due to the evolution of certain microstructural factors as suggested in Subsection 7.4.2.

7.6.1 Sensitivity study

The sensitivity of the strain with respect to the damage parameters must be explored in order to establish the uniqueness of solutions and correlations between parameters. The influence of a percentage change (ΔD_x) in the three damage parameters on creep curves of different durations is shown in Figure 7.12. Figure 7.12a-c show creep curves typical of accelerated testing (such as in Figure 7.11b and c), medium-term testing (Figure 7.11a) and long-term tests encountered in the work of Aghajani *et al.* (2009), respectively. It is clear that the effect of D_S is unique in all three test types, whereas D_C and D_P are difficult to distinguish in the shorter-term tests (Figure 7.12a and b) due to the long-term evolutionary nature of these parameters. It is therefore necessary to select a combination of two parameters that can be uniquely determined through a minimisation of a suitable objective function.

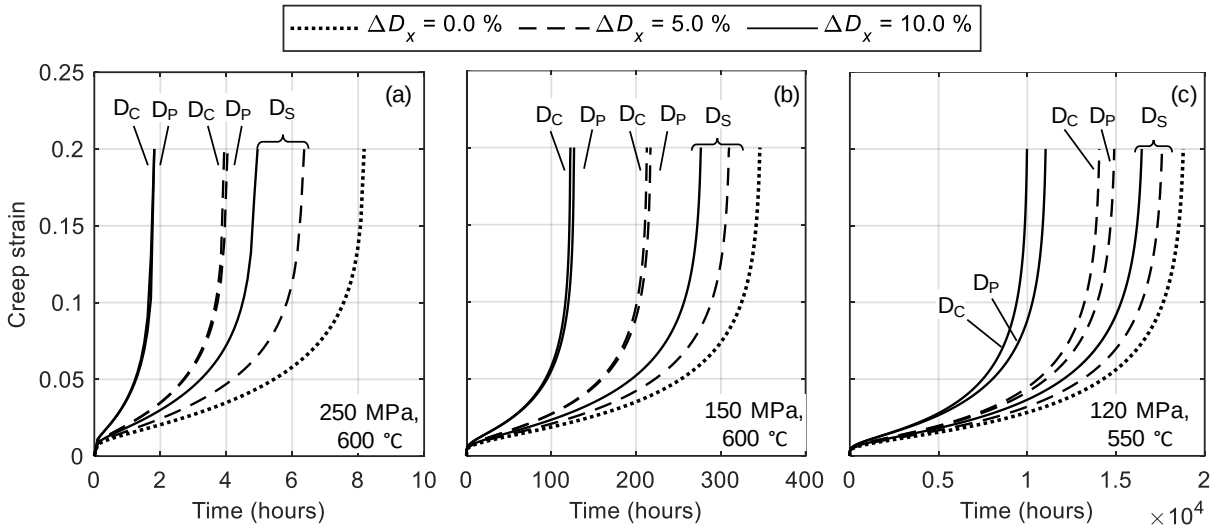

Figure 7.12: Sensitivity of creep curves to subgrain, precipitate and cavity damage parameters for (a) accelerated, (b) medium-term and (c) long-term tests

Although not presented here, several objective functions were considered including a creep stage-based weighting function as suggested by Christopher and Choudhary (2018). Nonetheless, it was found that a smooth and low stiffness evolution is available through a normalised version of Equation (7.13) where $F_{nor} = \left(\frac{1}{n_p}\right) F_{min}$. In an approach similar to Roux and Bouchard (2015), a numerical framework is used whereby a simulated creep curve is generated using nominal damage parameter values typical of ex-service material ($D_S = 0.20$, $D_P = 0.05, D_C = 0.02$) and compared using F_{nor} to creep curves generated from damage parameters varying within 10 % of the nominal values. Because three parameters are involved, the minimisation involves a 3D function that is represented by the three cross-sectional response surfaces shown in Figure 7.13a – c. A steeper gradient is noticed along one diagonal of these surfaces with a more gradual slope towards a global minimum at a 90° angle from this diagonal as indicated by the presence of ellipses in Figure 7.13a and b. In agreement with Figure 7.12,

this test shows that optimising for either $D_S - D_P$ or $D_S - D_C$ parameter sets is possible for medium-term testing. Although not shown here, the $D_P - D_C$ set does not show a unique solution for these medium-term tests due to the correlation between the parameters along a diagonal with an approximate 1:1 gradient.

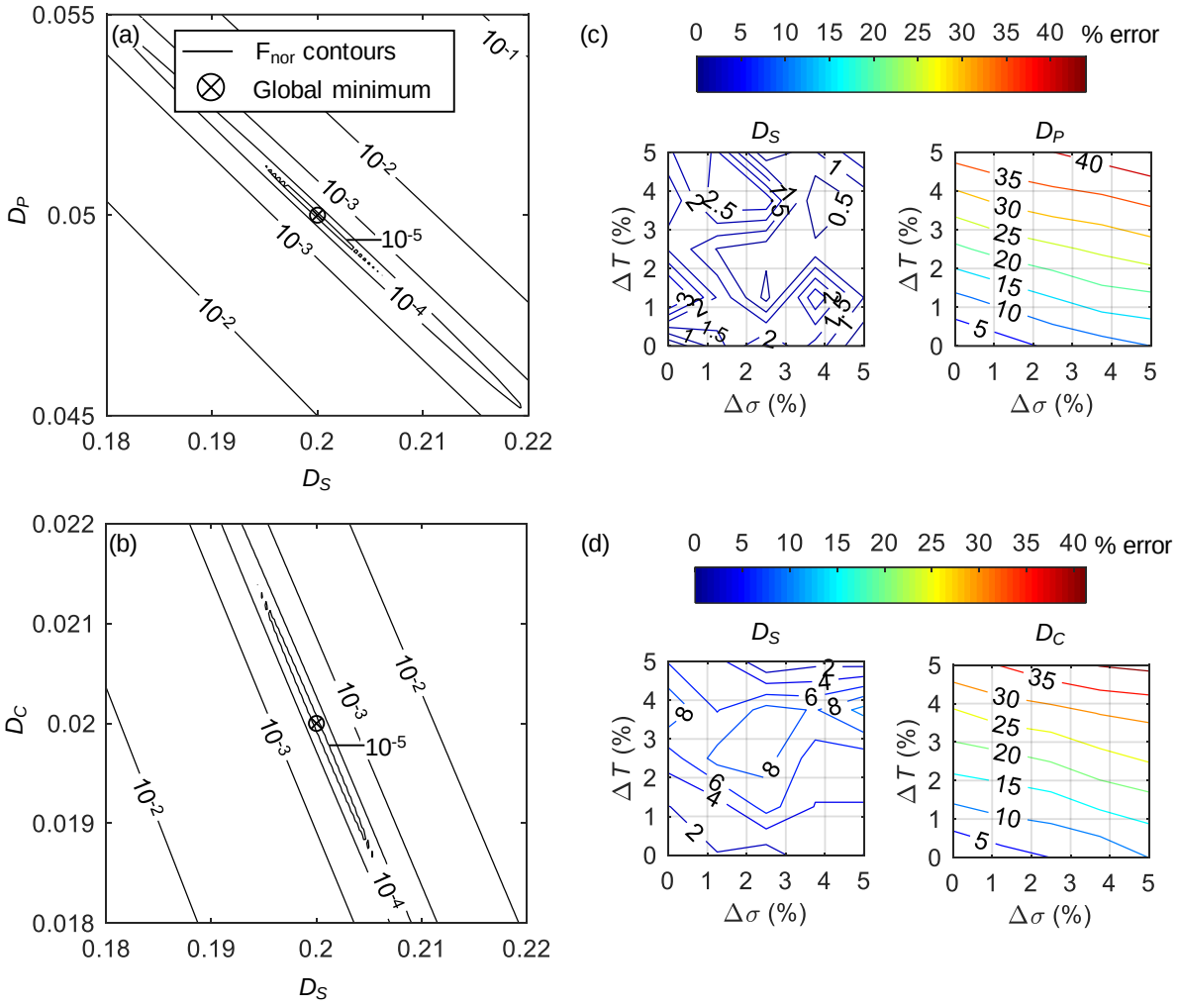

Figure 7.13: (a,b) Response surfaces of the objective function for medium-term creep tests and (c,d) percentage error in parameter identification as a function of errors in temperature and stress for D_S – D_P and D_S – D_C parameter combinations, respectively

Further consideration is given to the effect of stress and temperature measurement error on the confidence in optimised damage parameter values (determined as the absolute difference between nominal and identified parameters normalised by the search range) in Figure 7.13c – d. The simulated creep curves in this case include a Gaussian distribution of strain noise with a standard deviation of 150 με which corresponds with the longitudinal temporal noise floor in Table 7.2 calculated for the DIC-measured creep curves.

Several deductions are possible from these plots. Firstly, the same percentage change in temperature, ΔT, results in higher error in parameter identification than for corresponding changes in stress, $\Delta\sigma$. This is likely due to the presence of T in the pre-exponential function of the strain rate Equation (7.2) and emphasises the need for a uniform temperature distribution in

the gauge section of Figure 7.2. Secondly, for the stress and temperatures errors considered, Figure 7.13c and d show relatively low errors in D_S (< 10 %) compared to D_C and D_P (< 40 %). This is most likely due to the dependence of these parameters on the tertiary stage for their unique identification (Figure 7.12) coupled with the sensitivity of the tertiary stage and damage evolution equations to small changes in T and σ (Yin & Faulkner, 2006; Hore & Ghosh, 2011).

For the purpose of this study, the $D_S - D_P$ parameter set will be optimised based on several considerations. Firstly, the convergence to a minimum is most likely for this set as evident from Figure 7.13a. The use of D_S in this set also appears to be more robust to uncertainties in stresses and temperatures. In this work, temperature is maintained within 2 °C of the gauge region and stress uncertainty is attributed to load cell accuracy and positional accuracy of the DIC virtual strain gauge relative to the specimen geometry. This results in estimated uncertainties of 0.33 % and 0.30 %, respectively for temperature and stress, resulting in relatively low damage parameter errors of < 1.4 % and < 3 %, respectively for D_S and D_P as predicted in Figure 7.13c. Moreover, both D_S and D_P have direct microstructural definitions (Equations (7.9) and (7.10)) whereas D_C in Equations (7.6) and (7.11) depends on cavitation and strain accumulation relations observed during monotonic tensile creep tests.

It should be noted that the optimised D_P is mathematically equivalent to a combination of D_P and D_C on account of the similar responses of accelerated and medium-term creep curves as shown in Figure 7.12 as well as their identical location within the master Equation (7.2). Compared to D_P, relatively low values for D_C are expected due to the nature of Equation (7.6) that limits the upper bound to 0.1 (= k_N). This is bolstered by the observation that the higher, pre-test cavity densities for high damage states did not reduce the rupture ductility when compared to the virgin counterpart as shown in the conventional creep data in Figure 7.6 (Dyson, 2000). Although the distinction between D_P and D_C cannot be made, it is expected that a larger portion of the optimised D_P will consist of precipitate contributions.

7.6.2 Subgrain and precipitate damage optimisation

The same optimisation procedure outlined in Section 7.5 is followed for the extraction of D_S and D_P. The high creep curve density offered by DIC provides sufficient input data to the CDM model in the medium-term, variable stress creep tests discussed here. For comparison, model fitting is also applied to medium-term, conventional data as well as accelerated, variable temperature test data.

As with the calibration process for the CDM model previously discussed in Section 7.5, solving coupled differential equations requires estimates of initial points for the minimisation routine that can be approximated from microstructural observations. Due to the heterogeneity of microstructural data, a range of initial estimates are calculated in Table 7.5, including the estimates of D_C that were kept constant and not optimised for during the optimisation procedure. Note that although the initial values of D_C are not optimised for, its evolution ($\dot{D}_C$) from this constant initial value still continues according to Equation (7.6) based on the observations of Figure 7.9. The lower bounds of the estimated ranges were used as initialisers.

The experimental and fitted curves for the ex-service material states are shown in Figure 7.14 for accelerated, variable temperature creep tests (top row), medium-term, variable stress creep tests (middle row) and medium-term, conventional creep tests (bottom row). Similar to the baseline fits in Figure 7.11, a satisfactory match is observed between the model predictions and

medium-term data in the last two rows of Figure 7.14 whereas relatively poorer fits are noted for the accelerated creep tests (top row) for the same reasons as mentioned in Section 7.5.

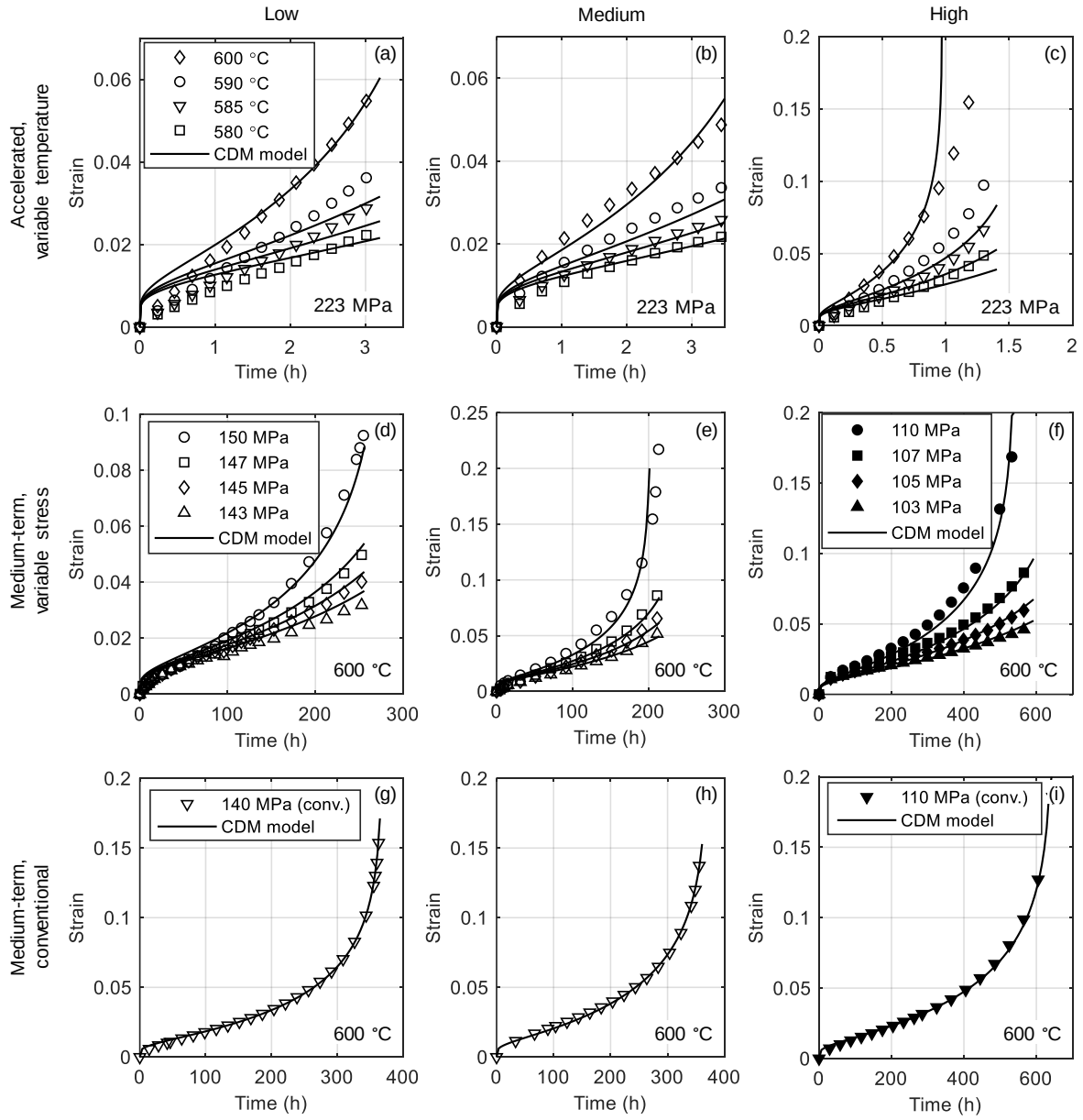

Figure 7.14: Comparison of CDM model predictions and experimental creep curves for low, medium and high damage X20 (left to right columns, respectively) during accelerated, variable temperature; medium-term, variable stress; and conventional, medium-term tests (top to bottom rows, respectively)

The optimised damage parameters obtained from the accelerated and medium-term tests are provided in Table 7.5. Apart from the D_S values for the low damage X20, most damage parameters extracted from the medium-term tests are within or close to the microstructural estimates. Relatively higher D_S values are recorded in comparison to D_P values. Values of $D_S \approx 0$ are obtained for low damage X20, whereas medium and high damage states exceed values of 0.1 and 0.3, respectively. Medium damage X20 shows the lowest D_P values of less

than 0.02 which is a third of the low damage D_P of about 0.06. High damage X20, on the other hand, displays the highest D_P values which exceed 0.1.

7.7 Discussion

Differences in creep behaviour between service-exposed X20 steels with varying levels of service histories are identified through the DIC technique. Microstructural deterioration is also revealed through subgrain, precipitate, cavity density and hardness measurements. These aspects are combined using a microstructurally-sensitive CDM framework to reveal quantitative differences in damage levels between the ex-service states.

7.7.1 Full-field methods in creep damage modelling

The DIC technique is shown to extract multiple, spatially-resolved creep curves at several stresses using a waisted specimen geometry during medium-term tests. These variable stress tests share similarities with the authors' previous studies (van Rooyen *et al.*, 2020) where multiple accelerated creep curves were measured across a varying temperature field generated through a Gleeble thermomechanical machine. Such approaches are ideal when material efficiency is a key requirement, such as in the damage assessment of service-retrieved power plant materials. Accelerated creep tests demonstrated time-saving and economy of material advantages over longer-term, conventional versions. Special feedback control from a Gleeble thermal system is required however to maintain a specific temperature profile across the specimen, making adaptation to longer-term, independent testing difficult. The tests performed in this work, on the other hand, are conducted within a traditional creep rig modified for integration with DIC and are better suited to measurement of medium-term creep curves.

Both approaches produce creep curve data that are representative of the damage levels of service-exposed X20 steels with varying levels of service histories. Specifically, differences in damage states are revealed through qualitative comparisons of curves in terms of minimum creep rates and failure times (Figure 7.6). Previous approaches (van Rooyen *et al.*, 2019a) of quantifying levels of damage employed simple conventional creep relations (such as the threshold stress-modified Bird-Mukherjee-Dorn and Zener-Hollomon equations) together with DIC-obtained, accelerated creep curves. Within this work, the application of accelerated and medium-term data to CDM models is highlighted.

Calibration of the Oruganti *et al* (2011) CDM model (modified to include cavitation damage) for virgin X20 benefits from the data richness offered by DIC analysis over nonuniform temperature and stress fields. From a single test, a range of curves in various stages of development can be systematically input to the model to extract baseline constants. For instance, primary- and secondary-regime-dominated curves can be used to extract reference stress (Equation (7.3)) and subgrain (Equation (7.4)) baseline parameters, respectively. Tertiary segments of the curves are useful in identifying baseline constants related to slow-evolving subgrain and precipitate damage relations although the final acceleration to failure is only captured for the maximum temperature or stress condition (Figure 7.6).

Medium-term testing is successfully simulated by the model whose calibrated parameters are within ranges predicted from literature. For accelerated tests, the primary stage is not properly modelled as shown in Figure 7.11.

Table 7.5: Summary of ranges for estimated initial and optimised damage parameters. Lower bounds indicated by * are used as initialisers for the optimisation routine of subgrain and precipitate parameters and for constants set for cavitation damage. A = accelerated tests. MT = medium-term tests

Initial estimate calculation method	Original damage class	Microstructural data			Range of initial estimates	Optimised parameters	
		Feature	Size range	Source		A	MT
$D_S = 1 - \frac{S_i}{S}$	Virgin	S_i (nm)	409 – 423	Marx (2019)	–	–	
	Low	S (nm)	520 – 560	Current work, van Rooyen *et al.* (2019a)	*0.18 – 0.26	≈ 0	0 – 0.06
	Medium		410 – 622		*0.18 – 0.34	0.10	0.17 – 0.23
	High		710 – 790		*0.40 – 0.48	0.39	0.21 – 0.35
$D_P = 1 - \frac{P_i}{P}$	Virgin	P_i (nm)	136 – 168	Marx (2019)	–	–	
	Low	P (nm)	173 – 191	Current work, van Rooyen *et al.* (2019a)	*0.02 – 0.28	0.05	0.02 – 0.06
	Medium		161 – 183		*0.02 – 0.25	≈0	0.01 – 0.02
	High		194 – 198		*0.13 – 0.31	≈0	0.12 – 0.17
$D_C = \frac{\pi {d_c}^2 N_c}{4}$	Virgin	–	–	–	–	–	
	Low	d_c (µm), N_c (cavities/mm^2)	1.2 – 3.4, 71 – 167	Marx (2019)	*0 – 0.001	N/A	
	Medium		1.0 – 2.4, 146 – 250	Current work, van Rooyen *et al.* (2019a)	*0.0001 – 0.001	N/A	
	High		0.9 – 2.2, 60 – 960		*0 – 0.004	N/A	

This disparity can be attributed to the lack of a stress-dependent evolutionary equation for the backstress contribution to the primary creep through H^* in Equation (7.2) (Christopher & Choudhary, 2018) or the difficulty of Equation (7.3) in capturing the stress-dependent evolution of primary creep (Oruganti *et al.*, 2011). Nonetheless, the model predicts the remainder of the curves well considering the difficulties commonly encountered with CDM modelling at higher stresses (Christopher & Choudhary, 2019).

7.7.2 Comparison with alternative damage indicators

Application of the calibrated CDM model to ex-service X20 creep curves from various test types provides a set of optimised D_S and D_P parameters. Figure 7.15 compares these parameters between ex-service states and between test durations. For comparison, two additional creep damage evaluation methods are included. Firstly, the accumulated damage in the form of a life fraction $\frac{t}{t_r}$ (where t is the exposure time and t_r is the time to rupture) is related to the cavity density ratio $\frac{N_c}{N_r}$ using a creep ductility factor λ_D according to the van Zyl *et al.* (2005) creep life model:

$$\frac{t}{t_r} = 1 - \left(1 - \frac{N_c}{N_r}\right)^{\lambda_D} \tag{7.14}$$

The cavity density at failure, N_r, is taken as 10 000 cavities/mm^2 and λ_D is taken as 3.4 from previous investigations on service-retired X20 (Molokwane, 2013). This model is commonly used for life estimates by the local power utility due to its relatively simple relationship with the common site-investigative damage monitoring technique of cavity density measurement from surface replicas.

Secondly, the hardness model of Endo *et al.* (2003) is also included as:

$$\frac{t}{t_r} = \frac{1 - \frac{h_e}{h_o}}{0.19} \tag{7.15}$$

where h_e and h_o are the ex-service and virgin X20 Vickers hardness measurements, respectively, as indicated in the pre-test values of Figure 7.8. It is necessary to note that the higher the damage parameter, the greater the material's life exhaustion as indicated with the aid of Robinson's rule (Cardoso *et al.*, 2015).

Figure 7.15 demonstrates that comparative damage assessments between ex-service states using optimised damage parameters correspond generally well with traditional damage sensors (using Equations (7.14) and (7.15), for instance). Interestingly, these latter methods suggest that low and medium damage X20 have similar damage levels. This is clear from the higher hardness values for medium damage traded off with higher cavity densities (Figure 7.8 and Table 7.5, respectively) as well as from the similar Zener-Hollomon parameters determined for these states in van Rooyen *et al.* (2019a).

It is also evident from Figure 7.15a that only one parameter from the $D_S - D_P$ set can be discerned from the accelerated creep curves whilst the other attains an insignificant value. Specifically, low damage X20 demonstrates superior subgrain properties but weaker precipitate contributions in comparison to the medium counterpart. Although measurements in Figure 7.7e

indicate smaller subgrains for medium damage X20, the values are close considering the typical scatter presented by heterogeneous microstructural features within these materials.

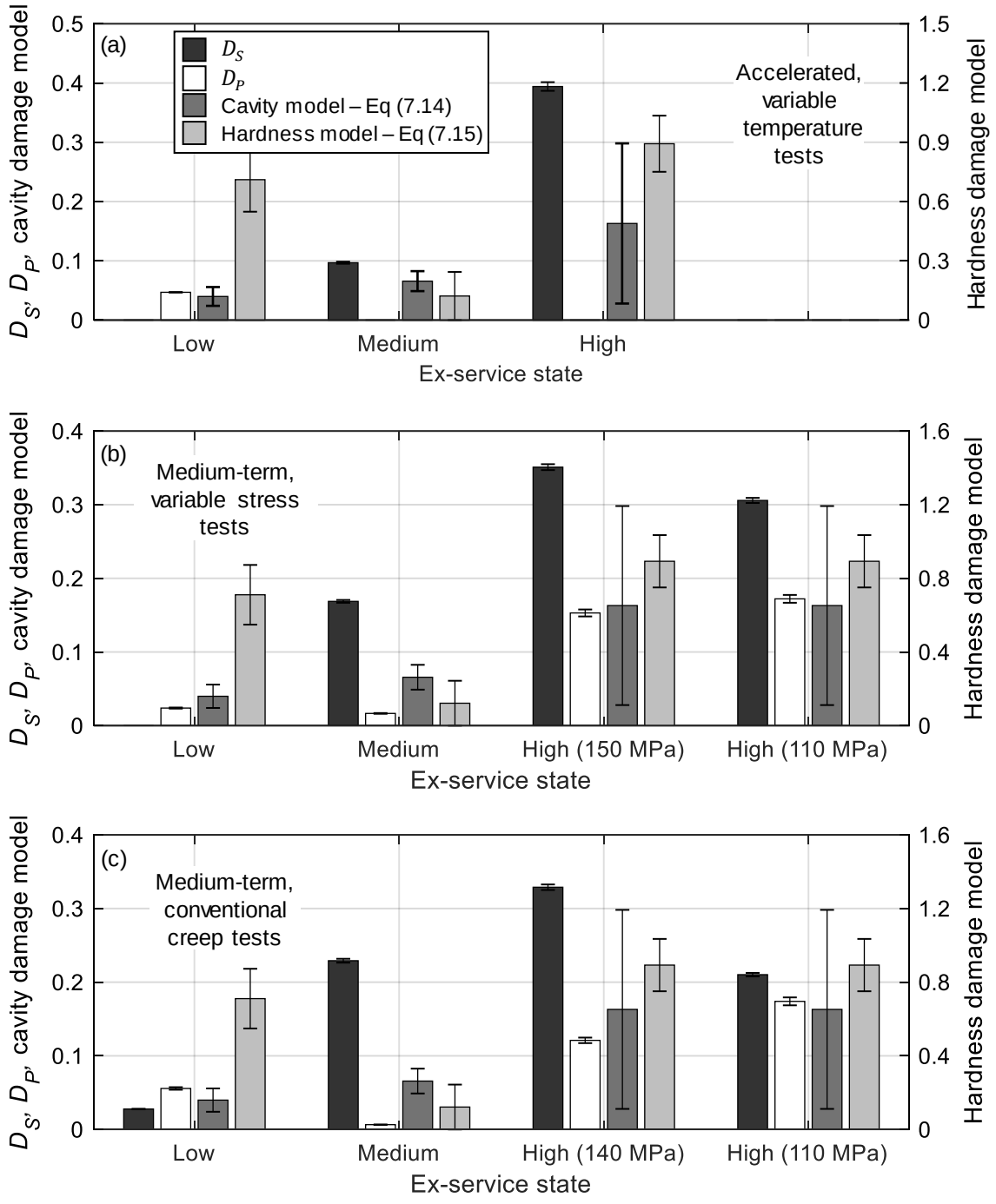

Figure 7.15: Optimised D_S and D_P damage parameter sets from (a) accelerated, variable temperature, (b) medium-term, variable stress and (c) medium-term, conventional creep tests compared with hardness and cavity density damage assessments

Nonetheless, the optimised damage parameters are in agreement with microstructural data previously sampled from these specimens (van Rooyen *et al.*, 2019a), that indicated larger grains but denser $M_{23}C_6$ distributions for medium damage when compared to the low damage

state. This would also explain why medium damage X20 has similar long-term creep behaviour to low damage X20 (Figure 7.14(e,h) and (d,g), respectively) on account of the strengthening benefits offered by precipitates for intermediate stresses (Murchú *et al.*, 2017). Similarly, high damage X20 showed higher D_S values corresponding to large, equiaxed subgrains. In this case, however a meaningful value of D_P was not obtained due to the lack of tertiary data in these fast-developing curves. High D_P values are anticipated as high damage X20 exhibits lower $M_{23}C_6$ number densities and larger particle diameters compared to other states (van Rooyen *et al.*, 2020). The relatively low values of D_P for the lower damage states coupled with the slow development of this parameter (Christopher & Choudhary, 2018), makes it difficult to obtain discernable values from creep curves generated from accelerated tests.

For accelerated and medium-term tests, it is also difficult to discern whether optimised D_P values are actually disguised D_C values given their similar mathematical implementation in the master CDM Equation (7.2). Given that finite values are measured for the apparent D_P values which are in accordance with microstructural evidence of differences in precipitate distributions, however, it is more likely that D_P is the outcome of the optimisation routine than D_C which is estimated to have near-zero values (Table 7.5). By contrast, D_S parameters are relatively larger and show the same trend in damage as indicated by the commonly employed cavity density method. This is most likely due to the respective sensitivities of the secondary and tertiary creep regimes to D_S and D_P (Christopher & Choudhary, 2018) coupled with the limitations of the current technique in measuring full curve development into the tertiary stage, as mentioned in Subsection 7.4.1.

As the test duration increases from Figure 7.15a to Figure 7.15(b,c) for medium-term tests, both D_S and D_P can be discerned with the same conclusions drawn as before, barring higher D_P values for high damage X20 as expected from the microstructural analysis in Figure 7.7f. Consistent damage parameters are extracted across the different medium-term tests at different stresses as evident from the high damage X20 values. It is useful to understand that the variations in measured damages for high damage X20 (as seen in the larger differences between the variable stress tests in Figure 7.15b and the 110 MPa conventional test in Figure 7.15c) could also be attributed to the extreme microstructural heterogeneity of this material especially when considering the microstructural and cavity density spread in Figure 7.7f and Figure 7.9, respectively.

7.7.3 Recommended CDM-based damage philosophy

CDM-based damage extraction is an effective and material-efficient damage assessment tool especially when combined with the high density of creep curves available through DIC measurement. The quantitative correlation between the extracted damage parameters and original classifications of the ex-service material bears testimony to this approach. By contrast, the hardness methodology demonstrates less consistency in terms of the observed creep behaviour. For instance, higher hardness damage observed for low damage X20 compared to medium damage X20 disagrees with the longer rupture times observed in medium-term, low damage tests in Figure 7.14d. The optimised damage parameters also display less scatter than the cavity model, especially with regards to high damage X20. Furthermore, higher consistency and hence confidence in parameters is noted for the medium-term, variable stress tests than the single-specimen, conventional tests. This is attributed to the use of multiple creep curves in the optimisation routine in the latter approach which allows for more meaningful parameter extraction.

Based on these grounds, the following DIC/CDM damage assessment philosophy is recommended. Conservative assessments of service-retrieved material required in entry-level integrity evaluation procedures can involve using DIC to measure multiple accelerated creep curves (as shown in the top row of Figure 7.14) from single specimens and optimising for D_S through a curve-fitting routine. This will identify ex-service states with large differences in apparent deterioration, viz. high damage X20 in this work. In this case, D_S can be used as a good sensor for damage as it usually exceeds 0.1 (as noted in Figure 7.15). The higher damage parameter value is most often used as the basis of comparison between states (EPRI, 2007; Cardoso *et al.*, 2015).

For more subtle differences, in the case of medium and low damage X20, consideration should be given to creep test duration as subgrain strength usually dominates within medium-term creep tests whereas precipitate hardening has longer-term advantages (Murchú *et al.*, 2017). To this end, medium-term testing using variable stress profiles can refine the assessment in terms of both D_S and D_P. For testing exceeding 1 000 h, consideration should be given to D_C as well as other forms of microstructural deterioration, including precipitation of new phases and solid solution strengthening. Additional modes of damage characterisation should also be considered including cavity density and hardness measurements. This is particularly necessary in the instance when one parameter dominates for a particular ex-service material, as demonstrated previously from the accelerated tests.

Although beyond the current scope, this technique can then be used to estimate times to failure of components in a similar manner to the hardness and cavity damage evaluation techniques (Molokwane, 2013; Cardoso *et al.*, 2015). Operating temperatures and stresses along with the optimised damage parameters can be applied to the CDM model to predict evolution to failure. This has a considerable advantage over wholly empirical methods as the CDM model is directly tied to microstructural evolution. Relative comparisons of the parameters between ex-service materials can also allow refinement of traditional damage classification techniques (viz. the cavity-based classification used in Abe *et al.* (2008: 650)) to include more subcategories that reduce the uncertainties in expended life fractions. Demonstrative of this is the apparent disparity in damage verdicts for medium damage X20 when considering cavity density, D_P parameter, microstructural and hardness measurements (Figure 7.15). Results suggest that the medium damage has a life exhaustion extent closer to that of low damage material than the high damage counterpart, necessitating an updated subclassification of damage. Identifying possible overconservatisms in this manner hosts great economical and plant availability benefits in the context of power plant maintenance.

7.8 Conclusions

The emphasis of this work is damage assessment using the wealth of creep curve data available from the DIC measurement of strain fields across spatially varying stress profiles within a microstructurally-relevant CDM framework. This technique is ideal for applications in the power industry due to the preservation of material volume and it introduces a new potential benchmarking technique for future damage evaluation procedures. The key conclusions are:

- The use of a waisted specimen geometry allows the development of a spatially distributed stress field across the gauge region with minimal stress triaxiality. This allows an array of creep curves to be measured from a single specimen using the full-field strain measurement capabilities of DIC.

- This technique is applied to both virgin and ex-service states of the 12 % Cr power engineering alloy known as X20. DIC-resolved creep curves obtained at central (maximum stress) as well as off-centre locations show good agreement with conventional, standardised creep tests. Creep curve regimes at the latter locations are not completely developed as they are regulated by the failure at the central positions.
- Microstructural characterisation using BSE-SEM images demonstrate the evolution of subgrains, $M_{23}C_6$ precipitates and cavity distributions during testing, resulting in the adaptation of a CDM model with representative damage parameters and evolutionary equations.
- Following baseline parameter calibration on virgin X20, optimisation of subgrain and precipitate damage parameters is performed on ex-service X20 using creep curves from medium-term, variable stress DIC tests and medium-term conventional tests together with accelerated, variable temperature DIC tests and accelerated conventional tests. Medium-term tests result in measureable values of these parameters, especially in terms of subgrain damage, which are larger for highly exhausted material. Smaller differences in intermediate exhausted states can also be identified by pairing the optimised damage parameters with traditional forms of creep damage assessment.
- Good agreement is demonstrated with alternative evaluation philosophies, demonstrating the potential of the technique for use as a life assessment tool. Relatively lower damage parameter values and higher hardness values for the medium damage material suggest an expended life fraction closer to that of the low damage counterpart, despite a higher cavity density and original damage categorisation.

8 Discussions and recommendations

The structure of the preceding chapters mirrored that of a journal article, consisting of introductory sections, results, discussions and conclusions. The goal of this chapter is to expand on the discussions of the previous chapters in terms of the objectives outlined in Section 3.2. This is achieved by coupling the central aspects of the dissertation tied to the most important inputs to creep analysis, namely, time, temperature, stress and microstructure (Kloc, 2015).

Previous chapters indicated that damage characterisation can be performed on ex-service X20 at multiple temperatures or stresses on single specimens using the full-field strain mapping capabilities of DIC. These specimens, however, are still equivalent in size to conventional creep test pieces which result in high costs and extensive weld repair requirements when they are extracted from in-service components. Future work surrounding small-sample testing using DIC is explored in Section 8.5 (supplemented with Appendix B) which leads to a summary of recommendations on the applicability of this work to Eskom power plants.

8.1 Thermomechanical material property measurement

Chapter 4 introduces the concept of simultaneous tensile property measurements at multiple temperatures from single specimens of X20 steel using a combined DIC-IR imaging setup. With the overarching aim related to creep deformation measurement in mind, this setup provides some spatial control over one of the main drivers of creep behaviour: temperature. To this end, the Gleeble thermomechanical simulator serves as a useful tool for the generation of nonuniform thermal fields through resistive heating with some control offered over the gradients through specimen geometry and material selection (Zhang *et al.*, 2011; Kardoulaki *et al.*, 2014).

The concept of integrating DIC strain measurements with nonuniform full-field temperature data is not unique with several works using integrated DIC-IR field measurements to observe the thermomechanical coupling behaviour associated with strain localisation in monotonic tension tests (Chrysochoos *et al.*, 2010; Nowak & Maj, 2018) or for the conversion of nonuniform temperature fields into stress fields through thermoelastic stress analysis during cyclic loading (Silva & Ravichandran, 2011). The translation to quantitative material property measurement of thermal power plant steels at high temperatures, however, is unique to this work as far as the author is aware.

As demonstrated in Chapter 4, temperature-dependent values of elastic modulus and Poisson's ratio of virgin X20 were calculated from full-field displacements. Such an approach is valuable when testing material is in short supply (for instance, in-service piping sections in thermal power plants) as it allows tensile property measurement at several temperatures from single specimens as opposed to the one specimen per temperature requirement of conventional techniques such as required in the standard ASTM E21 (ASTM, 2009). Such properties serve as input to creep deformation models such as the BMD formulation in Equation (6.1); estimations of fracture toughness from the *J*-integral approach (Molteno & Becker, 2015); creep damage models (Storesund *et al.*, 2006); as well as the FE modelling of welds (Moriyama *et al.*, 2009) and small punch specimens (Wen *et al.*, 2019) that involve a range of high temperatures.

Although not formally reported in this work, the technique can additionally be used to estimate the linear thermal expansion coefficient of X20 during specimen heating in a similar manner to

De Strycker *et al.* (2010). Practically, however, thermal gradients and the grip clamping required in this setup to enable electrical contact for resistive heating precludes free expansion of the specimen (De Strycker *et al.*, 2010; Pan *et al.*, 2011). Despite this, measurements of 11 – 15 μm/m °C are made for temperatures ranging from 20 – 600 °C which is within 20 % of the reported values of 10 – 12 μm/m °C (EPRI, 2006:5.2), demonstrating the potential to apply the technique to thermal expansion studies.

Furthermore, property measurement accuracy is directly tied to the quality of the underlying input displacements obtained using DIC, which is shown to be of concern in the determination of Poisson's ratio (Figure 4.10d). Displacement and strain error reduction is possible by increasing the ROI to span a larger portion of the camera FOV by increasing the magnification factor through longer focal length lenses. Schreve (2014) showed that, for a pinhole camera model, an increase in focal length results in an increase in measurement accuracy due to a reduction in quantisation error. It was also found that quantisation error largely limits the accuracy of a stereo-setup and can be minimised by also using higher resolution CCDs. Using larger subset sizes whilst maintaining spatial resolution through higher camera resolution provides a smoothing effect for noisier displacements (Jones & Iadicola, 2018).

Although previous studies have demonstrated DIC techniques with higher (but mostly uniform) temperature capabilities, the time, resource and material efficiency intrinsic to the current technique through simultaneous property measurement from single specimens can be realised for higher temperature tests through minor setup adjustments to mitigate strain error stemming from surface radiation. This includes blue bandpass filters with higher transmission and narrower bandwidth of transmitted wavelengths coupled with monochromatic blue LED illumination kits with peak output at the corresponding characteristic filter wavelength such as those employed in the work of Chen, Xu, *et al.* (2012). As noted from Equation (4.4), higher signal-to-noise ratios and higher temperature limits are possible before decorrelation occurs from saturation due to surface radiation. This is particularly useful for the property evaluation of creep resistant candidate materials for future generations of thermal power plants that are required to operate at temperatures exceeding 600 °C for enhanced plant efficiency. Narayanan *et al.* (2017) and Novak and Zok (2011), for instance, have demonstrated DIC-based property measurement at uniform temperatures exceeding 700 °C of Ni-based superalloys for ultra-supercritical power stations.

Moreover, the current DIC-IR technique can be applied to thermomechanical studies wherein plastic deformation (measured via DIC) results in heat dissipation (detected by IR). In these situations, the DIC displacements can be used to translate IR measurements from the Eulerian (IR) to Lagrangian (DIC) frame of reference as done by Nowak and Maj (2018). Alternatively, Silva and Ravichandran (2011) performed thermoelastic stress analysis using DIC directly on IR images using low-emissivity specks on a high-emissivity base as a speckle pattern. Regarding the application to ex-service thermal power plant steels, this approach can provide more insight to modes of failure due to inherent pre-test void damage by observing the coupled plastic strain-thermal interactions associated with localisation effects in the specimen gauge region (Chrysochoos *et al.*, 2010).

Within the same body of research geared towards improved material efficiency in the power engineering field, Huchzermeyer and Becker (2018) estimated multiple fracture and tensile properties from single samples using the virtual fields inverse method (optimising for material properties through the principle of virtual work). Such an approach as well as FEM updating (Wen *et al.*, 2019) whereby numerical displacements can be compared to experimental (DIC) displacements over the nonuniform thermal field in order to extract multiple temperature-

specific material properties is an alternative to the direct approach employed in this work. In summary, this technique provides multi-modal (DIC/IR) images that could serve as input for various means of thermomechanical property calculation methods whilst maintaining material efficiency.

8.2 Creep behaviour measurement

Chapter 5 expands the technique of Chapter 4 to accelerated creep deformation measurement of ex-service X20 across nonuniform temperature fields by considering another dependent variable of creep: time[23]. One of the main findings of this work is that creep strain and creep rate curves measured over accelerated time periods at multiple temperatures are discerning indicators in the creep resistance of damaged X20 with different levels of service exposure (Figure 5.6). Specifically, higher damage levels equate to faster creep rates and shorter rupture times. These accelerated tests reflect observations available from conventional longer-term constant-load and constant-temperature tests (ASTM, 2011a) as shown in Figure 5.9, providing a potential time saving advantage over the latter methods of damage comparison.

High stresses approaching the yield point of the material are employed to generate creep curves within 10 h as the current setup does not allow for longer, unsupervised tests typical of conventional tests. Such accelerated tests are not unusual to creep studies of TMF steels as demonstrated by Shrestha *et al.* (2013) on Grade 91 steel and by Xiao *et al.* (2019) on the novel G115 steel. The concern here is that the plastic deformation resulting from stresses above the athermal yield stress of the aged X20 introduces additional dislocations into the substructure (Abe *et al.*, 2008:277). This makes creep curve comparisons between ex-service material difficult as the introduced dislocations would mask the effects on the creep curve of the inherent (pre-test) creep obstacles such as precipitates and subgrains. However, qualitative comparisons of ADF-STEM images (Figure 5.14) do not illustrate evidence of increased dislocation densities in the specimen gauge regions taken from colder, low-crept areas. Further evidence for this can be found by considering the mobile dislocation density of aged X20 that is in the order of 1.5×10^{14} m^{-2} as estimated from Marx (2019:288) by assuming that the mobile dislocation density is half of the subgrain-internal density (Yadav, Kalácska, *et al.*, 2016). From Equation (2.3), an estimate of the limiting stress (280 MPa at 600 °C) is found to be sufficiently higher than the test stresses selected in this work (< 260 MPa).

It is worth reiterating that such tests are not meant for extrapolation to longer times due to the time-dependence of diffusion processes associated with particle coarsening as well as nucleation of new phases such as Z phase (Cipolla *et al.*, 2010; Oruganti, 2012). This is also apparent from the lack of particle growth observed in the specimen gauge regions (Table 5.6). Instead, qualitative comparisons between the curves are possible for distinguishing between damage levels. Unlike for the particles, subgrain growth was observed in the specimen gauge region as outlined in Subsection 5.3.4. This would later play an important role in identifying the key microstructural damage parameters and evolutionary equations employed in CDM models as discussed in Chapter 7. Dislocations were not quantitatively considered due to the unpredictable nature of TEM film preparation, the limited amount of material available (Marx, 2019), the heterogeneous nature of dislocation distributions and the need for X-ray diffraction (XRD) for mobile dislocation quantification (Yadav, Kalácska, *et al.*, 2016). Further discussion on dislocation analysis is provided in Sections 8.3 and 8.4.

[23] Here long-term tests are not considered. The “time” parameter is introduced by maintaining a constant load for < 10 h under the classification of accelerated creep testing as opposed to relatively fast, low-stress quasi-static tension tests conducted in Chapter 4.

One limitation of the current technique is the inability to perform constant-strain rate tensile testing mentioned in ASTM standard E8M (ASTM, 2011b) and applied in the work of El Rayes and El-Danaf (2017). On account of the thermal gradient, different longitudinal positions strain at different rates and there was, specifically within this work, no available live DIC processing system capable of providing feedback control to the Gleeble machine. There have since been vast developments in live strain measurement using DIC systems equipped with analog output for interfacing with other systems (Blug *et al.*, 2019). Future applications could consider using these real-time DIC processing systems to perform constant-strain rate testing by referring to strain development from a specific position, such as the highest temperature point, as a rate estimate.

An issue related to DIC in general is paint stability (Chen, Xu, *et al.*, 2012) especially at higher strains, such as those encountered near creep rupture (≈ 30 %). As a result, rupture strain near the necking point (approximately at the maximum temperature point) is subject to higher error due to speckle pattern instability. An example of this is shown in Figure 5.8. The black emissive paint for IR purposes applied to the back surface of the specimens showed increased susceptibility to local necking due to its brittle nature when compared to the white base paint of the speckle patterns. As shown in Figure 8.1, this makes it difficult to establish how excessive necking affects heat flow characteristics of the specimen and the resulting temperature distribution so that the final temperature at the failure point is assumed to be identical to prior-necking measurements. This is a minor issue as excessive necking usually occurs approximately in the final 2 % of the creep curve.

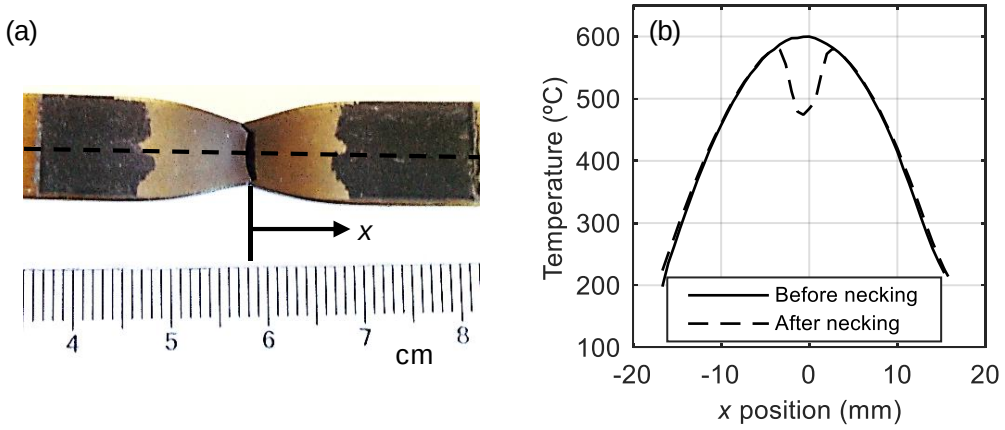

Figure 8.1: (a) The flaking of black paint on specimen rear after necking that results in (b) error in the longitudinal temperature measurement

Another important observation in terms of measurable curve parameters is that this technique (as well as the stress-variable technique of Chapter 7) measures multiple temperature-dependent minimum strain rates from a single specimen but is unable to measure multiple temperature-dependent rupture times and strains (t_r and ε_r, respectively in Figure 2.1) as these parameters can only be determined for the central temperature where failure occurs (also mentioned in Subsection 7.4.1). Analysis involving the Larson-Miller or Monkman-Grant parameters does not, therefore, benefit from this technique. Instead minimum creep rate models, such as the BMD model (Equation (6.1)) are better suited.

Finally, future work could consider additional specimen geometries beyond the ones discussed in Subsection 5.2.1 as a means of manipulating the resulting temperature distribution for a particular test type (Norris & Wilson, 1999). For instance, specimen geometry can be optimised for a uniform temperature field to allow single-specimen creep characterisation across different welding zones (Sakanashi *et al.*, 2017).

8.3 Microstructural and creep damage measurement over nonuniform thermal field

Whereas Chapter 5 focuses on the qualitative creep response of two extreme damage states (namely, low and high damage) along with the microstructural effect of accelerated testing, Chapter 6 homed in on quantitative measures of damage comparison between virgin, low, medium and high damage X20. This was achieved by considering the link between strain-based and quantitative creep parameters and a material-based variable of creep: microstructure. Creep is both dependent on microstructure and is the evolutionary driver of microstructural changes and so it is important to emphasise that pre-test microstructure is focused on in Chapter 6. As the discussion section of Chapter 6 is comprehensive in terms of the DIC-based mechanical damage indicators over nonuniform thermal fields, a brief synopsis is given here primarily on microstructural assessments.

Chapter 6 reflects the sentiments of Bhadeshia (1998: 227) regarding damage assessment of service-retrieved components that "no single measurement is sufficiently comprehensive to describe [life exhaustion] with requisite completeness." This is demonstrated by the similarity between the creep curves and resulting Zener-Holloman parameters of low and medium damage X20 (Figure 6.4 and Figure 6.21) despite the differences in cavity density and microstructure (Subsection 6.3.3). If judgement on the damage level is based on cavity density alone, the medium damage X20 would be considered to be at a higher life exhaustion grade than the low damage steel according to Eskom component cavity damage classifications (Molokwane, 2013), despite having similar creep resistance as shown in both Gleeble-DIC tests in Figure 6.4 and conventional creep tests in Figure 5.9. This overconservative assessment bears with it economic and plant productivity penalties (Larrosa *et al.*, 2017).

There also exists a relative effectiveness between microstructural observation methods. EBSD-measured orientation indicators discussed in Subsection 6.3.3, for instance, did not show a clear correlation with the damage states of ex-service material. Higher boundary density measurements in Table 6.4 for high damage X20 are in contrast to the findings by Payton *et al.* (2012) for long-term creep tested X20. Payton *et al.* (2012) also reported large scatter in these measurements, making it difficult to use these techniques for material health indication.

CBS imaging proved to be a comprehensive damage assessment tool and is proposed to be an alternative to the surface replication method for structural assessment as suggested by Dobrzański (2005) and demonstrated in van Rooyen *et al.* (2019b). CBS micrographs are suitable for simultaneous analysis of Laves phase, $M_{23}C_6$ and micrograin distributions, although the orientation resolution capabilities of CBS (and EBSD) is an ongoing challenge when identifying the latter element through crystallography, specifically the low boundary angles of subgrains (Humphreys, 2004). Nonetheless, CBS/BSE is recommended for micrograin identification as the quantification procedure is simpler and relies on fewer settings than for EBSD analysis (misorientation angles, filtering, noise removal, step size, etc.). The popularity of this technique for use on X20 in several research works bears testimony to this recommendation (Aghajani *et al.*, 2009; Hino *et al.*, 2013; Marx, 2019).

Dislocations were only qualitatively analysed between ex-service states for reasons mentioned in Section 8.2. Although dislocation strain softening is considered one of the main damage mechanisms for short-term tests (Kadoya *et al.*, 1997), quantitative measurement of dislocation densities is onerous and subject to large amounts of scatter (Yadav, Kalácska, *et al.*, 2016). This also hinders implementation of such measurements into microstructural damage evolution formulations (such as the Kocks–Mecking–Estrin relationship (Estrin & Mecking, 1984)) for CDM applications (Basirat *et al.*, 2012). This is one of the main reasons for not including such formulations in the CDM analysis of Chapter 7. Oruganti (2012) postulated that particle-dislocation interactions are more relevant in the long-term exposure (relevant to service-exposed material) of ferritic-martensitic steels than dislocations interactions on their own. Furthermore, reductions in mobile dislocation densities were not as obvious between ex-service states (Marx, 2019) than they are for conventional creep tested X20 (Aghajani *et al.*, 2009). Future work could focus on using electron channelling contrast imaging in SEMs for dislocation density measurement on specimens that have the same (relatively simple) metallographic preparation steps as those analysed using CBS (Cazottes *et al.*, 2019).

It is necessary to distinguish between laboratory creep tests on virgin X20 samples and service-retrieved samples that have been subjected to variable loading during plant operation. Several works have been dedicated to analyse the expected evolution of microstructure in conventional creep tests yet very few attempt to differentiate between ex-service materials[24]. One of the main difficulties associated with this type of comparative analysis is the slow evolution of microstructural features at certain life fractions as demonstrated in Figure 8.2 which has been adapted from Dobrzański *et al.* (2011:261).

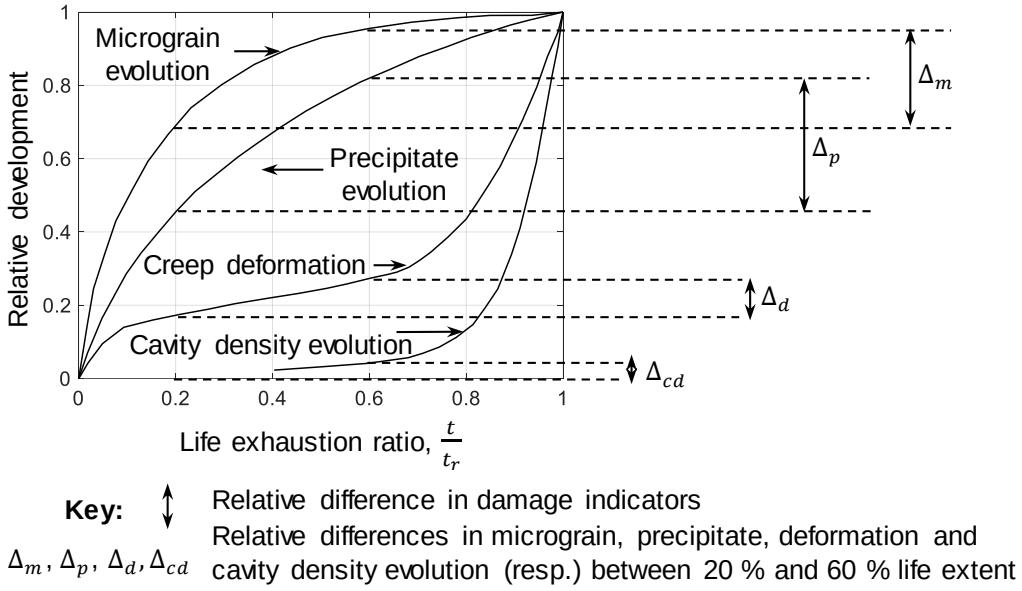

Figure 8.2: Illustration of the relative development of internal defect and microstructural damage processes vs life exhaustion. Adapted from Dobrzański *et al.* (2011:261)

[24] A literature summary is provided in Section 6.1.

The difference in sensitivity of the various damage processes to the relative comparisons of remnant life is illustrated, with micrograin and particle development being the most sensitive and cavity development being the least sensitive between 20 % and 60 % life extent as, for instance, between low and medium damage states. This is a possible explanation for why subgrain and $M_{23}C_6$ quantities were distinguishing factors between these ex-service states in Figure 6.22. The opposite is true when considering development between a 20 % life fraction and end of life, indicating that cavity quantificaiton is useful for larger differences in damage states (low and high damage states). This sensitivity coupled with microstructural scatter (Figure 6.15), material inhomogenieties (Figure 6.17), sensitivities to equipment resolutions (Subsection 6.3.3.2) and small sample populations of damage accelerating particles (Z phase in Figure 6.16) suggests that there is a difficulty in soley relying on microstructural features as a damage assessment technique. Complementary methods should be used, such as the strain-based Zener-Holloman parameter in Chapter 6 or the damage parameter optimisation method in Chapter 7, to make informed judgements of damage status.

8.4 Microstructural and creep damage measurement over nonuniform stress field

Chapter 7 focusses on the simultaneous measurement of multiple creep responses of virgin and service-aged X20 at 600 °C using DIC. This is achieved by using a hourglass specimen geometry (Muyupa *et al.*, 2017) to generate a spatial distribution of the final variable of relevance to creep in this work: stress. Unlike the previously discussed Gleeble-based techniques, the following technique is integrated into a conventional creep test setup that allows for mostly unattended and automatic testing. For this reason, longer-term testing is possible. Carrying the same theme forward from Chapter 6, creep strain-based methods related to CDM modelling are coupled with quantitative microstructural observations of the pre- and post-tested material states to make relative assessments of damage states.

The applicability of the DIC technique and CDM model employed in Chapter 7 can be expanded to the creep damage investigation of ex-service X20 on two different fronts. Firstly, Christopher and Choudhary (2018) differentiated between the effects of different heat treatments on the creep resistance of a 9 % Cr steel by comparing optimised baseline constants (ε_0', K_P, etc.). A similar approach was exploited by Hore *et al.* (2011) for the comparison of creep resistance between different power plant steels, altogether. However, as shown in the model calibration at higher stresses in Section 7.5, some baseline constants cannot be compared across wide stress ranges. This work considers, on the other hand, a second method that applies the calibrated (from virgin X20) baseline constants to service-aged X20 where the damage level is measured by fitting the initial damage parameters (D_S, D_P, D_C). These parameters are good sensors of the extent of life exhaustion when used on their own and show sound agreement with standard practices of damage evaluations.

In Chapter 7, CDM models are selected in lieu of the more mechanism-based empirical relations employed in Chapter 6 (specifically, Equation (6.1)). This is because findings of Subsection 6.4.2 suggested that little or no correlation occurred between the level of service exposure of X20 and some of the constants including stress exponents, activation energies and threshold stresses. Such expressions are also only representative of the secondary stage of creep, masking differences in other creep regimes. By contrast, CDM models have predictive capabilities that span over large ranges of stresses and temperatures and are easy to computationally implement using an automated coupled differential equation solver and

minimisation algorithm. For this reason, CDM serves as a versatile method for component life prediction.

The question that remains is why semi-empirical CDM is not as popular as purely empirical approaches amongst plant maintenance engineers. The answer lies in the efficacy of material and damage parameter estimations as well as the multiplicity of damage mechanisms that can result in the same curve shapes (see Dyson and Mclean (1998)). As a demonstration of the consistency of the damage parameters measured from the different tests discussed in this work, the approach of Ghosh (2013) is employed here. Figure 8.3 illustrates the comparison of experimental data of high damage X20 at 110 MPa from Figure 7.6c with a range of model simulations based on the range of optimised range of D_S values provided in Table 7.5. An average D_P value calculated from the medium-term tests is kept constant within this range. High damage X20 was selected due to the high scatter in properties of these samples taken from the same pipe section especially concerning hardness (Figure 7.8), cavity density (Figure 7.9), subgrain and precipitate (Figure 7.7) measurements. As noted in Figure 8.3, small changes in damage parameters result in large differences in the predicted curves due to their presence within the sinh function in Equation (7.2). More significantly, however, the experimental creep strains are encapsulated by the predicted range – showing that the CDM method in the current approach is still viable in the presence of experimental scatter typical of creep and on account of different test types. The accuracy of the extraction process is greatly improved by the high number of creep curves available per specimen through the proposed DIC methods yet the importance of repeat tests is also emphasised.

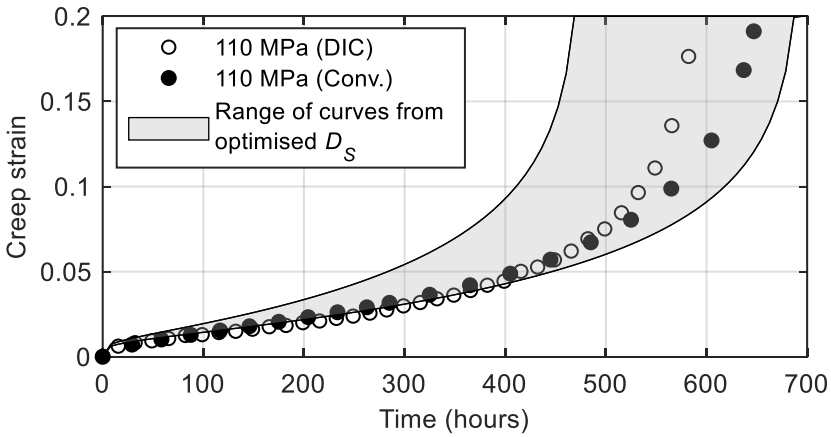

Figure 8.3: Comparison between two experimental curves for high damage X20 at 110 MPa and 600 °C and CDM model simulations calculated from a range of optimised subgrain damage parameters

Within this work, the CDM parameter optimisation benefitted heavily from the richness in creep response data offered by spatially resolving strains using DIC over nonuniform temperature and stress fields. Reflecting the sentiments of Sakanashi *et al.* (2017), the measurement of over 20 curves per specimen is not meant to directly replace 20 individual creep tests. As discussed in Subsection 7.4.1, only the curve at the centre of the specimen is complete in terms of the three creep regimes: primary, secondary and tertiary. Curves measured at lower stresses at offset locations are restricted in their development due to specimen failure. Parameters that require tertiary development, such as D_P and D_C, therefore do not directly benefit from this approach

unless longer-term tests are employed with more gradual stress profiles resulting from, for instance, an increased specimen curvature radius R in Equation (7.1).

Nonetheless, primary and secondary creep regime development in off-centre locations is more conducive to parameter optimisation based on substructure features, including D_S and dislocation hardening. As evident from higher stress tests in Figure 7.11 and Figure 7.14, the current model is unable to follow the trace of the primary region, resulting in relatively poor agreement. It is argued that this is possibly due to lack of consideration given to substructure contributions including dislocation density evolution. Physical models of substructure development, such as the dislocation-based CDM model proposed by Basirat *et al.* (2012) and Zhao *et al.* (2018), demonstrate improved accelerated (< 10 h) curve and primary creep predictions, respectively, for virgin TMF steels. Complications may arise, however, due to the difficulty involved in dislocation density characterisation as well as the lack of an apparent primary region for service-exposed materials at higher stresses as evident in Figure 7.14 and demonstrated by Roy *et al.* (2015).

Previously, Chapter 6 observed the increased presence of Laves phase as well as small volume fractions of Z phase in the higher damage states of X20. New Laves phase and Z phase precipitation is not modelled in this work due to the relatively short nature of the tests. Isik *et al.* (2014) found Laves phase to begin to nucleate after 800 h of aging at 550 °C although their size was considerably small (<100 nm), whereas Z phase was found to only nucleate after 150 000 h of aging at 600 °C (Danielsen & Hald, 2006). Chapters 5 and 6 have also shown that $M_{23}C_6$ volume fractions are significantly higher than both Z phase and Laves phase, bearing testimony to their inclusion in the precipitate damage evolution model. The coarsening rate of $M_{23}C_6$ is not greatly affected by the presence of Laves and Z phase (Prat *et al.*, 2010). The nucleation and continued growth of Laves phase is also not considered in the context of shorter-term tests on account of the balancing aspects of weakening due to solid solution depletion of Mo from the matrix and the strengthening stemming from additional subgrain wall pinning offered by the newly formed particles (Aghajani *et al.*, 2009; Yadav, Sonderegger, *et al.*, 2016). In terms of long-term (>10^5 h) testing (for example, in Figure 7.12c which is a prediction of the long-term test conducted by Aghajani *et al.* (2009)), however, the current model underpredicts times to failure by orders of magnitudes. This suggests the complex interactions of substructure evolution, precipitate morphologies and nucleation, solid solution strengthening and cavity evolution should be taken into account in future model developments for long-term predictions. For instance, this technique can be applied to the physical-based precipitate modelling methodology of Christopher and Choudhary (2019) that takes the long-term interactions of several microstructural factors into account.

8.5 Recommendations for Eskom and future work

Pacing with the fast development of power industries and efficiency demands, research has been actively oriented to the development of techniques that can provide (1) pertinent measures for the condition assessment of in-service, aged steels within an (2) accelerated time frame using (3) low volumes of sampled material. The current work is one such effort that is specifically aimed at our local power utility, Eskom.

In terms of DIC-based techniques, previous works have also contributed to (1) by providing frameworks for the assessment of fracture (Molteno & Becker, 2015) and tensile properties (Huchzermeyer & Becker, 2018). Chapters 4 – 7 considered a range of damage characterisation techniques based on several microstructural features, cavity damage, hardness, accelerated and

medium-term creep behaviour and CDM damage parameter extraction. Current life management philosophies employed by Eskom (van Zyl *et al.*, 2005) rely heavily on subjective interpretation of metallurgical replicas to provide estimates of remnant life during advanced inspection stages. Comparisons between low and medium damage X20 in this work, however, revealed the deficiencies of surface replication in fully characterising the damage state of service-exposed components. For this reason, the alternative techniques proposed in this work can complement existing techniques especially when heterogeneity of cavity distributions is encountered in the material or small differences exist between ex-service states. Although these evaluation approaches were tested on X20 in this work, all aspects can be directly translated to the assessment of P91 which is the replacement steel for X20 in modern power stations in SA (Bendick *et al.*, 1993). In fact, the temperatures and stresses employed in this work are in the ideal testing range for P91 (Murchú *et al.*, 2017).

Although it is appropriate to quantitatively compare the damage verdicts of the proposed techniques, their adequacy should not be judged on the agreement of numbers. This is because they assess different elements of creep strength in TMF steels that evolve in very complicated and interconnected ways during service exposure. The expected trends in subgrain growth, for instance, in a monotonic, uniaxial creep test performed in a laboratory setting should not be expected in service-exposed materials that undergo variable loading conditions, welding procedures, environmental attacks, etc. In this sense, all structural health assessment techniques approach qualification of service-exposed material in different manners yet none of them can exactly account for the complex nature of creep in service. Extensive archiving of site experience and evaluations of different service-exposed component materials is therefore necessary before the techniques of the current work can be prescribed for the general assessment of damage in high energy piping.

DIC is an excellent tool for achieving (2) and (3) above due to the richness in data from full-field approaches. As evident from Chapters 4 and 5, oftentimes these techniques can provide the same amount of data from a single specimen and test compared to several conventional test pieces and tests. Chapters 6 and 7 showed that accelerated tests can also provide comparative damage evaluations of ex-service material. This is particularly important in the power industry as fast turnaround times for material evaluation can assist in maintaining timely repair schedules and preventing unnecessary breakdowns (EPRI, 2007). It is also worth mentioning that on-site strain monitoring of pipe surfaces using DIC is not new to the power industry as demonstrated by the development of the ARCMAC (auto-reference creep management and control) systems for in-service life monitoring (Morris *et al.*, 2007) as well as feasibility studies of on-site DIC systems conducted by EPPEI students (Cardenas, 2018).

Within the power industry, one of the most common modes of material preservation in terms of (3) is small-sample techniques of which small punch creep testing (SPT) is the most documented (Maharaj *et al.*, 2009). In the context of Eskom, several EPPEI research projects have been directed at using SPT for plant steel characterisation, including embrittlement studies on ex-service steam turbine material at UCT by Tshamano (2017) as well as commercial projects aimed at site-specific weld characterisation through the eNtsa institute at NMU[25]. As plant maintenance engineers become more accepting of and familiar with this testing technique, future work is appropriately aligned with adapting SPT for use with DIC. Advantages of this integration include the ability to translate the standard output of SPT (load-displacement) into equivalent forms useful to material property and damage characterisation (stress-strain) using the full-field properties of DIC and FEM. As part of achieving these future aims with ongoing

[25] Headed by Prof. DG Hattingh: https://entsa.mandela.ac.za/research

work, a preliminary study in collaboration with UoB on *ex situ* DIC-SPT integration was conducted as outlined in Appendix B[26]. Highlights of this study include the ability to capture strain field development from interrupted small punch creep tests on X20 which (with ongoing work) can be combined with FEM-calculated stress fields to provide input to the CDM models presented in Chapter 7. At the date of writing of this document, one EPPEI project is underway on advancing this concept[27]. The technique was also employed for room temperature assessment of P91 properties in collaboration with the UoB (Alaleeli, 2019). Future extensions to *in situ* implementations are considered to be a useful advancement for material-efficient damage monitoring methods, especially at service-weakened and site-specific locations, such as welds.

Although beyond the scope of this work, it is envisaged that this work can assist Eskom in the future in terms of (1) above by adopting these techniques into their assessment philosophies through compiling a database of microstructural (subgrain and $M_{23}C_6$ precipitates) features, hardness values, Zener-Hollomon parameters and CDM-based damage parameters measured from a wide range of service exposures. This has the potential to subcategorise remnant life classifications beyond the four damage levels currently employed by Eskom (Molokwane, 2013). Estimated initial damage states could also serve to predict the remnant life of component materials. More informed maintenance decisions can be made in this way by eliminating overconservatism with resulting cost and plant service continuity benefits.

[26] This work benefitted notably from the collaboration with the Solid Mechanics research group under the supervision of Dr. Mahmoud Mostafavi of the University of Bristol.
[27] MSc project (I. Stracey): http://www.mateng.uct.ac.za/mateng/people/postgraduate-students/msc/stracey

9 Conclusions

This work was motivated through four objectives as highlighted in Chapter 1. An experimental setup that generates variable temperature fields was developed and consequently used to extract multiple properties, including creep responses, of virgin and ex-service X20 using DIC. The niche of DIC-based creep deformation measurements in damage evaluation of ex-service X20 was then explored together with underlying microstructural features of creep deterioration. The broadening of these techniques to medium-term tests with variable stress fields was then achieved using conventional creep testing setups. The results highlighted the need for simultaneous consideration of multiple damage sources when making comparative integrity classifications of materials. The key contributions are outlined below:

- Multiple measurements of temperature-sensitive material properties are achieved through synchronisation of DIC-obtained full-field strain, stress and temperature maps over nonuniform temperature fields generated by Gleeble testing. The capability of the DIC setup, which is adapted for high signal-to-noise measurement of strains at elevated temperatures, is demonstrated by measuring strain-sensitive Young's moduli and Poisson's ratios of virgin (undamaged) X20 at temperatures ranging from 480 – 600 °C. The potential exists for measurements at temperatures approaching 900 °C. The simultaneous measurement of tensile properties over a nonuniform thermal field is a unique contribution of this work.
- Creep curve measurement over nonuniform thermal fields is achieved by applying the Gleebe-DIC technique to accelerated creep (high stress) tests lasting for less than 10 h. Differences in creep response between ex-service X20 with varying conditions of exposure is perceptible by this technique. Specifically, higher creep rates and shorter rupture times are encountered for higher damage states that were initially categorised for damage based on a cavity density assessment using surface replicas. The Gleeble-DIC technique is a viable complement to conventional damage evaluations, such as the surface replication technique. The simultaneous measurement of accelerated creep curves over a nonuniform thermal field is a unique contribution of this work.
- Several accelerated creep curves over a temperature range of 550 – 600 °C are extracted from single specimens of virgin and ex-service X20 of varying damage qualifications. Microstructural characterisation of subgrain and precipitate distributions are achieved through advanced electron microscopy techniques and complement the observed deformation behaviour which was modelled using an analytical expression of the minimum creep rate. In general, higher Zener-Hollomon values correlated with higher damage states. The gap in creep resistance between the low and medium damage states encountered in this work was not as wide as the assessment of Laves phase and cavity densities would suggest. Instead, dense $M_{23}C_6$ distributions and similar Zener-Hollomon values to the low damage counterpart would place the medium damage X20 in a lower damage category than initially indicated by surface replication. The simultaneous measurement of quantitative damage indicators based on creep deformation and microstructural elements over a nonuniform thermal field is a unique contribution of this work.
- Medium-term creep testing (at lower stresses) is realised using DIC to measure strains over a nonuniform stress field generated by a waisted specimen geometry. The dense collection of creep curves in various stages of regime development from this technique is ideal for the calibration of baseline constants of a CDM model which was selected based on microstructural observations of the specimen gauge regions. Good agreement between CDM-predicted and experimental data is realised for medium-term tests. Subgrain and

precipitate damage parameters are then optimised for by fitting to the experimental creep responses of ex-service materials. These parameters serve as damage sensors, have direct foundations in observable microstructure and their measurement from waisted specimens preserves material volume. The simultaneous measurement of CDM-based, quantitative damage parameters over a nonuniform stress field is a unique contribution of this work.

- From future endeavors, maintenance strategies of Eskom power plants could benefit from supplementing existing life exhaustion estimation techniques with the strain-based indicators discussed in this work. Such approaches include integrating damage modelling with small punch creep-DIC setups for small sample, accelerated creep testing. Spatially resolved weld damage characterisation using DIC is also a consideration for future industrial application. These processes are essential contributors to achieving stable power supply from reliable plant operation.

Appendix A Experimental testing matrix

Table A.1 provides a summary of the material type, applied stress (given as the nominal engineering stress), load and temperature parameters and specimen geometry type of all the mechanical tests conducted in this work.

Test type	Material	T (°C)	Stress (MPa)	No. of tests	Geometry
Variable T tensile (Gleeble)	Virgin X20	550-600	< 200	5	Flat
				1	Square
Accelerated, variable T creep (Gleeble)			250	2	Flat
			200	1	Square
			260	1	
	Low damage (LD) X20		200	1 | 1	Flat | Square
			250	1	Flat
			260	1	
			180	1	Square
			190	1	
	Medium damage (MD) X20		250	2 | 1	Flat | Square
			350	1	
			260	2	
			300	1	
	High damage (HD) X20		200	1 | 1	Flat | Square
			250	1 | 1	Flat | Square
			260	1 | 1	Flat | Square
Medium-term, variable stress	Virgin X20	600	150 (max)	1	Hourglass
	LD X20			1	
	MD X20			1	
	HD X20			1	
			110 (max)	1	
Medium-term, conventional	Virgin X20	600	140	1	ASTM E139 ⌀5.65 mm
			250	1	
	LD X20		140	1	
			250	1	
	MD X20	580	185	1	ASTM E139 ⌀5.65 mm with flat gauge region
		600	250	1	ASTM E139 ⌀5.65 mm
			140	1	
	HD X20		110 | 140	1 | 1	
Test type	**Material**	**T (°C)**	**Load (N)**	**No. of tests**	**Geometry**
Small punch	P91	600	314	3	CWA 15627 disc
	Virgin X20	600	500	5	
		600	475	2	
		600	675	1	
	LD X20	600	475	1	
		630	520	1	
	MD X20	630	520	1	
	HD X20	600	500	5	
	PM-10	630	520	4	

Table A.1: Experimental matrix for mechanical tests. T: temperature

Appendix B Digital image correlation technique for the small punch testing of aged material

This appendix serves as a supplement to the discussions in Section 8.5 with regards to future work concerning the use of digital image correlation in small punch creep testing for damage assessment. It is written in the form of a brief article to provide context to a preliminary study that has originated from this work.

B.1 Introduction

Small punch testing (SPT) has garnered increased attention in the maintenance programmes of aging power plants. Typical constant-force small punch creep testing (SPCT) involves penetrating a disc of material using a hemispherical punch or ball at constant load, high temperatures and within an inert atmosphere whilst punch displacement and/or disc deflection is measured. Such an approach boasts a significant advantage for life assessment of in-service plant materials due to the small disc sizes (Ø8 mm, 0.5 mm thickness) that makes sample extraction possible without impairing the operability of the host component (Rouse *et al.*, 2013). Site-specific material property assessment of, for instance, welds and heat-affected zone (HAZ) regions, is also possible through this technique.

The popularity of the technique is highlighted in the extensive literature presence of applications to in-service power plant materials. Applications of SPT include tensile property measurement from load-displacement curves of aged rotor steels (Fleury & Ha, 1998; Madia *et al.*, 2013) as well as across different weld regions (Komazaki *et al.*, 2009). This technique was also expanded to characterise the embrittlement of aged materials through the measurement of temperature-dependent fracture toughness and energy (Ha & Fleury, 1998; Madia *et al.*, 2013). The SPCT has been applied to creep property measurement of numerous virgin (Ma *et al.*, 2009; Selent *et al.*, 2016), aged base (Evans & Wang, 2008; Yang *et al.*, 2017) and weldment (Kim & Lim, 2008; Blagoeva & Hurst, 2009; Izaki *et al.*, 2009) rotor, steam piping and boiler steels. Several researchers have also employed SPCT within the framework of the European collaborative COPERNICUS project with the aim of assessing the remnant life of X20CrMoV12-1 (X20) and other steels using creep stress exponents and activation energies from Dorn relations (Ule *et al.*, 1999).

Despite the wide-scale applications of SPCT, the technique involves several challenges that are not normally associated with traditional testing including sensitivities to: geometrical uncertainties in the experimental setup such as the indenter size and eccentricity from the disc centre (Cortellino *et al.*, 2014; Komazaki *et al.*, 2017); upper die clamping conditions (Andrés & Dymáček, 2016); differences in disc specimen thickness with a direct effect on creep rupture times (Ule *et al.*, 2003); atmospheric conditions (Nakata *et al.*, 2016a); oxidation (Kobayashi & Takei, 2014) as well as friction between punch components and the disc (Nakata *et al.*, 2016b).

Although these issues have been largely mitigated through the introduction of a code of practice (CEN, 2007) with strict specifications placed on disc and punch geometry and test procedures, the interpretation of the SPCT data (displacement and load) and its equivalence to standard creep test data (specifically strain and stress) remains the focal point of many research works due to the complex stress and strain states (Hyde *et al.*, 2010). For establishing the equivalent

stress, conversion factors (calculating equivalent stress from load) based on Chakrabarty membrane stretching theory (Holmström *et al.*, 2018) as well as stress distributions calculated from finite element (FE) modelling (Nakata *et al.*, 2016b) have been employed. Maximum equivalent strains can be estimated from simple analytical relationships with the central deflection (Yang & Wang, 2003), thickness changes at the thinnest point in the disc (Lee *et al.*, 2016) as well as from FE models (Dymáček & Milička, 2009). The former two methods only provide single point strain estimates whereas the strain field output from FE analysis is sensitive to numerous unknown parameters, such as friction coefficients and the selected creep model parameters (Zhou *et al.*, 2010). To the authors' knowledge, no attempts have been made to measure the full-field, surface strain maps of SPCT specimens.

To this end, digital image correlation (DIC) is considered an ideal candidate for full-field strain measurement of SPCT disc samples due to its noncontact nature as well as its lack of restriction on measurement length scales (Berfield *et al.*, 2007). Aydin *et al.* (2018) applied two-camera DIC to the *in situ* measurement of the fracture ball heights of steel sheets during an Erichsen cupping test which shares many similarities with a small punch test. However, no strain distributions were presented from the DIC data. Strain measurement using a stereo-microscope-DIC technique during a hydraulic bulge test on specimens with dimensions similar to that of SPCT was achieved by Ren *et al.* (2015).

This work investigates the feasibility of using a stereo-microscope-DIC technique on the measurement of strain fields across a small punch creep tested disc of virgin and ex-service X20 steel. This includes: the design of a small punch creep setup; design of a stereo-microscope DIC setup to capture images with a durable, high resolution speckle pattern for strain measurement; development of a strain-processing algorithm; suggestions of a FE model to verify steady-state stresses; and comparisons between the strain developments between various states of X20. Due to the physical difficulties associated with obtaining images on a fine scale in a confined space (< Ø4 mm viewing field) at high temperatures and under argon atmosphere, DIC images are captured *ex situ*.

B.2 Experimental details

B.2.1 Materials and specimen geometry

The chemical composition of the X20 material used in this study is given in Table 5.1. Rods of 8 mm diameter longitudinally aligned with the pipe axis were cut from the centre of the pipe thickness as shown in Figure B.1a. Discs of ~1.0 mm were wire cut from the rods and then polished down using 220 grit followed by 1000 grit silica carbide paper on both sides until an average thickness of approximately 0.5 ± 0.01 mm was measured. A comparison of the disc size with traditional creep specimen geometries is shown in Figure B.1b.

B.2.2 Small punch creep testing

The punch setup and geometric detail of the punch body is shown in Figure B.2a and b, respectively. The punch was designed in accordance with the CEN CWA 15627 guidelines (CEN, 2007) and consists of an alumina oxide ceramic ball of 2.5 mm diameter and a Nimonic 80A punch body. Load is applied at 2 N/s using an Instron 1341 servohydraulic tester through the punch head onto the ceramic ball, which then causes the disc to bulge into a 4 mm diameter recess. Temperature is measured by a K-type thermocouple positioned against the disc and is kept within 2 °C of the setpoint as the punch is heated within a single-zone tube furnace. The periphery of the disc is clamped by the upper die as in a classic "small punch bulge test" as

outlined in CWA 15627. Argon gas is supplied to the bottom disc surface by a capillary tube at a rate of 0.2 L/min. Deflection of the punch was measured using an LVDT with a resolution of 1 μm.

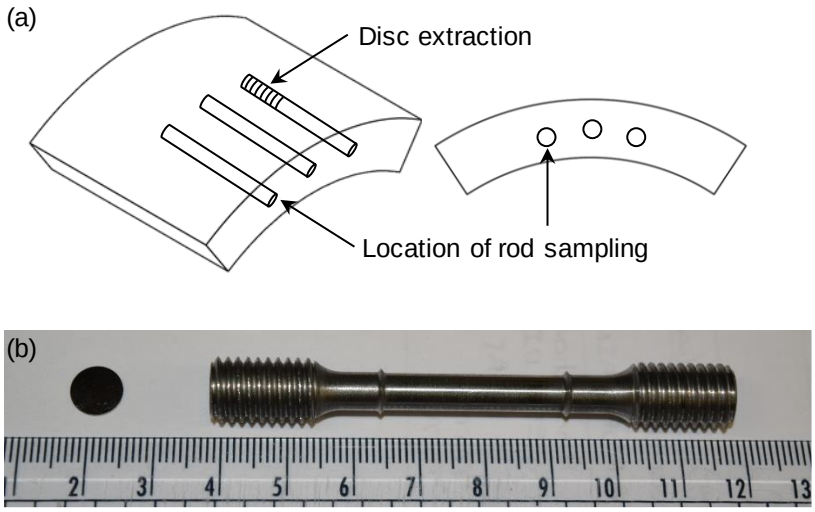

Figure B.1: (a) Sampling schematic of rods from which discs are wire cut and (b) a visual comparison of dimensions of small punch creep discs (left) versus traditional creep testing specimen geometries (right)

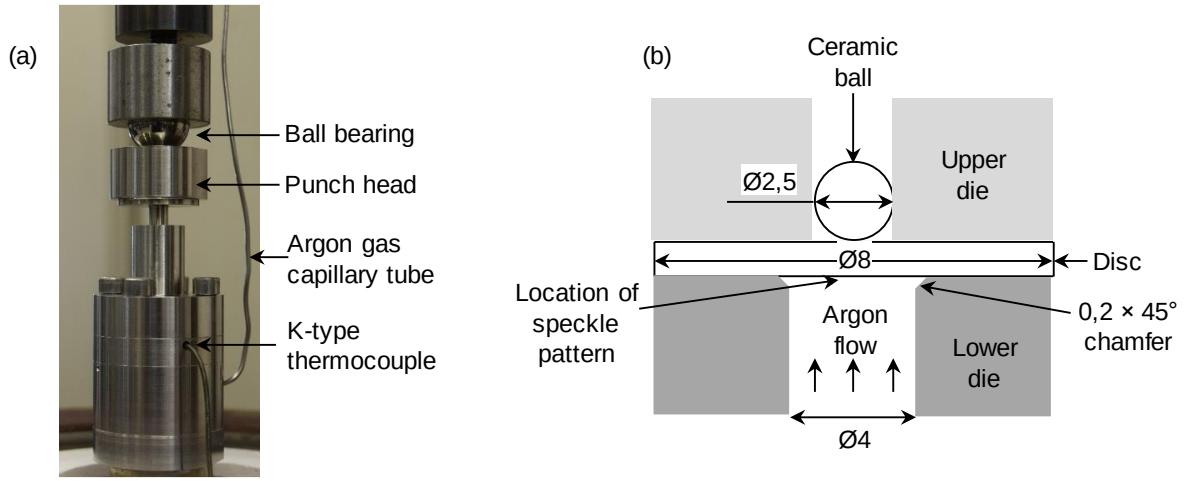

Figure B.2: (a) Photograph of small punch creep setup and (b) dimensions of the punch body geometry supplied in mm

In order to prevent speckle pattern flaking due to excessive strains, the discs are prebulged at the same temperature and to the same loading used in the subsequent creep test. Such an approach was shown by Ule *et al.* (2003) to have no effect on the creep curve development in terms of rupture time and minimum creep rates. Following the prebulging, the load is removed and the "sombrero"-shaped disc is removed for speckle patterning.

B.2.3 Speckle pattern application

The bulged-out surface of the disc was ultrasonically cleaned with acetone and coated with white VHT Flameproof heat-resistant paint. Because speckle sizes produced from normal spray can application are too large (30 – 80 μm) for the current work, an airbrush was employed. A fine mist of undiluted VHT black speckles was applied to the wet paint surface using a generic model SP180KTG airbrush with a 0.2 mm needle using a 30 cm stand-off distance, a medium airflow (based on three full turns of the air regulating screw) and 25 kPa working pressure. These settings were selected based on the guidelines offered by Lionello and Cristofolini (2014) for applying optimal speckle distributions. Resulting speckle sizes ranged from 10 – 13 μm as measured using image thresholding in ImageJ (Johannes *et al.*, 2012) of micrographs taken by a Zeiss Imager M2 Axio light microscope at 200× magnification. With the magnification factor of 0.24 pixels/μm encountered in the calibrated DIC images, the average speckle size was therefore covered by approximately 3 pixels as recommended by Schreier *et al*. (2009) for optimal correlation. The speckle pattern, as shown in Figure B.3b, was air cured for 24 h before testing to harden the pattern for handling.

B.2.4 Stereo-microscope DIC setup

The patterned sombrero-shaped disc (shown in Figure B.3b) is recorded using the DIC hardware summarised in Table B.1. Image acquisition was performed using a Zeiss SteREO Discovery.V12 stereo-microscope retrofitted by LaVision to include two cameras and 3D micropositioning translation stages within an integrated system. Diffuse illumination was provided by a 7 W, pure white colour temperature ring light mounted over the microscope lens. Disc samples were mounted on a sample holder fixed to a rigid tripod at about 240 mm from the lens front. A photograph of the setup is provided in Figure B.3a. Prior to creep testing, a reference image is taken of the painted, sombrero-shaped disc with markings made on the specimen holder to assist in aligning the disc to its original (prior to testing) position. At a chosen time stamp, the test is interrupted with load removed followed by gradual cooling and removal of the crept disc. This disc is aligned and again imaged, and the process is repeated for a new disc.

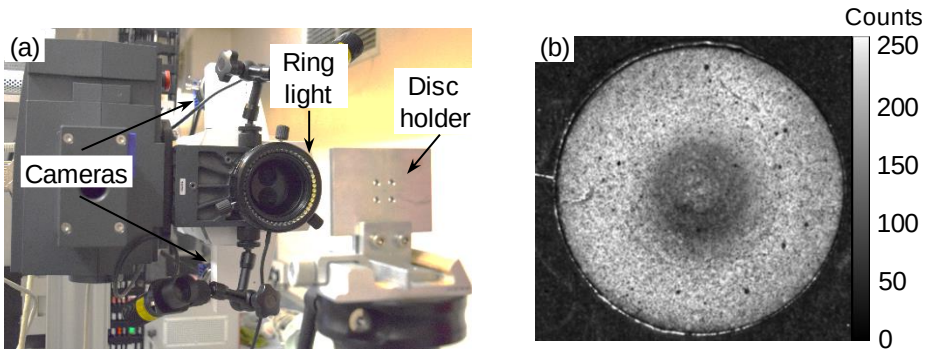

Figure B.3: Photograph of the (a) stereo-microscope DIC setup and (b) an example view of a speckled preformed disc

Table B.1: DIC hardware details for small punch creep test

Cameras	Imager M-lite 5M on a Zeiss SteREO Discovery. V12 stereo-microscope
Image resolution	2464 × 2056 pixels^2
Lighting	48 LED VisiLight R-LED-66 ring light (7 W)
Lens	Achromat S lens, ×0.3 magnification
Aperture	Open position
Field of view	10.5 × 8.7 mm^2
Image magnification	240 pixels/mm
Stereo-angle	5.8°
Free working distance	236 mm
Patterning method	White, heat-resistant base coat with fine black speckles applied using airbrush
Approximate pattern feature size	3 pixels (13 μm)

B.2.5 Processing methodology

Due to the inherent complexities of the stress and strain state of small punch testing (Yang & Wang, 2003), DIC measured displacements were fitted with a piecewise second-order polynomial over a square window of 11 points using MATLAB R2019a. Prior to fitting, outlier removal based on values greater than three local standard deviations from the local mean was performed to eliminate spurious measurements caused by image artefacts (for instance, dust particles on the microscope lenses). Strains are obtained through differentiation of the fitted displacement fields. A summary of the software parameters is provided in Table B.2. For improving the disc alignment relative to the reference disc position, subpixel rigid body shift and rotation correction is performed by using correlation windows of 121 pixels size on larger speckle features on the disc periphery.

B.2.6 Rigid body translation and noise floor tests

In order to characterise displacement variance and bias error in the current setup, baseline noise and rigid body translation tests were conducted, respectively, according to Jones and Iadicola (2018). The displacements and associated strains were computed using a subset size of 41 pixels and 10 pixel step size based on the processing methodology outlined in Appendix B.2.5. The maximum applied translations were selected based on the anticipated deformations resulting from the small punch creep testing (Stoyanov, 2013). Comparisons between applied and DIC in-plane and out-of-plane displacements is shown in Figure B.4a and b, respectively. Displacement measurements correspond well in both directions with average root-mean-square values of 8 μm and 9 μm, respectively.

Insignificant differences were noted in the error analysis for other subset sizes (21 – 81 pixels). Consequently, a subset size of 41 pixels was selected based on the speckle size analysis discussed in Appendix B.2.3. This results on average in 7 × 7 speckles per subset (assuming 50 % speckle coverage) and a displacement measurement spatial resolution of about 250 μm. Self-correlation tests performed on a set of five stationary images using the selected subset size resulted in baseline displacement and strain errors as shown in Table B.2.

Table B.2: DIC software details for small punch creep test

DIC software	LaVision DaVis, 8.4.0
Subset size	41 pixels (0.17 mm)
Step size	10 pixels (0.04 mm)
Displacement noise floor	In-plane: 0.03 pixels (0.11 μm), Out-of-plane: 0.2 pixels (0.8 μm)
Strain noise floor	32 με (averaged between vertical and horizontal directions)
Subset shape function	First-order
Matching criterion	Zero-normalised sum of square differences (ZNSSD)
Grey level interpolant	Sixth-order spline
Prefiltering of displacements	Spatial piecewise second-order fit with moving mean outlier removal
Strain window	11 data points
Virtual strain gauge (VSG) size	131 pixels (0.55 mm)

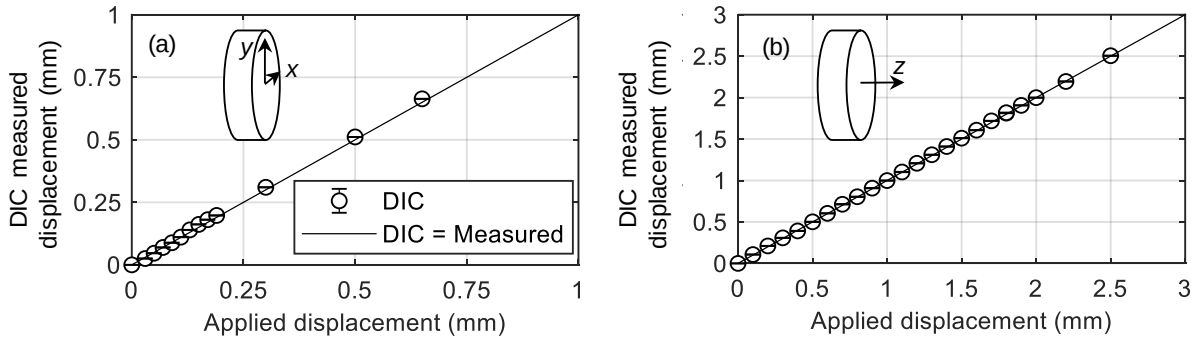

Figure B.4: Comparison between DIC measured displacements and applied translations for (a) in-plane and (b) out-of-plane rigid body tests for a 41 × 41 pixels^2 subset and 10 pixel step size

B.2.7 Stress analysis

Although not shown in this work, a FE elastic-plastic-creep damage model is currently in development for the assessment of equivalent von Mises stresses for future applications of this work[28] using the ABAQUS FE solver. Briefly, this two-dimensional axisymmetric model uses bilinear 4-node CAX4R elements to mesh the disc and considers the punch ball, upper and lower dies as rigid bodies. Coulomb friction is modelled between all contact points. Load is applied as a point force through the punch ball centre. Deformation from initial loading is established from elastic-plastic data obtained from Chapter 5, whilst a combination of CREEP, UVARM and USDFLD user subroutines calculates subsequent creep deformation as a function of the equivalent stress through the Oruganti *et al.* (2011) damage model employed in Chapter 7.

B.3 Examples of results

A demonstration of the *ex situ* small punch strain measurements using DIC is shown in Figure B.5 along with the corresponding time-displacement curves. The tested material was extracted from the fusion region of a weldment between high damage X20 and low damage X20 as well as from the low damage parent material. For the weldment, a load of 520 N and a temperature of 630 °C was selected in order to accelerate creep curve development within 3 h. The strain maps are measured when the tests are interrupted at the indicated times on the time-displacement curves.

Several observations can be made from the resulting distributions of maximum normal strains on the disc surfaces. Firstly, strains on the disc periphery are near zero due to the clamping mechanism of the upper die. Secondly, a concentrated annulus of high strains forms around the centre of the disc and corresponds to the contact area between the ball and the disc (Chen, Xie, *et al.*, 2012). This ring proceeds to widen and increase in strain magnitude with increasing punch displacement as a larger area of the ball contacts the deforming disc, resulting in a switch from plastic bending behaviour to plastic membrane stretching as the disc deflection exceeds the initial thickness of the disc (Yang & Wang, 2003). Finally, the low damage X20 demonstrates less creep resistance than the weldment for identical testing conditions. As shown in the top left of Figure B.5, this results in higher strain values and a thicker annulus than the weldment disc strain maps. This observation also confirms the FE predictions of Cortellino *et al.* (2017) where peak equivalent plastic strains and simulated creep damage develop at the base of the disc at off-centre contact regions with the punch. This strain concentration also correlates with the locations of through thickness cracks that results in disc failure as shown in the top right of Figure B.5 for high damage parent X20.

DIC strain maps of SPC-tested virgin X20 is shown in Figure B.6 for a 3 h test time at 600 °C and 500 N. This gridded data is easily converted to polar coordinates through standard strain transformation equations, with circumferential $\varepsilon_{\theta\theta}$ and meridional ε_{RR} strains shown in Figure B.6a and b, respectively. As expected, ε_{RR} values are negative near the clamped edge as material is pulled into the disc centre where material is, in turn, radially stretched by the ball punch. Such plots can also be used to assess the geometric concentricity and uniformity of clamping conditions by considering the deviations from axisymmetric distributions as shown in Figure B.6b.

[28] In collaboration with Dr. S. Dey of the Solid Mechanics Research Group of the University of Bristol

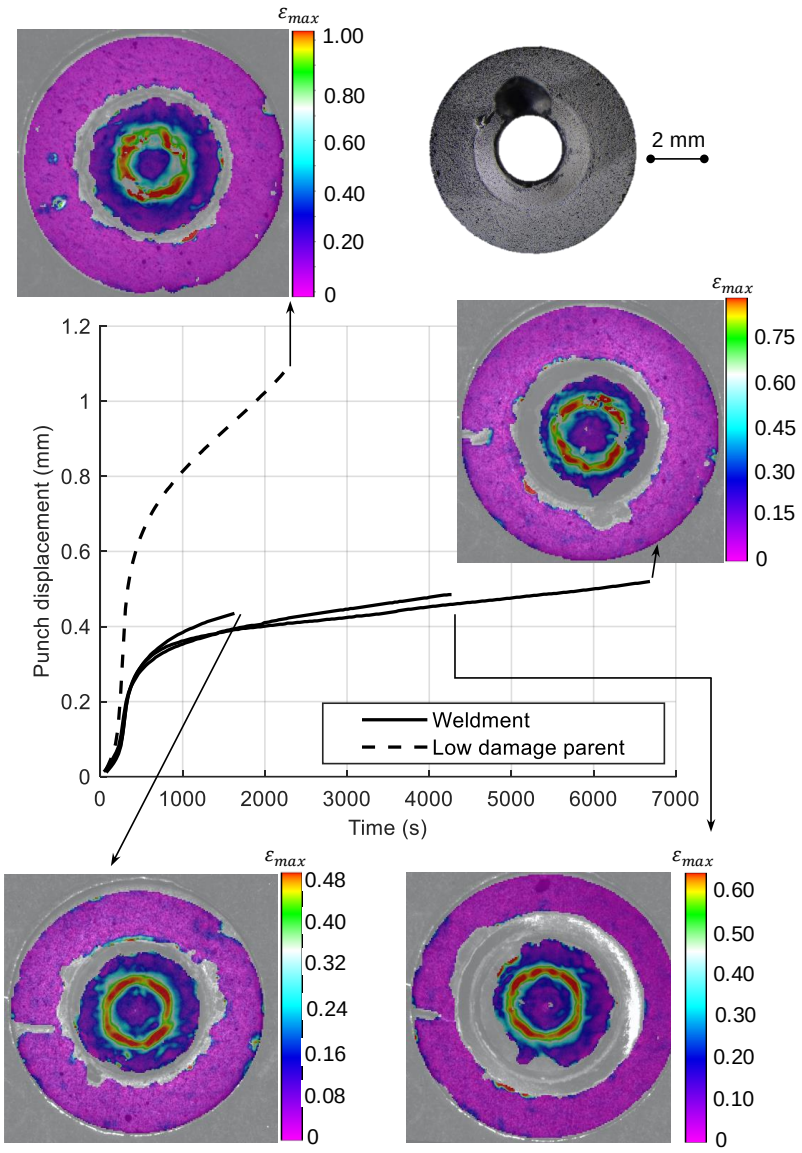

Figure B.5: DIC measurements of maximum normal strain maps across small punch tested weldment and low damage parent discs with corresponding time-punch displacement curves

B.4 Future considerations and improvements

The conversion of load-displacement data output from small punch testing into stress-strain relations required by creep analysis has long been a challenge encountered by researchers (Yang & Wang, 2003). This appendix has highlighted the application of full-field strain mapping to SPCT. Future aims for this technique include combining the DIC strain fields with data from other streams to aid damage assessment. This is illustrated in Figure B.7 where average interrupted strains measured from the disc surface using DIC is combined with the stress evolution generated by the FE model proposed in Appendix B.2.7. For instance, radial locations of maximum equivalent creep strain from DIC maps can be used to correlate with the corresponding equivalent stress from a FE model. Temperature from thermocouple measurements is also included in the dataset. This data is combined at timesteps for direct input into CDM formulations presented in Chapter 7 (specifically Equations (7.2) to (7.7)) or through

a FEM-updating scheme to extract damage parameters. This forms part of ongoing work aimed at material-efficient damage extraction methods for service-retrieved power plant steels.

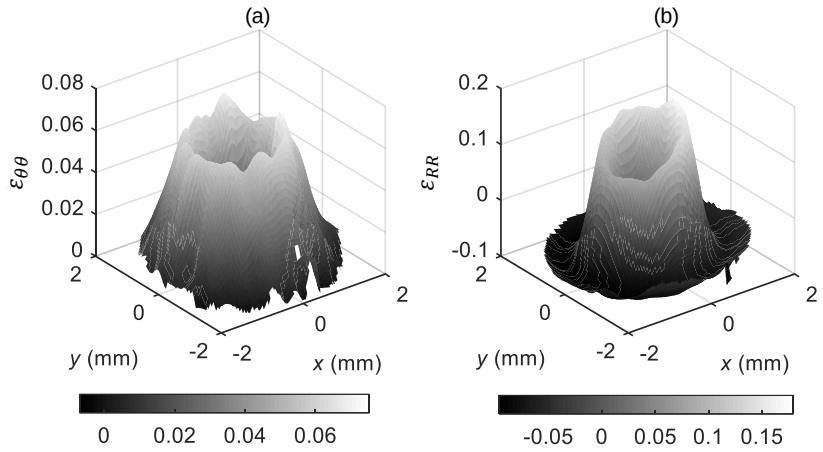

Figure B.6: Maps of DIC-measured (a) circumferential and (b) meridional strains obtained from small punch creep testing of virgin X20

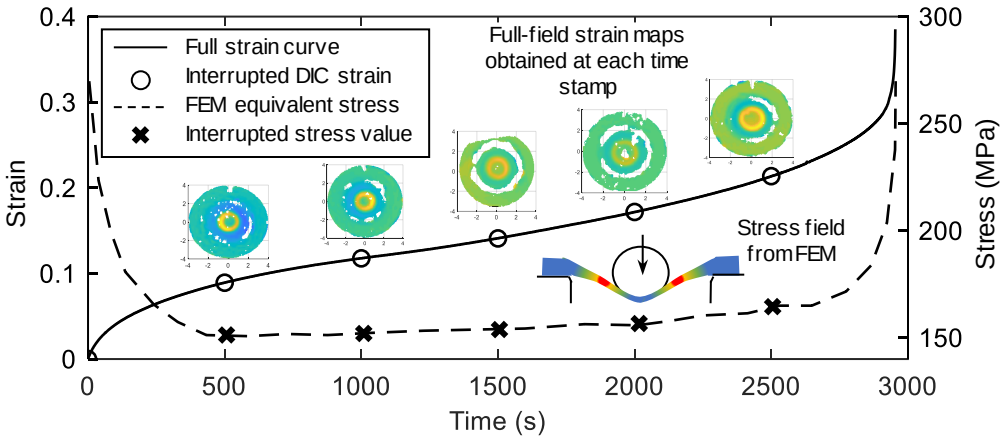

Figure B.7: Combination of small punch data stress using DIC and FEM

Further improvements related to DIC-SPCT techniques involve stream-lining the measurement process. *Ex situ* DIC analysis of SPC tested specimens investigated in the current work involves many experimental difficulties including the laborious task of interrupting tests, the requirement of more specimens and the sensitivity of the speckle pattern during handling. For this reason, future efforts should be directed to *in situ* SPCT using DIC. There are several challenges associated with this that will require experimental ingenuity, including the positioning of cameras with sufficient lighting within a confined space (< Ø4 mm viewing field) at high temperatures and under argon atmosphere. If successful, the combination of this method with the FE analysis for steady-state stresses calculation will allow for direct conversion of load-displacement curves into their equivalent stress-strain counterparts which is essential for predictive material models (Chen *et al.*, 2013). Such maps can also be exploited by FEM-updating or virtual work methods for the determination of material properties (Huchzermeyer & Becker, 2018) whilst preserving material economy.

List of references

Abdallah, Z., Gray, V., Whittaker, M. & Perkins, K. 2014. A critical analysis of the conventionally employed creep lifing methods. *Materials*, 7(5):3371-3398.

Abe, F. 2014. Development of creep-resistant steels and alloys for use in power plants, in A. Shirzadi & S. Jackson (eds.). *Structural alloys for power plants: Operational challenges and high-temperature materials*. Cambridge: Woodhead Publishing. 250-293.

Abe, F. 2015. Creep behavior, deformation mechanisms, and creep life of mod.9Cr-1Mo steel. *Metallurgical and Materials Transactions A: Physical Metallurgy and Materials Science*, 46(12):5610-5625.

Abe, F., Kern, T-U. & Viswanathan, R. (eds.). 2008. *Creep-resistant steels*. Cambridge: Woodhead Publishing.

Aghajani, A. 2009. *Evolution of microstructure during long term creep of a tempered martensite ferritic steel*. Published doctoral dissertation. Göttingen: Cuvillier Verlag.

Aghajani, A., Somsen, C. & Eggeler, G. 2009. On the effect of long-term creep on the microstructure of a 12 % chromium tempered martensite ferritic steel. *Acta Materialia*, 57(17):5093-5106.

Alaleeli, M. 2019. Characterisation of tensile properties and creep damage using the small punch test. Unpublished Master's thesis. Bristol: University of Bristol.

Ali, B. 2014. Development of non-destructive small specimen creep testing techniques. Unpublished doctoral dissertation. Nottingham: University of Nottingham [Online]. Available: http://eprints.nottingham.ac.uk/14121/ [2019, September 9].

Andrés, D. & Dymáček, P. 2016. Study of the upper die clamping conditions in the small punch test. *Theoretical and Applied Fracture Mechanics*, 86:117-123.

Ankit, K. 2009. Remaining creep life assessment techniques based on creep cavitation modeling. *Metallurgical and Materials Transactions A: Physical Metallurgy and Materials Science*, 40(5):1013-1018.

APEC. 2005. *Costs and effectiveness of upgrading and refurbishing older coal-fired power plants in developing APEC economies: Energy Working Group project EWG 04/2003T*. Cypress, TX: APEC [Online]. Available: https://www.apec.org/-/media/APEC/Publications/2004/6/Costs-and-Effectiveness-of-Upgrading-and-Refurbishing-Older-CoalFired-Power-Plants-in-Developing-APE/APECReport204RE017.pdf [2018, April 17].

Armaki, H.G., Chen, R., Maruyama, K. & Igarashi, M. 2011. Creep behavior and degradation of subgrain structures pinned by nanoscale precipitates in strength-enhanced 5 to 12 pct Cr ferritic steels. *Metallurgical and Materials Transactions A: Physical Metallurgy and Materials Science*, 42:3084-3094.

Arzt, E. & Rosler, J. 1988. The kinetics of dislocation climb over hard particles II. Effects of an attractive particle-dislocation interaction. *Acta Metallurgica*, 36(4):1053-1060.

Arzt, E. & Wilkinson, D.S. 1986. Threshold stresses for dislocation climb over hard particles: The effect of an attractive interaction. *Acta Metallurgica*, 34(10):1893-1898.

Ashby, M.F. 1972. A first report on deformation-mechanism maps. *Acta Metallurgica*, 20(7):887-897.

ASTM. 2002. *ASTM E 1351: Standard practice for production and evaluation of field metallographic replicas*. West Conshohocken, PA, USA: ASTM International.

ASTM. 2009. *ASTM E21: Standard test methods for elevated temperature tension tests of metallic materials*. West Conshohocken, PA: ASTM International.

ASTM. 2011a. *ASTM E139: Standard test methods for conducting creep, creep-rupture, and stress-rupture tests of metallic materials*. West Conshohocken, PA, USA: ASTM International.

ASTM. 2011b. *ASTM E8/E8M: Standard test methods for tension testing of metallic materials*. West Conshohocken, PA, USA: ASTM International.

ASTM. 2012. *ASTM E384: Standard test method for Knoop and Vickers hardness of materials*. West Conshohocken, PA, USA: ASTM International.

Auerkari, P., Holmström, S., Veivo, J. & Salonen, J. 2007. Creep damage and expected creep life for welded 9-11% Cr steels. *International Journal of Pressure Vessels and Piping*, 84(1-2):69-74.

Auerkari, P., Salonen, J., Holmström, S., Laukkanen, A., Rantala, J. & Nikkarila, R. 2013. Creep damage and long term life modelling of an X20 steam line component. *Engineering Failure Analysis*, 35:508-515.

Avril, S., Bonnet, M., Bretelle, A.-S., Grédiac, M., Hild, F., Ienny, P., Latourte, F., Lemosse, D., Pagano, S., Pagnacco, E. & Pierron, F. 2008. Overview of identification methods of mechanical parameters based on full-field measurements. *Experimental Mechanics*, 48(4):381-402.

Aydin, M., Wu, X., Cetinkaya, K., Yasar, M. & Kadi, I. 2018. Application of digital image correlation technique to Erichsen cupping test. *Engineering Science and Technology, an International Journal*, 21(4):760-768.

Bachmann, F., Hielscher, R. & Schaeben, H. 2010. Texture analysis with MTEX – Free and open source software toolbox. *Solid State Phenomena*, 160:63-68.

Bakic, G., V., S.Z., Djukic, M.B., Perunicic, V., Prodanovic, A., Rajicic, B., Gajic, I., Sekeljic, P. & Gregorjev, N. 2014. Material characterization of the main steam gate valve made of X20CrMoV 12.1 steel after long term service. *Procedia Materials Science*, 3:1512-1517.

Baldi, A. 2018. Digital image correlation and color cameras. *Experimental Mechanics*, 58(2):315-333.

Baldi, A. & Bertolino, F. 2015. Experimental analysis of the errors due to polynomial interpolation in digital image correlation. *Strain*, 51(3):248-263.

Basirat, M., Shrestha, T., Potirniche, G.P., Charit, I. & Rink, K. 2012. A study of the creep behavior of modified 9Cr-1Mo steel using continuum-damage modeling. *International Journal of Plasticity*, 37:95-107.

Becker, T.H., Mostafavi, M., Tait, R.B. & Marrow, T.J. 2012. An approach to calculate the J -integral by digital image correlation displacement field measurement. *Fatigue & Fracture of Engineering Materials & Structures*, 35(10):971-984.

Benaarbia, A., Xu, X., Sun, W., Becker, A.A. & Jepson, M.A.E. 2018. Investigation of short-term creep deformation mechanisms in MarBN steel at elevated temperatures. *Materials Science and Engineering A*, 734:491-505.

Bendick, W., Haarmann, K., Wellnitz, G. & Zschau, M. 1993. Properties of 9 to 12 % chromium steels and their behaviour under creep conditions. *VGB Kraftwerkstechnik*, 73(1):73-79.

Benham, P., Crawford, R. & Armstrong, C. 1996. *Mechanics of engineering materials*. 2nd edition. Essex: Pearson Education Limited.

Berfield, T.A., Patel, J.K., Shimmin, R.G., Braun, P. V., Lambros, J. & Sottos, N.R. 2007. Micro-and nanoscale deformation measurement of surface and internal planes via digital image correlation. *Experimental Mechanics*, 47(1): 51-62.

Berke, R.B. & Lambros, J. 2014. Ultraviolet digital image correlation (UV-DIC) for high temperature applications. *Review of Scientific Instruments* [Electronic], 85(4). Available: http://dx.doi.org/10.1063/1.4871991 [2014, September 22].

Bhadeshia, H.K.D.H., Strang, A. & Gooch, D.J. 1998. Ferritic power plant steels: remnant life assessment and the approach to equilibrium. *International Materials Reviews*, 43(2):45-69.

Black Thursday. 2014. *Inside Mining*, 7(5):22-23, May.

Blagoeva, D.T. & Hurst, R.C. 2009. Application of the CEN (European Committee for Standardization) small punch creep testing code of practice to a representative repair welded P91 pipe. *Materials Science and Engineering A*, 510-511:219-223.

Blug, A., Regina, D.J., Eckmann, S., Senn, M., Bertz, A., Carl, D. & Eberl, C. 2019. Real-time GPU-based digital image correlation sensor for marker-free strain-controlled fatigue testing. *Applied Sciences* [Electronic], 9(10). Available: https://doi.org/10.3390/app9102025 [2020, April 21].

Bolton, C.J., Dyson, B.F. & Williams, K.R. 1980. Metallographic methods of determining residual creep life. *Materials Science and Engineering*, 46(2):231-239.

Bornert, M., Brémand, F., Doumalin, P., Dupré, J.C., Fazzini, M., Grédiac, M., Hild, F., Mistou, S., Molimard, J., Orteu, J.J., Robert, L., Surrel, Y., Vacher, P. & Wattrisse, B. 2009. Assessment of digital image correlation measurement errors: Methodology and results. *Experimental Mechanics*, 49: 353-370.

Bose, S.C., Singh, K., Swaminathan, J. & Sarma, D.S. 2004. Prediction of creep life of X10CrMoVNbN-91 (P-91) steel through short term stress relaxation test methodology. *Materials Science and Technology*, 20(10):1290-1296.

Bruck, H., McNeill, S., Sutton, M. & Peters, W.P. 1989. Digital image correlation using Newton-Raphson method of partial differential correction. *Experimental Mechanics*, 261-267.

Busca, D., Fazzini, M., Lorrain, B., Mistou, S., Karama, M. & Pastor, M.L. 2014. High-speed stereo digital image correlation: Application to biaxial fatigue. *Strain*, 50(5):417-427.

Callister, W.D. 2007. *Materials science and engineering: An introduction*. New York: John Wiley & Sons.

Cardenas, N. 2018. Feasibility study into the use of digital image correlation for creep strain monitoring of fossil power plant welds. Unpublished Master's thesis. Cape Town: University of Cape Town [Online]. Available: https://open.uct.ac.za/handle/11427/29595 [2019, March 20].

Cardoso, B.R., Matt, C.F.T., Furtado, H.C. & de Almeida, L.H. 2015. Creep damage evaluation in high-pressure rotor based on hardness measurement. *Journal of Materials Engineering and Performance*, 24(7):2784-2791.

Cazottes, S., Bechis, A., Lafond, C., L'Hôte, G., Roth, C., Dreyfus, T., Steyer, P., Douillard, T. & Langlois, C. 2019. Toward an automated tool for dislocation density characterization in a scanning electron microscope. *Materials Characterization* [Electronic], 158. Available: https://doi.org/10.1016/j.matchar.2019.109954 [2020, March 14].

CEN. 2007. *CWA 15627 Workshop agreement: Small punch test method for metallic materials*. Brussels: European Committee for Standardization.

Cengel, Y.A. & Boles, M.A. 2011. Vapor and combined power cycles, in *Thermodynamics: An engineering approach*. 7th edition. New York: McGraw-Hill. 551-605.

Chakrabarty, J. 1998. Large deflections of a clamped circular plate pressed by a hemispherical-headed punch. *Metals and Materials*, 4(4):680-684.

Chapra, S.C. 2008. *Applied Numerical Methods with MATLAB for Engineers and Scientists*. 2nd edition. New York: McGraw-Hill.

Chen, F., Chen, X., Xie, X., Feng, X. & Yang, L. 2013. Full-field 3D measurement using multi-camera digital image correlation system. *Optics and Lasers in Engineering*, 51(9):1044-1052.

Chen, X., Xu, N., Yang, L. & Xiang, D. 2012. High temperature displacement and strain measurement using a monochromatic light illuminated stereo digital image correlation system. *Measurement Science and Technology* [Electronic], 23(12). Available: https://doi.org/10.1088/0957-0233/23/12/125603 [2014, August 23].

Chen, X., Xie, X., Sun, J. & Yang, L. 2012. Full field strain measurement of punch-stretch tests using digital image correlation. *SAE International Journal of Materials and Manufacturing*, 5(2):345-351.

Christopher, J. & Choudhary, B.K. 2018. Applicability of improved Dyson–McLean approach to creep deformation behaviour of tempered martensitic P9 steel. *Materials at High Temperatures*, 35(4):387-397.

Christopher, J. & Choudhary, B.K. 2019. Prediction of long-term creep behaviour of Grade 91 steel at 873 K in the framework of microstructure-based creep damage mechanics approach. *International Journal of Damage Mechanics*, 28(6):877-895.

Chrysochoos, A., Huon, V., Jourdan, F., Muracciole, J.-M., Peyroux, R. & Wattrisse, B. 2010. Use of full-field digital image correlation and infrared thermography measurements for the thermomechanical analysis of material behaviour. *Strain*, 46:117-130.

Cipolla, L., Danielsen, H.K., Venditti, D., Di Nunzio, P.E., Hald, J. & Somers, M.A.J. 2010. Conversion of MX nitrides to Z-phase in a martensitic 12% Cr steel. *Acta Materialia*, 58(2):669-679.

Conradie, J.H. 2015. Characterising failure of structural materials using digital images. Unpublished Master's thesis. Stellenbosch: Stellenbosch University [Online]. Available: https://scholar.sun.ac.za/handle/10019.1/96755 [2019, August 8]

Cortellino, F., Sun, W., Hyde, T.H. & Shingledecker, J. 2014. The effects of geometrical inaccuracies of the experimental set-up on small punch creep test results. *Journal of Strain Analysis for Engineering Design*, 49(8):571-582.

Cortellino, F., Rouse, J.P., Cacciapuoti, B., Sun, W. & Hyde, T.H. 2017. Experimental and numerical analysis of initial plasticity in P91 steel small punch creep samples. *Experimental Mechanics*, 57(8):1193-1212.

Danielsen, H.K. & Hald, J. 2006. Behaviour of Z phase in 9–12 % Cr steels. *Energy Materials*, 1(1):49-57.

Danielsen, H.K., Somers, M.A.J. & Hald, J. 2007. Z-phase in 9-12 % Cr steels. Unpublished doctoral dissertation. Lyngby: Technical University of Denmark. [Online]. Available: https://orbit.dtu.dk/ws/files/4899462/HilmarThesis.pdf [2018, August 4].

Danielsen, H.K., Di Nunzio, P.E. & Hald, J. 2013. Kinetics of Z-phase precipitation in 9 to 12 pct Cr steels. *Metallurgical and Materials Transactions A: Physical Metallurgy and Materials Science*, 44(5):2445-2452.

Dimmler, G., Weinert, P., Kozeschnik, E. & Cerjak, H. 2003. Quantification of the Laves phase in advanced 9-12 % Cr steels using a standard SEM. *Materials Characterization*, 51(5):341-352.

DIN. 1979. *DIN 17175: Seamless tubes of heat-resistant steels - Technical conditions of delivery*. Berlin: German Institute for Standardisation (DIN).

Dobrzański, J. 2005. The classification method and the technical condition evaluation of the critical elements' material of power boilers in creep service made from the 12Cr-1Mo-V. *Journal of Materials Processing Technology*, 164-165:785-794.

Dobrzański, J., Hernas, A. & Moskal, G. 2011. Microstructural degradation in boiler steels: Materials developments, properties and assessment, in J. Oakey (ed.). *Power plant life management and performance improvement*. Oxford: Woodhead Publishing. 222-271.

Douglas, J. 1996. High value for condition assessment. *EPRI Journal*, 21(5):26.

Dymáček, P. & Milička, K. 2009. Creep small-punch testing and its numerical simulations. *Materials Science and Engineering A*, 510-511:444-449.

Dyson, B.F. 2000. Use of CDM in materials modeling and component creep life prediction. *Journal of Pressure Vessel Technology*, 122: 281-296.

Dyson, B.F. & Leckie, F.A. 1988. Physically based modelling of remnant creep life. *Materials Science and Engineering*, 103(1):111-114.

Dyson, B.F. & McLean, M. 1998. Microstructural evolution and its effects on the creep performance of high temperature alloys, in A. Strang, J. Cawley, & G.W. Greenwood (eds.). *Microstructural stability of creep resistant alloys for high temperature alloys*. London: Institute of Materials. 371-393.

Dyson, B.F. & Osgerby, S. 1993. *NPL Report DMA A116: Modelling and analysis of creep deformation and fracture in a 1 Cr 1/2 Mo ferritic steel*. Teddington, UK: National Physical Laboratory.

Eggeler, G., Earthman, J.C., Nilsvang, N. & Ilschner, B. 1989. Microstructural study of creep rupture in a 12 % chromium ferritic steel. *Acta Metallurgica*, 37(1):49-60.

Eisenträger, J., Naumenko, K., Altenbach, H. & Gariboldi, E. 2017. Analysis of temperature and strain rate dependencies of softening regime for tempered martensitic steel. *Journal of Strain Analysis for Engineering Design*, 52(4):226-238.

Endo, T., Masuyama, F. & Park, K.-S. 2003. Change in Vickers hardness and substructure during creep of a mod.9Cr-1Mo steel. *Materials Transactions*, 44(2):239-246.

Ennis, P.J. 2014. Ferritic and martensitic steels for power plants, in A. Shirzadi & S. Jackson (eds.). *Structural alloys for power plants: Operational challenges and high-temperature materials*. Cambridge: Woodhead Publishing. 188-220.

EPRI. 2006. *X20 CrMoV12-1 steel handbook*. Palo Alto, CA: EPRI.

EPRI. 2007. *Fossil plant high-energy piping damage: Theory and practice, Volume 1: Piping fundamentals (report no. 1012201)*. Palo Alto, CA: EPRI.

Estrada, J.B. & Franck, C. 2015. Intuitive interface for the quantitative evaluation of speckle patterns for use in digital image and volume correlation techniques. *Journal of Applied Mechanics* [Electronic], 82(9). Available: https://doi.org/10.1115/1.4030821 [2016, March 27].

Estrin, Y. & Mecking, H. 1984. A unified phenomenological description of work hardening and creep based on one-parameter models. *Acta Metallurgica*, 32(1):57-70.

Evans, M. & Wang, D. 2008. The small punch creep test: Some results from a numerical model. *Journal of Materials Science*, 43(6):1825-1835.

Fazzini, M., Dalverny, O. & Mistou, S. 2011. Identification of materials properties using displacement field measurement. *Key Engineering Materials*, 482:57-65.

Fedorova, I., Belyakov, A., Kozlov, P., Skorobogatykh, V., Shenkova, I. & Kaibyshev, R. 2014. Laves-phase precipitates in a low-carbon 9% Cr martensitic steel during aging and creep at 923 K. *Materials Science and Engineering A*, 615:153-163.

Fleming, A., Maskell, R. V, Buchanan, L.W. & Wilson, T. 2000. Material developments for supercritical boilers and pipework, in A. Strang (ed.). *Materials for high temperature power generation and process plant applications*. London: IOM Communications. 33-77.

Fleury, E. & Ha, J.S. 1998. Small punch tests to estimate the mechanical properties of steels for steam power plant: I. Mechanical strength. *International Journal of Pressure Vessels and Piping*, 75(9):699-706.

Forsey, A. & Gungor, S. 2016. Demosaicing images from colour cameras for digital image correlation. *Optics and Lasers in Engineering*, 86:20-28.

Frost, H.J. & Ashby, M.F. 1982. *Deformation-mechanism maps: The plasticity and creep of metals and ceramics*. Oxford: Pergamon Press.

Fujiyama, K., Mori, K., Matsunaga, T., Kimachi, H., Saito, T., Hino, T. & Ishii, R. 2009. Creep-damage assessment of high chromium heat resistant steels and weldments. *Materials Science and Engineering A*, 510-511:195-201.

Fujiyama, K., Kimachi, H., Watanabe, Y., Hijikuro, K. & Tsuboi, T. 2011. The concept of "eBSD strain analysis" and its application to creep and creep-fatigue damage assessment of ferritic and austenitic heat resistant steels. *Strength, Fracture and Complexity*, 7(2):123-135.

Gales, J.A., Bisby, L.A. & Stratford, T. 2012. New parameters to describe high-temperature deformation of prestressing steel determined using digital image correlation. *Structural Engineering International*, 22(4):476-486.

Ghoniem, N.M., Po, G. & Sharafat, S. 2013. Deformation mechanisms in ferritic/martensitic steels and the impact on mechanical design. *Journal of Nuclear Materials*, 441(1-3):704-712.

Ghosh, R.N. 2013. Creep life predictions of engineering components: Problems & prospects. *Procedia Engineering*, 55:599-606.

Gokhale, A.M. 2004. Quantitative characterization and representation of global microstructural geometry, in G.F. Vander Voort (ed.). *ASM Handbook Volume 9: Metallography and Microstructures*. Ohio, USA: ASM International. 428–447.

Goldberg, A. 2015. The economic impact of load shedding: The case of South African retailers. Unpublished master's thesis. Pretoria: University of Pretoria [Online]. Available: https://repository.up.ac.za/handle/2263/52398 [2019, April 6].

Grant, B.M.B., Stone, H.J., Withers, P.J. & Preuss, M. 2009. High-temperature strain field measurement using digital image correlation. *Journal of Strain Analysis for Engineering Design*, 44(4):263-271.

Grediac, M., Pierron, F., Avril, S. & Toussaint, E. 2006. The virtual fields method for extracting constitutive parameters from full-field measurements: a review. *Strain*, 42:233-253.

Greenwood, G.W. 2007. Comparisons and contrasts in creep behaviour. *Materials Science and Engineering A*, 463(1-2):166-170.

Gregory, O.J. & Luo, Q. 2001. Self-compensated ceramic strain gage for use at elevated temperatures. *Sensors and Actuators A*, 88(3):234-240.

Gupta, C., Toda, H., Schlacher, C., Adachi, Y., Mayr, P., Sommitsch, C., Uesugi, K., Suzuki, Y., Takeuchi, A. & Kobayashi, M. 2013. Study of creep cavitation behavior in tempered martensitic steel using synchrotron micro-tomography and serial sectioning techniques. *Materials Science and Engineering A*, 564:525-538.

Gupta, C., Toda, H., Mayr, P. & Sommitsch, C. 2015. 3D creep cavitation characteristics and residual life assessment in high temperature steels: a critical review. *Materials Science and Technology*, 31(5):603-626.

Ha, J.S. & Fleury, E. 1998. Small punch tests to estimate the mechanical properties of steels for steam power plant: II. Fracture toughness. *International Journal of Pressure Vessels and Piping*, 75(9):707-713.

Hald, J. 2008. Microstructure and long-term creep properties of 9-12 % Cr steels. *International Journal of Pressure Vessels and Piping*, 85(1-2):30-37.

Haney, E.M., Dalle, F., Sauzay, M., Vincent, L., Tournié, I., Allais, L. & Fournier, B. 2009. Macroscopic results of long-term creep on a modified 9Cr-1Mo steel (T91). *Materials Science and Engineering A*, 510-511:99-103.

Helm, J.D., McNeill, S.R. & Sutton, M.A. 1996. Improved three-dimensional image correlation for surface displacement measurement. *Optical Engineering*, 35(7):1911-1920.

Hertzberg, R.W., Vinci, R.P. & Hertzberg, J.L. 2012. Time-dependent deformation, in *Deformation and fracture mechanics of engineering materials*. 5th edition. New York: John Wiley & Sons. 189-245.

Hild, F. & Roux, S. 2006. Digital image correlation: From displacement measurement to identification of elastic properties - a review. *Strain*, 42(2):69-80.

Hild, F., Bouterf, A. & Roux, S. 2015. Damage measurements via DIC. *International Journal of Fracture*, 191(1-2):77-105.

Hino, M., He, Y., Li, K., Chang, J. & Shin, K. 2013. Microstructural evolution of X20CrMoV12.1 steel upon short-term creep rupture test. *Applied Microscopy*, 43(4):164-172.

Hoffmann, K. 1989. *An introduction to measurements using strain gages*. Darmstadt: Hottinger Baldwin Messtechnik.

Holmström, S., Li, Y., Dymacek, P., Vacchieri, E., Je, S.P., Lancaster, R.J., Omacht, D., Kubon, Z., Anelli, E., Rantala, J., Tonti, A., Komazaki, S., Bruchhausen, M., Hurst, R.C., Hähner, P., Richardson, M. & Andres, D. 2018. Creep strength and minimum strain rate estimation from small punch creep tests. *Materials Science & Engineering A*, 731:161-172.

Holzer, I. 2010. *Modelling and simulation of strengthening in complex martensitic 9-12 % Cr steel and a binary Fe-Cu alloy*. Published doctoral dissertation. Graz: Verlag der Technischen Universität Graz.

Hore, S. & Ghosh, R.N. 2011. Computer simulation of the high temperature creep behaviour of Cr-Mo steels. *Materials Science and Engineering A*, 528(19-20):6095-6102.

Hosford, W.F. 2009. *Mechanical behavior of materials*. 2nd edition. New York: Cambridge University Press.

Hosseini, E., Holdsworth, S.R. & Mazza, E. 2012. Creep constitutive model considerations for high-temperature finite element numerical simulations. *Journal of Strain Analysis*, 47(6):341-349.

Hoult, N.A., Andy Take, W., Lee, C. & Dutton, M. 2013. Experimental accuracy of two dimensional strain measurements using digital image correlation. *Engineering Structures*, 46:718-726.

Hu, Z.F. & Yang, Z.G. 2003. Identification of the precipitates by TEM and EDS in X20CrMoV12.1 after long-term service at elevated temperature. *Journal of Materials Engineering and Performance*, 12(1):106-111.

Hu, Z.F. & Yang, Z.G. 2004. An investigation of the embrittlement in X20CrMoV12.1 power plant steel after long-term service exposure at elevated temperature. *Materials Science and Engineering A*, 383(2):224-228.

Hu, Z.F., He, D. & Mo, F. 2015. Carbides evolution in 12Cr martensitic heat-resistant steel with life depletion for long-term service. *Journal of Iron and Steel Research International*, 22(3):250-255.

Hu, Z.F., Yang, Z.G., He, G.Q. & Chen, C.S. 2008. Damage and residual life assessment of bends for X20CrMoV12.1 main steam pipe after long-term service. *Journal of Failure Analysis and Prevention*, 8(1):41-47.

Huchzermeyer, R. 2017. Measuring mechanical properties using digital image correlation: Extracting tensile and fracture properties from a single sample. Unpublished Master's thesis. Stellenbosch: University of Stellenbosch [Online]. Available: http://hdl.handle.net/10019.1/102805 [2019, September 9].

Huchzermeyer, R.L. & Becker, T.H. 2018. The application of full-field techniques to estimate both tensile and fracture properties: An investigation into modifications to standard sample geometries. *Experimental Techniques*, 42(6):671-683.

Humphreys, F.J. 2004. Reconstruction of grains and subgrains from electron backscatter diffraction maps. *Journal of Microscopy*, 213(3):247-256.

Hursa, A., Rolich, T. & Ercegovic Razic, S. 2009. Determining pseudo Poisson's ratio of woven fabric with a digital image correlation method. *Textile Research Journal*, 79(17):1588-1598.

Hurst, R.C. & Matocha, K. 2015. A renaissance in the use of the small punch testing technique, in *Proceedings of the ASME 2015 Pressure Vessels and Piping Conference*. 19-23 July, Boston, Massachusetts, USA: ASME [Electronic]. Available: https://doi.org/10.1115/PVP2015-45095 [2017, September 24].

Hyde, T.H. & Sun, W. 2009. A novel, high-sensitivity, small specimen creep test. *The Journal of Strain Analysis for Engineering Design*, 44(3):171-185.

Hyde, T.H., Stoyanov, M., Sun, W. & Hyde, C.J. 2010. On the interpretation of results from small punch creep tests. *Journal of Strain Analysis for Engineering Design*, 45(3):141-164.

Ion, J.C., Barbosa, A., Ashby, M.F. & Dyson, B.F. 1986. *NPL report DMA A115: The modelling of creep for engineering design-Part 1*. Teddington, UK: National Physical Laboratory: Division of Materials Applications.

Isik, M.I., Kostka, A. & Eggeler, G. 2014. On the nucleation of Laves phase particles during high-temperature exposure and creep of tempered martensite ferritic steels. *Acta Materialia*, 81:230-240.

Isik, M.I., Kostka, A., Yardley, V.A., Pradeep, K.G., Duarte, M.J., Choi, P.P., Raabe, D. & Eggeler, G. 2015. The nucleation of Mo-rich Laves phase particles adjacent to $M_{23}C_6$ micrograin boundary carbides in 12 % Cr tempered martensite ferritic steels. *Acta Materialia*, 90:94-104.

Izaki, T., Kobayashi, T., Kusumoto, J. & Kanaya, A. 2009. A creep life assessment method for boiler pipes using small punch creep test. *International Journal of Pressure Vessels and Piping*, 86(9):637-642.

Jesper, H. 1985. Arguments for the material choice of X 20 CrMoV 12 1 to be used for the high temperature pipework of THTR 300 as seen from an operator's viewpoint. *Nuclear Engineering and Design*, 87:399-405.

Jestin, L., Fawkes, M., Maccoll, B. & Koko, M. 2014. *Eskom Power Plant Engineering Institute (EPPEI) 5-years research strategic plan*. Johannesburg: ESKOM.

Johannes, S., Ignacio, A.-C., Erwin, F., Verena, K., Mark, L., Tobias, P., Stephan, P., Curtis, R., Stephan, S., Benjamin, S., Jean-Yves, T., Daniel, J.W., Volker, H., Kevin, E., Pavel, T. & Albert, C. 2012. Fiji: an open-source platform for biological-image analysis. *Nature Methods*, 9(7):676-682.

Jones, E.M.C. & Iadicola, M.A. (eds.). 2018. *A good practices guide for digital image correlation*. International Digital Image Correlation Society (iDICs). Available: https://doi.org/10.32720/idics/gpg.ed1 [2019, August 28].

Jones, E.M.C. & Reu, P.L. 2018. Distortion of digital image correlation (DIC) displacements and strains from heat waves. *Experimental Mechanics*, 58(7):1133-1156.

Kadoya, Y., Nishimura, N., Dyson, B.F. & McLean, M. 1997. Origins of tertiary creep in high chromium steels, in J.C. Earthman & F.A. Mohamed (eds.). *Creep and fracture of engineering materials and structures*. Warrendale, PA, USA: The Minerals, Metals and Materials Society. 343–352.

Kaibyshev, R.O., Skorobogatykh, V.N. & Shchenkova, I.A. 2010. Formation of the Z-phase and prospects of martensitic steels with 11 % Cr for operation above 590 °C. *Metal Science and Heat Treatment*, 52(3-4):90-99.

Kalwa, G. 1985. State of the development and application techniques of the steel X 20 CrMoV 12 1. *Nuclear Engineering and Design*, 84(2):87-95.

Kardoulaki, E., Lin, J., Balint, D. & Farrugia, D. 2014. Investigation of the effects of thermal gradients present in Gleeble high-temperature tensile tests on the strain state for free cutting steel. *Journal of Strain Analysis for Engineering Design*, 49(7):521-532.

Kassner, M.E. 2009. *Fundamentals of creep in metals and alloys*. 2nd edition. Amsterdam: Elsevier.

Ke, X.D., Schreier, H.W., Sutton, M.A. & Wang, Y.Q. 2011. On error assessment in stereo-based deformation measurements. Part II: Experimental validation of uncertainty and bias estimates. *Experimental Mechanics*, 51:405-422.

Key to Metals AG. 2015. *Total Materia: X20 CrMoV 12 1* [Online]. Available: http://www.totalmateria.com/ [2015, September 15].

Kim, B. & Lim, B. 2008. Local creep evaluation of P92 steel weldment by small punch creep test. *Acta Mechanica Solida Sinica*, 21(4):312-317.

Kim, W.G., Kim, S.H. & Lee, C.B. 2011. Long-term creep characterization of Gr. 91 steel by modified creep constitutive equations. *Metals and Materials International*, 17(3):497-504.

Kinoshita, Y., Yardley, V.A. & Tsurekawa, S. 2011. Relation between microstructures of martensite and prior austenite in 12 wt% Cr ferritic steel. *Journal of Materials Science*, 46(12):4261-4269.

Kloc, L. 2015. Critical view on the creep modelling procedures. *Acta Physica Polonica A*, 128(4):540-542.

Kobayashi, K. & Takei, S. 2014. Influence of testing environment on SP creep rupture lives, in *Proceedings of the ASME 2013 Pressure Vessels and Piping Conference*. 14-18 July, Paris, France: ASME [Electronic]. Available: https://doi.org/10.1115/PVP2013-97545 [2017, December 13].

Komazaki, S., Nakata, T., Kohno, Y. & Tanigawa, H. 2017. Effects of geometry and dimension of specimen and rig on small punch creep property. *Experimental Mechanics*, 57:487-494.

Komazaki, S., Kato, T., Kohno, Y. & Tanigawa, H. 2009. Creep property measurements of welded joint of reduced-activation ferritic steel by the small-punch creep test. *Materials Science and Engineering A,* 510-511:229-233.

Kostka, A., Tak, K.G., Hellmig, R.J., Estrin, Y. & Eggeler, G. 2007. On the contribution of carbides and micrograin boundaries to the creep strength of tempered martensite ferritic steels. *Acta Materialia*, 55(2):539-550.

Kovpak, K.I. 1998. In-service creep of materials for steam lines of thermal power plants and extension of their life. *Strength of Materials*, 30(3):282-285.

Lagarias, J.C., Reeds, J.A., Wright, M.H. & Wright, P.E. 1998. Convergence properties of the Nelder-Mead simplex method in low dimensions. *SIAM Journal on Optimization*, 9(1):112-147.

Larrosa, N.O., Ainsworth, R.A., Akid, R., Budden, P.J., Davies, C.M., Hadley, I., Tice, D.R., Turnbull, A. & Zhou, S. 2017. 'Mind the gap' in fitness-for-service assessment procedures-review and summary of a recent workshop. *International Journal of Pressure Vessels and Piping* [Electronic], 158. Available: https://doi.org/10.1016/j.ijpvp.2017.09.004 [2017, 6 November].

Larson, F. & Miller, J. 1952. A time-temperature relationship for rupture and creep stresses. *Transactions of the ASME,* 74:765-775.

LaVision. 2017. *StrainMaster product manual for DaVis 8.4*. Göttingen: LaVision GmbH.

Lee, T., Ibupoto, F.A., Lee, J.H., Kim, B.J. & Kim, M.K. 2016. A direct methodology for small punch creep test. *Experimental Mechanics,* 56(3):395-405.

Lemaitre, J. 1996. *A course on damage mechanics*. 2nd edition. Berlin: Springer.

Leplay, P., Lafforgue, O. & Hild, F. 2015. Analysis of asymmetrical creep of a ceramic at 1350°C by digital image correlation. *Journal of the American Ceramic Society*, 98(7):2240-2247.

Li, Q. 2006. Precipitation of Fe_2W laves phase and modeling of its direct influence on the strength of a 12Cr-2W steel. *Metallurgical and Materials Transactions A: Physical Metallurgy and Materials Science,* 37(1):89–97.

Lin, P.D. & Sung, C.K. 2007. Comparing two new camera calibration methods with traditional pinhole calibrations. *Optics Express*, 15(6):3012-3022.

Lin, J., Liu, Y. & Dean, T.A. 2005. A review on damage mechanisms, models and calibration methods under various deformation conditions. *International Journal of Damage Mechanics*, 14(4):299-319.

Lionello, G. & Cristofolini, L. 2014. A practical approach to optimizing the preparation of speckle patterns for digital-image correlation. *Measurement Science and Technology*

[Electronic], 25(10). Available: https://iopscience.iop.org/article/10.1088/0957-0233/25/10/107001 [2016, October 11].

Liu, J., Sutton, M., Lyons, J. & Deng, X. 1998. Experimental investigation of near crack tip creep deformation in alloy 800 at 650 °C. *International Journal of Fracture*, 91:233-268.

Lyons, J.S., Liu, J. & Sutton, M.A. 1996. High-temperature deformation measurements using digital-image correlation. *Experimental Mechanics*, 36:64-70.

Ma, Y.W., Shim, S. & Yoon, K.B. 2009. Assessment of power law creep constants of Gr91 steel using small punch creep tests. *Fatigue and Fracture of Engineering Materials and Structures*, 32(12):951-960.

Maddi, L., Deshmukh, G.S., Ballal, A.R., Peshwe, D.R., Paretkar, R.K., Laha, K. & Mathew, M.D. 2016. Effect of Laves phase on the creep rupture properties of P92 steel. *Materials Science and Engineering A*, 668:215-223.

Madia, M., Foletti, S., Torsello, G. & Cammi, A. 2013. On the applicability of the small punch test to the characterization of the 1CrMoV aged steel: Mechanical testing and numerical analysis. *Engineering Failure Analysis*, 34:189-203.

Maharaj, C., Dear, J.P. & Morris, A. 2009. A review of methods to estimate creep damage in low-alloy steel power station steam pipes. *Strain*, 45:316-331.

Manahan, M., Argon, A. & Harling, O. 1981. The development of a miniaturized disk bend test for the determination of postirradiation mechanical properties. *Journal of Nuclear Materials*, 104:1545-1550.

Maruyama, K., Sawada, K. & Koike, J. 2001. Strengthening mechanisms of creep resistant tempered martensitic steel. *ISIJ International*, 41(6):641-653.

Marx, G. 2016. Quantitative microstructural evaluation of 12Cr creep aged steels after welding. Unpublished Master's thesis. Port Elizabeth: Nelson Mandela University.

Marx, G. 2019. Microstructural evolution of welded creep aged 12 % Cr martensitic stainless steel. Unpublished doctoral dissertation. Port Elizabeth: Nelson Mandela University.

Masuyama, F. 2009. Hardness model for creep-life assessment of high-strength martensitic steels. *Materials Science and Engineering A*, 510-511(C):154-157.

Mathew, M.D., Naveena & Ganesh Kumar, J. 2016. Characterisation of mechanical properties of materials using innovative small specimen testing methods. *Transactions of the Indian Institute of Metals*, 69(10):1871-1887.

McLean, M. & Dyson, B.F. 2002. Modeling the effects of damage and microstructural evolution on the creep behavior of engineering alloys. *Journal of Engineering Materials and Technology*, 122(3):273-278.

Mitsuhara, M., Yamasaki, S., Miake, M., Nakashima, H., Nishida, M., Kusumoto, J. & Kanaya, A. 2016. Creep strengthening by lath boundaries in 9Cr ferritic heat-resistant steel. *Philosophical Magazine Letters*, 96(2):76-83.

Molokwane, T. 2013. Microstructural and property assessment of creep aged 12Cr steel after welding. Unpublished Master's thesis. Cape Town: University of Cape Town.

Molteno, M.R. 2017. Measuring fracture properties using digital image and volume correlation: decomposing the J -integral for mixed-mode parameters. Unpublished doctoral dissertation. Stellenbosch: University of Stellenbosch [Online]. Available: https://scholar.sun.ac.za/handle/10019.1/102804 [2019, September 9].

Molteno, M.R. & Becker, T.H. 2015. Mode I – III decomposition of the J -integral from DIC displacement data. *Strain*, 51(6):492-503.

Moriyama, K., Kanaya, A., Kusumoto, J., Koba, K., Kamisasanuki, T., Imazato, T. & Nakashima, K. 2009. Estimation of material properties and maintenance of pressure parts of thermal power plant boilers under long-term service of 300,000 hours. *Materials Science and Engineering A*, 510-511:142-148.

Morris, A., Kourmpetis, M., Dear, I.D., Sjödahl, M. & Dear, J.P. 2007. Optical strain monitoring techniques for life assessment of components in power generation plants. *Proceedings of the Institution of Mechanical Engineers, Part A: Journal of Power and Energy*, 221(8):1141-1152.

Morris, J.W., Kinney, C., Pytlewski, K. & Adachi, Y. 2013. Microstructure and cleavage in lath martensitic steels. *Science and Technology of Advanced Materials* [Electronic], 14(1). Available: https://doi.org/10.1088/1468-6996/14/1/014208 [2018, March 15].

Murchú, C.Ó., Leen, S.B., O'Donoghue, P.E. & Barrett, R.A. 2017. A physically-based creep damage model for effects of different precipitate types. *Materials Science and Engineering A*, 682:714–722.

Murchú, C.Ó., Leen, S.B., O'Donoghue, P.E. & Barrett, R.A. 2019. A precipitate evolution-based continuum damage mechanics model of creep behaviour in welded 9Cr steel at high temperature. *Proceedings of the Institution of Mechanical Engineers, Part L: Journal of Materials: Design and Applications*, 233(1):39-51.

Müsch, H., Remment, H., Körner, P., Tolksdorf, E. & Wachter, O. 1992. *Guidelines for the assessment of microstructural and damage development of creep exposed materials for pipes and boiler components (report no. VGB-TW 507)*. Essen: VGB Technical Association of Large Power Plant Operators.

Muyupa, E., Gungor, S., Forsey, A.N. & Bouchard, P.J. 2017. Determination of creep properties from a single specimen using DIC. Unpublished paper delivered at the *British Society for Strain Measurement's 12th International Conference on Advances in Experimental Mechanics*. 29-31 August, Sheffield, UK.

Nakata, T., Komazaki, S-I., Kohno, Y. & Tanigawa, H. 2016a. Development of a small punch testing method to evaluate the creep property of high Cr ferritic steel: Part I - Effect of atmosphere on creep deformation behavior. *Materials Science and Engineering A*, 666:54-60.

Nakata, T., Komazaki, S-I., Kohno, Y. & Tanigawa, H. 2016b. Development of a small punch testing method to evaluate the creep property of high Cr ferritic steel: Part II - Stress

analysis of small punch test specimen by finite element method. *Materials Science and Engineering A*, 666:80-87.

Narayanan, A., Dubey, K., Davies, C.M. & Dear, J.P. 2017. The creep of alloy 617 at 700 °C: Material properties, measurement of strain and comparison between finite element analysis and digital image correlation. *International Journal of Solids and Structures*, 129:195-203.

NERSA. 2008. *Inquiry into the national electricity supply shortage and load shedding*. Pretoria: National Energy Regulator of South Africa.

Nitta, H., Yamamoto, T., Kanno, R., Takasawa, K., Iida, T., Yamazaki, Y., Ogu, S. & Iijima, Y. 2002. Diffusion of molybdenum in α-iron. *Acta Materialia*, 50(16):4117-4125.

Norris, S.D. & Wilson, I. 1999. Application of 3D numerical modelling for thermal profile optimization on the Gleeble thermomechanical simulator. *Modelling and Simulation in Materials Science and Engineering*, 7:297-309.

Novak, M.D. & Zok, F.W. 2011. High-temperature materials testing with full-field strain measurement: experimental design and practice. *Review of Scientific Instruments* [Electronic], 82(11). Available: https://doi.org/10.1063/1.3657835 [2014, October 27].

Nowak, M. & Maj, M. 2018. Determination of coupled mechanical and thermal fields using 2D digital image correlation and infrared thermography: Numerical procedures and results. *Archives of Civil and Mechanical Engineering*, 18(2):630-644.

Nyyssönen, T., Peura, P. & Kuokkala, V.T. 2018. Crystallography, morphology, and martensite transformation of prior austenite in intercritically annealed high-aluminum steel. *Metallurgical and Materials Transactions A: Physical Metallurgy and Materials Science*, 49(12):6426-6441.

Olbricht, J., Bismarck, M. & Skrotzki, B. 2013. Characterization of the creep properties of heat resistant 9-12 % chromium steels by miniature specimen testing. *Materials Science and Engineering A*, 585:335-342.

Olsson, U. 2005. Confidence intervals for the mean of a log-normal distribution. *Journal of Statistics Education* [Electronic], 13(1). Available: https://doi.org/10.1080/10691898.2005.11910638 [2019, March 8].

Orteu, JJ. 2009. 3-D computer vision in experimental mechanics. *Optics and Lasers in Engineering*, 47(3-4):282-291.

Orteu, J., Cutard, T., Garcia, D., Cailleux, E. & Robert, L. 2007. Application of stereovision to the mechanical characterisation of ceramic refractories reinforced with metallic fibres. *Strain*, 43(2):96-108.

Oruganti, R. 2012. A new approach to dislocation creep. *Acta Materialia*, 60(4):1695-1702.

Oruganti, R., Karadge, M. & Swaminathan, S. 2011. Damage mechanics-based creep model for 9-10 % Cr ferritic steels. *Acta Materialia*, 59(5):2145-2155.

Pan, B. 2011. Recent progress in digital image correlation. *Experimental Mechanics*, 51:1223-1235.

Pan, B., Xie, H., Wang, Z., Qian, K. & Wang, Z. 2008. Study on subset size selection in digital image correlation for speckle patterns. *Optics Express*, 16(10):7037-7048.

Pan, B., Qian, K., Xie, H. & Asundi, A. 2009. Two-dimensional digital image correlation for in-plane displacement and strain measurement: a review. *Measurement Science and Technology* [Electronic], 20(6). Available: https://doi.org/10.1088/0957-0233/20/6/062001 [2014, July 15].

Pan, B., Wu, D., Wang, Z. & Xia, Y. 2011. High-temperature digital image correlation method for full-field deformation measurement at 1 200 °C. *Measurement Science and Technology* [Electronic], 22(1). Available: https://doi.org/10.1088/0957-0233/22/1/015701 [2015, October 14].

Panait, C.G., Zielińska-Lipiec, A., Koziel, T., Czyrska-Filemonowicz, A., Gourgues-Lorenzon, A.-F. & Bendick, W. 2010. Evolution of dislocation density, size of subgrains and MX-type precipitates in a P91 steel during creep and during thermal ageing at 600 °C for more than 100,000 h. *Materials Science and Engineering A*, 527(16-17):4062-4069.

Panait, C.G., Bendick, W., Fuchsmann, A., Gourgues-Lorenzon, A.-F. & Besson, J. 2010. Study of the microstructure of the Grade 91 steel after more than 100,000 h of creep exposure at 600 °C. *International Journal of Pressure Vessels and Piping*, 87(6): 326-335.

Parker, J. 2013. Creep cavitation in CSEF steels, in *Advances in Materials Technology for Fossil Power Plants - Proceedings from the 7th International Conference*. Waikoloa: ASM International. 714–731.

Parker, J.D. & Siefert, J.A. 2018. Creep fracture in tempered martensitic steels. *Materials at High Temperatures*, 35(6):491-503.

Paterson, I.R. & Wilson, J.D. 2002. Use of damage monitoring systems for component life optimisation in power plant. *International Journal of Pressure Vessels and Piping*, 79:541-547.

Payton, E.J., Aghajani, A., Otto, F., Eggeler, G. & Yardley, V.A. 2012. On the nature of internal interfaces in a tempered martensite ferritic steel and their evolution during long-term creep. *Scripta Materialia*, 66(12):1045-1048.

Penny, R.K. & Marriott, D.L. 1995. *Design for creep*. 2nd edition. London: Chapman & Hall.

Perrin, I.J. & Hayhurst, R. 1996. Creep constitutive equations for steel in the temperature range 600–675 °C. *Journal of Strain Analysis*, 31(4):299-314.

Pešička, J., Aghajani, A., Somsen, C., Hartmaier, A. & Eggeler, G. 2010. How dislocation substructures evolve during long-term creep of a 12% Cr tempered martensitic ferritic steel. *Scripta Materialia*, 62(6):353-356.

Pešička, J., Dronhofer, A. & Eggeler, G. 2004. Free dislocations and boundary dislocations in tempered martensite ferritic steels. *Materials Science and Engineering A*, 387-389:176-180.

Pešička, J., Kužel, R., Dronhofer, A. & Eggeler, G. 2003. The evolution of dislocation density during heat treatment and creep of tempered martensite ferritic steels. *Acta Materialia*, 51(16):4847-4862.

Ponce, J. & Forsyth, D. 2003. *Computer vision: A modern approach*. London: Prentice Hall.

Prat, O., Garcia, J., Rojas, D., Carrasco, C. & Kaysser-Pyzalla, A.R. 2010. Investigations on coarsening of MX and $M_{23}C_6$ precipitates in 12% Cr creep resistant steels assisted by computational thermodynamics. *Materials Science and Engineering A*, 527(21-22):5976-5983.

Qin, Y., Götz, G. & Blum, W. 2003. Subgrain structure during annealing and creep of the cast martensitic Cr-steel G-X12CrMoWVNbN 10-1-1. *Materials Science and Engineering A*, 341(1-2):211-215.

El Rayes, M.M. & El-Danaf, E.A. 2017. High temperature deformation behavior of as-produced and retired 9-12 % Cr power plant steel. *Materials Science and Engineering A*, 697:203-210.

Regis, V. & D'Angelo, D. 1989. Advanced residual life methods for improved design and operation. *Nuclear Engineering and Design*, 116:399-406.

Ren, M., Liang, J., Li, L., Wei, B., Wang, L. & Tang, Z. 2015. Accurate three-dimensional shape and deformation measurement at microscale using digital image correlation. *Review of Scientific Instruments* [Electronic], 86(7). Available: https://doi.org/10.1063/1.4926645 [2018, 23 September].

Reu, P. 2012. Stereo-rig design: Creating the stereo-rig layout – Part 1. *Experimental Techniques*, 36(5):3-4.

van Rooyen, M. 2019. *Data for: Creep damage assessment of ex-service 12 % Cr power plant steel using digital image correlation and quantitative microstructural evaluation* [Online]. Available: http://dx.doi.org/10.17632/hz6ptn66d6.1 [2019, July 9].

van Rooyen, M. & Becker, T. 2015. A 3D-DIC method for high temperature application. Unpublished paper delivered at the *British Society for Strain Measurement's 10th International Conference on Advances in Experimental Mechanics*. 1-3 September, Edinburgh, UK.

van Rooyen, M. & Becker, T. 2017. Characterising creep damage directly from digital image correlation displacement data. Unpublished paper delivered at the *British Society for Strain Measurement's 12th International Conference on Advances in Experimental Mechanics*. 29-31 August, Sheffield, UK.

van Rooyen, M. & Becker, T.H. 2016a. Accelerated creep strain measurement using high-temperature digital image correlation. Unpublished paper delivered at the *British Society for Strain Measurement's 11th International Conference on Advances in Experimental Mechanics*. 5-7 September, Exeter, UK.

van Rooyen, M. & Becker, T.H. 2016b. Accelerated creep deformation measurement of thermal power plant steel using digital image correlation. Unpublished paper delivered at the *South African Institute of Mechanical Engineering: Mechanical, Manufacturing and Materials Engineering Conference*. 4 November, Cape Town.

van Rooyen, M. & Becker, T.H. 2018. High-temperature tensile property measurements using digital image correlation over a non-uniform temperature field. *Journal of Strain Analysis for Engineering Design*, 53(3):117-129.

van Rooyen, M., Becker, T.H., Westraadt, J. & Marx, G. 2019a. Creep damage assessment of ex-service 12 % Cr power plant steel using digital image correlation and quantitative microstructural evaluation. *Materials* [Electronic], 12(19). Available: https://doi.org/10.3390/ma12193106 [2019, September 25].

van Rooyen, M., Becker, T., Westraadt, J. & Marx, G. 2019b. Microstructural deterioration of ex-service power plant steel using concentric backscatter imaging. Unpublished paper delivered at the *56th Congress of the Microscopy Society of Southern Africa*. 1-5 December, Langebaan.

van Rooyen, M., Becker, T.H., Westraadt, J.E. & Marx, G. 2020. Measurement of creep deformation of ex-service 12% Cr steel using digital image correlation. *Journal of Strain Analysis for Engineering Design*, 55:71–85.

Rouse, J.P., Sun, W. & Hyde, T.H. 2013. The effects of scoop sampling on the creep behaviour of power plant straight pipes. *Journal of Strain Analysis for Engineering Design*, 48(8):494-511.

Roux, E. & Bouchard, P.O. 2015. On the interest of using full field measurements in ductile damage model calibration. *International Journal of Solids and Structures*, 72:50-62.

Roy, N., Bagui, S., Sahu, J.K. & Ray, A.K. 2013. Creep characterization and damage assessment of long term service exposed P-22 grade of steel. *Materials Science and Engineering A*, 560:802-810.

Roy, N., Das, A. & Ray, A.K. 2015. Simulation and quantification of creep damage. *International Journal of Damage Mechanics*, 24(7): 1086-1106.

Sakanashi, Y., Gungor, S., Forsey, A.N. & Bouchard, P.J. 2017. Measurement of creep deformation across welds in 316H stainless steel using digital image correlation. *Experimental Mechanics*, 57(2):231-244.

Scheepers, R., Newby, M., Doubell, P. & Bezuidenhout, M.E.J. 2010. Structural integrity and lifing of components with defects, an Eskom perspective. Unpublished paper delivered at the International HIDA-5 Plant Integrity, Defect Assessment, Fitness-for-Service Conference. 23 June, Guildford, UK.

Schreier, H. & Sutton, M.A. 2002. Systematic errors in digital image correlation due to undermatched subset shape functions. *Experimental Mechanics*, 42(3):303-310.

Schreier, H., Orteu, J.J. & Sutton, M.A. 2009. *Image correlation for shape, motion and deformation measurements: basic concepts, theory and applications*. New York: Springer.

Schreve, K. 2014. How accurate can a stereovision measurement be?, in *15th International Workshop on Research and Education in Mechatronics (REM)*. 9-11 September, El Gouna, Egypt. New York City, USA: IEEE [Electronic]. Available: https://ieeexplore.ieee.org/document/6920229 [2015, November 9].

Selent, M., Abendroth, M. & Kuna, M. 2016. Experimental and numerical investigations on the creep behaviour of heat-resisting chromium steel X10CrMoVnb9-1 by means of small punch test. *Transactions of the Indian Institute of Metals*, 69(2):629-633.

Semba, H., Dyson, B. & McLean, M. 2008. Microstructure-based creep modelling of a 9 % Cr martensitic steel. *Materials at High Temperatures*, 25(3):131-137.

Shampine, L.F. & Reichelt, M.W. 1997. The MATLAB ODE suite. *SIAM Journal of Scientific Computing*, 18(1): 1-22.

Shibli, A. 2011. Boiler steels, damage mechanisms, inspection and life assessment, in J. Oakey (ed.). *Power plant life management and performance improvement*. Cambridge: Woodhead Publishing. 272-303.

Shrestha, T., Basirat, M., Charit, I., Potirniche, G.P., Rink, K.K. & Sahaym, U. 2012. Creep deformation mechanisms in modified 9Cr-1Mo steel. *Journal of Nuclear Materials*, 423(1-3):110-119.

Shrestha, T., Basirat, M., Charit, I., Potirniche, G.P. & Rink, K.K. 2013. Creep rupture behavior of Grade 91 steel. *Materials Science and Engineering A*, 565:382-391.

Silva, M.L. & Ravichandran, G. 2011. Combined thermoelastic stress analysis and digital image correlation with a single infrared camera. *Journal of Strain Analysis for Engineering Design*, 46:241-255.

Singh, R. 1995. Remaining life assessment of high temperature components using threshold stress concept. *Sādhanā,* 20(1):87-101.

Sonderegger, B., Mitsche, S. & Cerjak, H. 2008. Microstructural analysis on a creep resistant martensitic 9-12% Cr steel using the EBSD method. *Materials Science and Engineering A*, 481-482:466-470.

Sosa, J.M., Huber, D.E., Welk, B. & Fraser, H.L. 2014. Development and application of MIPAR^{TM}: A novel software package for two- and three-dimensional microstructural characterization. *Integrating Materials and Manufacturing Innovation*, 3(1):123-140.

Spigarelli, S. 2013. Microstructure-based assessment of creep rupture strength in 9Cr steels. *International Journal of Pressure Vessels and Piping*, 101:64-71.

Sposito, G., Ward, C., Cawley, P., Nagy, P.B. & Scruby, C. 2010. A review of non-destructive techniques for the detection of creep damage in power plant steels. *NDT and E International*, 43(7):555-567.

Storesund, J., Borggreen, K. & Zang, W. 2006. Creep behaviour and lifetime of large welds in X 20 CrMOV 12 1-results based on simulation and inspection. *International Journal of Pressure Vessels and Piping*, 83(11-12):875-883.

Stoyanov, M. 2013. Investigation of small punch creep testing. Unpublished doctoral dissertation. Nottingham, UK: University of Nottingham [Online]. Available: http://eprints.nottingham.ac.uk/28105/1/606096.pdf [2018, September 16].

Stracey, M.G. 2016. Continuum damage mechanics (CDM) modelling of dislocation creep in 9-12 % Cr creep resistant steels. Unpublished Master's thesis. Cape Town: University of Cape Town [Online]. Available: https://open.uct.ac.za/handle/11427/22994 [2017, August 10].

Straub, S. 1995. *Verformungsverhalten und mikrostruktur warmfester martensitischen 12 %-chromästhle*. Dűsseldorf: Fortschritt-Berichte VDI.

Straub, S., Blum, W., Röttger, D., Polcik, P., Eifler, D., Borbély, A. & Ungár, T. 1997. Microstructural stability of the martensitic steel X20CrMoV12-1 after 130000 h of service at 530 °C. *Steel Research*, 68(8):368-373.

De Strycker, M., Schueremans, L., Van Paepegem, W. & Debruyne, D. 2010. Measuring the thermal expansion coefficient of tubular steel specimens with digital image correlation techniques. *Optics and Lasers in Engineering*, 48(10):978-986.

Sun, W., Hyde, T.H. & Brett, S.J. 2008. Application of impression creep data in life assessment of power plant materials at high temperatures. *Proceedings of the Institution of Mechanical Engineers, Part L: Journal of Materials: Design and Applications*. 222(3):175-182.

Sutton, M., Wolters, W., Peters, W., Ranson, W. & McNeill, S. 1983. Determination of displacements using an improved digital correlation method. *Image and Vision Computing*, 1(3):133-139.

Sutton, M., McNeill, S., Helm, J. & Chao, Y.J. 2000. Advances in two-dimensional and three-dimensional computer vision, in P.K. Rastogi (ed.). *Topics in Applied Physics: Photomechanics*, vol. 77. Berlin: Springer. 323-372.

Sutton, M.A., Yan, J.H., Tiwari, V., Schreier, H.W. & Orteu, J.J. 2008. The effect of out-of-plane motion on 2D and 3D digital image correlation measurements. *Optics and Lasers in Engineering*, 46(10):746-757.

Swaminathan, B., Lambros, J. & Sehitoglu, H. 2013. Digital image correlation study of mechanical response of nickel superalloy Hastelloy X under thermal and mechanical cycling: Uniaxial and biaxial stress states. *Journal of Strain Analysis for Engineering Design*. 49(4):233-243.

Szabó, P.J. 2004. Microstructure development of creep resistant ferritic steel during creep. *Materials Science and Engineering A*, 387-389:710-715.

Tak, K.G., Schulz, U. & Eggeler, G. 2009. On the effect of micrograin crystallography on creep of FeCr alloys. *Materials Science and Engineering A*, 510-511:121-129.

Terada, D., Yoshida, F., Nakashima, H., Abe, H. & Kadoya, Y. 2008. *In-situ* observation of dislocation motion and its mobility in Fe-Mo and Fe-W solid solutions at high temperatures. *ISIJ International*, 42(12):1546-1552.

Tong, W. 2005. An evaluation of digital image correlation criteria for strain mapping applications. *Strain*, 41:167-175.

Touboul, M., Crepin, J., Rousselier, G., Latourte, F. & Leclercq, S. 2012. Identification of local viscoplastic properties in P91 welds from full field measurements at room temperature and 625 °C. *Experimental Mechanics*, 53(3):455-468.

Trück, B., Schneider, K. & Bürgel, R. 1991. Creep damage behaviour of 12 % Cr steel. *Nuclear Engineering and Design*, 130(1):7-11.

Tshamano, L.O. 2017. Development of the small punch test platform to evaluate the embrittlement of power plant materials. Unpublished Master's thesis. Cape Town: University of Cape Town [Online]. Available: http://hdl.handle.net/11427/27546 [2019, September 9].

Tuma, J.V. & Kosec, G. 2007. Effect of microstructure on the accelerated creep of 20CrMoV12-1 and P 91 steels. *Steel Research International*, 78(8):643-647.

Turski, M., Smith, M.C., Bouchard, P.J., Edwards, L. & Withers, P.J. 2009. Spatially resolved materials property data from a uniaxial cross-weld tensile test. *Journal of Pressure Vessel Technology* [Electronic], 131(6). Available: https://doi.org/10.1115/1.4000196 [2017, November 16].

Ule, B., Šuštar, T., Dobeš, F., Milička, K., Bicego, V., Tettamanti, S., Maile, K., Schwarzkopf, C., Whelan, M.P., Kozlowski, R.H. & Klaput, J. 1999. Small punch test method assessment for the determination of the residual creep life of service exposed components: outcomes from an interlaboratory exercise. *Nuclear Engineering and Design*, 192(1):1–11.

Ule, B., Strum, R. & Leskovsek, V. 2003. Effects of test specimen geometry on creep behaviour of 12Cr steel in miniaturised disc bend tests. *Materials Science and Technology*, 19:1771-1776.

Vijayanand, V.D., Mokhtarishirazabad, M., Peng, J., Wang, Y., Gorley, M., Knowles, D.M. & Mostafavi, M. A novel methodology for estimating tensile properties in a small punch test employing in-situ DIC based deflection mapping. *Journal of Nuclear Materials* [Electronic], 538. Available: https://doi.org/10.1016/j.jnucmat.2020.152260 [2020, August 13].

Viswanathan, R., Coleman, K. & Rao, U. 2006. Materials for ultra-supercritical coal-fired power plant boilers. *International Journal of Pressure Vessels and Piping*, 83(11-12):778-783.

Walsh, D.W., Cieslak, M.J. & Savage, W.F. 1986. Temperature measurements in resistance-heated specimens: Longitudinal gradients. *Welding Journal*, 65:184-192.

Wang, Z.Y., Li, H.Q., Tong, J.W. & Ruan, J.T. 2007. Statistical analysis of the effect of intensity pattern noise on the displacement measurement precision of digital image correlation using self-correlated images. *Experimental Mechanics*, 47(5):701-707.

Wedderburn, I., Doubell, P., Hattingh, D.G. & Newby, M. 2012. Condition monitoring of high temperature, high stress components by means of core sampling and friction weld

repair, in *18th World Conference on Nondestructive Testing*. Pretoria: South African Institute for Non-Destructive Testing.

Wen, J.F., Tu, S.T., Xuan, F.-Z., Zhang, X.-W. & Gao, X.-L. 2016. Effects of stress level and stress state on creep ductility: Evaluation of different models. *Journal of Materials Science and Technology*, 32(8):695-704.

Wen, W., Jin, X., Liu, H. & Sun, W. 2019. Determination of creep damage properties from small punch creep tests considering pre-straining effect using an inverse approach. *Mechanics of Materials* [Electronic], 139. Available: https://doi.org/10.1016/j.mechmat.2019.103171 [2020, February 28].

Wittevrongel, L., Lava, P., Lomov, S.V. & Debruyne, D. 2015. A self adaptive global digital image correlation algorithm. *Experimental Mechanics*, 55:361-378.

Woodford, D.A. 2005. Accelerated high temperature performance evaluation for alloy optimization, embrittlement and life assessment, in *Proceedings of 2005 Corrosion Conference*. 3-7 April, Houston. Houston, TX: NACE International [Electronic]. Available: https://store.nace.org/05417-accelerated-high-temperature-performance [2014, July 12].

Wu, R. & Sandström, R. 1995. Creep cavity nucleation and growth in 12Cr-Mo-V steel. *Materials Science and Technology*, 11(6):579-588.

Xiao, B., Xu, L., Zhao, L., Jing, H. & Han, Y. 2019. Deformation-mechanism-based creep model and damage mechanism of G115 steel over a wide stress range. *Materials Science and Engineering A*, 743:280-293.

Xu, Y., Liu, J.S. & Jiao, Y.X. 2019. Hot deformation behavior and dynamic recrystallization characteristics of 12Cr ultra-super-critical rotor steel. *Metals and Materials International*, 25(4):823-837.

Yadav, S.D., Sonderegger, B., Sartory, B., Sommitsch, C. & Poletti, C. 2015. Characterisation and quantification of cavities in 9Cr martensitic steel for power plants. *Materials Science and Technology*, 31(5):554-564.

Yadav, S.D., Kalácska, S., Dománková, M., Yubero, D.C., Resel, R., Groma, I., Beal, C., Sonderegger, B., Sommitsch, C. & Poletti, C. 2016. Evolution of the substructure of a novel 12% Cr steel under creep conditions. *Materials Characterization*, 115:23-31.

Yadav, S.D., Sonderegger, B., Stracey, M. & Poletti, C. 2016. Modelling the creep behaviour of tempered martensitic steel based on a hybrid approach. *Materials Science and Engineering A*, 662:330-341.

Yan, W., Wang, W., Shan, Y.-Y. & Yang, K. 2013. Microstructural stability of 9-12 % Cr ferrite/martensite heat-resistant steels. *Frontiers of Materials Science*, 7(1):1-27.

Yang, Z. & Wang, Z. wen. 2003. Relationship between strain and central deflection in small punch creep specimens. *International Journal of Pressure Vessels and Piping*, 80(6):397-404.

Yang, S., Ling, X. & Zheng, Y. 2017. Creep behaviors evaluation of Incoloy800H by small punch creep test. *Materials Science and Engineering A*, 685:1–6.

Yin, Y.F. & Faulkner, R.G. 2006. Continuum damage mechanics modelling based on simulations of microstructural evolution kinetics. *Materials Science and Technology*, 22(8):929-936.

Yin, Y., Faulkner, R. & Starr, F. 2014. Austenitic steels and alloys for power plants, in A. Shirzadi & S. Jackson (eds.). *Structural alloys for power plants: Operational challenges and high-temperature materials*. Cambridge: Woodhead Publishing. 105-152.

Yoneyama, S. 2016. Basic principle of digital image correlation for in-plane displacement and strain measurement. *Advanced Composite Materials*, 25(2):105-123.

Zhang, C., Bellet, M., Bobadilla, M., Shen, H. & Liu, B. 2011. Inverse finite element modelling and identification of constitutive parameters of UHS steel based on Gleeble tensile tests at high temperature. *Inverse Problems in Science and Engineering*, 19(4):485-508.

Zhang, D., Eggleton, C.D. & Arola, D.D. 2002. Evaluating the mechanical behavior of arterial tissue using digital image correlation. *Experimental Mechanics*, 42(4):409-416.

Zhang, X.Z., Wu, X.J., Liu, R., Liu, J. & Yao, M.X. 2017. Influence of Laves phase on creep strength of modified 9Cr-1Mo steel. *Materials Science and Engineering A*, 706:279-286.

Zhao, J., Gong, J., Saboo, A., Dunand, D.C. & Olson, G.B. 2018. Dislocation-based modeling of long-term creep behaviors of Grade 91 steels. *Acta Materialia*, 149:19-28.

Zhou, Z., Zheng, Y., Ling, X., Hu, R. & Zhou, J. 2010. A study on influence factors of small punch creep test by experimental investigation and finite element analysis. *Materials Science and Engineering A*, 527(10-11):2784-2789.

van Zyl, F.H., von dem Bongart, G., Bezuidenhout, M.E.J., Doubell, P., Havinga, F.C., Pegler, D.A.H., Newby, M. & Smit, W. 2005. Life assessment and creep damage monitoring of high temperature pressure components in South Africa's power plant, in *ECCC Creep Conference: Creep and Fracture in High Temperature Components-Design and Life assessment Issues*. London: DEStech Publications. 932-943.